

Connecting real glasses to mean-field models: A study of structure, dynamics and thermodynamics

by

Ujjwal Kumar Nandi

10PP17J26052

A thesis submitted to the
Academy of Scientific & Innovative Research
for the award of the degree of
DOCTOR OF PHILOSOPHY

in

SCIENCE

Under the supervision of
Dr. Sarika Maitra Bhattacharyya



CSIR- National Chemical Laboratory, Pune

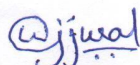


Academy of Scientific and Innovative Research
AcSIR Headquarters, CSIR-HRDC campus
Sector 19, Kamla Nehru Nagar,
Ghaziabad, U.P. – 201 002, India

July, 2021

Certificate

This is to certify that the work incorporated in this Ph.D. thesis entitled, "Connecting real glasses to mean-field models: A study of structure, dynamics and thermodynamics", submitted by Mr. Ujjwal Kumar Nandi to the Academy of Scientific and Innovative Research (AcSIR) in fulfillment of the requirements for the award of the Degree of Doctor of Philosophy in Science, embodies original research work carried-out by the student. We, further certify that this work has not been submitted to any other University or Institution in part or full for the award of any degree or diploma. Research material(s) obtained from other source(s) and used in this research work has/have been duly acknowledged in the thesis. Image(s), illustration(s), figure(s), table(s) etc., used in the thesis from other source(s), have also been duly cited and acknowledged.



Ujjwal Kumar Nandi

(Student)

30th July, 2021



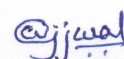
Dr. Sarika Maitra Bhattacharyya

(Supervisor)

30th July, 2021

STATEMENTS OF ACADEMIC INTEGRITY

I, Mr. Ujjwal Kumar Nandi, a Ph.D. student of the Academy of Scientific and Innovative Research (AcSIR) with Registration No. 10PP17J26052 hereby undertake that, the thesis entitled "Connecting real glasses to mean-field models: A study of structure, dynamics and thermodynamics" has been prepared by me and that the document reports original work carried out by me and is free of any plagiarism in compliance with the UGC Regulations on "Promotion of Academic Integrity and Prevention of Plagiarism in Higher Educational Institutions (2018)" and the CSIR Guidelines for "Ethics in Research and in Governance (2020)".



Signature of the Student

Name : Ujjwal Kumar Nandi

Date : 30th July 2021

Place : Pune

It is hereby certified that the work done by the student, under my/our supervision, is plagiarism-free in accordance with the UGC Regulations on "Promotion of Academic Integrity and Prevention of Plagiarism in Higher Educational Institutions (2018)" and the CSIR Guidelines for "Ethics in Research and in Governance (2020)".



Signature of the Supervisor

Name : Dr. Sarika Maitra Bhattacharyya

Date : 30th July, 2021

Place : Pune

Dedicated to my Parents and Brothers

Acknowledgements

I am really fortunate to have come across many people, who have been inspirational and supportive through my journey to Ph.D. I wish to thank all the people whose assistance was a milestone in the completion of this thesis.

I would first like to pay my special regards to my advisor Dr. Sarika Maitra Bhattacharyya for giving me the opportunity to work under her and it was very wonderful experience for me to pursue the research work under her supervision. Her immense knowledge in science has helped me to understand very deep concepts of our field in a very simple way. Her support throughout my PhD journey helped me to overcome my fears and actively present myself against every hurdle coming my way. Her student-friendly nature helped me to have long discussions with her and ask whatever comes to my mind with ease and grab more and more knowledge from her.

I am grateful to my Doctoral Advisory Committee members Dr. Suresh Bhat, Dr. Ram Rup Sarkar and Dr. K. Krishanmoorthy for continuously evaluating my research work and offering insightful suggestions that helped me improve my research work. Their continuous assessment and recommendations encouraged me to explore the greater details of my research topic with an interdisciplinary perspective. I am also grateful to my former Doctoral Advisory Committee member Dr. Guruswami Kumaraswami for his critical analysis of my research work.

I offer my sincere gratitude to Dr. Suman Chakrabarty for giving wonderful ideas in my research work. I thank to Dr. Debasree Ghosh and Dr. Suman Chakrabarty for inspiring me to learn different new technique to write efficient code.

I acknowledge the former Directors of NCL, Dr. Saurav Pal and Dr. Ashwini Kumar Nangia, the present Director, Dr. Ashish Lele, and the HOD of the PSE Division, Dr. S.K. Asha for providing the infrastructure to carry out my research at CSIR-National Chemical Laboratory and for being prompt and responsive to students' requirements. I would like to thank Mr. P.K. Purushothaman, Ms. Komal, and other members of the Student Academic Office and Administrative Section of CSIR-NCL who have patiently entertained and guided us through all

our queries regarding AcSIR protocols, and fellowship and contingency disbursement. I am thankful to CSIR-HRDG for providing me the SRF fellowship to continue my research and AcSIR for providing me the platform to pursue the degree.

I express my sincere thanks to Prof. Walter Kob for giving me the opportunity to work with him.

I am privileged to work with Prof. Trond Ingebringtsen. I have discussed with him on many topics, when I visited Roskilde University, Denmark. He is an extraordinary as a scientist and as a person.

I express my sincere thanks to Prof. Shiladitya Sengupta for helping me in my PhD work.

I thank Prof. Chandan Dasgupta, Prof. Smarajit Karmakar, Prof. Prabal Maity and Dr. Mohd Moid who gave me the opportunity to work with them.

I am fortunate enough to have found brilliant lab mates. I thank my present and former group members Sanket, Palak, Mohit, Sayantan, Manoj, Alamgir, Atreyee and Indranil for the fruitful discussions and various questions in the group meetings. Sanket is the most junior in our group and he has very honest opinion. Mohit, a talented cool guy and very soft spoken. Palak, a very simple girl and she is very hard working and a quick learner. Manoj Da, a very talented guy who does whatever thing but very efficiently and passionately. I have discussed on many scientific and other topic and he was always ready to listen. Sayantantan Da, a multi skilled guy. We have spent lots of time for scientific discussion and for other activity.

I express my deepest appreciation for some very caring and warm-hearted room mates that include Dr. Souvik Chakrabarty, Dr. Aniruddha Basu, Dr. Saikat Chowdhury, Dr. Abhik Banerjee, Dr. Bipul Biswas. I always take many advice from Souvik da for my professional and personal life, according to me he is a wise and very realistic person. Anirudhha Da is very energetic and helpful guy. He was my cooking partner as well. Saikat da is himself a knowledge house. I have learnt lots of things from him. I have improved my general knowledge discussing with Souvik Da and Saikat Da. Bipul is very down to earth and highly intelligent guy. He is my university class mate as well. I have got lots of inspiration from him.

I want to give a special thanks to Sutanu, Rupa and Piyali for always being there with me to help whenever I am in need. I am lucky to have such friends in my PhD tenure.

I thank all my M.Sc batch mates for their inspiration. I am lucky to have friends like them.

I am really proud of my all friends from Belur Vidyamandira (my college). I thank all of them for their supports and encouragements. Getting a friend circle

like this is itself an achievement in my life.

I thank my school and college teachers for encouraging me to do better in my life and believing in me.

I want to give special thanks to Animesh, Asish for their presence in my life in the difficult situations.

I am privileged to have some friends from my childhood. I thank Chandan, Tanmoy, Ramakrishna for their love and support. Whenever I go home always I get lovely company from Tanmoy and Ramakrishna. I always get love and support from Chandan in every step of my life. Even though we have both changed a lot over the years, I still feel that I am as close to you as ever.

I am and will always remain indebted to my parents, Mr. Mahadeb Nandi and Mrs. Shyama Rani Nandi, and my brothers Mr. Gautam Nandi and Mr. Nitai Chandra Nandi for everything that I am and ever will be in my life. This thesis is the outcome of relentless struggles and innumerable sacrifices of my parents and my brothers who stood like pillars to support me throughout the journey. I am fortunate enough to have them as a family that has always been liberal and extremely supportive of my choices knowing not where it will take me, and yet believing in me, guiding me through the pros and cons of my decisions that has helped me grow as a person. Words can not explain their contributions in my life.

Synopsis

The aim of the thesis is threefold

1. To connect the mean-field behaviour with the real three dimensional system where structural, dynamic and thermodynamic properties have been studied.
2. To find the jamming transition in the mean-field system in the three dimensional limit.
3. To examine the glass forming ability and the role of mixing entropy in the system.

The thesis is divided into eight chapters. The outline of each chapters are given below

- Chapter1 introduces to the general area of research described in the thesis. A brief summary to the phenomenology of the dynamic and thermodynamic signatures of slow dynamics and the relevant theoretical approaches are discussed.
- Chapter2 describes the different properties of the glass transition. The definitions and different technique for the calculation of different properties are discussed.
- The dynamics and thermodynamics in the glass-forming system are still not completely understood. Most of the theories in the glass community are mean-field in nature. It cannot fully explain the experiments and simulations results, and thus we have found an innovative way where a 3 dimensional system develops mean-field like properties. In chapter3, we propose a novel model for a glass-forming liquid which allows to switch in a continuous manner from a standard three-dimensional liquid to a fully connected mean-field model. This is achieved by introducing k additional particle-particle interactions which thus augments the effective number of neighbors of each particle. Our computer simulations of this system show

that the structure of the liquid does not change with the introduction of these pseudo neighbors and by means of analytical calculations, we determine the structural properties related to these additional neighbors.

- In chapter4, we discuss the relaxation dynamics of the mean-field system slows down very quickly with increasing k and that the onset and the mode-coupling temperatures increase. The systems with high values of k follow the MCT power law behavior for a larger temperature range compared to the ones with lower values of k and the heterogeneity of the system decreases with increase in k .
- In chapter5, we study the thermodynamic properties of the mean-field model, we surprisingly find that the usual thermodynamic integration(TI) method of calculating the entropy provides unphysical results. It predicts the vanishing of configurational entropy at state points at which both the collective and the single-particle dynamics of the system show complete relaxation. We then employ a new method known as the two-phase thermodynamics (2PT) method to calculate the entropy. We find that in the temperature range studied, the entropy calculated via the 2PT method satisfies the Adam-Gibbs (AG) relationship between the relaxation time and the configurational entropy, whereas the entropy calculated via the TI method shows a strong violation of the same.
- In chapter6, we show the behavior of the mean-field system near the jamming transition. We find the jamming transition happens at lower volume fraction with increase in k and it shows a power-law behavior of pressure and energy of the system with volume fraction in the vicinity of the jamming transition. The contribution of the nearest neighbor in the coordination number at the jamming state decreases with increasing in k and the contribution of the pseudo neighbor increases with k .
- Most of the systems which show glassy behavior have global crystalline order. Glass forming ability (GFA) depends on the barrier to crystallize in the system. It can easily crystallize if the system crosses the barrier. With the increase of the computational facility, it has been found some glass forming systems show partial crystallinity. In chapter7, we have estimated the glass forming ability of some glass forming systems. We have shown which systems are best glass former. We have found some system shows higher free energy barrier because of the loss of demixing entropy but for some other system it has lower free energy barrier for

different crystalline structure which does not allow this system to be a good glass former.

- In chapter8, we finally conclude the whole work and discuss the future perspective of our work.

Contents

1	Introduction to glassy dynamics, thermodynamics and existing theories	14
1.1	Introduction	14
1.2	Slow Dynamics	15
1.2.1	Two step relaxation	15
1.2.2	Dynamical Heterogeneity	17
1.2.3	Fragility	18
1.3	Breakdown of Stokes-Einstein relationship	19
1.4	Jump in specific heat	21
1.5	Entropy crisis	21
1.6	Theories of glass	22
1.6.1	Free Volume Theory	23
1.6.2	Adam Gibbs Theory	24
1.6.3	Random First Order Transition theory	25
1.6.4	Mode coupling theory	27
1.7	Conclusions	28
2	Properties of glass transition	33
2.1	Structural properties	33
2.2	Dynamic properties	34
2.2.1	Relaxation time	34
2.2.2	Dynamic Fragility	37
2.2.3	MCT Power law behavior	37
2.2.4	Dynamic Heterogeneity	37
2.3	Thermodynamic Properties	38
2.3.1	Excess entropy	39
2.3.2	Vibrational Entropy	42
2.3.3	Configurational entropy	43
2.4	Hessian Calculation	43
2.5	Weight histogram analysis method	46

3	Connecting real glasses to mean-field models: A study of structure	51
3.1	Introduction:	51
3.2	Details of system and simulations	53
3.3	Results	54
3.3.1	Structure of the liquid	54
3.3.2	Static properties of the pseudo neighbors	55
3.4	Inherent structure in the mean-field system	60
3.5	Conclusion	60
4	Connecting real glasses to mean-field models:A study of dynamics	65
4.1	Introduction:	65
4.2	Results	66
4.2.1	Relaxation dynamics	66
4.2.2	MCT power law	74
4.2.3	Wave-vector Dependence of Relaxation Process	76
4.2.4	Dynamic Heterogeneity	76
4.3	Conclusion	87
5	Connecting real glasses to mean-field models:A study of thermodynamics	93
5.1	Introduction:	93
5.2	Details of system and simulations	95
5.3	Different methods to calculate entropy	95
5.4	Results for Mean-field system	96
5.4.1	Entropy using thermodynamic integration method	96
5.5	Possible reasons for the failure of the TI method	99
5.5.1	Ideal gas entropy	99
5.5.2	Excess entropy and the validity of the Rosenfeld relationship	102
5.5.3	Entropy using the 2PT method	103
5.6	Pair and higher order entropy terms	104
5.6.1	MCT power law behavior	105
5.6.2	Residual multiparticle entropy	108
5.7	Conclusion	111
6	Connecting real glasses to mean-field models:A study on jamming	119
6.1	Introduction:	119
6.2	Simulation details	121

6.3	System details	121
6.4	Inherent structure	122
6.5	Result and discussion	123
6.6	Conclusion	129
7	Composition dependence of the glass forming ability in binary mixtures: The role of demixing entropy	136
7.1	Introduction	136
7.2	Simulation Details	138
7.3	Definitions	139
7.3.1	Bond Orientational Order Parameter	139
7.3.2	Relaxation Time	141
7.4	Results	141
7.4.1	Melting Temperatures	141
7.4.2	Free Energy of Nucleation and Role of Demixing	143
7.4.3	Analysis from Energetics	148
7.4.4	Glass Forming Ability- Role of Demixing and Eutectic Point	152
7.5	Conclusion	153
8	Summary and future work	158
8.1	Summary	158
8.2	Future work	160

Chapter 1

Introduction to glassy dynamics, thermodynamics and existing theories

1.1 Introduction

Glass is very useful in our daily life and ubiquitous in nature. It is very important in the processing of foods. Best known engineered glass is made of silica. It has lots of use in optical fibre, preservation of insect life in extremely cold weather. Some metallic glasses are used in the soft magnetism and corrosion resistance. The basic features of the glass are solid and amorphous.

Glasses can be formed in many ways, and one of the methods is, to begin with, liquid and cool it down. If we cool a liquid, it undergoes crystallization below melting temperature (T_m) and forms a crystal. But if we cool the liquid fast enough, it does not get time to crystallize and remains in a liquid state below the melting temperature, called supercooled liquid. On further cooling the supercooled liquid, it goes to a glassy state. Glass is mechanically solid and structurally liquid. There is no specific definition of glass transition temperature (T_g). It depends on the rate of cooling of the liquid. It is assumed that the liquid reaches to glassy state if the viscosity of the liquid becomes 10^{12} to 10^{13} poise. The schematic diagram (Fig.1.1) shows how T_g depends on the rate of cooling. There are few dynamic properties in the glassy systems that show the signature of the glassy nature.

As the supercooled liquid state remains in the metastable state, the dynamic and thermodynamic properties of the glass are predicted by the study of the equilibrium supercooled liquid state. Most of the theories in the glass are mean-field theory, and mean-field systems in experiments and simulation are very

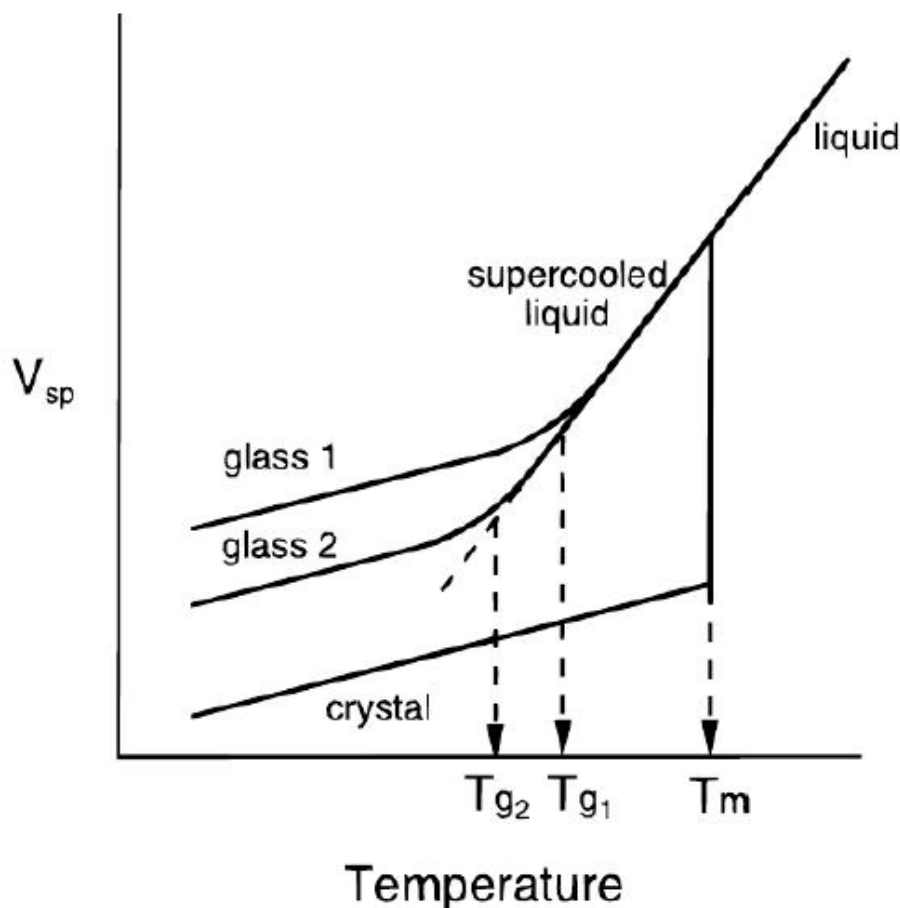


Figure 1.1: Schematic representation of glass transition phenomena. T_g depends on the rate of cooling. Reprinted with permission from [1]. Copyright [1996] American Chemical Society.

rare.

1.2 Slow Dynamics

As the liquid bypasses the crystallization, then upon cooling the liquid, its dynamics slows down very fast. In the end, the relaxation time of the system exceeds the experimental time scale and this out of equilibrium liquid forms glass. Most of the properties of glass are found in the equilibrium supercooled liquid state. The properties of the supercooled liquid are still not fully understood.

1.2.1 Two step relaxation

The most accepted definition of glass transition is purely dynamic. Viscosity or diffusion, which marks the onset of glassiness, is the integral of some dynamic

correlation functions. These integrals give a number wrapping up the entire correlation function. Thus lots of information on the glass are lost behind the number. So it is good to study the correlation function instead of its integration. The dynamic correlation function is defined as

$$c(t) = \frac{1}{N} \sum_{k=1}^N \langle \phi_k(t) \phi_k(0) \rangle$$

where $c(t)$ is the correlation function between two generic quantities $(\phi_k(t), \phi_k(0))$ with time difference t and k is the particle identity. The most studied correlation function in the liquid is the correlation between the Fourier transform of the density fluctuations. Fourier transform of the density fluctuation is $\delta\rho_k(q, t) = \exp[-iq \cdot r_k(t)]$ for fixed momentum q . This dynamic correlation is correlated with the intermediate scattering function $F_S(q, t)$ [3]. The correlation at high temperature decays very quickly. It shows a very short-time ballistic regime (see Fig.1.2) without colliding other particles and then followed by a dissipate regime, which shows exponential decay

$$c(t) = c_0 \exp(-t/\tau)$$

τ is the relaxation time and c_0 is constant.

With lowering the temperature, τ grows rapidly. As the system goes towards glass transition temperature, the numerical value of τ increases, which does not show any qualitative signature of glass. But the dynamic correlation shows the qualitative shape, which changes significantly when the system approaches T_g . As the temperature is lowered, the correlation function starts to show two-step relaxation, as shown in Fig.1.2. Two-step relaxation is the most insightful remark in the study of glass transition. One is short time relaxation called β relaxation, and another is long time relaxation called α relaxation. β relaxation overlaps with the early α relaxation process. β process shows the plateau in the decay of the correlation. Region of plateau increases with decreasing temperature, i.e. approaching T_g , plateau region becomes large. The origin of the two-step relaxation is the caging in the system, i.e. when particles can not move for a while when their neighbor can not move. This arresting time increases with lowering the temperature, which is the β region, and after a while, the correlation function decay, which is the α relaxation.

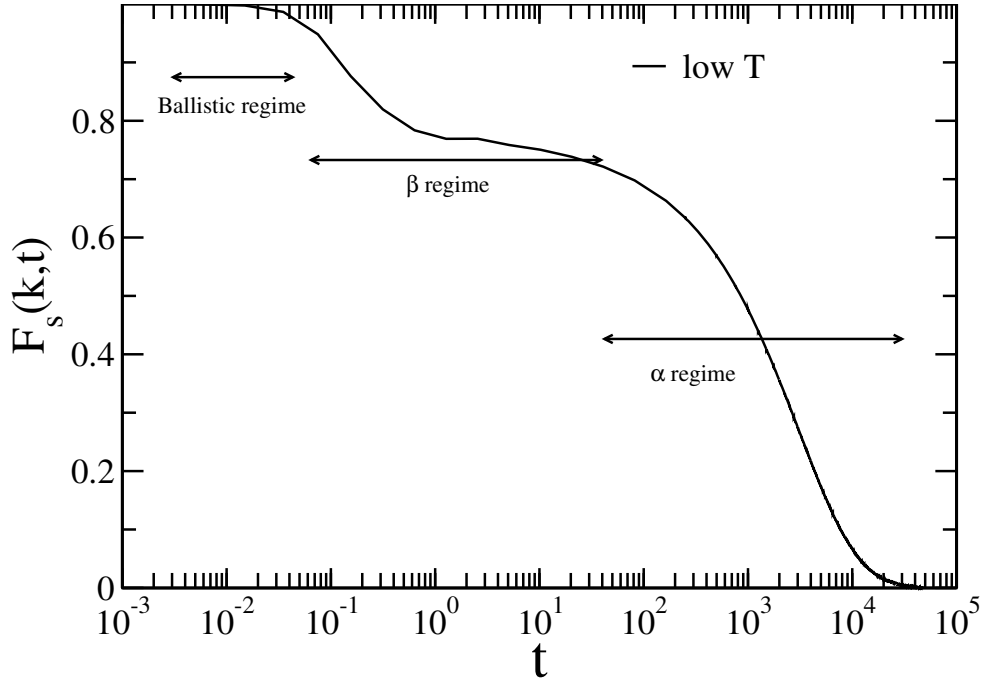


Figure 1.2: $F_s(k, t)$ at low temperature. Three regions of the relaxation are shown here.

1.2.2 Dynamical Heterogeneity

The dynamic correlation function decays into two steps at a lower temperature, which does not mean that the decay from the plateau is exponential. This late relaxation is non-exponential. The late relaxation follows Kohlraush-Williams-Watts[4, 5] stretched exponential form.

$$c(t) = c_0 \exp(-(t/\tau)^\beta)$$

Where $\beta < 1$. The value of β decreases with decreasing the temperature [6]. But $\beta = 1$ at high temperature where correlation function decays exponentially. The origin of the non-exponential relaxation is due to the heterogeneous dynamics in the system. When the different region of the system has different relaxation time with pure relaxation then averaging over all region would give a non-exponential decay. Another explanation is homogeneous relaxation, where each region has equally non-exponential relaxation.

The supercooled liquids in experiment[7, 8, 9, 10] and numerical simulation [11, 12, 13] have showed the relaxation is heterogeneous. Thus there are some regions where particles move fast and some regions where particles move slow. The slowing down of the dynamics is associated with the length scale of the system. This dynamic length scale increases with decreasing temperature or increasing density.

1.2.3 Fragility

The Arrhenius law is the benchmark for the increase of relaxation time. That's why the data is generally plotted as the function of $\frac{1}{T}$.

$$\tau = \tau_0 \exp(\Delta E/T)$$

where ΔE is the activation energy. The Angell's plot [14, 15] shows how the viscosity of different systems changes with temperature with respect to their glass transition temperature. Some systems show that the logarithmic of viscosity increases linearly with $\frac{1}{T}$ which follows Arrhenius behaviour. Some other systems show that the increase of viscosity becomes steeper and steeper with decreasing temperature. When both kinds of systems reach a glassy state, one which follows Arrhenius law is called strong glass. The other has steeper relaxation time with decreasing temperature (non-Arrhenius), which is called fragile glass. For strong liquid and high temperature fragile glass-former liquid, this ΔE is independent of temperature. Thus the logarithmic viscosity shows the linear behavior. But the activation energy of supercooled liquid at low temperature has temperature dependence and one possible model for the temperature dependence of relaxation time in supercooled liquids is the Vogel-Fulcher-Tammann (VFT) expression,

$$\tau = \tau_0 \exp\left[\frac{A}{T - T_0}\right] \quad (1.1)$$

where τ_0 is the high temperature relaxation time, A is the temperature dependent fragility index and T_0 is the divergence temperature where the relaxation time of the system diverges and the temperature is known as the VFT temperature. The fragility of a system measures how steeply the viscosity (or relaxation time) increases and fragility increases as the system approaches the glass transition temperature. Fragility is estimated as

$$m = \left[\frac{d(\log(\tau/\tau_0))}{d(T_g/T)} \right]_{T=T_g} = K \left(1 + K \frac{T_0}{A} \right) \quad (1.2)$$

where $K = \log(\tau(T_g)/\tau_0)$

1.3 Breakdown of Stokes-Einstein relationship

Diffusion coefficient is very important parameter in the study of the glass transition. The diffusion equation of a tagged particle in a liquid with a given density $\rho(r, t)$ is

$$\frac{\partial \rho(x, t)}{\partial t} = D \frac{\partial^2 \rho(x, t)}{\partial x^2} \quad (1.3)$$

where D is the diffusion coefficient of the tagged particle. Mean-square displacement is the average distance travelled by particle.

$$\langle x^2(t) \rangle = \int_0^\infty dx x^2 \rho(x, t) \quad (1.4)$$

Time derivative of the mean-square displacement relates the diffusion and the mean-square displacement as

$$\frac{d}{dt} \langle x^2(t) \rangle = \frac{d}{dt} \int_0^\infty dx x^2 \rho(x, t) \quad (1.5)$$

Now if we apply Eq.1.3 into Eq.1.5 then we get

$$\frac{d}{dt} \langle x^2(t) \rangle = D \int_0^\infty dx x^2 \frac{\partial^2 \rho(x, t)}{\partial x^2} \quad (1.6)$$

$$\frac{d}{dt} \langle x^2(t) \rangle = D \left[x^2 \frac{\partial \rho(x, t)}{\partial x} \Big|_0^\infty - 2 \int_0^\infty dx x \frac{\partial \rho(x, t)}{\partial x} \right] \quad (1.7)$$

Using the boundary condition, the solution of the Eq.1.7 becomes

$$\langle x^2(t) \rangle = 2Dt \quad (1.8)$$

Mean-square displacement can be calculated directly from the particle velocity

$$\langle x^2(t) \rangle = \int_0^t dt' \int_0^t dt'' \langle v(t') v(t'') \rangle \quad (1.9)$$

where $v(t')$ and $v(t'')$ are the velocity of particle at time t' and t'' respectively.

If we use the concept of time translation and compare Eq.1.9 and Eq.1.8 we get

$$D = \int_0^t dt' \langle v(t') v(0) \rangle \quad (1.10)$$

We can link diffusion to friction using the Langevin equation for the particle

of mass m

$$m\dot{v}(t) = -\zeta v(t) + f(t) \quad (1.11)$$

ζ is the frictional coefficient and $f(t)$ noise with delta-correlated in time. The solution of the differential equation (Eq.1.11) is given as

$$v(t) = \exp(-\zeta t/m)v(0) + \int_0^t dt' \exp(-\zeta(t-t')/m)f(t')/m \quad (1.12)$$

The relation between amplitude of friction and temperature is given by the static fluctuation dissipation theorem

$$\langle f(t)f(t') \rangle = 2\zeta k_B T \delta(t-t') \quad (1.13)$$

Now if we compare Eq.1.5 and Eq.1.13 and put into Eq.1.10 then we obtain the Einstein's relation for the diffusion coefficient.

$$D = \frac{k_B T}{\zeta} \quad (1.14)$$

The stoke's relation links viscosity (η) of the system with the frictional coefficient (ζ) as

$$\zeta = C\eta R \quad (1.15)$$

where C is constant and R is the radius of the particle.

Combining Einstein's relation and Stoke's relation, we get the Stokes-Einstein relation given by

$$D = \frac{k_B T}{C\eta R} \quad (1.16)$$

The Stokes-Einstein relation usually holds for a diffusing sphere with a size larger than the size of molecules which comprises the fluid. It also shows similar behavior whether describing self-diffusion of a molecules surrounded by the same size of molecule. $\frac{D\eta}{T}$ should be constant irrespective of the temperature of the system. Usually, we use α relaxation time equivalent of $\frac{\eta}{T}$ to save the computational cost. Some time the Stokes-Einstein relation fails when the viscosity of the system becomes very high. The breakdown of the Stokes-Einstein relation happens because of the dynamic heterogeneity in the system. Most of the glass-forming system follows this relation at high temperature and break down happens when the system undergoes supercooling.

1.4 Jump in specific heat

When the system reaches a glassy state, then the system can not visit the whole phase space. Below the glass transition temperature, it is impossible for the system to be in equilibrium. Because of the unavailability of the whole phase space system lacks accessibility of the degrees of freedom. Thus the inaccessibility of the degrees of freedom reduces the specific heat of the system. It causes a drop of specific heat of the order 2 or 3 at T_g . The experimental time scale becomes smaller than the ergodicity time. The time taken by the system to visit a representative fraction of the phase space is called the ergodicity time. The specific heat (C_p) drops to the value of the crystalline phase. The crystal is thermodynamically at global energy minima vibrates around its equilibrium position with a frequency without any configurational rearrangement. The nature of the specific heat shows that the particles in the glassy state vibrate around their equilibrium position without any rearrangement of the configurations. However, the ergodicity is broken in the glass and the confined particle position analogue to crystal particle results in a similar specific heat below the glass transition temperature.

1.5 Entropy crisis

It seems impossible to look at the system at low temperatures because we do not have enough time to make an equilibrium measurement. Kauzmann [15] extrapolated equilibrium data to low temperature and predicted the thermodynamic properties (entropy, enthalpy, free energy) at that temperature. The most famous analysis was the entropy at low temperature. The entropy of the liquid decreases with decreasing temperature, and it decreases faster than the crystal since the entropy is the derivative of specific heat and the specific heat of liquid is higher than the crystal.

$$\left. \frac{dS}{dT} \right|_p = \frac{C_p}{T} \quad (1.17)$$

The difference between the liquid and the crystal entropy is called excess entropy

$$\Delta S(T) = S_{liquid}(T) - S_{crystal}(T) \quad (1.18)$$

ΔS decreases when the temperature is decreased. Normalizing the ΔS with its value at melting temperature (T_m), i.e. if we plot $\frac{\Delta S(T)}{\Delta S(T_m)}$ vs $\frac{T}{T_m}$ then we can see different liquids in the same plot (Fig.1.3). For some liquids, we find that extrapolated excess entropy goes to zero at finite temperature, and that

temperature is defined as the Kauzmann temperature (T_K). This suggests that the entropy of the supercooled liquid is lower than the entropy of the crystal below T_K . This phenomenon is called the Kauzmann paradox or entropy in crisis. Though the glass is in a metastable state, the entropy is lower than the crystal, energetically more stable state. This is counterintuitive. Thus T_K is a very significant quantity to study on.

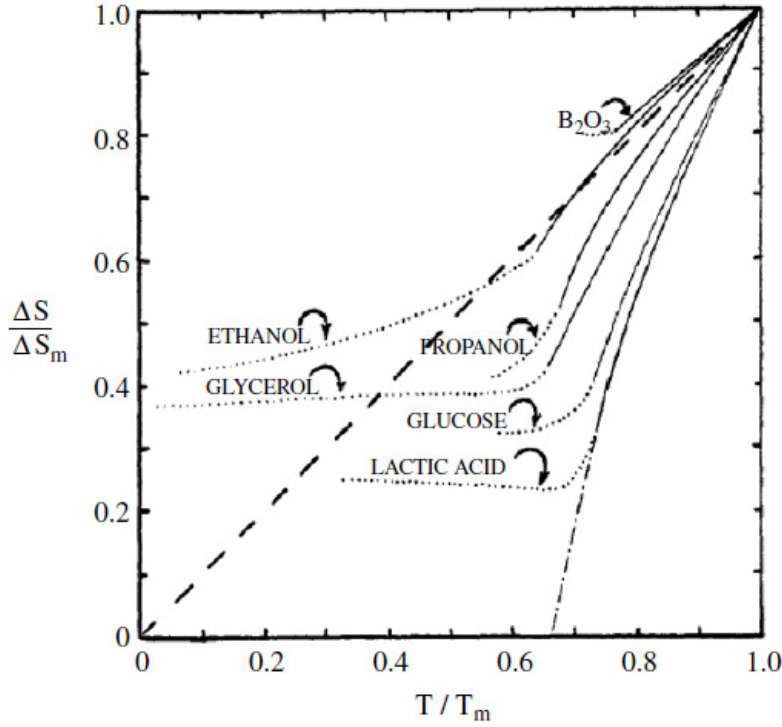


Figure 1.3: Kauzmann entropy crisis. The low temperature extrapolation of the entropy normalizing by the melting point value. In several cases excess entropy vanishes at temperature larger than zero. [Figure is taken from [24]]

The other thermodynamic variables also show the difference between crystal and liquid vanishes at finite temperature. But the temperature at which ΔS disappears, the free energy difference (ΔF) does not vanish. Kauzmann noticed that ΔF does not go to zero extrapolating the equilibrium data. Thus T_K can not be the locus of continuous transition from liquid to crystal.

1.6 Theories of glass

As how a supercooled liquid becomes amorphous rigid solid is poorly understood, glass transition remains an active problem in the field of statistical mechanics. There are several theories and models for the glass transition, and no one is superior to the other. There is no so-called “The Theory” for glass transition, and all the theories have their advantages and disadvantages. We will discuss

some of them which are more popular.

1.6.1 Free Volume Theory

Free Volume Theory in the glassy system [17] is one of the earlier theories to understand the glass transition phenomenon. It was first introduced by Cohen and Turnbull [17, 18, 19] and later on it was extended by Cohen and Grest [19, 20]. The free volume theory in glass relies on a set of assumptions.

- A volume in molecular scale of each molecule can always be defined.
- There is a excess volume beyond a critical value v_c of v , $v_f = v - v_c$. This excess volume can be treated as free.
- The redistribution of the free volume $v_f = v - v_c$ does not associate with free energy.
- A molecule can only move when v_f for that molecule becomes larger than a certain value v_f^* .

From the last assumption, it can be said that when the local volume v exceeds some critical volume due to the spontaneous density fluctuation, it results in diffusive transport. Thus the molecular motion goes to a diffusive regime when v exceeds $v_c + v_f^*$, where v_f^* is the minimum amount of free volume required to diffuse. So we can write the average diffusion coefficient as below,

$$D = \int_{v_f^*}^{\infty} D(v)P(v)dv. \quad (1.19)$$

Where $D(v)$ is the diffusion coefficient of a molecule with free volume v and $P(v)$ is the probability density of finding a cell with a free volume between v and $v+dv$. Now, we have to find $P(v)$ for a system in which no energy exchange is associated with a redistribution of the free volume. The average free volume is

$$v_f = V_f/N \quad (1.20)$$

where V_f is the total free volume and N is the total number of molecules in the system. Total free volume can be divided into small regions with average free volume v_i of each molecule in the i^{th} region. If N_i is the number of molecules in the i^{th} region, then we can write

$$\gamma \sum_i N_i v_i = V_f \quad (1.21)$$

where γ is a geometric factor which corrects the overlap of the free volume.

$$\sum_i N_i = N \quad (1.22)$$

The number of ways of redistributing the free volume without changing the N_i is

$$\mathcal{W} = N_i / \prod_i N_i! \quad (1.23)$$

Now using Lagrange's multiplier method to maximize \mathcal{W} for a given N and V_f , we get

$$N_i = \exp[-(\lambda + \beta v_i)] \quad (1.24)$$

where λ and β are the Lagrangian multipliers. By obtaining λ and β from Eq.(1.21) and (1.24), and passing them to the continuum limit for v_i , we get

$$P(v) = (\gamma/v_f) \exp[-\gamma v/v_f] \quad (1.25)$$

As $D(v)$ is a slowly varying function, so we put it equal to $D_{v_f^*}$ in Eq. (1.19) and get

$$D = A \exp[-\gamma v_f^*/v_f] \quad (1.26)$$

Where A is constant. Thus it predicts that D will vanish when no free volume is available for the random redistribution (i.e. $v_f = 0$). Since the free volume may be assumed to possess a linear temperature dependence, over a narrow temperature interval (i.e. $v_f \propto \alpha_p(T - T_0)$, where α_p is the coefficient of thermal expansivity), so eq(1.26) can be written as

$$\eta(T) = A \exp[B/(T - T_0)] \quad (1.27)$$

which is the Vogel-Fulcher-Tamann (VFT) [21, 22, 23] form, where T_0 is the temperature at which the free volume vanishes (and thus viscosity diverges).

1.6.2 Adam Gibbs Theory

Adam, Gibbs and Di Marzio first attempted to connect the increase of correlation length with the decrease of configurational entropy. Adam-Gibbs[24, 25] first connected the dynamic quantity (relaxation time) with the thermodynamic quantity (configurational entropy). A remarkable calculation by Flory[26] in the context of the polymer where he obtains a temperature (melting temperature) below which the number of accessible configurations becomes less than 1. The basic idea of the Adam-Gibbs relation is that the relaxation happens at low

temperature through a larger region of correlated particles, and this region is called the cooperative rearranging region (CRR)[25, 27, 28]. Adam-Gibbs defined the CRR as the smallest region which can be rearranged without affecting the surroundings. The number of states (Ω) available to a CRR is constant, and it is independent of temperature (T) or size of the CRR. So the total number of available states can be found in the global system is

$$\mathcal{N} = \Omega^{N/n}, \quad (1.28)$$

where N is the total number of particles in the system and n is the average number of particles in each CRR. Then the total number of CRRs is N/n. The configurational entropy S_c of the system is the logarithmic density of the number of the locally stable states.

$$S_c = \frac{1}{N} \log \mathcal{N} = \frac{\log \Omega}{n}. \quad (1.29)$$

The above equation can be rearranged and the average number of particles in each CRR can be written as

$$n = \log \Omega / S_c. \quad (1.30)$$

As S_c decreases with decreasing temperature and Ω is constant, there is an increase in n with decreasing temperature. As the increase in n is equivalent to the increase in the length scale of CRR, which is related as $n \propto \xi^d$ where ξ is the linear size of CRR. The relation between the size of the CRR and the energy barrier (Δ) to rearrange the region is proportionate in nature. According to the AG theory, $\Delta \sim n \sim 1/S_c$. If we compare it with the Arrhenius Law, we get

$$\tau = \tau_0 \exp\left(\frac{B}{TS_c(T)}\right), \quad (1.31)$$

where B is a constant. Thus AG theory can explain how the length scale of the system and the relaxation time increases when the configurational entropy and the temperature decreases. This theory is very useful and well accepted in the study of glass-forming liquids to understand the behaviour of relaxation time with configurational entropy.

1.6.3 Random First Order Transition theory

Random first-order transition (RFOT) theory [29, 30, 31, 32] proposed by Kirkpatrick, Thirumalai and Wolynes give insight into the relation between supercooled liquid and p-spin class of mean-field glasses. If we agree that the finite-dimensional system has many states, then a different physical portion of the

system can be found in different states. An interface separates each portion of the system. There is some energy cost associated with the interface because of the dissimilar amorphous configuration between two physical portions of the system. Thus we have two different states separated by an interface that causes surface tension. The energy cost is proportional to the surface tension and the surface area. As the surface tension is the free energy cost per unit area to create an interface, free energy cost in the supercooled liquid can be written as,

$$\Delta F_{cost} = Y R^\theta \quad (1.32)$$

$\theta \leq d - 1$, where d is the physical dimension of the system. Y is the generalised surface tension to create an interface, and R is the size of the domain. This R is the range of the CRR region as shown by the AG theory. Now the question is that what fixes the critical size of the region. AG theory fixes the size by the pure combinatorial way neglecting the surface tension between the CRRs. In contrast, RFOT theory takes inspiration from the classical nucleation theory (CNT), where the size of the critical nucleus is fixed, balancing surface tension cost and thermodynamic gain. Surface tension cost is already defined earlier. The thermodynamic drive comes from the fact that to rearrange a droplet of radius R , having an exponential number of states in the region, the rearrangement can happen to any state. If the region does not rearrange, the region stays in a single state, which results in an entropic penalty. Thus the thermodynamic drive is the free energy contribution coming from the configurational entropy of that region.

$$\Delta F_{gain} = -T S_c R^d \quad (1.33)$$

Where T is the temperature and S_c is the configurational entropy. Thus the total free energy of the system will be,

$$F_{tot} = \Delta F_{cost} + \Delta F_{gain} = Y R^\theta - T S_c R^d \quad (1.34)$$

Classical nucleation theory states that a new state will form when the two opposing forces (surface tension and thermodynamic gain) will balance, $\frac{dF_{tot}}{dR} = 0$ and as a result a new length scale comes out,

$$\xi = \left(\frac{Y(T)}{T S_c} \right)^{\frac{1}{d-\theta}} \quad (1.35)$$

1.6.4 Mode coupling theory

Mode coupling theory (MCT) is a microscopic theory[33, 34, 35, 36] for the glassy dynamics. This is the first theory, which can quantify and predicts the dynamics in glass-forming systems. In the earlier sections, it has been discussed about the physical picture of the glass forming system considering cooperativity or the number of accessible states. MCT was introduced to make more quantitative measures and to predict the dynamics of the system. Earlier, we have found that supercooled liquid shows a two-step relaxation at low temperatures. The physical reason behind the two-step relaxation is the cage effect, where one particle is stuck by its neighbor, and the particle is arrested temporarily, and it comes out of the cage after a while, which causes the two-step relaxation in the system. MCT predicts the cage formation perfectly[37]. The main assumption in the MCT is the absence of activation energy in the system, which makes this theory mean-field in nature. The crucial part of the MCT is that it takes the structure of the system as input in the equation and gives the dynamics of the system as an output. Though we know that the structure near the glass transition temperature is a boring quantity that does not change much, on the other hand, the dynamics of the system changes a lot. But the MCT shows a lot of change in dynamics for the small change in structure. MCT predicts the way the correlation function reach the plateau and leaves the plateau in a quantitative manner. Thus MCT can explain both the β and α relaxation. So far, MCT captures both the short time and large time relaxation along with quantitative predictions about the approach and departure from the plateau. It shows good agreement with the experimental data.

One drawback of the MCT is that it predicts the length of the plateau and results in the divergence in the α relaxation time at finite temperature T_c . MCT predicts the power-law divergence as

$$\tau_\alpha \simeq (T - T_c)^{-\gamma} \tag{1.36}$$

Where γ is the fitting parameter and T_c is the divergence temperature. It has been found that T_c is finite and experimental data does not show such divergence. Thus it can be treated as the artefact of the theory. Despite some drawbacks, in theory, it has lots of contribution to understand the dynamics of the glass-forming liquids.

1.7 Conclusions

Many theories and models have been studied in glass physics, and some of them have been discussed here. None of the theories or models can explain the properties of glass completely. Thus it requires lots of studies to understand the glass better. We have seen that MCT, the most popular theory which predicts the dynamics or the RFOT, which predicts the length scale in the glass-forming system, are mean-field in nature, and we know that mean-field means each particle is connected with the rest of the system. Suppose we increase the dimensions of the system, then the connectivity increases. But the experiments and most computer simulation studies are three or lower dimensional systems. Though the MCT is a mean-field theory, it does not entirely explain even the higher dimensional systems. Thus, it is important to connect the mean-field theory with the real glass-forming system by modifying its mean-field nature.

In this thesis, we have made a novel real system that can go d dimensional system to mean-field system continuously. In practice, we do this by increasing for each particle the number of particles it can interact with, thus increasing the effective interaction of the particle with the rest of the system. In contrast to the studies discussed above, our method does not modify in a significant manner the local structure of the liquid even when the MF limit is reached, i.e. the structure is always similar to the one of the 3D system. So this allows us to study how increasing connectivity affects the relaxation dynamics without modifying in a noticeable manner the structure, and hence to probe the dynamics upon approaching the MF limit. We will discuss structure and dynamics of this novel mean-field system in chapter3 and chapter4 respectively. In chapter5, we have studied the thermodynamics of the mean-field system and its correlation with the dynamics and we find that the regular thermodynamic integration (TI) method of calculating the entropy provides unphysical results. It predicts that while both the collective and the single-particle dynamics of the system survives, the entropy disappears. We then employ the two-phase thermodynamics(2PT) method to calculate the entropy. We find that with an increase in k , the difference in the entropy calculated using the two methods (2PT and TI) increases. We also find that in the temperature range studied, the entropy calculated via the 2PT method shows a validity of the AG relationship, whereas the entropy calculated via the TI method shows a strong violation of the same. We have studied the jamming transition in the mean-field system and how the properties of the jamming transition change as we go from the real 3D system to the mean-field system, which is described in chapter6. We find that the jamming transition point (ϕ_j) goes to a lower volume fraction with an

increasing mean-field nature.

In chapter7, we present a comparative study of the glass-forming ability of binary systems with varying compositions, where the systems have similar global crystalline structures (CsCl+fcc). Most of the systems which show glassy behavior have global crystalline order. Glass forming ability (GFA) depends on the barrier to crystallize in the system. It can easily crystallize if the system crosses the barrier. With the increase of the computational facility, it has been found that some glass-forming systems show partial crystallinity. In this thesis, we have tried to estimate the glass-forming ability of some glass-forming systems. We have shown which systems are the best glass former. We have found some systems show a higher free energy barrier because of the loss of demixing entropy, but for some other systems, it has a lower free energy barrier for a different crystalline structure which does not allow this system to be a good glass former.

Bibliography

- [1] M. D. Ediger, C. A. Angell, and S. R. Nagel, *The Journal of Physical Chemistry* **100**, 31, 13200-13212 (1996).
- [2] A. Cavagna, *Physics Reports* **476**, 4, 51-124 (2009).
- [3] J. P. Hansen and I. R. McDonald, Elsevier, Amsterdam (1986).
- [4] J. Phillips, *Journal of Non-Crystalline Solids* **172-174**, 98 (1994), *Relaxations in Complex Systems*.
- [5] G. Williams and D. C. Watts, *Trans. Faraday Soc.* **66**, 80 (1970).
- [6] C. A. Angell, K. L. Ngai, G. B. McKenna, P. F. McMillan, and S. W. Martin, *Journal of Applied Physics* **88**, 3113 (2000), <https://doi.org/10.1063/1.1286035>.
- [7] K. Schmidt-Rohr and H. W. Spiess, *Phys. Rev. Lett.* **66**, 3020 (1991).
- [8] F. Fujara, B. Geil, H. Sillescu, and G. Fleischer, *Zeitschrift für Physik B Condensed Matter* **88**, 195 (1992).
- [9] M. T. Cicerone and M. D. Ediger, *The Journal of Chemical Physics* **103**, 5684 (1995), <https://doi.org/10.1063/1.470551>.
- [10] G. Williams and J. Fournier, *The Journal of Chemical Physics* **104**, 5690 (1996), <https://doi.org/10.1063/1.471770>.
- [11] M. M. Hurley and P. Harrowell, *Phys. Rev. E* **52**, 1694 (1995).
- [12] A. I. Mel'cuk, R. A. Ramos, H. Gould, W. Klein, and R. D. Mountain, *Phys. Rev. Lett.* **75**, 2522 (1995).
- [13] W. Kob, C. Donati, S. J. Plimpton, P. H. Poole, and S. C. Glotzer, *Phys. Rev. Lett.* **79**, 2827 (1997).
- [14] W. T. Laughlin and D. R. Uhlmann, *The Journal of Physical Chemistry* **76**, 2317 (1972).

- [15] C. A. Angell, P. H. Poole, and J. Shao, *Il Nuovo Cimento D* **16**, 993 (1994).
- [16] W. Kauzmann, *Chemical Reviews* **43**, 219 (1948).
- [17] D. Turnbull and M. H. Cohen, *The Journal of chemical physics* **34**, 120 (1961).
- [18] D. Turnbull and M. H. Cohen, *The journal of chemical physics* **52**, 3038 (1970).
- [19] G. Gallavotti and E. G. D. Cohen, *Journal of Statistical Physics* **80**, 931 (1995).
- [20] C. Jarzynski, *Physical Review Letters* **78**, 2690 (1997).
- [21] H. Vogel, *Phys. Z* **22**, 645 (1921).
- [22] G. S. Fulcher, *Journal of the American Ceramic Society* **8**, 339 (1925).
- [23] G. Tammann and W. Hesse, *Zeitschrift für anorganische und allgemeine Chemie* **156**, 245 (1926).
- [24] G. Adam and J. H. Gibbs, *J. Chem. Phys.* **43**, 139 (1965).
- [25] J. H. Gibbs and E. A. DiMarzio, *The Journal of Chemical Physics* **28**, 373 (1958).
- [26] P. J. Flory, Phase equilibria in solutions of rod-like particles, in *Proceedings of the Royal Society of London A: Mathematical, Physical and Engineering Sciences* Vol. 234, pp. 73–89, The Royal Society, 1956.
- [27] H. Tanaka, *Physical Review E* **68**, 011505 (2003).
- [28] T. Kawasaki and H. Tanaka, *Proceedings of the National Academy of Sciences* **107**, 14036 (2010).
- [29] T. Kirkpatrick and D. Thirumalai, *Physical review letters* **58**, 2091 (1987).
- [30] T. Kirkpatrick and D. Thirumalai, *Physical Review B* **36**, 5388 (1987).
- [31] T. Kirkpatrick and P. Wolynes, *Physical Review A* **35**, 3072 (1987).
- [32] T. Kirkpatrick, D. Thirumalai, and P. G. Wolynes, *Physical Review A* **40**, 1045 (1989).
- [33] W. G. U Bengtzelius and A. Sjolande, *J. Phys. C: Solid State Phys* **17**, 5915 (1984).

- [34] E. Leutheusser, Phys. Rev. A **29**, 2765 (1984).
- [35] W. Götze, Oxford University Press (2008).
- [36] W. Kob, arXiv preprint cond-mat/0212344 (2002).
- [37] W. Götze, Journal of Physics: Condensed Matter **11**, A1 (1999).

Chapter 2

Properties of glass transition

2.1 Structural properties

The structure of supercooled liquids (even the glass) is very much similar to high-temperature liquids. The easiest way to express the structural quantity is the radial distribution function, $g(r)$ [1, 2] (See Fig.2.1[Left]).

$$g(r) = \frac{1}{4\pi r^2 \rho} \left\langle \sum_{i=1}^N \sum_{j \neq i}^N \delta(r - r_{ij}) \right\rangle \quad (2.1)$$

where ρ is the density of the system and N is the total number of particles in the system. $r_{ij} = r_j - r_i$.

It shows the local density of the particle ($\rho g(r)$) in the system at a distance r . The total number of particles in the system can be calculated using the following equation

$$\int_0^\infty dr 4\pi r^2 \rho g(r) = N - 1 \quad (2.2)$$

Different phases of the system can be understood very well using rdf. As the local density of the system changes at different phases, the peak height of rdf changes at a different phases of the system.

The easiest way to analyze the structure in the experiment is the structure factor, $S(q)$, which is computed using the inelastic neutron scattering. This is the Fourier integral of the radial distribution function.

$$S(q) = 1 + 4\pi\rho \int_0^\infty dr r^2 \frac{\sin(qr)}{qr} (g(r) - 1) \quad (2.3)$$

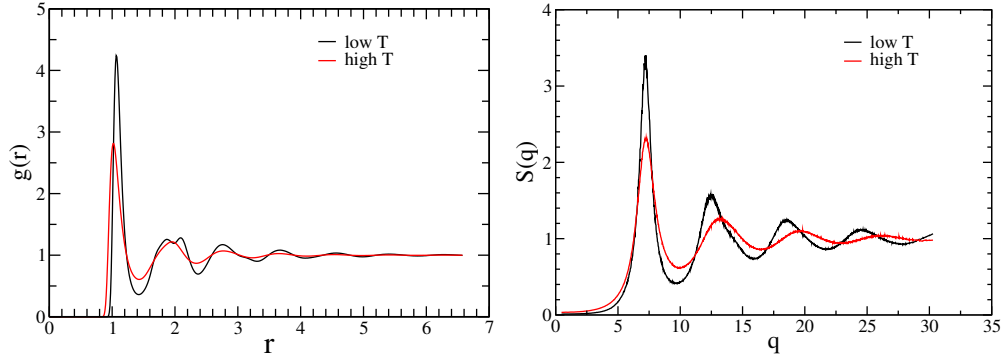


Figure 2.1: (Left) Radial distribution function at different temperatures. As the temperature decreases, the peak height of the plot increases. (Right) $S(q)$ shows the similar effect at low and high temperatures.

It shows the structural properties in the momentum space q . As the density of the system is increased or the temperature is lowered, these structural quantities become sharper, and the peak height also increases (See Fig.2.1[Right]).

2.2 Dynamic properties

Most of the predicted theories for the glass transition are dynamic in nature. It shows lots of changes in dynamics near the glass transition temperature. Most of the dynamic properties are computed from the time correlation function and the displacements.

2.2.1 Relaxation time

We have calculated the relaxation times obtained from the decay of the overlap function $q(t)$, where $q(t = \tau_\alpha, T)/N = 1/e$. It is defined as

$$\begin{aligned}
 \langle Q(t) \rangle &\equiv \left\langle \int dr \rho(r, t_0) \rho(r, t + t_0) \right\rangle \\
 &= \left\langle \sum_{i=1}^N \sum_{j=1}^N \delta(\mathbf{r}_j(t_0) - \mathbf{r}_i(t + t_0)) \right\rangle \\
 &= \left\langle \sum_{i=1}^N \delta(\mathbf{r}_i(t_0) - \mathbf{r}_i(t + t_0)) \right\rangle \\
 &\quad + \left\langle \sum_{i=1}^N \sum_{j \neq i}^N \delta(\mathbf{r}_i(t_0) - \mathbf{r}_j(t + t_0)) \right\rangle
 \end{aligned} \tag{2.4}$$

The overlap function is a two-point correlation function of local density $\rho(r, t)$. In the thesis, we consider only the self-part of the total overlap function (i.e.

neglecting the $i \neq j$ terms in the double summation). Earlier it has been shown to be a good approximation to the full overlap function. So, the self part of the overlap function can be written as,

$$\langle Q(t) \rangle \approx \left\langle \sum_{i=1}^N \delta(\mathbf{r}_i(t_0) - \mathbf{r}_i(t + t_0)) \right\rangle \quad (2.5)$$

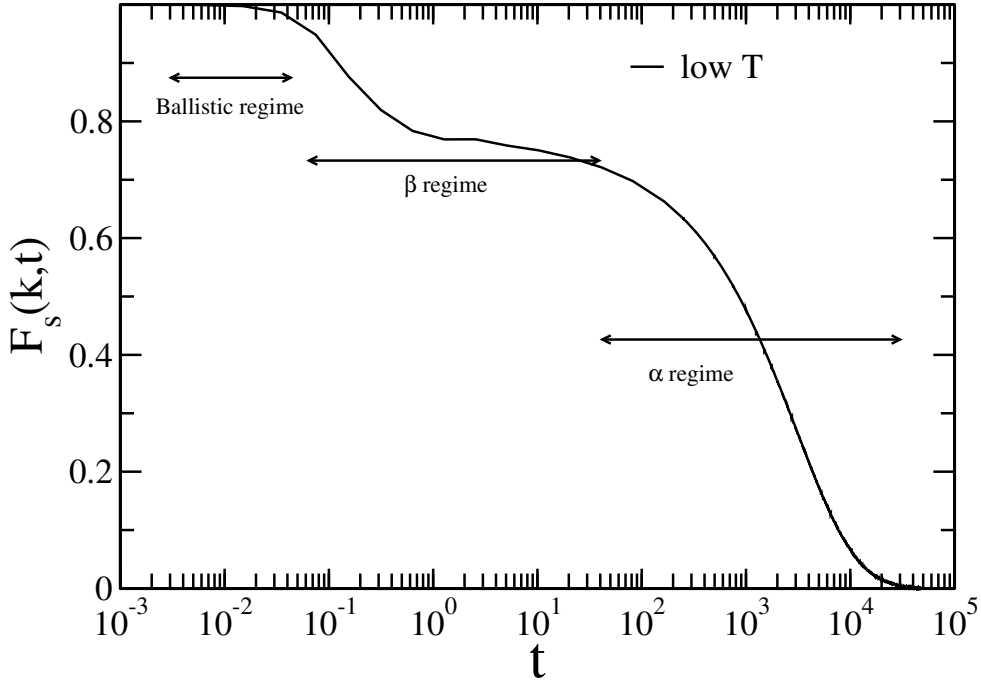


Figure 2.2: $F_s(k, t)$ at low temperature. Three regions of the relaxation are shown here.

Again, the δ function is approximated by a window function $\omega(x)$ which defines the condition of “overlap” between two-particle positions separated by a time interval t :

$$\langle Q(t) \rangle \approx \left\langle \sum_{i=1}^N \omega(|\mathbf{r}_i(t_0) - \mathbf{r}_i(t + t_0)|) \right\rangle$$

$$\omega(x) = 1, x \leq a \text{ implying “overlap”}$$

$$= 0, \text{ otherwise} \quad (2.6)$$

where the function $\omega(x)$ is 1 if $0 \leq x \leq a$ and $\omega(x) = 0$ otherwise. The parameter a is chosen to be 0.3, a value that is slightly larger than the size of the cage. Thus the quantity $Q(t)$ tells whether or not at time t a tagged particle is still inside the cage it occupied at $t = 0$. Another way to calculate the relaxation time is from the self part of the intermediate scattering function. This is the

self part of the density-density time correlation function in momentum space.

$$F_s(k, t) = \frac{1}{N} \left\langle \sum_{i=1}^N \exp(-i\mathbf{k} \cdot (\mathbf{r}_i(\mathbf{t}) - \mathbf{r}_i(\mathbf{0}))) \right\rangle \quad (2.7)$$

Dynamics shows the two-step relaxation when the system undergoes a super-cooled state, as shown in Fig.2.2 . One is small-time relaxation which is called β relaxation, and another one is long time relaxation which is called α relaxation.

Mean square displacement

The origin of the two-step relaxation can be analyzed with the mean square displacement (MSD) with respect to a tagged particle.

$$\langle r^2(t) \rangle = \frac{1}{N} \sum_{i=1}^N \left\langle |\mathbf{r}_i(\mathbf{t}) - \mathbf{r}_i(\mathbf{0})|^2 \right\rangle \quad (2.8)$$

MSD has the early regime where $r \propto t$ (See Fig.2.3). In this regime, the particle shows ballistic motion without colliding other particles, and the size of this regime is the cage size of the system. Particle enters into the diffusive regime when collisions happen with other particles. Then $\langle r^2 \rangle \propto t$.

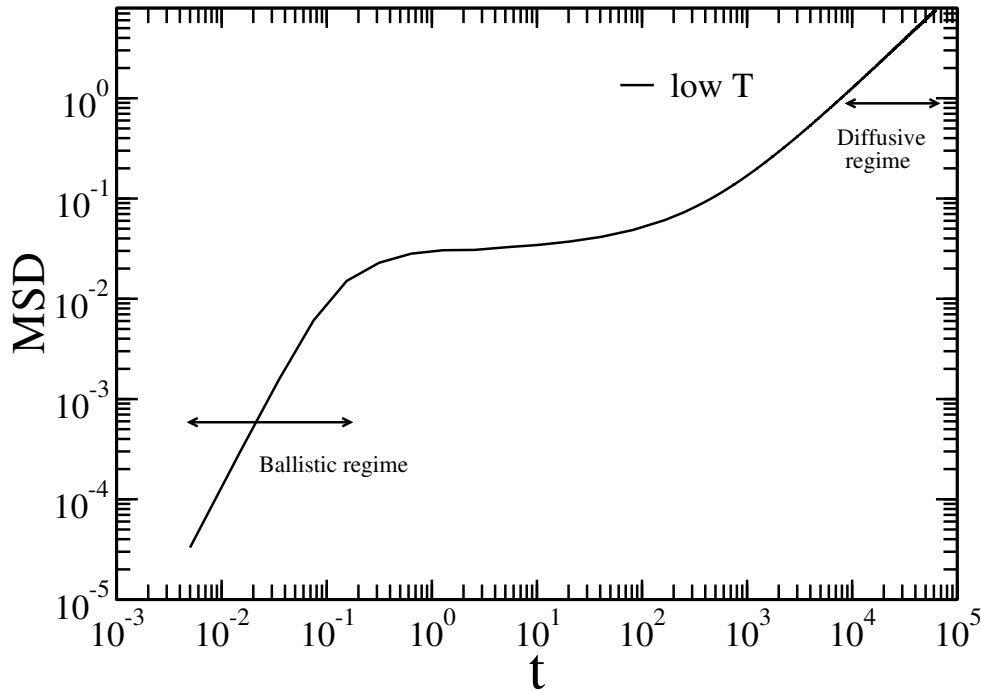


Figure 2.3: Mean square displacement at low temperature.

2.2.2 Dynamic Fragility

A rapid increase in relaxation time with decreasing temperature is a signature of the glass-forming liquids. When the relaxation time increases exponentially with decreasing temperature (Arrhenius behavior) then it is called strong glass, and in some systems, the relaxation time grows faster than the exponential behavior, which is called fragile glass. The fragile system follows the Vogel-Fulcher-Tamann (VFT) equation

$$\tau(T) = \tau_0 \exp \left[\frac{1}{K(T/T_0 - 1)} \right] \quad . \quad (2.9)$$

Here T_0 is the so-called VFT temperature at which the relaxation time of the system is predicted to diverge. The parameter K describes the curvature of the data in an Arrhenius plot and hence can be considered as a measure for the fragility of the glass-former.

2.2.3 MCT Power law behavior

Mode coupling theory (MCT) predicts that close to the critical temperature T_c of the theory the relaxation times show a power-law divergence:

$$\tau(T) = \tau_{\text{MCT}}(T - T_c)^{-\gamma} \quad . \quad (2.10)$$

Using this functional form to fit the temperature dependence of the relaxation time, we obtain $T_c(k)$. However, at the lowest T 's deviations are observed, and the increase in τ is weaker than the power-law predicted by MCT. This deviation is usually attributed to the existence of ‘‘hopping processes’’, i.e. a component in the relaxation dynamics that is not taken into account in the *idealized* version of the MCT.

2.2.4 Dynamic Heterogeneity

One of the hallmarks of glassy dynamics is that time correlation functions are stretched in time. The reason for this non-Debye relaxation has been a long-standing puzzle with the contrasting views that each small domain of the sample shows the same stretched time dependence or, alternatively, that the stretching is related to dynamical heterogeneities [28]. Experiments and simulations have shown that the homogeneous scenario is not compatible with the observations, i.e. glass-forming systems do have a significant amount of dynamical heterogeneities (DH) [4, 5, 6, 7].

One first step to probe the DH is to look at the so-called non-Gaussian parameter (NGP) $\alpha_2(t)$ which is defined by

$$\alpha_2(t) = \frac{3 \langle r^4(t) \rangle}{5 \langle r^2(t) \rangle^2} - 1 \quad (2.11)$$

where $r(t)$ is the displacement of a tagged particle within a time t . Thus $\alpha_2(t)$ measures whether or not the distribution of the particle displacement is Gaussian [8, 9, 4, 10].

Next, we discuss the other parameter that is often related to the dynamic heterogeneity i.e. the dynamic susceptibility. The fluctuations of the overlap function $Q(t)$ are related to a dynamic susceptibility, which indicates whether or not the system relaxes in a cooperative manner, i.e., shows dynamical heterogeneities [12, 12, 13] Thus, one defines as,

$$\chi_4(t) = \frac{1}{N} [\langle Q^2(t) \rangle - \langle Q(t) \rangle^2] \quad (2.12)$$

as a measure to quantify this cooperativity.

2.3 Thermodynamic Properties

Ideal gas entropy

Particles in the ideal gas limit do not interact with each other with any kind of potential; they only have momentum. The total Hamiltonian of the ideal gas system

$$H(\{p_i\}) = \sum_i \frac{p_i^2}{2m_i}$$

where p_i is the momentum and m_i is the mass of the i^{th} particle.

The partition function for the monodisperse ideal gas in d - dimensional system at temperature T ($\beta = \frac{1}{k_B T}$) can be written as

$$\begin{aligned} Z(\beta) &= \prod_{i=1}^N \frac{1}{h^d} \int d^d q_i d^d p_i \exp \left[-\beta \frac{p_i^2}{2m_i} \right] \\ &= \frac{V^N}{h^{dN}} \left\{ \int d^d p_i \exp \left[-\beta \frac{p^2}{2m} \right] \right\}^N \\ &= \frac{V^N}{\lambda^{dN}} \end{aligned} \quad (2.13)$$

where $\lambda = \sqrt{\frac{\beta h^2}{2\pi m}}$ and h is the planck constant.

Now for the indistinguishable particles, the partition function is written as

$$Z(\beta) = \frac{1}{N!} \frac{V^N}{\lambda^{dN}}$$

We know $S_{id} = -\frac{dF}{dT}$. Where F is the free energy. F can be written as

$$F = -k_B T \ln Z$$

If we consider $d=3$ then S_{id} can be written as

$$\frac{S_{id}}{k_B} = \ln(V) + \frac{3}{2} \ln \frac{2\pi m T}{h^2} - \ln N + \frac{5}{2} \quad (2.14)$$

Since most of the systems studied in this thesis are binary, a similar analysis can be done for the binary system (with type A and type B particles).

$$Z(\beta) = \frac{1}{N_A! N_B!} \frac{V^{N_A+N_B}}{\lambda_A^{dN_A} \lambda_B^{dN_B}}$$

where $\lambda_A = \sqrt{\frac{\beta h^2}{2\pi m_A}}$ and $\lambda_B = \sqrt{\frac{\beta h^2}{2\pi m_B}}$. m_A is the mass of type A particles and m_B is the mass of type B particles.

The ideal gas entropy for the binary system in 3D can be written as

$$\frac{S_{id}}{k_B} = N \ln(V) - N_A \ln N_A - N_B \ln N_B - 3N_A \ln \lambda_A - 3N_B \ln \lambda_B + \frac{5}{2} N \quad (2.15)$$

However, if the particles are divided into 'M' distinguishable species such that $N = \sum_{i=1}^M N_i$ then the ideal gas entropy per particle can be written as,

$$S_{ideal}^d = \frac{5}{2} - \ln(\rho) + \frac{3}{2} \ln \left(\frac{2\pi T}{h^2} \right) + \frac{1}{N} \ln \frac{N!}{\prod_{i=1}^M N_i!} \quad (2.16)$$

2.3.1 Excess entropy

The excess entropy (S_{ex}) is the loss of entropy in the system due to the interaction between particles i.e. the differences between the total entropy (S_{tot}), and the ideal gas entropy.

$$S_{tot} = S_{ideal} + S_{ex} \quad (2.17)$$

$$S_{ex} = S_{tot} - S_{id} \quad (2.18)$$

We have calculated S_{tot} using two different methods one is thermodynamic integration (TI) and another is the two-phase thermodynamic (2PT) method. If we subtract S_{id} from the S_{tot} then we get the S_{ex} from both the methods.

Thermodynamic integration

The method for the calculation of excess entropy is described in details in Reference[14]. S_{ex} is evaluated via thermodynamics integration from infinite temperature to the target temperature (T^*) using the Eq.2.19

$$S_{ex}(\beta^*) = \beta^* \langle U \rangle - \int_0^{\beta^*} d\beta \langle U \rangle \quad (2.19)$$

where $\beta^* = \frac{1}{k_B T^*}$ and $\langle U \rangle$ is the average per particle potential energy of the system at target temperature.

Two-phase thermodynamic method

2PT is another conventional method to compute the entropy of liquid[15, 16]. In 2PT, the thermodynamics quantities can be computed using the density of state (DOS) of the liquid. One can decompose the DOS of liquid as a sum of solid-like and gas-like contributions. To compute the thermodynamic quantities, the phonon in the solid-like DOS was treated as a non-interacting harmonic oscillator, as in the Debye model[17]. On the other hand, gas-like DOS was described as a low-density hard-sphere fluid, which can be computed analytically[17]. Using the 2PT description, Lin et al.,[15, 16] demonstrated that the thermodynamics quantities of the LJ fluid can be computed very accurately over a wide range of thermodynamics state points using a very small MD trajectory. In a later work, Lin et al.[18] calculated entropy of the binary fluid using the 2PT method. Here, we provide a brief overview of the decomposition of DOS in 2PT. Nevertheless, we refer the reader to the original papers[15, 16] for a full 2PT description.

The density of state function, $g(\nu)$, can be computed from the mass-weighted atomic spectral densities, defined as[15, 16],

$$g(\nu) = \frac{2}{k_B T} \sum_{j=1}^N \sum_{k=1}^3 m_j s_j^k(\nu) \quad (2.20)$$

where m_j is the mass of the j^{th} atom, k denotes the direction in the Cartesian coordinates, and $s_j^k(\nu)$ are the atomic spectral densities defined as,

$$s_j^k(\nu) = \lim_{\tau \rightarrow \infty} \frac{\left| \int_{-\tau}^{\tau} v_j^k(t) e^{-i2\pi\nu t} dt \right|^2}{2\tau} \quad (2.21)$$

where $v_j^k(t)$ denotes the velocity component of j^{th} atom in the k^{th} direction. Atomic spectral density, $s_j^k(\nu)$, can be computed from the Fourier transform of the velocity auto-correlation function (VACF) $c_j^k(t)$.

$$s_j^k(\nu) = \lim_{\tau \rightarrow \infty} \int_{-\tau}^{\tau} c_j^k(t) e^{-i2\pi\nu t} dt \quad (2.22)$$

where $c_j^k(t)$ is given by:

$$c_j^k(t) = \lim_{\tau \rightarrow \infty} \frac{1}{2\tau} \int_{-\tau}^{\tau} v_j^k(t+t') v_j^k(t') dt' \quad (2.23)$$

Thus, Eq. 2.20 can be rewritten as:

$$g(\nu) = \frac{2}{k_B T} \lim_{\tau \rightarrow \infty} \int_{-\tau}^{\tau} \sum_{j=1}^N \sum_{k=1}^3 m_j c_j^k(t) e^{-i2\pi\nu t} dt \quad (2.24)$$

As we mentioned above, $g(\nu)$ can be decomposed into solid and gas-like components in 2PT formalism. Based on the diffusivity of the system compared to hard-sphere gas at the same density, Lin et al.[15] proposed a self-consistent fluidity factor, f , which decides the degree of freedom shared in solid and gas components. The relationship between f and dimensionless diffusivity, Δ , can be derived (for the details of the derivation, readers are referred to ref [15]).

$$\begin{aligned} 2\Delta^{-9/2} f^{15/2} - 6\Delta^{-3} f^5 - \Delta^{-3/2} f^{7/2} + \\ 6\Delta^{-3/2} f^{5/2} + 2f - 2 = 0 \end{aligned} \quad (2.25)$$

The dimensionless diffusivity constant, Δ , depends on the material properties.

$$\Delta(T, \rho, m, g_0) = \frac{2g_0}{9N} \left(\frac{6}{\pi}\right)^{2/3} \left(\frac{\pi k_B T}{m}\right)^{1/2} \rho^{1/3} \quad (2.26)$$

where, $g_0 = g(0)$ is the DOS of the system at zero-frequency. Using f obtained from Eq. 2.25, 2.26, the DOS in the gas-like diffusive component can be obtained using a hard-sphere diffusive model:

$$g^g(\nu) = \frac{g_0}{1 + \left[\frac{\pi g_0 \nu}{6fN}\right]^2} \quad (2.27)$$

Given the DOS in the gas-like component, one can compute the solid-like DOS, $g^s(\nu)$, using the equation,

$$g(\nu) = g^g(\nu) + g^s(\nu) \quad (2.28)$$

Once the decomposition of DOS has been done, any thermodynamic quantity, A , can be computed using the corresponding weight function

$$A = \beta^{-1} \left[\int_0^\infty g^g(\nu) W_A^g d\nu + \int_0^\infty g^s(\nu) W_A^s d\nu \right] \quad (2.29)$$

The weight function for entropy in solid, W_S^s , and gas like, W_S^g , component is defined as

$$W_S^s(\nu) = W_S^{HO}(\nu) = \frac{\beta \hbar \nu}{\exp(\beta \hbar \nu) - 1} - \ln [1 - \exp(-\beta \hbar \nu)] \quad (2.30)$$

where $\beta = \frac{1}{kT}$ and \hbar is the Plank's constant.

$$W_S^g(\nu) = \frac{1}{3} \frac{S^{HS}}{k} \quad (2.31)$$

where, S^{HS} denotes the entropy of the hard sphere. Using the Eq.2.28,2.31, the total entropy of the system can be written as,

$$S_{tot} = S^s + S^g \quad (2.32)$$

2.3.2 Vibrational Entropy

Stillinger and Weber first introduced the formalism of the inherent structure and established the concept of the basin in the potential energy surface [19]. Vibrational entropy is calculated by making a harmonic approximation about a local minimum [20, 21, 22, 23]. To obtain the vibrational density of states (DOS), we calculate the Hessian (see section 2.4) and then diagonalize it. Once we obtain the DOS, S_{vib} is calculated using the following calculations.

First we calculate the canonical partition function of a harmonic oscillator in one dimension with frequencies ω_i and mass 'm' is given by,

$$\begin{aligned} z_{harm}(\omega, T, V) &= \int \frac{dpdq}{h} \exp\left(-\frac{\beta p^2}{2m} - \frac{\beta m \omega^2 q^2}{2}\right) \\ &= \frac{1}{h^{3N}} \int d^{3N} p \exp\left(-\frac{\beta p^2}{2m}\right) \\ &\quad \times \int d^{3N-3} q \exp\left(-\frac{\beta m \omega_i^2 q^2}{2}\right) \int d^3 q \\ &= \frac{1}{h^{3N}} \left(\frac{2m\pi}{\beta}\right)^{\frac{3N}{2}} \prod_{i=1}^{3N-3} \left(\frac{2\pi}{\beta m \omega_i^2}\right)^{\frac{1}{2}} V \\ &= \Lambda^{-3N} \prod_{i=1}^{3N-3} \left(\frac{2\pi}{\beta m \omega_i^2}\right)^{\frac{1}{2}} V \end{aligned} \quad (2.33)$$

where Λ is the thermal de Broglie wavelength. $\Lambda = \sqrt{\frac{\beta \hbar^2}{2\pi m}}$

$$\beta f_{basin} = -\ln z_{harmonic},$$

$$\beta f_{basin} = -\frac{3N}{2} \ln\left(\frac{2\pi}{h^2\beta}\right) - \ln(V) - \frac{1}{2} \sum_{i=1}^{3N-3} \ln\left(\frac{2\pi}{\beta m \omega_i^2}\right) \quad (2.34)$$

The basin entropy, S_{basin} can be written as,

$$N s_{vib} = S_{basin} = -\frac{\delta f_{basin}}{\delta T}$$

$$= \frac{3N}{2} \ln\left(\frac{2\pi}{h^2\beta}\right) + \ln(V) + \frac{1}{2} \sum_{i=1}^{3N-3} \ln\left(\frac{2\pi}{\beta m \omega_i^2}\right) + T\left[\frac{3N}{2} \frac{1}{T} + \frac{1}{2}(3N-3) \frac{1}{T}\right]$$

$$= \frac{3N}{2} \ln\left(\frac{2\pi}{h^2\beta}\right) + \ln(V) + \frac{1}{2} \sum_{i=1}^{3N-3} \ln\left(\frac{2\pi}{\beta m \omega_i^2}\right) + (3N - \frac{3}{2}) \quad (2.35)$$

$$S_{vib} = \frac{3}{2} \ln\left(\frac{2\pi T}{h^2}\right) + \frac{\ln(V)}{N} + \frac{1}{2N} \sum_{i=1}^{3N-3} \ln\left(\frac{2\pi T}{m \omega_i^2}\right) + 3 - \frac{3}{2N} \quad (2.36)$$

2.3.3 Configurational entropy

Configurational entropy is the count of minimum in the potential energy landscape. In the supercooled liquid regime, the configurational space can be divided into inherent structure minima and vibrational motion around them. The number of these inherent structure minima are called the configurational entropy (S_c) of the system, which can be calculated by subtracting vibrational entropy, S_{vib} from the total entropy of the system.

$$S_c = S_{tot} - S_{vib}$$

$$= S_{ideal} + S_{ex} - S_{vib} \quad (2.37)$$

2.4 Hessian Calculation

We need to calculate the frequencies (ω) for the calculation of vibrational entropy (S_{vib}). We calculate ω from the hessian calculation. Hessian is the double derivative of the two-body potential (u_{jk}) with respect to the coordinate of particles j and k. For the mean-field system, the total interaction energy $u_{tot} = u + u^{pseudo}$ which will be discussed in detail in chapter3.

The total hessian for this system is

$$H_{tot}(j, k) = \frac{\partial}{\partial \vec{r}_j} \frac{\partial}{\partial \vec{r}_k} u_{tot} = \frac{\partial}{\partial \vec{r}_j} \frac{\partial}{\partial \vec{r}_k} (u + u^{pseudo})$$

Here

$$H(j, k) = \frac{\partial}{\partial \vec{r}_j} \frac{\partial}{\partial \vec{r}_k} u$$

and

$$H^{pseudo}(j, k) = \frac{\partial}{\partial \vec{r}_j} \frac{\partial}{\partial \vec{r}_k} u^{pseudo}$$

We are going to calculate hessian for the potential energy of the pseudo particles.

$$H^{pseudo}(j, k) = \frac{\partial}{\partial \vec{r}_j} \frac{\partial}{\partial \vec{r}_k} u^{pseudo}(r_{jk} - L_{jk})$$

Let us assume $r_{jk} - L_{jk} = r'_{jk}$

$$\frac{\partial r'_{jk}}{\partial x_j} = \frac{\partial(r_{jk} - L_{jk})}{\partial x_j} = \frac{x_j - x_k}{r_{jk}} = \frac{x_{jk}}{r_{jk}} \quad (2.38)$$

$$\frac{\partial r'_{jk}}{\partial x_k} = \frac{\partial(r_{jk} - L_{jk})}{\partial x_k} = -\frac{x_j - x_k}{r_{jk}} = -\frac{x_{jk}}{r_{jk}} \quad (2.39)$$

First derivative:

$$\frac{\partial u^{pseudo}(r'_{jk})}{\partial \vec{r}_k} = \hat{i} \frac{\partial u^{pseudo}(r'_{jk})}{\partial x_k} + \hat{j} \frac{\partial u^{pseudo}(r'_{jk})}{\partial y_k} + \hat{k} \frac{\partial u^{pseudo}(r'_{jk})}{\partial z_k} \quad (2.40)$$

$$\hat{i} \frac{\partial u^{pseudo}(r'_{jk})}{\partial x_k} = \hat{i} \frac{\partial r'_{jk}}{\partial x_k} \frac{\partial u^{pseudo}(r'_{jk})}{\partial r'_{jk}} \quad (2.41)$$

$$\frac{\partial u^{pseudo}(r'_{jk})}{\partial \vec{r}_k} = -\frac{\partial u^{pseudo}(r'_{jk})}{\partial r'_{jk}} \hat{r}_{jk} \quad (2.42)$$

Second derivative:

$$\frac{\partial}{\partial \vec{r}_j} \left(-\frac{\partial u^{pseudo}(r'_{jk})}{\partial r'_{jk}} \hat{r}_{jk} \right) = \left(\hat{i} \frac{\partial}{\partial x_j} + \hat{j} \frac{\partial}{\partial y_j} + \hat{k} \frac{\partial}{\partial z_j} \right) \left(-\frac{\partial u^{pseudo}(r'_{jk})}{\partial r'_{jk}} \hat{r}_{jk} \right) \quad (2.43)$$

$$\hat{i} \frac{\partial}{\partial x_j} \left(-\frac{\partial u^{pseudo}(r'_{jk})}{\partial r'_{jk}} \hat{r}_{jk} \right) = \hat{i} \frac{\partial}{\partial x_j} \left(-\frac{\partial u^{pseudo}(r'_{jk})}{\partial r'_{jk}} \right) \otimes \hat{r}_{jk} - \frac{\partial u^{pseudo}(r'_{jk})}{\partial r'_{jk}} \left(\hat{i} \frac{\partial}{\partial x_j} \otimes \hat{r}_{jk} \right) \quad (2.44)$$

Let us do the calculation for first term

$$-\hat{i} \frac{\partial}{\partial x_j} \left(\frac{\partial u^{pseudo}(r'_{jk})}{\partial r'_{jk}} \right) \otimes \hat{r}_{jk} = -\hat{i} \frac{\partial r'_{jk}}{\partial x_j} \frac{\partial}{\partial r'_{jk}} \left(\frac{\partial u^{pseudo}(r'_{jk})}{\partial (r'_{jk})} \right) \otimes \hat{r}_{jk} = -\hat{i} \frac{x_{jk}}{r_{jk}} \frac{\partial^2 u^{pseudo}(r'_{jk})}{\partial^2 r'_{jk}} \otimes \hat{r}_{jk} \quad (2.45)$$

$$= -\frac{\partial^2 u^{pseudo}(r'_{jk})}{\partial^2 r'_{jk}} \frac{\vec{r}_{jk}}{r_{jk}} \Big|_{x\text{-component}} \otimes \frac{\vec{r}_{jk}}{r_{jk}} \quad (2.46)$$

$$= -\frac{1}{r_{jk}^2} \frac{\partial^2 u^{pseudo}(r'_{jk})}{\partial^2 r'_{jk}} (\vec{r}_{jk} \otimes \vec{r}_{jk})_{\mathbf{x}\text{-component}} \quad (2.47)$$

Now looking at the second term

$$-\frac{\partial u^{pseudo}(r'_{jk})}{\partial r'_{jk}} \left(\hat{i} \frac{\partial}{\partial x_j} \otimes \hat{r}_{jk} \right) \quad (2.48)$$

$$= -\frac{\partial u^{pseudo}(r'_{jk})}{\partial r'_{jk}} \left(\hat{i} \frac{\partial}{\partial x_j} \otimes \frac{x_{jk}\hat{i} + y_{jk}\hat{j} + z_{jk}\hat{k}}{r_{jk}} \right) \quad (2.49)$$

$$= -\frac{\partial u^{pseudo}(r'_{jk})}{\partial r'_{jk}} \left[\frac{\hat{i}}{r_{jk}} \otimes \frac{\partial}{\partial x_j} (x_{jk}\hat{i} + y_{jk}\hat{j} + z_{jk}\hat{k}) + \hat{i} \frac{\partial}{\partial x_j} \left(\frac{1}{r_{jk}} \right) \otimes \vec{r}_{jk} \right] \quad (2.50)$$

$$= -\frac{\partial u^{pseudo}(r'_{jk})}{\partial r'_{jk}} \left[\frac{1}{r_{jk}} \hat{i} \otimes \hat{i} + \hat{i} \frac{\partial r_{jk}}{\partial x_j} \frac{\partial}{\partial r_{jk}} \left(\frac{1}{r_{jk}} \right) \otimes \vec{r}_{jk} \right] \quad (2.51)$$

$$= -\frac{\partial u^{pseudo}(r'_{jk})}{\partial r'_{jk}} \left[\frac{1}{r_{jk}} \hat{i} \otimes \hat{i} + \hat{i} \frac{x_{jk}}{r_{jk}} \left(-\frac{1}{r_{jk}^2} \right) \otimes \vec{r}_{jk} \right] \quad (2.52)$$

$$= -\frac{\partial u^{pseudo}(r'_{jk})}{\partial r'_{jk}} \left[\frac{1}{r_{jk}} \hat{i} \otimes \hat{i} - \hat{i} \frac{x_{jk}}{r_{jk}^3} \otimes \vec{r}_{jk} \right] \quad (2.53)$$

$$= -\frac{1}{r_{jk}} \frac{\partial u^{pseudo}(r'_{jk})}{\partial r'_{jk}} (I)_{\mathbf{x}\text{-component}} + \frac{1}{r_{jk}^3} \frac{\partial u^{pseudo}(r'_{jk})}{\partial r'_{jk}} \vec{r}_{jk} \otimes \vec{r}_{jk} \Big|_{\mathbf{x}\text{-component}} \quad (2.54)$$

Combining first and second term , the second derivative becomes

$$\begin{aligned}
H^{pseudo}(j, k) &= \frac{\partial}{\partial \vec{r}_j} \frac{\partial}{\partial \vec{r}_k} u^{pseudo}(r_{jk} - L_{jk}) \\
&= \left(-\frac{1}{r_{jk}^2} \frac{\partial^2 u^{pseudo}(r'_{jk})}{\partial^2 r'_{jk}} \right. \\
&\quad \left. + \frac{1}{r_{jk}^3} \frac{\partial u^{pseudo}(r'_{jk})}{\partial r'_{jk}} \right) \vec{r}_{jk} \otimes \vec{r}_{jk} - \frac{1}{r_{jk}} \frac{\partial u^{pseudo}(r'_{jk})}{\partial (r'_{jk})} \mathbf{I}
\end{aligned} \tag{2.55}$$

If we follow the similar calculation for the regular hessian ($H(j, k)$) then we get,

$$\begin{aligned}
H(j, k) &= \frac{\partial}{\partial \vec{r}_j} \frac{\partial}{\partial \vec{r}_k} u(r_{jk}) \\
&= \left(-\frac{1}{r_{jk}^2} \frac{\partial^2 u(r_{jk})}{\partial r_{jk}^2} \right. \\
&\quad \left. + \frac{1}{r_{jk}^3} \frac{\partial u(r_{jk})}{\partial r_{jk}} \right) \vec{r}_{jk} \otimes \vec{r}_{jk} - \frac{1}{r_{jk}} \frac{\partial u(r_{jk})}{\partial (r_{jk})} \mathbf{I}
\end{aligned} \tag{2.56}$$

2.5 Weight histogram analysis method

In many systems, it has been found that the systems stuck in a local minimum of the free energy surface because of the high activation energy barrier from the trapped state to the surrounding state. Then system spends a large time in the trapped state and apparently undergoes the breakdown of the ergodicity. In order to avoid this problem, we employ a biased potential in the system so that the probability of visiting the low probability state increases. We remove the effect of the bias potential and get an estimation of the free energy surface of that phase space. Glassy system is such an example where the system stuck in the metastable state many a time at low temperature. The most effective method to estimate free energy is the weight histogram analysis method (WHAM)[24]. Now, we will work on the WHAM equation.

In the umbrella sampling and in the free energy perturbation methods the Hamiltonian $H_{\{\lambda\}}(x)$

$$H_{\{\lambda\}}(x) = H_0(x) + \sum_{i=1}^L \lambda_i V_i(x) = \sum_{i=0}^L \lambda_i V_i(x) \tag{2.57}$$

where $\lambda_0 = 1$ and $V_0(x)$ is identical to $H_0(x)$, x is the coordinate of the particles, λ_i are the coupling parameter. L is the number of independent sets of simulation with L different coupling parameter (λ_i). The $\{\lambda\}$ represents the set of values $\lambda_1, \lambda_2, \lambda_3, \dots, \lambda_L$. $V_1(x), V_2(x), \dots, V_L(x)$ are the restraining potential, and it

is function of x . The restraining potential is chosen such a way that sampling distribution to be shifted along the reaction coordinate. The reaction coordinate (ξ) is function of x . The sample can be equilibrated at any reaction coordinate by adjusting the coupling parameter. The potential mean force (PMF) or free energy at that state point can be estimated with the correction in the restraining potential.

The probability density from a simulation with hamiltonian $H_{\{\lambda\}}(x)$ can be written as

$$P_{\{\lambda\},\beta}(\xi) = \exp[-\beta W_{\{\lambda\},\beta}(\xi)] = \langle \delta[\xi - \hat{\xi}(x)] \rangle_{\{\lambda\},\beta} \quad (2.58)$$

where $\beta = \frac{1}{k_B T}$, k_B is the boltzmann constant and T is temperature. $W_{\{\lambda\},\beta}(\xi)$ is the PMF for the simulation with coupling parameter $\{\lambda\}$ and temperature T .

The single histogram equation is used to calculate the free energy of a single simulation. Let us assume that a simulation is carried out at temperature $T_1 = \frac{1}{k_B \beta_1}$ with $\lambda_0 = 1$ and with the restraining potentials weighted by the coupling parameter $\lambda_1, \lambda_2 \dots \lambda_L$. The quantity of interest is then the probability $P_{\beta_2}(\xi)$ where the coordinate ξ would take the system to a equivalent state like a simulation is done with $\lambda_0 = 1$ and other coupling parameters are set to zero at temperature $T_2 = \frac{1}{k_B \beta_2}$. PMF profiles can be generated by taking the logarithm of the probabilities. The histogram is generated by putting the data into bins and the single histogram equation becomes,

$$\begin{aligned} & \tilde{P}_{\beta_2} [\xi \in (\xi_m, \xi_{m+1})] \\ &= \frac{\sum_{j=1}^{\eta(m)} \exp \left[(\beta_1 - \beta_2) \tilde{V}_{0,j}^{(m)} + \sum_{i=1}^L \lambda_i \beta_1 \tilde{V}_{i,j}^{(m)} \right]}{\sum_{k=1}^B \sum_{j=1}^{\eta(k)} \exp \left[(\beta_1 - \beta_2) \tilde{V}_{0,j}^{(k)} + \sum_{i=1}^L \lambda_i \beta_1 \tilde{V}_{i,j}^{(k)} \right]} \end{aligned} \quad (2.59)$$

where the expression gives the probability that the ξ has value between ξ_m and ξ_{m+1} in the m^{th} bin at temperature T_2 . $\hat{V}_{i,j}^{(k)}$ is the value that the restraining potential V_i takes at the j^{th} snapshot of the k^{th} bin. $\eta(k)$ is the total number of data points that the simulation yields in the k^{th} bin; it is just the value taken on by the histogram at the bin numbered k . B is the total number of bins that the data has been divided into.

Eq.2.59 can be rewritten in terms of $N_{\{\lambda\},\beta_1}(V, \xi)$, which is the value taken by the histogram at $\{V\}$ and ξ for the simulation at temperature T_1 with the coupling parameter $\{\lambda\}$.

$$\begin{aligned}
\tilde{P}_{\beta_2}(\xi) = & \\
& \sum_{\{V\}} N_{\{\lambda\},\beta_1}(\{V\}, \xi) \exp \left[(\beta_1 - \beta_2) V_0 + \sum_{i=1}^L \lambda_i \beta_1 V_i \right] \\
& \sum_{\{V\},\xi} N_{\{\lambda\},\beta_1}(\{V\}, \xi) \exp \left[(\beta_1 - \beta_2) V_0 + \sum_{i=1}^L \lambda_i \beta_1 V_i \right]
\end{aligned} \tag{2.60}$$

The WHAM equations are the generalization of the single histogram equations. Let us consider R sets of simulations with i^{th} simulation is performed at temperature T_i with coupling parameter $\{\lambda\}$ using Eq.2.57 and the number of snapshots taken from the i^{th} simulation is n_i . So the probability histogram can be written as,

$$P_{\{\lambda\},\beta}(\{V\}, \xi) = \frac{\sum_{k=1}^R N_k(\{V\}, \xi) \exp \left(-\beta \sum_{j=0}^L \lambda_j V_j \right)}{\sum_{m=1}^R n_m \exp \left(f_m - \beta_m \sum_{j=0}^L \lambda_{j,m} V_j \right)} \tag{2.61}$$

and the free energy can be written as,

$$\exp(-f_j) = \sum_{\{V\},\xi} P_{\{\lambda\},\beta_j}(\{V\}, \xi) \tag{2.62}$$

where f_j is the dimension less free energy. $f_j = \beta_j A_j$ where A_j is the Helmholtz free energy of the system during j^{th} simulation. Eq.2.61 and Eq.2.62 are together called WHAM equations and these can be derived minimizing the error in the overlapping probability distribution function[25, 26].

Bibliography

- [1] J. P. Hansen and I. R. McDonald, Theory of Simple Liquids, 2nd ed. (Academic, London, 1986).
- [2] M. Allen and D. Tildesley, Computer Simulations of Liquids (Clarendon Press, Oxford, 1987).
- [3] M. D. Ediger, Annual Review of Physical Chemistry **51**, 99 (2000).
- [4] W. Kob, C. Donati, S. J. Plimpton, P. H. Poole, and S. C. Glotzer, Phys. Rev. Lett. **79**, 2827 (1997).
- [5] B. Doliwa and A. Heuer, Phys. Rev. Lett. **80**, 4915 (1998).
- [6] M. M. Hurley and P. Harrowell, The Journal of Chemical Physics **105**, 10521 (1996).
- [7] K. Kim and S. Saito, The Journal of Chemical Physics **138**, 12A506 (2013).
- [8] T. Odagaki and Y. Hiwatari, Phys. Rev. A **43**, 1103 (1991).
- [9] W. Kob and H. C. Andersen, Phys. Rev. E **51**, 4626 (1995).
- [10] F. W. Starr, J. F. Douglas, and S. Sastry, The Journal of Chemical Physics **138**, 12A541 (2013).
- [11] L. Berthier *et al.*, The Journal of Chemical Physics **126**, 184503 (2007).
- [12] L. Berthier *et al.*, The Journal of Chemical Physics **126**, 184504 (2007).
- [13] D. Coslovich, M. Ozawa, and W. Kob, The European Physical Journal E **41**, 62 (2018).
- [14] M. Ozawa, W. Kob, A. Ikeda, and K. Miyazaki, Proceedings of the National Academy of Sciences **112**, 6914 (2015),
- [15] S.-T. Lin, M. Blanco, and W. A. Goddard, The Journal of Chemical Physics **119**, 11792 (2003).

- [16] W. A. G. Shiang-Tai Lin, Prabal K. Maiti, *Journal of Physical Chemistry B* **114**, 8191 (2010).
- [17] D. A. McQuarrie, *Statistical Mechanics* book (1975).
- [18] P.-K. Lai, C.-M. Hsieh, and S.-T. Lin, *Phys. Chem. Chem. Phys.* **14**, 15206 (2012).
- [19] F. H. Stillinger and T. A. Weber, *Phys. Rev. A* **25**, 978 (1982).
- [20] S. Sastry, *Nature* **409**, 164 (2001).
- [21] S. Sengupta, F. Vasconcelos, F. Affouard, and S. Sastry, *The Journal of Chemical Physics* **135**, 194503 (2011).
- [22] F. Sciortino, *Journal of Statistical Mechanics: Theory and Experiment* **2005**, P05015 (2005).
- [23] B. Doliwa and A. Heuer, *Phys. Rev. Lett.* **80**, 4915 (1998).
- [24] S. Kumar, J. M. Rosenberg, D. Bouzida, R. H. Swendsen, and P. A. Kollman, *Journal of Computational Chemistry* **13**, 1011 (1992).
- [25] A. M. Ferrenberg and R. H. Swendsen, *Phys. Rev. Lett.* **61**, 2635 (1988).
- [26] A. M. Ferrenberg and R. H. Swendsen, *Phys. Rev. Lett.* **63**, 1195 (1989).

Chapter 3

Connecting real glasses to mean-field models: A study of structure

3.1 Introduction:

The details of the relaxation dynamics of glassy system and the properties of the glass has been and continues to be in the focus of an intense research activity [1]. These investigations are motivated by the fact that glasses are not only important for many daily and technological applications but are also an intellectual challenge for fundamental studies since so far there is no theoretical framework that is able to give a satisfactory description of the unusual properties of glassy systems and glasses. Although there are sophisticated mean-field theories, like the mode-coupling theory (MCT) of the glass transition [2, 3, 4, 5], or the random first order transition theory [6, 7, 11], that are able to give in some cases a surprisingly good description of real glass former [8, 5, 11, 12, 13, 6], these approaches still have many flaws since they fail to give a reliable description of many features of glass-forming systems opening thus the door to other approaches that attempt to describe glassy systems [15, 30, 17, 18, 19, 20]. Note that these theories are mean-field in nature, whereas the experiments and computer simulation studies are three or lower dimensional systems. Moreover, it has been found that MCT, although expected to be mean-field in nature, does not become exact even at high dimensions [21, 22], a flaw which might, however, be related to the approximations used to describe the structure of the liquid in high dimensions. Thus it is important to understand how these theories are connected to real glass-forming systems and how the properties change as the mean-field character of the system is modified. To establish such a connection

it is useful to study systems whereby varying a parameter one can go from d dimensional system to mean-field (MF) system. In the past various possibilities have been proposed to take this limit, see Ref. mari-kurchan for an overview, but most of them do have some drawbacks that prevent to reach a solid understanding how three-dimensional (3d) and MF systems are related to each other [28].

One interesting model that allows approaching the MF limit in a continuous manner has been proposed by Mari and Kurchan (MK) [28]. The MK-model is a hard-sphere system in which the interaction range between two particles i and j is a random variable with a variance that allows switching from a standard three-dimensional system to MF like system. For this model, it is found that with increasing interaction range the Stokes-Einstein relation holds down to lower temperatures and that the dynamic heterogeneity of the system, measured by the four-point susceptibility and non-Gaussian parameter, decreases. The increase in interaction range also makes the system follow MCT like behaviour for a larger range in temperature. Although all these results indicate that the MK model can indeed be used to study the transition from 3d to MF, there are certain features of the model that are disturbing. First of all, the structural properties of the system becomes very different from the one of a normal liquid if the MF limit is approached in that, e.g., the radial distribution function becomes gas-like. Related to this is the fact that the three-point correlation functions vanish. As a consequence one loses the property that nearest neighbors can cage a tagged particle, a notion that is fundamental for the slowing down of the dynamics in real glass-forming systems [1]. Secondly, the maximum attainable packing fraction diverges in the MF limit, a behavior that is very different from the one found in finite dimensions. Some of these oddities are avoided if one considers models on a lattice [24]. However, lattice models, notably kinetic Ising models with non-conserved particle density, do have the drawback that it is not obvious to what extent their relaxation dynamics is related to any off-lattice systems. As a consequence one has to be cautious when applying results from lattice models to describe the dynamics of real systems.

In the present chapter we introduce a simple approach that allows crossing over in a continuous manner from a normal 3d liquid to a MF system. In practice we do this by increasing for each particle the number of particles it can interact with, thus increasing the effective interaction of the particle with the rest of the system. In contrast to the studies discussed above, our method does not modify in a significant manner the local structure of the liquid even when the MF limit is reached, i.e. the structure is always similar to the one of the 3d system.

3.2 Details of system and simulations

As mentioned in the Introduction, our system is given by N particles that interact with each other via a standard short-range potential. In addition, each particle interacts also with “pseudo neighbors”, i.e. particles that are not necessarily close in space. Hence the total interaction potential of the system is given by

$$U_{\text{tot}}(r_1, \dots, r_N) = \sum_{i=1}^N \sum_{j>i}^N u(r_{ij}) + \sum_{i=1}^N \sum_{j=1}^k u^{\text{pseudo}}(r_{ij}) \quad (3.1)$$

$$= U + U_k^{\text{pseudo}} \quad . \quad (3.2)$$

The first term on the right-hand side is the regular interaction between particles while the second term is the interaction each particle has with its pseudo neighbours. Here we consider the case that the regular interaction describes a binary Lennard-Jones (LJ) system, with 80% of the particles of type A and 20% of the particles of type B. Thus the interaction between the particles i and j is given by

$$u(r_{ij}) = 4\epsilon_{ij} \left[\left(\frac{\sigma_{ij}}{r_{ij}} \right)^{12} - \left(\frac{\sigma_{ij}}{r_{ij}} \right)^6 \right] \quad , \quad (3.3)$$

where r_{ij} is the distance between the particles, σ_{ij} is the effective diameter of the particle and ϵ_{ij} is the interaction strength. We use σ_{AA} and ϵ_{AA} as the unit of length and energy, setting the Boltzmann constant $k_B = 1$. The values of the other parameters are given in Ref. [8], i.e. $\sigma_{AB} = 0.8$, $\sigma_{BB} = 0.88$, $\epsilon_{AB} = 1.5$, and $\epsilon_{BB} = 0.5$, a choice which makes this binary system to be a good glass-former. This potential is cut and shifted at $r_c = 2.5\sigma_{ij}$. The masses are $m_A = m_B = 1$ and time is expressed in units of $\sqrt{m_A \sigma_{AA}^2 / \epsilon_{AA}}$.

The interaction potential with the pseudo neighbours is modelled in terms of a modified LJ potential,

$$u^{\text{pseudo}}(r_{ij}) = u(r_{ij} - L_{ij}) \quad (3.4)$$

$$= 4\epsilon_{ij} \left[\left(\frac{\sigma_{ij}}{r_{ij} - L_{ij}} \right)^{12} - \left(\frac{\sigma_{ij}}{r_{ij} - L_{ij}} \right)^6 \right] \quad , \quad (3.5)$$

where L_{ij} is a random variable defined below. In our simulations we impose the restriction that any two particles interact either via $u(r_{ij})$ or via $u^{\text{pseudo}}(r_{ij})$. This condition determines how for a given configuration equilibrated with the potential u the pseudo neighbors and the values L_{ij} are chosen: Taking this

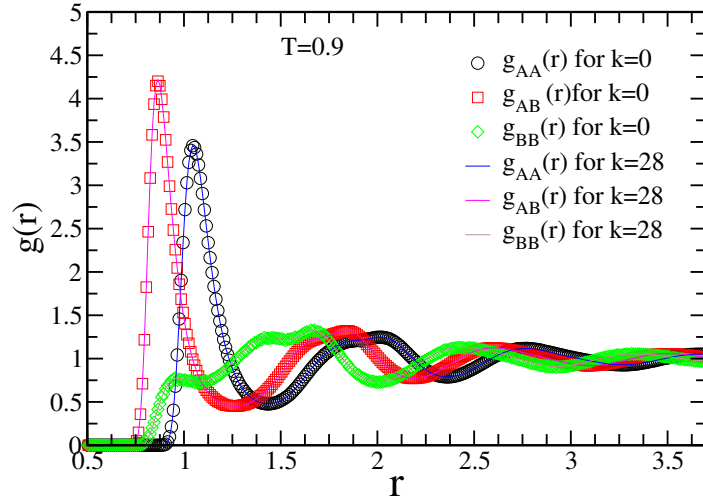


Figure 3.1: The partial radial distribution functions for $k = 0$ and $k = 28$ at $T = 0.9$. The structure remains invariant under the introduction of the pseudo neighbours.

configurations we select for each particle, i , k random numbers L_{ij} in the range $r_c \leq L_{ij} \leq L_{\max}$, where $L_{\max} \leq L_{\text{box}}/2 - r_c$, with L_{box} the size of the simulation box. (The distribution of these random variables will be denoted by $\mathcal{P}(L_{ij})$ and in the following, we will consider the case that the distribution is uniform.) Subsequently we choose k distinct particles j with $r_{ij} > r_c$ and use the L_{ij} to fix *permanently* the interaction between particles i and j . This procedure thus makes that each particle i interacts not only with the particles that are within the cutoff distance but in addition to k particles that can be far away. Note that once the particle j is chosen as a pseudo neighbour of particle i , automatically particle i becomes a pseudo neighbour of particle j . The system, as defined here, can then be simulated using a standard simulation algorithms.

The molecular dynamics (MD) simulation have been done using $N = 2744$ particles. We have performed constant volume, constant temperature simulations (velocity rescaling) at density $\rho = 1.2$, thus $L_{\text{box}} = 13.1745$, using a time integration step of $\Delta t = 0.005$. For L_{\max} we have taken 4.0, slightly below the maximum value of 4.09. We have simulated four different systems with the number of pseudo neighbours, $k = 0, 4, 12$, and 28.

3.3 Results

3.3.1 Structure of the liquid

To start, we discuss the effect of the pseudo neighbours on the structure of the liquid. In Fig. 3.1 we show the three partial radial distribution function, $g_{\alpha\beta}(r)$ with $\alpha, \beta \in \{A, B\}$ [14], for the $k = 0$ and the $k = 28$ systems. The temperature

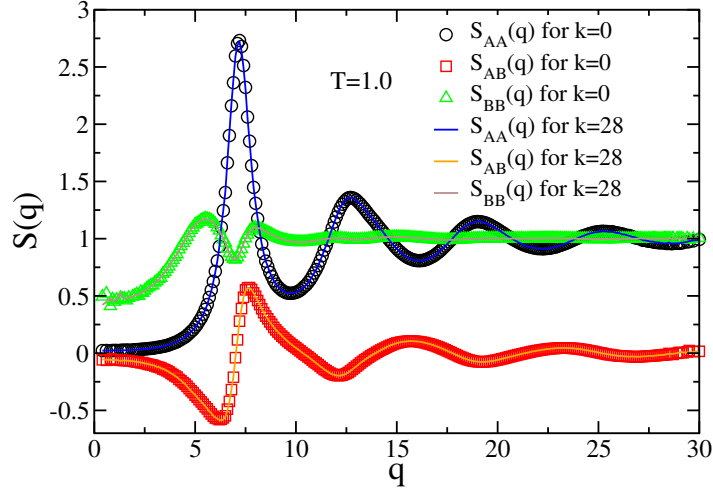


Figure 3.2: The partial structure factors for $k = 0$ and $k = 28$ at $T = 1.0$. Similar to what we have obtained in the radial distribution function, the structure remains invariant under the introduction of the pseudo neighbours.

is $T = 0.9$, which for the $k = 0$ system is slightly above the onset temperature, see Ref. [8], while for the $k = 28$ system it corresponds to a state at which the system is already rather viscous (see below). The graph shows that the radial distribution functions for the two systems overlap perfectly well, i.e. the structure is independent of k for this value of k . Thus this indicates that the interactions due to the pseudo neighbours do not affect the local structure of the system, one of the reasons for our choice of the interactions of the model.

To probe whether the structure of the liquid on a large scale is influenced by the introduction of the pseudo neighbors we have calculated the partial static structure factors and show them in Fig. 3.2 for the case of $k = 0$ and $k = 28$. Since the two sets of curves match each other perfectly well, we can conclude that also the large scale structure is not influenced by the additional neighbors.

3.3.2 Static properties of the pseudo neighbors

In this subsection, we characterize some of the structural properties of the pseudo neighbors with respect to a tagged particle.

To start, we first calculate the probability P_L that a given pseudo neighbor j interacts with the tagged particle i , where $L = L_{ij}$. Neglecting the indirect interactions (via the direct neighbors) between the tagged particle and the pseudo neighbor one can express P_L as

$$P_L = \frac{\int_{V_{\text{acc}}} d\mathbf{r} e^{-\beta u(r-L)} y(r)}{\int_{V_{\text{acc}}} d\mathbf{r} e^{-\beta u(r-L)}}. \quad (3.6)$$

Here $\beta = 1/k_B T$, V_{acc} is the volume accessible to the pseudo neighbor, and $y(r)$

is a step function that takes into account that the potential is cut off at $2.5\sigma_{\alpha\beta}$, i.e. $y(r) = 1$ if $L \leq r \leq L + 2.5\sigma_{\alpha\beta}$ and $y(r) = 0$ for all other values of r . The volume integrals in Eq. (3.6) can be decomposed into a spherical part that is contained inside the cubic box, and the rest. The latter volume is given by

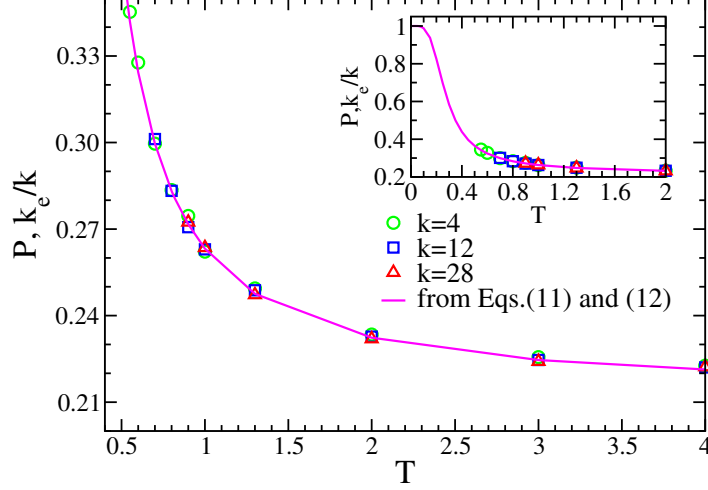


Figure 3.3: Probability that a pseudo neighbour is within the interaction range as a function of temperature. The pink line is the theoretical prediction from Eqs. (3.11) and (3.12). Inset: Same quantities extending the temperature range to $T = 0$. The theoretical curve shows a sigmoidal shape.

$$\Delta V = L_{\text{box}}^3 - \frac{4}{3}\pi\left(\frac{L_{\text{box}}}{2}\right)^3 \quad (3.7)$$

$$= L_{\text{box}}^3\left(1 - \frac{\pi}{6}\right) \quad (3.8)$$

A spherical integration in Eq. (3.6) gives then

$$P_L = \frac{\int_L^{L+r_c} dr r^2 e^{-\beta u(r-L)}}{\int_L^{L_{\text{box}}/2} dr r^2 e^{-\beta u(r-L)} + \Delta V} \quad (3.9)$$

Note that in the above expression, $L = L_{ij}$ is fixed. Hence for a distribution of L , the probability of finding a pseudo neighbour within the interaction range of the tagged particle is given by

$$P = \int_{r_c}^{L_{\text{max}}} dL \mathcal{P}(L) \frac{\int_L^{L+r_c} dr r^2 e^{-\beta u(r-L)}}{\int_L^{L_{\text{box}}/2} dr r^2 e^{-\beta u(r-L)} + \Delta V} \quad (3.10)$$

In the numerator we make the substitution $r' = r - L$ which allows to interchange the two integrals:

$$P = \int_0^{r_c} dr' \int_{r_c}^{L_{\text{max}}} dL \mathcal{P}(L) \frac{(r' + L)^2 e^{-\beta u(r')}}{\int_L^{L_{\text{box}}/2} dr r^2 e^{-\beta u(r-L)} + \Delta V} \quad (3.11)$$

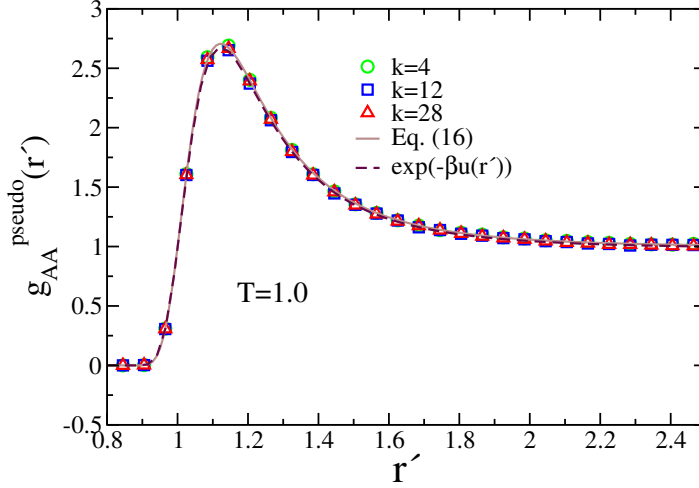


Figure 3.4: Radial distribution function for pseudo neighbours from simulations at $T = 1.0$ for $k = 4, 12$ and 28 . The distribution function of the pseudo neighbours is independent of k . The solid line is the result from the theoretical expression given by Eq. (3.16). The dashed line is the theoretical prediction from the bare potential.

We thus find that this probability is independent of k , a result that is reasonable since we have neglected any correlations between the pseudo neighbors. Also note that P depends on the interaction potential via $u(r)$ and r_c . For a binary system, we can generalize this calculation to obtain the partial probabilities $P_{\alpha\beta}$ and then the total probability is given by

$$P = x_A^2 P_{AA} + 2x_A x_B P_{AB} + x_B^2 P_{BB} \quad , \quad (3.12)$$

where x_α is the concentration of species α . In the simulation, this probability can be obtained by calculating the ratio k_e/k , where k_e is the number of pseudo neighbors that have a non-zero interaction with the tagged particle. In Fig. 3.3 we show the temperature dependence of P as obtained from Eqs. (3.11) and (3.12) (solid line) and compare it with the corresponding quantity k_e/k determined from the simulations (symbols). One recognizes that k_e/k is as expected independent of k and that the simulation data matches perfectly well the theoretical prediction given by Eqs. (3.11) and (3.12). Note that at the lowest temperatures at which we could equilibrate the systems for the different value of k the probability is around 0.3, i.e. for the glassy dynamics we will discuss below only a relatively small part of the pseudo neighbors are actually interacting with the tagged particle. The inset of the figure shows that P becomes 0.5 at around $T = 0.4$, a temperature at which already the $k = 0$ system is very viscous [15], and for $T \rightarrow 0$ the probability becomes 1, as expected.

To characterize the relative position of a pseudo-neighbor j with respect to a tagged particle i we can consider the corresponding radial distribution function

$$g^{\text{pseudo}}(r') = \frac{\rho_k}{4\pi r'^2} \sum_{i=1}^N \sum_{j(i)}^k \langle \delta(r' - |\mathbf{r}_i - \mathbf{r}_j| + L_{ij}) \rangle, \quad (3.13)$$

where in the second sum the index runs over the pseudo neighbors of the tagged particle i and ρ_k is the average pseudo neighbour density,

$$\rho_k = \int_{r_c}^{L_{\max}} \frac{k \mathcal{P}(L)}{V - \frac{4}{3}\pi L^3} dL, \quad (3.14)$$

where V is the total volume of the system.

To calculate $g^{\text{pseudo}}(r)$ analytically we can make use of our result for P given by Eqs. (3.11) and (3.12). The number k_e of pseudo neighbours within the interaction range can be expressed in terms of $g^{\text{pseudo}}(r')$ as

$$k_e = \rho_k \int_0^{r_c} dr' g^{\text{pseudo}}(r') \int_{r_c}^{L_{\max}} dL \mathcal{P}(L) 4\pi (r' + L)^2. \quad (3.15)$$

Since k_e can also be written as $k_e = k \times P$ we get, using Eq. (3.11) and Eq. (3.15)

$$\begin{aligned} & g^{\text{pseudo}}(r') \rho_k \int_{r_c}^{L_{\max}} dL \mathcal{P}(L) 4\pi (r' + L)^2 \\ &= k \int_{r_c}^{L_{\max}} dL \mathcal{P}(L) \frac{(r' + L)^2 e^{-\beta u(r')}}{\int_L^{L_{\text{box}}/2} dr r^2 e^{-\beta u(r-L)} + \Delta V} \end{aligned} \quad (3.16)$$

from which one obtains directly $g^{\text{pseudo}}(r')$. Note that $g^{\text{pseudo}}(r')$ is independent of k , since ρ_k is directly proportional to k , see Eq. (3.14).

Fig. 3.4 shows the radial distribution function $g^{\text{pseudo}}(r')$ from the simulations of three different values of k (symbols) and we recognize that, as predicted by Eq. (3.16) the function is indeed independent of k . We have also included the analytical result from Eq. (3.16) and we see that the theory describes perfectly well the simulation data, thus demonstrating that the approximation that the structure of the pseudo neighbors can be obtained well by the bare interaction with the tagged particle is very accurate, at least for the k values considered in the present work. We also note that since one has the relation $g^{\text{pseudo}}(r') = \exp(-\beta u(r'))$, which can be derived from Eq. (3.16), the function $g^{\text{pseudo}}(r')$ can also be obtained directly from the bare interaction potential $u(r')$ as shown in Fig.3.4.

Within the standard theory of liquids, the radial distribution function allows to obtain the potential energy [14]. Due to the presence of the pseudo neighbors this is no longer possible, and thus the usual expression has to be modified as follows. (Note that in the following we give the expressions for a one-component

system. For the binary system considered here, one will have to do the sum over the various partials.) Since the potential energy of the system has two contributions, one is the regular neighbour and the other the pseudo neighbour (see Eq. (6.2)), the total potential energy U_{tot} is given by,

$$\begin{aligned} \frac{U_{\text{tot}}}{N} &= \frac{\rho}{2} \int_0^\infty u(r)g(r)4\pi r^2 dr \\ &+ \frac{\rho_k}{2} \int_0^\infty u(r)g^{\text{pseudo}}(r) \int_{r_c}^{L_{\text{max}}} \mathcal{P}(L)4\pi(r+L)^2 dL dr. \end{aligned} \quad (3.17)$$

At this stage it is useful to introduce an “effective radial distribution” function $g^{\text{eff}}(r)$ by defining

$$\rho_{\text{eff}}g^{\text{eff}}(r) = \rho g(r) + \rho_k g^{\text{pseudo}}(r) \frac{\int_{r_c}^{L_{\text{max}}} \mathcal{P}(L)(r+L)^2 dL}{r^2}, \quad (3.18)$$

where the effective particle density is given by

$$\rho_{\text{eff}} = \rho + \rho_k \quad . \quad (3.19)$$

Note that since ρ_k increases linearly with k , for large k the density ρ_{eff} is dominated by ρ_k and hence in that limit g^{eff} will be directly proportional to $g^{\text{pseudo}}(r)$.

Using $g^{\text{eff}}(r)$ we now can express the total potential energy of the system as a function of the radial distribution function $g^{\text{eff}}(r)$:

$$\frac{U_{\text{tot}}}{N} = \frac{\rho_{\text{eff}}}{2} \int_0^\infty u(r)g^{\text{eff}}(r)4\pi r^2 dr \quad . \quad (3.20)$$

In Fig. 3.5 we present $g^{\text{eff}}(r)$ for the A-A correlation for different values of k . Since the regular radial distribution function $g(r)$ is independent of k (see Fig. 3.1) and $g^{\text{pseudo}}(r)$ can be calculated analytically from Eq. (3.16) it is possible to obtain g^{eff} for arbitrary values of k . The graph shows that with increasing k , the radial distribution function loses its characteristic structure with the multiple peaks and converges toward a distribution that has a single peak at $r = 1$. This result can be understood directly from Eq. (3.18) since for large k the first term on the right-hand side vanishes (if divided by ρ_{eff}) while the second term is $g^{\text{pseudo}}(r)$ multiplied by an r -dependent factor that is independent of k . So we see that in the large k limit the effective radial distribution function develops a dominant sharp peak at a finite distance. With decreasing temperature, this peak increases since most of the pseudo neighbors will condensate at the optimal distance L_{ij} . It is this growing peak that signals the increasing number of constraints in the system which induce the slowing down of the relaxation dynamics. This loss of structure of the radial distribution

function is a typical signature of mean-field-like systems, such as the hard-sphere system of Ref. [mari-kurchan]. (However, unlike the results in the present study, in the hard-sphere system there is no peak at $r = 1$.)

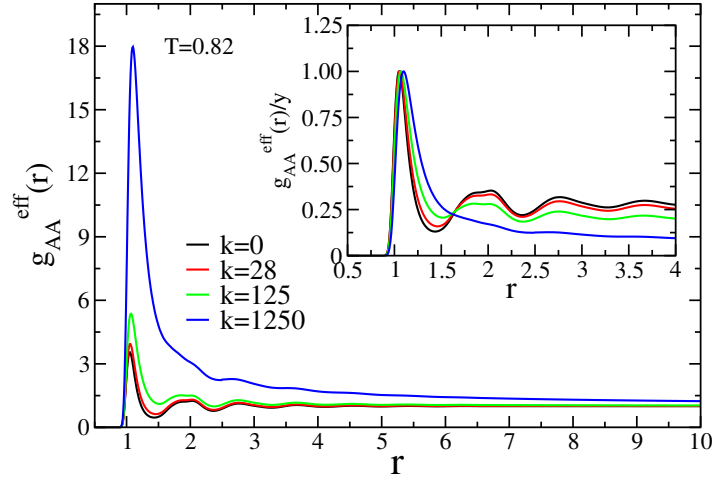


Figure 3.5: The effective A-A particle radial distribution function for $k = 0, 28, 125$, and 1250 . With increasing k the multi-peak structure disappears. Inset: $g_{AA}^{\text{eff}}/y(k)$ vs r where $y(k)$ is the height of the main peak. The smoothing of the undulation with increasing k is clearly seen.

3.4 Inherent structure in the mean-field system

We have found so far that there is no change in local structure between the $k=0$ and other k systems and $g^{\text{pseudo}}(r)$ is also independent of k . But the situations change when we consider the zero temperature configurations. We find that the inherent normal neighbor structure of mean-field systems reach effective at high temperature states than the $k=0$ system. Fig.3.6 shows that peak height of radial distribution function of the inherent structure of $k=28$ system become higher than the $k=0$ system, although the equilibrium temperature is same for both the systems. On the other hand, the $g^{\text{pseudo}}(r)$ becomes sharper for $k=28$ system than the $k=0$ system (see Fig.3.7). Radial distribution function using two body potential gives the similar result as $g^{\text{pseudo}}(r)$ of the equilibrium state.

3.5 Conclusion

We have introduced a simple glass-forming system which allows to tune in a smooth manner its mean-field character. This is achieved by introducing additional k “pseudo neighbors” with which a particle can interact. These additional interactions are long-ranged and hence with increasing k , each particle becomes increasingly connected with the rest of the system. However, since we also keep

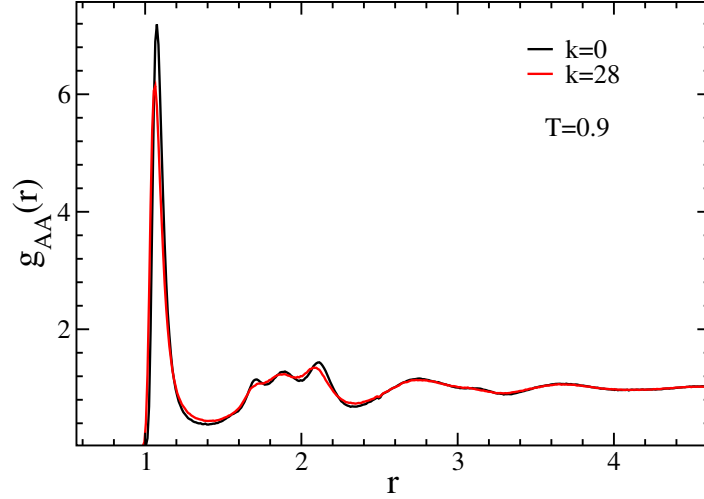


Figure 3.6: Comparison of radial distribution function of the regular neighbor at minimum energy state between $k=0$ and $k=28$ systems. Both the equilibrium structure are at $T=0.9$.

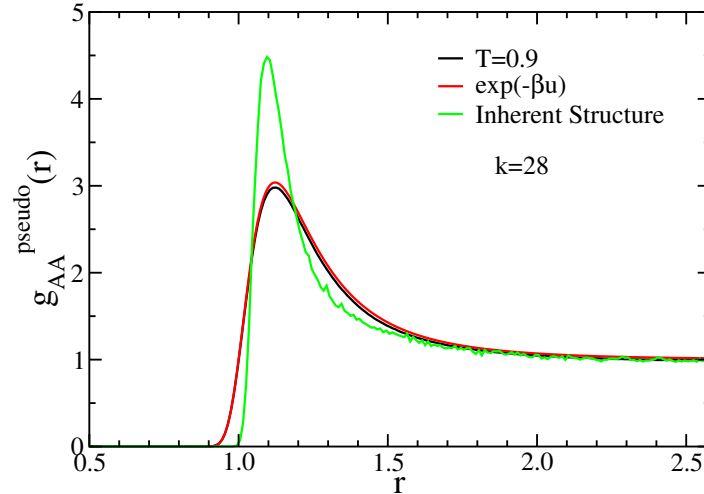


Figure 3.7: g_{AA}^{pseudo} at $T=0.9$ both from simulation, analytical expression and at minimum energy state.

the original interaction between nearest-neighbor particles, our model has the advantage of maintaining a liquid-like structure even in the mean-field limit, i.e. the nearest neighbor distances are always of the order of the particle diameter, which is in contrast to other models that allow tuning their mean-field character [28].

We find that the structure of the system, as characterized by the radial distribution function or the static structure factor, remains unchanged with the addition of the pseudo neighbours, also this in contrast to previous models. Due to the way the model is set up, it is possible to analytically calculate all the static structural properties of the system from the knowledge of the $k = 0$ system. This allows us to understand that the additional interactions give rise to an effective

potential that increases with k , thus influencing the relevant temperature scale of the system.

In an earlier study involving different glass-formers evidence was given that the locally preferred structures (LPS) are connected to the dynamics only for systems which are not mean field like [48]. The ability of the present model to continuously tune the mean-field behaviour makes it thus an ideal system to check the validity of this observation. Since we find that with increasing number of pseudo neighbours the LPS remains unchanged whereas the dynamics slows down, this suggests that with an increase in the mean field nature the correlation between the LPS and the dynamics decreases, a result that corroborates the earlier findings from Ref. [48].

The range of k that we were able to access in the present simulation is relatively modest since for larger k the relaxation dynamics became too slow to equilibrate the system within a reasonable amount of computer time. It is, however, of interest to make an educated guess on what will happen if k is increased further. Our analytical results for the structure, Fig. 3.5, shows that with increasing k the main peak in the effective radial distribution function becomes very high. In this limit one can thus expect that the contribution from the pseudo neighbors will start to dominate the one from the real nearest neighbors and hence will make the system mean-field like. However, from the graph we recognize that this increase becomes strong only once k is larger than $O(10^2)$, i.e., a value that is at present somewhat beyond the reach of standard computer simulations. It can be expected, however, that in the near future improved algorithms will allow to deal with this bottleneck. In that case our approach will thus allow to make more stringent investigations on how the properties of a normal three dimensional glass-former can be connected to the corresponding system in the mean field limit.

This summary clearly indicates that the details how the mean-field limit is approached are important and future studies are needed to clarify this point. Finally, we note that the approach we propose here on how the mean-field character is tuned can be applied to any system. Hence it will be interesting to study whether other types of interaction potentials, such as the Coulomb potentials used to describe oxide glass-formers, will give qualitatively the same behavior, or in other words, whether the approach to the mean-field limit depends on the nature of the local structure of the system.

Bibliography

- [1] W. Kob and K. Binder, *Glassy Materials and Disordered Solids: An Introduction to Their Statistical Mechanics* (World Scientific, 2011).
- [2] W. Götze, *Journal of Physics: Condensed Matter* **11**, A1 (1999).
- [3] W. Götze, *Complex Dynamics of Glass-Forming Liquids: A Mode-Coupling Theory* (Oxford Science Publication, 2008).
- [4] L. M. C. Janssen, *Frontiers in Physics* **6**, 97 (2018).
- [5] S. P. Das, *Statistical Physics of Liquids at Freezing and Beyond* (Cambridge University Press, 2011).
- [6] T. R. Kirkpatrick and P. G. Wolynes, *Phys. Rev. A* **35**, 3072 (1987).
- [7] X. Xia and P. G. Wolynes, *Proceedings of the National Academy of Sciences* **97**, 2990 (2000).
- [8] V. Lubchenko and P. G. Wolynes, *The Journal of Chemical Physics* **119**, 9088 (2003).
- [9] W. Kob and H. C. Andersen, *Phys. Rev. E* **51**, 4626 (1995).
- [10] W. Kob and H. C. Andersen, *Phys. Rev. E* **52**, 4134 (1995).
- [11] W. Kob, T. Gleim, and K. Binder, *AIP Conference Proceedings* **489**, 68 (1999).
- [12] S. M. Bhattacharyya, B. Bagchi, and P. G. Wolynes, *Proceedings of the National Academy of Sciences* **105**, 16077 (2008).
- [13] M. K. Nandi and S. M. Bhattacharyya, *Journal of Physics: Condensed Matter* **32**, 064001 (2019).
- [14] S.-H. Chong, *Phys. Rev. E* **78**, 041501 (2008).
- [15] E. Flenner and G. Szamel, *The Journal of Chemical Physics* **138**, 12A523 (2013).

-
- [16] M. K. Nandi, A. Banerjee, S. Sengupta, S. Sastry, and S. M. Bhattacharyya, *The Journal of Chemical Physics* **143**, 174504 (2015).
- [17] M. K. Nandi, A. Banerjee, C. Dasgupta, and S. M. Bhattacharyya, *Phys. Rev. Lett.* **119**, 265502 (2017).
- [18] M. K. Nandi and S. M. Bhattacharyya, arXiv:2011.02299 (2020).
- [19] J. P. Garrahan and D. Chandler, *Phys. Rev. Lett.* **89**, 035704 (2002).
- [20] Y. Jung, J. P. Garrahan, and D. Chandler, *The Journal of Chemical Physics* **123**, 084509 (2005).
- [21] A. Ikeda and K. Miyazaki, *Phys. Rev. Lett.* **104**, 255704 (2010).
- [22] B. Schmid and R. Schilling, *Phys. Rev. E* **81**, 041502 (2010).
- [23] R. Mari and J. Kurchan, *The Journal of Chemical Physics* **135**, 124504 (2011).
- [24] L. Berthier, G. Biroli, D. Coslovich, W. Kob, and C. Toninelli, *Phys. Rev. E* **86**, 031502 (2012).
- [25] J. P. Hansen and I. R. McDonald, *Theory of Simple Liquids* (Elsevier, Amsterdam, 1986).
- [26] D. Coslovich, M. Ozawa, and W. Kob, *The European Physical Journal E* **41**, 62 (2018).
- [27] C. A. Angell, *Science* **267**, 1924 (1995).
- [28] A. Cavagna, I. Giardinà, and G. Parisi, *Journal of Physics A: Mathematical and General* **34**, 5317 (2001).
- [29] B. Doliwa and A. Heuer, *Phys. Rev. Lett.* **80**, 4915 (1998).
- [30] T. Odagaki and Y. Hiwatari, *Phys. Rev. A* **43**, 1103 (1991).
- [31] M. Nauroth and W. Kob, *Phys. Rev. E* **55**, 657 (1997).
- [32] G. M. Hocky, D. Coslovich, A. Ikeda, and D. R. Reichman, *Phys. Rev. Lett.* **113**, 157801 (2014).

Chapter 4

Connecting real glasses to mean-field models: A study of dynamics

4.1 Introduction:

Another approach to connect the properties of 3d systems with the MF behavior has been proposed in a series of papers by Miyazaki and coworkers who have studied the properties of the Gaussian-Core-Model (GCM) [8, 9, 10]. Due to the long interaction range, each particle has a large number of neighbours, and hence the system can be expected to be MF like. These authors showed that compared to the (short-ranged) Kob-Andersen (KA) model [8], in the GCM the Stokes-Einstein relation is followed till a lower temperature regime and that the relaxation dynamics shows a qualitatively better agreement with the MCT predictions [9]. Furthermore, it was found that the GCM shows less dynamic fluctuation and that activated processes are suppressed [8], in agreement with recent studies of the thermodynamic properties of this system [11].

A further possibility to connect the properties of low dimensional systems with the MF predictions is to consider systems with increasingly higher dimensions. Sengupta *et al.* have studied the properties of some standard glass formers in 2, 3, and 4 dimensions and found that with increasing dimensionality the breakdown of the Stokes-Einstein relation becomes less pronounced and that the dynamical heterogeneity decrease [12]. Charbonneau *et al.* have studied systems up to 6 dimensions and found that the shape of the cage does not become Gaussian-like, as expected from MF [13], showing that the approach to this limit might be more complex than expected.

In the present paper we introduce a simple approach that allows crossing over

in a continuous manner from a normal 3d liquid to a MF system. In practice we do this by increasing for each particle the number of particles it can interact with, thus increasing the effective interaction of the particle with the rest of the system. In contrast to the studies discussed above, our method does not modify in a significant manner the local structure of the liquid even when the MF limit is reached, i.e. the structure is always similar to the one of the 3d system. So this allows us to study how increasing connectivity affects the relaxation dynamics, without modifying in a noticeable manner the structure, and hence to probe the dynamics upon approaching the MF limit.

4.2 Results

4.2.1 Relaxation dynamics

We now analyze how the presence of the pseudo neighbours affects the relaxation dynamics. To characterize this dynamics we consider the self part of the overlap function $Q(t)$ and the mean squared displacement (MSD) of a tagged particle, $\Delta r^2(t)$. The former observable is defined as

$$Q(t) = \frac{1}{N} \sum_{i=1}^N \langle \omega(|\mathbf{r}_i(t) - \mathbf{r}_i(0)|) \rangle \quad , \quad (4.1)$$

where the function $\omega(x)$ is 1 if $0 \leq x \leq a$ and $\omega(x) = 0$ otherwise. The parameter a is chosen to be 0.3, a value that is slightly larger than the size of the cage (determined from the height of the plateau in the MSD at intermediate times [8].) Thus the quantity $Q(t)$ tells whether or not at time t a tagged particle is still inside the cage it occupied at $t = 0$.

In Fig. 4.1 we show the time dependence of $Q(t)$ for different values of k . The temperature is $T = 0.9$ which corresponds for $k = 0$ to a T that is around the onset temperature [8, 2]. The graph demonstrates that with increasing k , the relaxation dynamics slows down quickly, in that the correlator for $k = 28$ decays on a time scale that is about two orders of magnitude larger than the one for $k = 0$. Also note that for the largest k we clearly see a two-step relaxation, i.e., the hallmark of glassy dynamics in which the particles are temporally trapped by their neighbors [1], while for $k = 0$ one has just a simple one-step relaxation, i.e., a normal liquid state relaxation. These results demonstrate that the presence of the pseudo neighbors does have the sought after effect of strongly slowing down the relaxation dynamics of the system, although, as demonstrated above, the overall structure of the liquid is not changed. Interestingly the shape of the time correlation function in the α -relaxation regime does not seem to

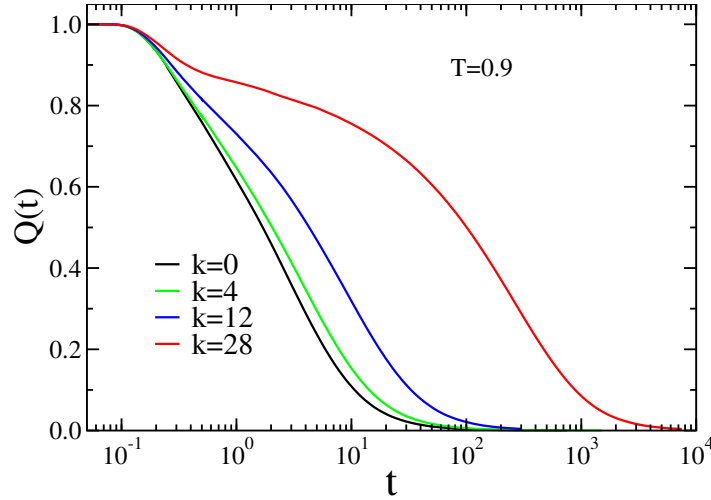


Figure 4.1: Time dependence of the self part of overlap function $Q(t)$ for systems with different values of k at $T = 0.9$. With increasing k the relaxation dynamics quickly slows down.

have a noticeable dependence on k , indicating that the relaxation mechanism is weakly dependent on k . However, this conclusion only holds for length scales on the order of ' a ' while it could be that on larger scales differences become noticeable. Here we also note that for other mean-field like models, such as the one introduced by Mari and Kurchan [28], an increase of the interaction range leads to an *acceleration* of the dynamics, i.e. the hoped for slowing down of the dynamics is not necessarily guaranteed.

Next, we compare the time dependence of the mean squared displacement, averaged over all the particles, of two systems, $k = 0$ and $k = 28$, Fig. 4.2. For

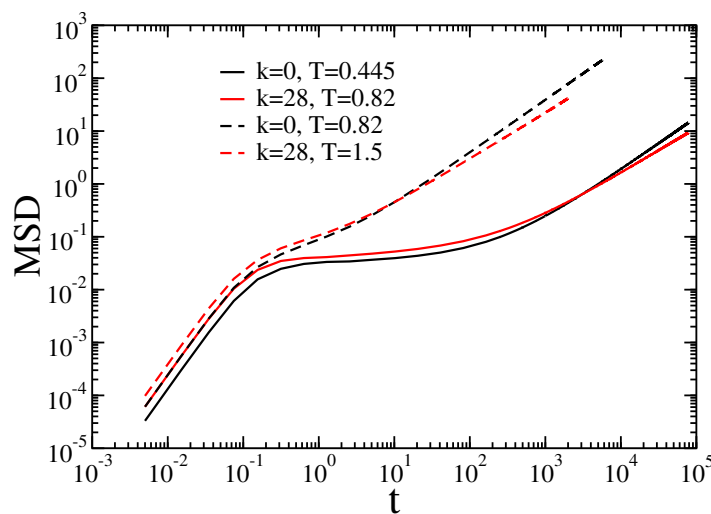


Figure 4.2: Time dependence of the mean squared displacement for the $k = 0$ and $k = 28$ systems in the high and low temperature regimes. The curves are for similar value of relaxation time. The $k = 28$ system shows a weak sub-diffusive behaviour at high and low temperature.

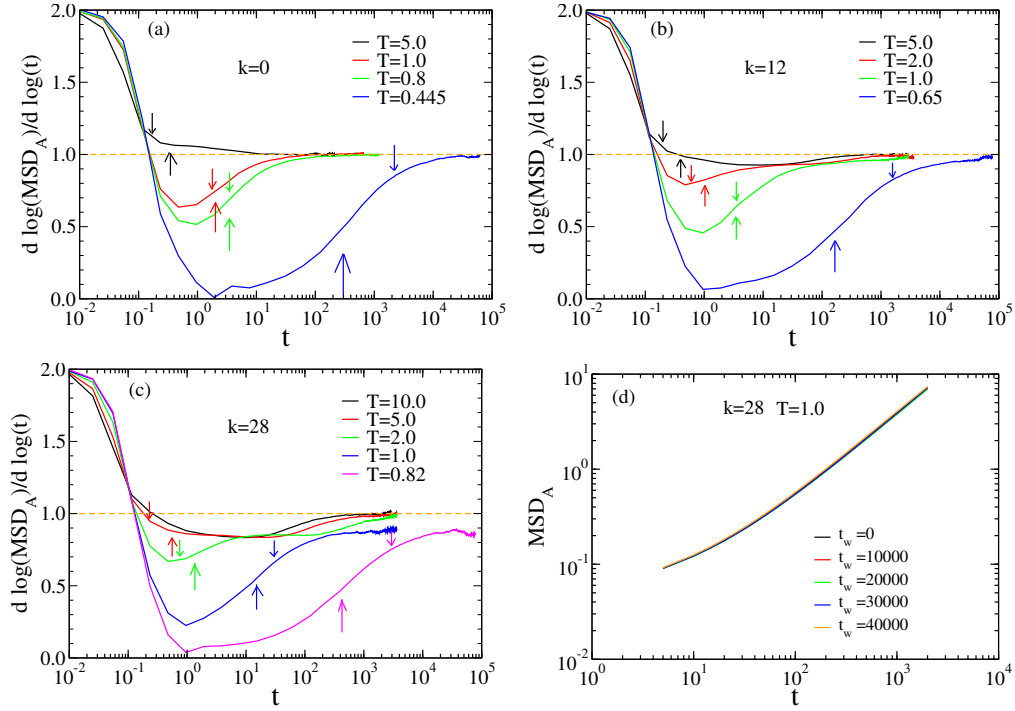


Figure 4.3: Double-logarithmic derivative of the MSD of the A particles as a function of time. (a) System for $k = 0$. If temperature is decreased the derivative shows at low T a local minimum, indicating the presence of caging. (b) System for $k = 12$. Qualitatively the same time dependence as in panel (a) but now at higher temperatures. (c) System for $k = 28$. One sees that the curves show at intermediate times a plateau that is due to the caging caused by the pseudo neighbors. The arrows pointing upward [downward] in panels (a)-(c) indicate τ_2 [τ_4], the location of the peak in the non-Gaussian parameter $\alpha_2(t)$ [in the dynamic susceptibility $\chi_4(t)$]. (d) MSD of the A particles for different waiting times t_w (see legend). No waiting time dependence is noticeable.

the $k = 0$ system we show the MSD for $T = 0.82$, i.e., a temperature close to the onset T and as a consequence one sees that the curve shows between the ballistic regime at short times, $\Delta r^2(t) \propto t^2$, and the diffusive regime at long times, $\Delta r^2(t) \propto t^1$, a weak shoulder. Qualitatively the same time-dependence is found for the $k = 28$ system, but this time at the higher temperature, $T = 1.5$, indicating that the increase of k leads to an increase of the onset temperature. If for the $k = 0$ system the temperature is lowered to 0.445, the MSD shows at intermediate times a very pronounced plateau that is due to the temporary caging of the particles [1]. The same behavior is found in the $k = 28$ system at $T = 0.82$ with a plateau height and length that is very close to the one of the $k = 0$ system. (This similarity is due to our choice of the temperature $T = 0.82$). Since we have seen above that the local structure of the system at fixed temperature hardly depends on k , see Fig. 3.1, the pronounced caging

for the $k = 28$ system (at $T=0.82$) is thus due to the pseudo neighbors, i.e., the non-local interactions. From these curves we hence can conclude that the presence of the additional interactions leads to a substantial slowing down of the relaxation dynamics while the details of the MSD, such as the height of the plateau or its width, at the same effective temperature (discussed below) are modified only mildly, at least in the parameter regime probed here.

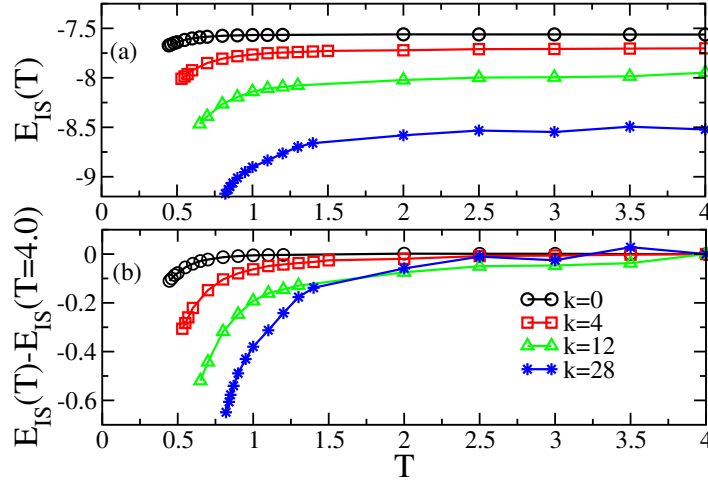


Figure 4.4: (a) Inherent structure energy, E_{IS} , as a function of temperature for the $k = 0, 4, 12$, and 28 systems. (b) Shifted (by $E_{IS}(T = 4.0)$) inherent structure energy vs. T . Near T_{onset} the energy starts to deviate from its high temperature value allowing to determine T_{onset} . With increasing k , T_{onset} moves to higher temperatures.

At sufficiently long times the motion of the particles is expected to be diffusive, and hence the MSD should increase linearly in time. Fig. 4.2 shows that for the $k = 0$ system, this is indeed the case and that this diffusion sets in once the MSD has reached a value around 1.0. Interestingly one observes for the $k = 28$ system even at the longest times a sub-diffusive behavior, with an exponent that is around 0.8, and this even for values of the MSD that are on the order of 10. This behavior can be noticed better by calculating the slope of the MSD in the log-log presentation, see Fig. 4.3. For $k = 0$, panel (a), we see that at short times the slope is 2.0, as expected for a ballistic motion. At high temperatures the slope crosses over to 1.0 at around $t = 3$, i.e. the system becomes diffusive. If T is lowered, the slope starts to show a dip with a depth and width that increase rapidly with decreasing temperature. For long times we see, however, that the curves again attain the value of 1.0, i.e. the system is diffusive. Qualitatively the same behavior is found for $k = 4$ (not shown) and $k = 12$, panel (b). However, a closer inspection of the curve for $T = 2.0$ reveals that after the first dip in the slope, the curve does not rise immediately to the value 1.0 but shows instead a plateau at a height of around 0.9 in the time window $5 \leq t \leq 200$. The

asymptotic value 1.0 is thus reached only at longer times, i.e. the MSD shows a sub-diffusive regime. Qualitatively the same behavior is found for $k = 28$, panel (c), but now the mentioned plateau at intermediate times becomes more visible since its height has decreased to 0.8, i.e. the deviation from the diffusive regime become more pronounced. We now clearly see that if the temperature is lowered the curves reach this second plateau at a later time, but its height is unchanged (see the curves for $T = 1.0$ and 0.82). Note that this plateau at long times is indeed a distinct dynamic regime and not just a brief transient during which the system approaches the diffusive limit. We also exclude the possibility that this new plateau is just an out-of-equilibrium phenomenon since, see panel (d), the MSD for different waiting times show no waiting time dependence. We interpret this new regime as a consequence of the interaction of the tagged particle with its pseudo neighbors. These interactions will vanish only if all the involved pairs have moved by a radial distance of around r_c , and, because of geometrical reasons (the volume of the spherical cap increases with L_{ij}) and the fact that $L_{ij} > r_c$, this takes certainly more time than cutting just the interactions between the tagged particle and its nearest neighbors, which explains the long time tail in the MSD. Note, however, that for sufficiently long times the MSD can be expected to become diffusive for all values of k , see, e.g., the curve for $T = 2.0$ in panel (c). This behaviour is thus similar to that observed earlier in systems where there are two length-scales [17]. In order to distinguish in the following the two mentioned processes, we will refer to the one corresponding to the particles leaving their nearest neighbor cage as the “NN- α -process”, while the dynamics in which the pseudo-neighbors leave the interaction range of the tagged particle will be referred to as the “PN- α -process”. Note that although Fig. 4.3 clearly indicates that there are two processes, we will see in the following that not all observables reveal this in a direct manner. For example, the time dependence of $Q(t)$, presented in Fig. 4.1, does not indicate an obvious presence of two different α -processes, although the pseudo-neighbors can be expected to affect not only the relaxation time but also the details of the correlator.

Since the onset temperature is an important point on the energy scale of the system, we now have a closer look at the k -dependence of T_{onset} . As mentioned above, this temperature can be identified from the first occurrence of a plateau in the MSD. Alternatively one can study the inherent structure energy, E_{IS} , which shows at T_{onset} a marked change in its T -dependence [39, 29]. (We recall that E_{IS} of a configuration is the potential energy evaluated at the local minimum of the energy reached from the configuration via the steepest descent procedure.) In Fig. 4.4(a) we show E_{IS} as a function of T , with the different curves corresponding to different values of k . From the graph, one recognizes

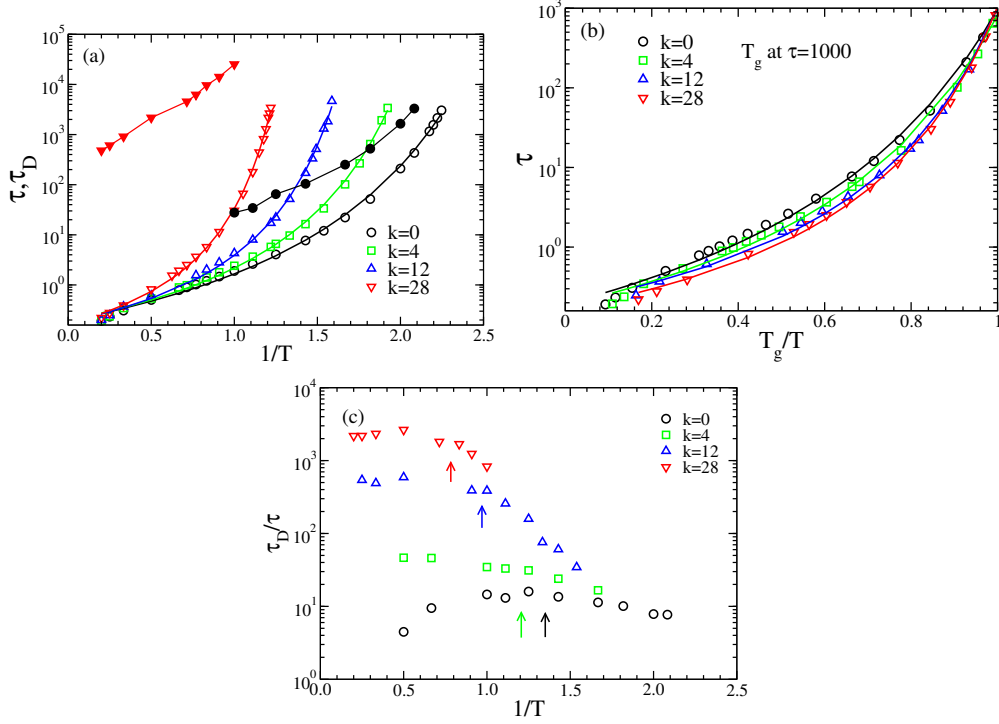


Figure 4.5: (a) Arrhenius plot of the α -relaxation time, τ , and the relaxation time obtained from the MSD, τ_D , for systems with different values of k . Open and full symbols are for τ and τ_D , respectively. The lines are fits to τ with the Vogel-Fulcher-Tammann expression, Eq. (4.2). (b) Same data as in (a) but now as a function of the scaled temperature T_g/T , with $\tau(T_g) = 10^3$. (c) Temperature dependence of the ratio τ_D/τ for different values of k . The arrows indicate T_{onset} .

that with increasing k the energy decreases, an effect that is due to the presence of the pseudo neighbors which can lower the energy by occupying the well in the interaction potential. Less trivial is the fact that the temperature at which the curve starts to decrease rapidly, i.e. the onset temperature, increases with increasing k . Thus the increase of T_{onset} with k can be seen directly from this static observable. In order to see better the k -dependence of T_{onset} , we plot in Fig. 4.4(b) the inherent structure energy shifted by $E_{\text{IS}}(T = 4.0)$. (The choice of $T = 4.0$ for this normalization is not crucial.) The resulting graph clearly shows that the bend in the inherent structure energy occurs at higher temperatures with growing k , demonstrating the increase of the onset temperature. Fitting two straight lines to the data for $T > T_{\text{onset}}$ and $T < T_{\text{onset}}$, their intersection point can be used to determine T_{onset} . As we will show elsewhere [20], the so obtained values are compatible with the values of onset temperature as determined from the entropy [2]. In Table 5.1 we list the values of T_{onset} obtained from these curves and one sees that for $k = 28$ this temperature is about 90% higher than T_{onset} for $k = 0$.

Table 4.1: The value of the characteristic temperatures and the kinetic fragility parameter for systems with different values of k . T_{onset} is the onset temperature at which the inherent structure energy starts to deviate significantly from its high temperature value. T_c is the MCT transition temperature. T_0 is the singular temperature of the Vogel-Fulcher-Tammann equation, Eq.(4.2). All characteristic temperatures increase with increasing k . Also included are the normalized differences between various temperatures. K is the kinetic fragility defined in Eq. (4.2). $x(k)$ is the prefactor needed for the scaling plot shown in Fig. 4.6(b).

k	T_{onset}	T_c	T_0	$\frac{T_{\text{onset}}-T_c}{T_c}$	$\frac{T_{\text{onset}}-T_c}{T_{\text{onset}}}$	$\frac{T_{\text{onset}}-T_0}{T_0}$	$\frac{T_c-T_0}{T_0}$	K	$x(k)$
0	0.74 ± 0.04	0.43	0.283	0.72	0.42	1.61	0.52	0.184	1.0
4	0.83 ± 0.08	0.51	0.362	0.63	0.38	1.29	0.41	0.237	1.55
12	1.03 ± 0.07	0.62	0.465	0.66	0.40	1.22	0.33	0.286	2.0
28	1.28 ± 0.22	0.80	0.610	0.60	0.38	1.10	0.31	0.297	2.1

A further important quantity to characterize the relaxation dynamics of a glass-former is the α -relaxation time τ . Here we define this time scale via $Q(\tau) = 1/e$. This definition is reasonable since we have seen in Fig. 4.1 that the shape of the time correlation functions is basically independent of k . (Note that with this definition of τ we do not distinguish between the NN- α -process and the PN- α -process discussed in the context of Fig. 4.1. For the values of k considered here, this is justified since the final decay of $Q(t)$ involves both processes.) Fig. 4.5(a) is an Arrhenius plot of τ for the different systems. One clearly sees that with increasing k , the dynamics quickly slows down and that the bending of the curve seems to increase, i.e. the system becomes more fragile. To quantify this trend as a function of k , we have fitted $\tau(T, k)$ at intermediate and low temperatures to a Vogel-Fulcher-Tammann(VFT)-law:

$$\tau(T) = \tau_0 \exp \left[\frac{1}{K(T/T_0 - 1)} \right] . \quad (4.2)$$

Here T_0 is the so-called VFT temperature at which the relaxation time of the system is predicted to diverge. The parameter K describes the curvature of the data in an Arrhenius plot and hence can be considered as a measure for the fragility of the glass-former. The figure demonstrates that this functional form gives a good fit to the data (solid lines) and hence allows to estimate T_0 and K .

The values of T_0 are included in Tab. 5.1 as well and one sees that T_0 changes by about a factor of two if k is increased from 0 to 28, i.e. a factor that is comparable to the one found for T_{onset} . In contrast to this we find that the parameter

K occurring in the Vogel-Fulcher-Tammann-law, Eq. (4.2), increases by about 30% in the considered k -range, see Tab. 5.1. This indicates that the introduction of the pseudo neighbors renders the system increasingly more fragile. Another way to see this is to define an effective glass transition temperature T_g via $\tau(T_g) = 10^3$ and to plot the relaxation time as a function of T_g/T [1, 21]. This is done in Fig. 4.5(b) and one sees that the curves for large k are indeed more bent than the ones for small k , i.e. the fragility of the system increases with k . This trend is thus qualitatively similar to the observation of Ref. sastry-SE in which it was found that increasing the dimensionality of a glass-former gives rise to a higher fragility.

Since the MSD has shown that the system has two kind of α -processes it is useful to study how the corresponding relaxation times relate to each other. For the $k > 0$ systems particles are caged by their nearest neighbours as well as by their pseudo neighbours. When a particle leaves its NN cage the overlap function decays and this timescale is captured by τ . We now define a relaxation time τ_D for the PN-process as the time scale at which the system becomes diffusive, i.e. the time where the logarithmic derivative of the MSD goes to 1 [22]. In practice we consider $t = \tau_D$ for which $\frac{d \log(\text{MSD})}{d \log(t)} = 0.97$. In Fig. 4.5(a) we have included the T -dependence of τ_D for the $k = 0$ and the $k = 28$ systems and one recognizes that τ_D is significantly larger than τ but that its T -dependence is weaker. To see the latter in a clearer way we show in panel (c) the T -dependence of the ratio τ_D/τ for all value of k considered. We recognize that the ratio starts to decrease quickly for temperatures that are below T_{onset} , i.e. once the systems start to show glassy dynamics. Since this decrease is very pronounced for $k > 0$, we conclude that the slowing down of the overall dynamics of the system is mainly governed by the NN α -process (which is strongly influenced by the presence of the pseudo neighbors).

These results show that the pseudo neighbors strongly influence the relaxation dynamics of a tagged particle in that the leaving of the cage formed by the nearest neighbors is strongly slowed down, as indicated by $\tau(T)$. In addition the pseudo neighbors also induce a new slow process, the PN- α process, which is related to the motion of the pseudo neighbors with respect to the tagged particle. However, this slow process does not depend very strongly on T since there is no structural correlation between the pseudo neighbors of a given tagged particle (this in contrast to the nearest neighbors which are correlated because of the local steric hindrance). As a consequence this slow PN- α process is *not* the mechanism responsible for the slowing down of the overall dynamics of the system. The relevant mechanism for this is thus given by the NN- α process.

4.2.2 MCT power law

Having presented our findings regarding the relaxation dynamics of the system we now probe whether this dynamics can be described by means of mode coupling theory. MCT predicts that close to the critical temperature T_c of the theory the relaxation times show a power law divergence:

$$\tau(T) = \tau_{\text{MCT}}(T - T_c)^{-\gamma} \quad . \quad (4.3)$$

Using this functional form to fit the temperature dependence of the relaxation time we obtain $T_c(k)$ (values are given in Tab. 5.1). In Fig. 4.6(a) we present a log-log plot of the relaxation time as a function of the normalized temperature $(T - T_c)/T_c$. One recognizes that for $k = 0$, the increase of τ with decreasing T is described well by a power law (dashed line), in agreement with previous simulations [23, 8]. However, at the lowest T 's deviations are observed, and the increase in τ is weaker than the power law predicted by MCT. This deviation is usually attributed to the existence of ‘‘hopping processes’’, i.e. a component in the relaxation dynamics that is not taken into account in the *idealized* version of the MCT. The two arrows in the plot delimit the T -range in which the power law gives a good description to the data.

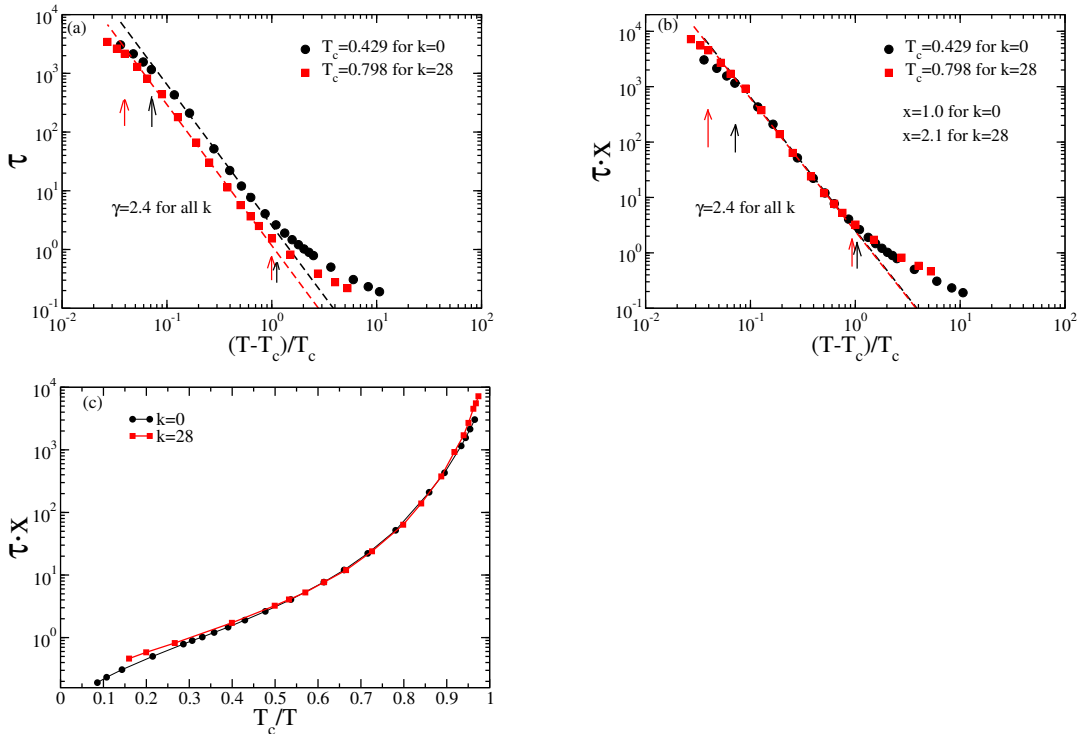


Figure 4.6: (a) The relaxation time obtained from the overlap function as a function of the scaled temperature $(T - T_c)/T_c$ for the $k = 0$ and the $k = 28$ systems. (b) Same data as in (a) but now with τ multiplied with a scaling factor $x(k)$. (c) Same data as in (b) as a function of $T_c(k)/T$.

For the system with $k = 28$ the temperature dependence of τ is qualitatively very similar to the one for the $k = 0$ system, *if* one plots the data as a function of the reduced temperature $(T - T_c)/T_c$. The highest temperature at which the data follows the power law (dashed line), marked by an arrow, is around $2T_c$, and very close to the corresponding reduced temperature for the $k = 0$ system. However, the lower (reduced) temperature at which τ starts to deviate from this power law, see arrow, is smaller for the $k = 28$ system than the corresponding T for the $k = 0$ system, showing that for the former system the mentioned hopping processes are less important, i.e., the system is more mean-field like. For the $k = 28$ system, this lower limit is about a factor of 3 smaller than the limit for $k = 0$; thus the T -range in which the idealized MCT can be expected to be reliable has increased significantly by the introduction of the pseudo neighbors. In Tab. 5.1 we have also included the value of T_c and one recognizes that the critical temperature for $k = 28$ is about 90% higher than the one for $k = 0$, i.e. the k -dependence of T_c is very similar to the one of T_{onset} .

According to the analytical calculations for the mean-field p -spin model, for which there is no activated dynamics, the onset temperature coincides with the MCT temperature which is also the temperature at which the dynamics diverges [24, 12, 26]. (Note that this is only true in the thermodynamic limit while for finite systems one has very strong finite-size effects that completely wash out these transitions, see Ref. [27]). For the GCM it was found that the relative distance between the three temperatures T_{onset} , T_c , and T_0 , is much smaller than the one we find here for the $k = 0$ system [9, 11]. Thus the reduction of this relative distance with increasing k , given in Tab. 5.1, can also be taken as a signature of increasing mean-field like behaviour.

From Fig. 4.6(a) we recognize that the relaxation times for the $k = 28$ system are shorter than the ones for the $k = 0$ system if compared at the same reduced temperature. In fact, as plotted in Fig. 4.6(b) on an intermediate time scale the two data sets can be superimposed with high accuracy by applying a multiplicative factor $x(k)$ (see Tab. 5.1 for values). Thus we conclude that the main difference in the two data sets is the prefactor τ_{MCT} in Eq. (4.3). A decrease in τ_{MCT} implies a faster motion inside the cage, and this is in fact very reasonable since with increasing k the tagged particle is interacting with more particles, thus making its effective cage stiffer. Another way to present this result is to plot the time scale $\tau \cdot x(k)$ as a function of T_c/T , see Fig. 4.6(c). We find that this representation of the data gives rise to a collapse of the curves for the different values of k , demonstrating that the T -dependence is indeed very similar at intermediate temperatures. Hence we conclude that the introduction of the pseudo neighbors does not only increase the α -relaxation time strongly

but also increase somewhat the attempt frequency with which the particle tries to leave the cage.

4.2.3 Wave-vector Dependence of Relaxation Process

The relaxation time of glass-forming systems depends on the observable considered. Within MCT this dependence is, however, encoded in a prefactor, τ_{MCT} in Eq. (4.3), while T_c and the exponent γ are expected to be independent of the observable. While for many glass-forming systems this is indeed the case, see e.g. Ref. kob-andersen-II, the present system has at least two relevant length scales, the nearest neighbor distance and the mean distance between the particles and their pseudo neighbors, and hence it is of interest whether the mention factorization works here as well. To probe this we consider the self intermediate scattering function $F_s(q, t)$, where q is the wave-vector [14]:

$$F_s(q, t) = \frac{1}{N} \sum_{j=1}^N \langle \exp[-i\mathbf{q} \cdot (\mathbf{r}_j(\mathbf{t}) - \mathbf{r}_j(\mathbf{0}))] \rangle \quad . \quad (4.4)$$

We define the relaxation time $\tau(q)$ via $F_s(q, \tau(q)) = 1/e$ and thus can study its dependence on the length scale. In Fig. 4.7 we show the q -dependence of $\tau(q)$ for three values of k . Since one expects that at small wave-vectors $\tau(q)$ is proportional to q^{-2} , i.e. the hydrodynamic behavior, we plot directly $q^2\tau(q)$. Panel (a) is for a fixed reduced temperature slightly below the onset temperature while panel (b) corresponds to a significantly supercooled state. In the context of Fig. 4.6(b) we have seen that, at a fixed reduced temperature, the relaxation time τ , obtained from the decay of the overlap function, shows a weak dependence on k , leading to the introduction of the factor $x(k)$. In order to take into account this k -dependence we have multiplied also in Fig. 4.7 the relaxation times $\tau(q)$ with the *same* factor $x(k)$. The graphs shows that for $q \approx 6.5$, i.e. close to the peak of the static structure factor, the relaxation times for the different systems coincide perfectly, which demonstrates that for this wave-vector the overlap and $F_s(q, t)$ probe the same type of dynamics. For the other wave-vectors considered, the $\tau(q)$ curves for the different systems show a q -dependence that depends on k , but this dependence is relatively weak. Hence we conclude that the presence of the pseudo neighbors does not introduce a new length scale that influences the relaxation dynamics in a significant manner.

4.2.4 Dynamic Heterogeneity

One of the hallmarks of glassy dynamics is that time correlation functions are stretched in time. The reason for this non-Debye relaxation has been a long-

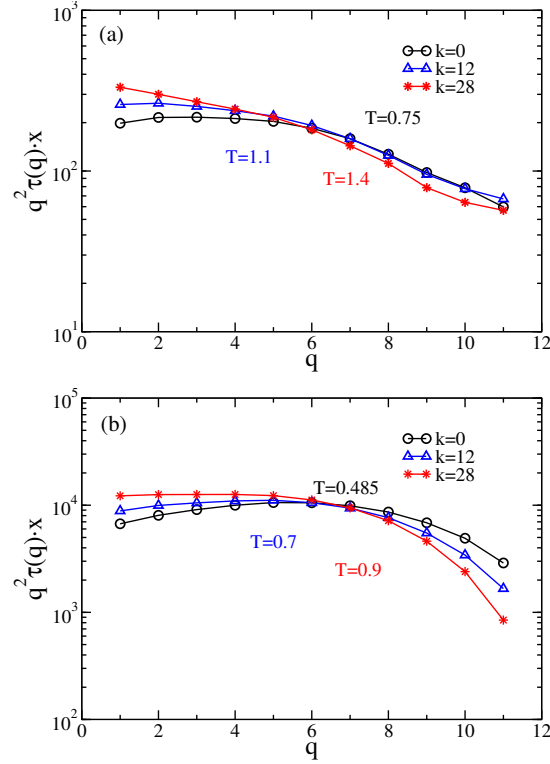


Figure 4.7: $q^2\tau(q) \cdot x(k)$ as a function of the wave-vector q . Panels (a) and (b) are for two different reduced temperatures. The values of $x(k)$ are given in Table 5.1

standing puzzle with the contrasting views that each small domain of the sample shows the same stretched time dependence or, alternatively, that the stretching is related to dynamical heterogeneities [28]. Experiments and simulations have shown that the homogeneous scenario is not compatible with the observations, i.e. glass-forming systems do have a significant amount of dynamical heterogeneities (DH) [29, 30, 31, 32, 33]. In this final section, we therefore discuss the k -dependence of these DH and probe whether with increasing k one does indeed find a decrease of these fluctuations, the behavior expected for a mean-field system.

One first step to probe the DH is to look at the so-called non-Gaussian parameter (NGP) $\alpha_2(t)$ which is defined by

$$\alpha_2(t) = \frac{3 \langle r^4(t) \rangle}{5 \langle r^2(t) \rangle^2} - 1 \quad , \quad (4.5)$$

where $r(t)$ is the displacement of a tagged particle within a time t . Thus $\alpha_2(t)$ measures whether or not the distribution of the particle displacement is Gaussian [34, 8, 29, 35].

In Fig.4.8(a) we plot the NGP for the $k = 28$ system. Interestingly one finds

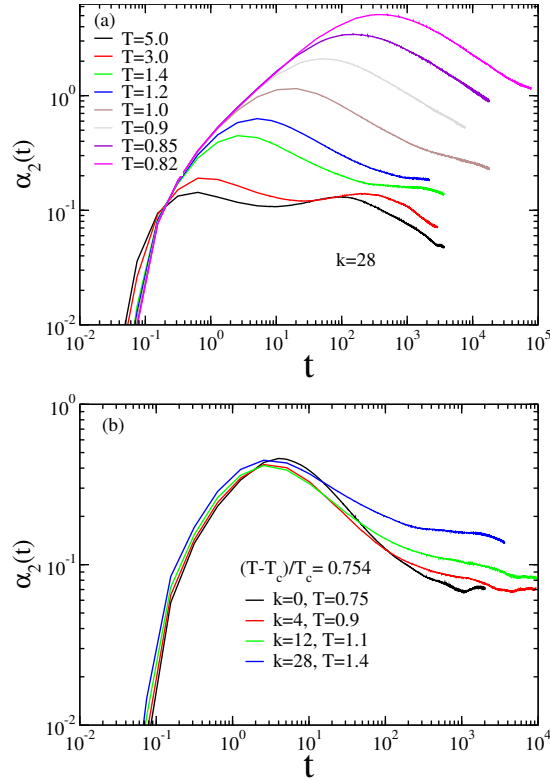


Figure 4.8: (a) The time dependence of the non-Gaussian parameter, α_2 , at different temperatures for the $k = 28$ system. $\alpha_2(t)$ shows a double peak structure. (b) $\alpha_2(t)$ at fixed reduced temperature and different values of k . The peak at short times is independent of k while the one at long times grows with increasing k .

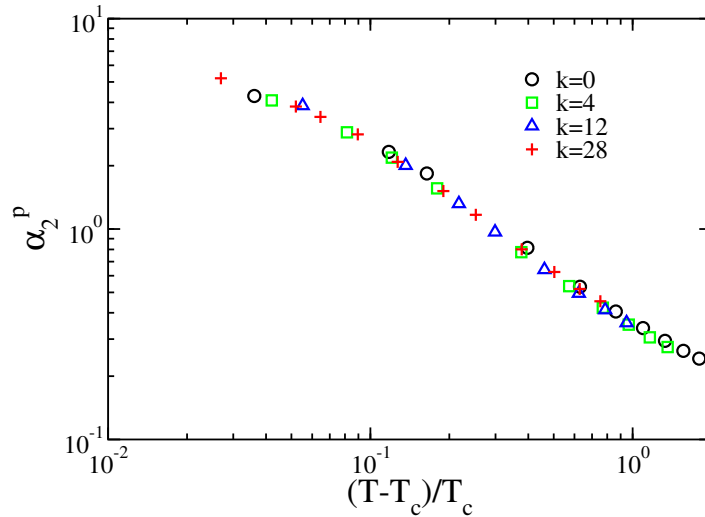


Figure 4.9: The peak height of α_2 as a function of the reduced temperature $(T - T_c)/T_c$ for different values of k .

that at high temperatures $\alpha_2(t)$ has *two* peaks: A first one at t around 0.6 and a second one at $t \approx 150$. The first time is close to the timescale at which the MSD crosses over from the ballistic regime to the diffusive one and thus corresponds

to the start of the NN- α -process, in agreement with earlier studies [8]. The second peak has so far not been seen in the glass-forming systems considered before and is likely due to the breaking of the bonds with the pseudo neighbors, i.e. the PN- α -relaxation. Note that the presence of this second peak is coherent with our findings for the MSD, see Fig. 4.3(c), for which we observed a plateau in the slope that, for $T = 2.0$, ended at around $t = 10^2$ and we had argued that this is due to the motion of the pseudo neighbors. If T is lowered, the first peak in $\alpha_2(t)$ rises quickly and dominates the second peak, i.e. on overall the time dependence of the NGP becomes again quite similar to the one that has been observed in previous studies of glass-forming systems. The main difference is that in our case the second peak will make the decay of $\alpha_2(t)$ slow since at long times the dynamics will be influenced by the pseudo neighbors, which decorrelate only slowly (see the data for the MSD in Fig. 4.3).

The influence of the pseudo neighbors on $\alpha_2(t)$ is shown in Fig. 4.8(b) where we plot this function for different values of k but keeping $(T - T_c)/T_c$ constant. One sees that at short and intermediate times, i.e. around the peak, the curves are independent of k , which shows that the NN- α -process is not affected by the presence of the pseudo-neighbors. Only at longer times, the curves for large k are higher than the ones for small k , showing that the pseudo neighbors affect the NGP only at time scales that are beyond the time scale of the first maximum in the NGP. Since with decreasing temperature the peak corresponding to the NN- α -relaxation grows quicker than the second peak we can conclude that the dominant feature in $\alpha_2(t)$ is due to the NN- α -process, except if k becomes much larger than the values we consider here.

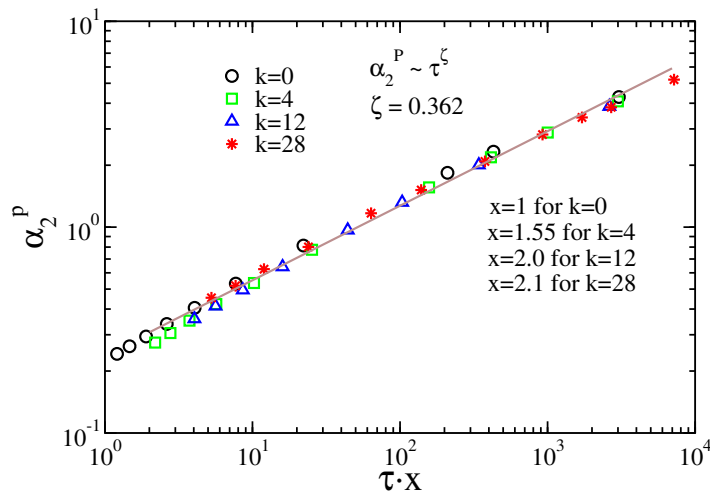


Figure 4.10: The peak height of α_2 as a function of the α -relaxation time τ multiplied by $x(k)$ for different values of k . Also included is a fit to the data with a power law.

In Fig. 4.9 we show α_2^p , the height of the peak in $\alpha_2(t)$, as a function of

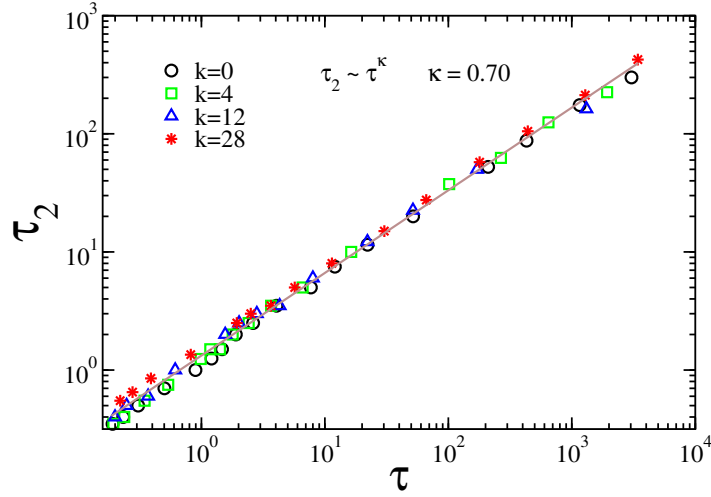


Figure 4.11: The time scale τ_2 at which $\alpha_2(t)$ peaks, as a function of the α -relaxation time τ . The solid line is a power law with an exponent $\kappa = 0.70$.

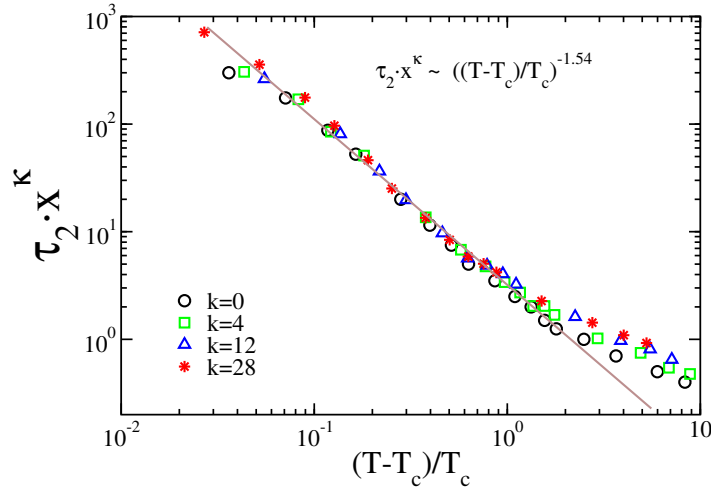


Figure 4.12: $\tau_2 x(k)^\kappa$ as a function of the reduced temperature $(T - T_c)/T_c$. The solid line is a power law with exponent -1.54 .

the reduced temperature $(T - T_c)/T_c$. Surprisingly we find that this quantity is completely independent of k , i.e. the strength of the non-Gaussianity of the relaxation dynamics does not depend on whether or not the system is mean-field like. In other words, the statistics of the displacement of a tagged particle is independent of the number of pseudo neighbors, if measured at the same reduced temperature. This result reflects the fact that the first peak in $\alpha_2(t)$ is dominated by the dynamics in which the tagged particle leaves the cage formed by its nearest neighbors.

Note that α_2^p shows a bend at around $(T - T_c)/T_c \approx 0.1$. Although we did not investigate the origin of this change in the T -dependence, we expect it to be the signature of the onset of the hopping processes mentioned above. The bend indicates that these processes start to become prominent at around 10%

above T_c , a value that seems to be coherent with the observation from Fig. 4.6 regarding the T -dependence of the relaxation times.

One might wonder whether the master curve in Fig. 4.9 is just due to the choice of the scaling factor of the temperatures, i.e. T_c . To test this possibility, we show in Fig. 4.10 the same data as a function of the relaxation time τ multiplied by the same factor $x(k)$ that was used to obtain a master curve in Fig. 4.6(b). We recognize that this representation leads to a very nice collapse of the data onto a master curve which, for intermediate and long relaxation times, can be described well with a power law with an exponent close to 0.36 (see solid line in the figure). It is remarkable that the hopping processes discussed above, which lead to the bends in the different curves if the temperature approaches T_c , do not seem to affect the validity of the power law. At present, it is not clear up to which value of τ this power law will hold, in particular, whether it will be observed at temperatures below T_c . Future studies on this point will certainly be of interest to understand better the relaxation dynamics of glass-forming liquids.

In Fig. 4.11 we plot τ_2 , the time at which $\alpha_2(t)$ peaks, as a function of the α -relaxation time τ . Surprisingly we find that the two quantities show a simple relation with each other in the form of a power law with an exponent $\kappa = 0.70$ (solid line). This result can be rationalized within the framework of MCT as follows: $\alpha_2(t)$ is related to the shape of the self part of the van Hove function in that it measures its deviation from a Gaussian [34, 8]. At the end of the caging regime, i.e. the β -relaxation, some of the particles will have already left their cage, thus giving rise to a tail to the right of the main peak of the van Hove function. It is this tail that is responsible for the non-Gaussian shape of the van Hove function and hence leads to an increase of $\alpha_2(t)$. Thus it is reasonable to assume that τ_2 is directly related to the time scale of the β -relaxation τ_β . MCT predicts that the latter time scale increases like

$$\tau_\beta \propto (T - T_c)^{-1/(2a)} \quad . \quad (4.6)$$

The α -relaxation time τ is instead predicted by MCT to increase like

$$\tau \propto (T - T_c)^{-1/(2a)-1/(2b)} = (T - T_c)^{-\gamma} \quad . \quad (4.7)$$

In Eqs. (4.6) and (4.7) the parameters a and b can in principle be calculated from the T -dependence of the static structure factor or, exploiting Eq. (4.7), determined from the T -dependence of the relaxation time [2, 1, 36]. For the $k = 0$ system it has been found that a is around 0.324 and b is around 0.627 [36, 8, 37, 38]. Combining these last two equations gives, under the assumption

that $\tau_2 \propto \tau_\beta$,

$$\tau_2 \propto \tau^{b/(a+b)} \quad . \quad (4.8)$$

Thus we find a power law dependence with an exponent of 0.66 (using the mentioned values of a and b), which is indeed very close to our exponent κ from the fit (0.7). We mention here that the observed power law extends over the whole accessible range of τ , i.e. it also includes the temperature regime in which we expect hopping processes to be present. To the best of our knowledge this simple connection between τ_2 and τ has not been reported before. Since, however, we find it to hold for all values of k , we expect it to be valid for other glass-forming systems as well and hence it will be of interest to check this in the future.

To get Eq. (4.8) we have made the assumption that τ_2 is proportional to τ_β . As argued above, this hypothesis is reasonable since it can be expected that the non-Gaussian parameter peaks at a time at which a substantial number of particles start to leave their cage and MCT defines τ_β as the time at which the correlator starts to drop below the plateau at intermediate times [3]. Previous studies have therefore made the assumption that τ_β can be determined from the minimum in the slope of the MSD [39]. However, we argue that such an identification might be misleading: For the case of a system with Newtonian dynamics, the phonons that govern the short-time dynamics mask the critical decay of the time correlation functions thus also masking the correlation between the above-mentioned minimum and τ_β . (This effect is, however, absent if the system has a Brownian dynamics [37].) Therefore we think it is more appropriate to determine τ_β from a quantity that is not directly influenced by these vibrational modes, such as the $\alpha_2(t)$ considered here. In Fig. 4.3(a)-(c) we have also included for the various curves the times τ_2 , arrows pointing upward, and one sees that they do not correspond to the location of the minimum in the curves but that they are located at somewhat larger times, as expected because of the mentioned effect of the phonons. Although at present we do not have any solid proof why τ_2 does indeed correspond to τ_β , our finding that the relation between τ_2 and τ given by Eq. (4.8) is obeyed by our data does speak in favour of this identification. More tests on this using a system with Brownian dynamics would certainly be useful to clarify this point further.

Finally we show in Fig. 4.12 the time at which $\alpha_2(t)$ peaks, τ_2 , as a function of $(T - T_c)/T_c$. Since we have argued in the context of Fig. 4.6 that the k -dependence of τ will include a factor $x(k)$ that is related to the short time dynamics, and we also showed that $\tau_2 \propto \tau^\kappa$ (Fig. 4.11), we plot directly $\tau_2 \cdot x(k)^\kappa$,

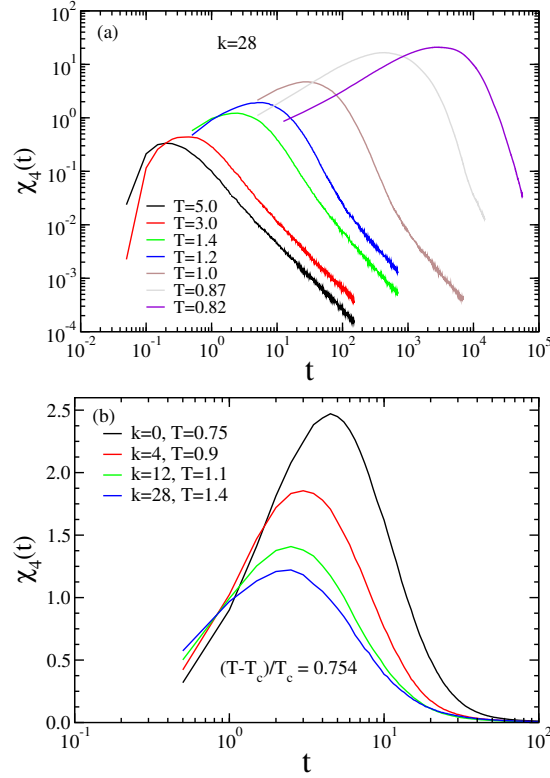


Figure 4.13: (a) The time dependence of the dynamical susceptibility $\chi_4(t)$ for different temperatures for the $k = 28$ system. $\chi_4(t)$ increases with decreasing temperature. (b) Time dependence of χ_4 at a fixed reduced temperature $(T - T_c)/T_c$ for different values of k .

with the values of $x(k)$ obtained from Fig. 4.6 and κ from Fig. 4.11. We recognize that the data for the different values of k fall nicely on a master curve which follows a power law with an exponent around -1.54. Also this result can be understood within the framework of MCT since Eq. (4.6) predicts that the slope should be given by $-1/(2a)$ which for $a = 0.324$ results in an exponent of -1.54, in excellent agreement with the data from the fit in Fig. 4.12.

Next we discuss the other parameter which is often related to the dynamic heterogeneity, the dynamic susceptibility. The fluctuations of the overlap function $Q(t)$ are related to a dynamic susceptibility which indicates whether or not the system relaxes in a cooperative manner, i.e. shows dynamical heterogeneities [40, 41, 15]. Thus one defines

$$\chi_4(t) = \frac{1}{N} [\langle Q^2(t) \rangle - \langle Q(t) \rangle^2] \quad (4.9)$$

as a measure to quantify this cooperativity. In Fig. 4.13(a) we show the time dependence of χ_4 for the system with $k = 28$ at different temperatures. In agreement with earlier studies,[12], we find that χ_4 shows a marked peak the height of which increases with decreasing temperature and also its position shifts to

larger times upon decreasing T , i.e. the cooperativity becomes more pronounced and occurs at later times. In panel (b) of the figure we present χ_4 for different values of k while keeping the normalized temperature $(T - T_c)/T_c$ constant. The graph demonstrates that with increasing k the height of the peak decreases quickly, indicating that the system does indeed become more mean-field like, as expected, and in agreement with previous simulations of mean-field like models [28, 12]. This k -dependence is thus very different from the one seen for the height of the peak in α_2 , highlighting the difference between the two quantities, despite their (apparently) similar time dependence. We also note that with increasing k the location of the peak in $\chi_4(t)$ shifts to shorter times, in qualitative agreement with the fact that, at fixed reduced temperature, the α -relaxation time decreases somewhat, see Fig. 4.6(a).

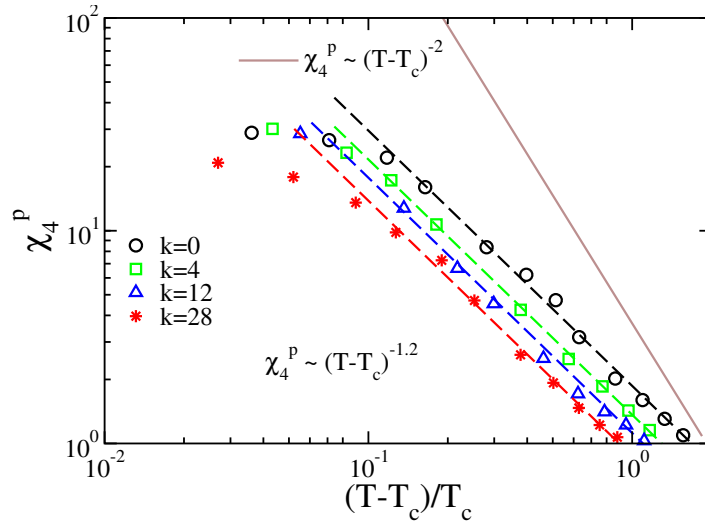


Figure 4.14: Height of the peak in $\chi_4(t)$ as a function of the reduced temperature for different values of k . The dashed lines are power laws with exponent -1.2 and the solid line is a power law with an exponent -2.

To probe in more detail how the height of the peak in $\chi_4(t)$, χ_4^p , depends on T and k we show in Fig. 4.14 this height as a function of the reduced temperature. We see immediately that this representation of the data does not give rise to a master curve. With increasing k , the curves move downwards, a k -dependence that is in contrast to the one we found for α_2^p shown in Fig. 4.9. Thus we conclude that with increasing k the dynamical heterogeneities decrease, i.e. the system becomes more mean-field like. However, we point out that even in the mean-field limit these heterogeneities cannot be expected to vanish completely [28, 42] which shows that this aspect of the dynamics is a delicate feature that is highly non-trivial.

From the figure, one can conclude that for reduced temperatures higher than around 0.1 the height of the peak shows a power law dependence on the reduced

temperature and we find an exponent of -1.2 that is independent of k , which implies that the dependence of χ_4^p on the number of pseudo neighbors is encoded in the prefactor of the power law.

The presence of power laws in χ_4^p can be rationalized by means of MCT. This theory predicts that the dynamical susceptibility in the NVT ensemble is given by

$$\chi_4^{\text{NVT}}(t) = \chi_4^{\text{NVE}}(t) + \frac{T^2}{c_V} \left(\frac{dQ(t)}{dT} \right)^2, \quad (4.10)$$

where c_V is the specific heat at constant volume [40, 41, 15]. Evaluating this expression at $t = \tau$, thus giving the height of the peak, χ_4^p , one finds that the first term on the right-hand side of the equation increases like $(T - T_c)^{-1}$ while the second one is found to be proportional to $(T - T_c)^{-2}$. Hence the power law with exponent -1.2 we find at intermediate and higher temperatures can be interpreted to be due to the power law from the first term, i.e. with an exponent -1.0, which is somewhat augmented by the presence of the second term, thus giving rise to a power law with an effective exponent smaller than -1. Thus if the mentioned hopping processes would be absent one would expect that at sufficiently low temperatures, the power law crosses over to one with an exponent -2. Whether this is indeed the case will have to be tested for systems in which one is able to suppress these hopping processes, a work that is left for the future.

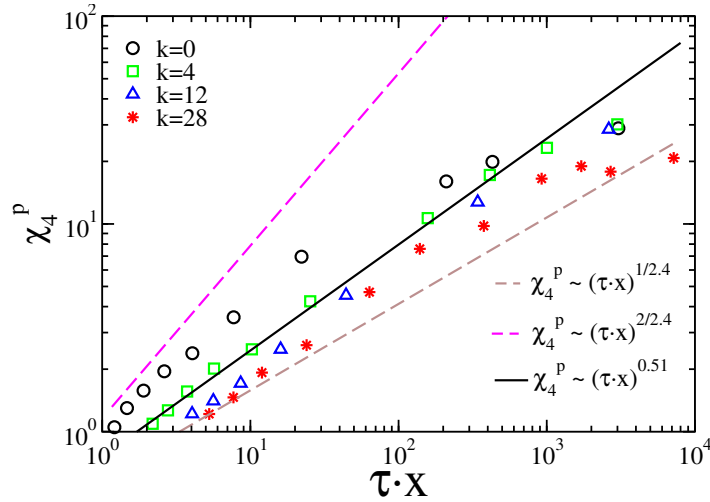


Figure 4.15: The height of the peak in χ_4 as a function of $\tau \cdot x(k)$ for different values of k . The solid line is a power law fit to the data for $k = 4$. The two dashed lines are power laws with exponents that correspond to the theoretical upper and lower bounds from Eq. (4.11).

Since the representation of the data in Fig. 4.14 depends on the choice of T_c , it is also useful to look at the k -dependence of χ_4^p in a more direct manner. This is done in Fig. 4.15 where we plot this quantity as a function of the α -relaxation

time τ . (Also here we use $\tau \cdot x(t)$ as abscissa, in order to take into account the trivial k dependence of the relaxation time.) We see that the shape of the curves for the different k is basically independent of k , but that the absolute value of χ_4^p at fixed $\tau \cdot x(k)$ decreases with increasing k . (The same conclusion is reached if one uses just τ as the abscissa.) Hence we confirm the conclusion from Fig. 4.13(b) that the heterogeneity of the system decreases with increasing k . For small and intermediate values of τ , the data falls approximately on a straight line, and a power law fit gives an exponent 0.51 (solid line). Expressing the T -dependence on the right hand side of Eq. (4.10) as a function of $\tau = (T - T_c)^{-\gamma}$, see Eq. (4.3), we obtain for the height of the peak

$$\chi_4^p = A\tau^{1/\gamma} + B\tau^{2/\gamma} \quad , \quad (4.11)$$

where A and B are expressions that have only a weak T -dependence. Using our value $\gamma = 2.4$ gives for the exponent of the first and second term 0.42 and 0.83, respectively. These values are thus upper and lower bounds (included in Fig. 4.15 as well) and the exponent we extract from our data, 0.51, is thus not too far from the lower limit. So, although our data do not allow to make strong statements about the validity of Eq. (4.11), because of the lack of sufficiently large window in the dynamics, we can at least say that our findings are compatible with the theoretical prediction, in agreement with the results from Ref. *coslovich_ozawa_k.ob*.

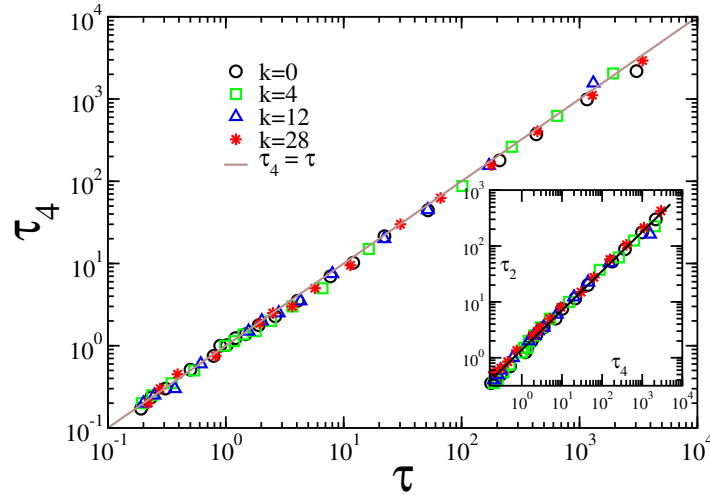


Figure 4.16: The location of the peak in $\chi_4(t)$ as a function of the α -relaxation time τ . The symbols are for different values of k and different T , and the solid line is a power law with exponent 1.0. Inset: τ_2 as a function of τ_4 showing a power law connection between the two quantities. The straight line has a slope of 0.70.

Finally, we note that for large τ we find clear deviations of our data from the predicted power law in that the growth of χ_4^p is weaker than predicted. So in

this regime, we can again invoke the argument that hopping processes decrease the cooperativity of the relaxation dynamics.

Fig. 4.13(a) shows that the location of the peak in $\chi_4(t)$, τ_4 , quickly moves to larger times if the temperature is lowered. To determine the connection between the α -relaxation time τ and the time scale τ_4 we plot in Fig. 4.16 τ_4 as a function of τ . Also included in the graph is the line $\tau_4 = \tau$ (solid line) and one recognizes that all the data points fall on this line with high accuracy. Hence we can conclude that the time scale at which the system shows maximum cooperativity is on the time scale of the α -process, which is in agreement with earlier results [35]. Also note that this conclusion is independent of k , i.e. the strength of the mean-field character does not play a role for this result. This result demonstrates that the α -relaxation process is tightly related to the presence of the dynamical heterogeneities and that hence it is useful to study the latter in order to understand the slowing down of the relaxation dynamics. Finally we mention that the direct proportionality of τ_4 to τ and the power law connection between τ_2 and τ , (see Fig. 4.11) implies that we have the simple connection $\tau_2 \propto \tau_4^\kappa$, with an exponent κ given by $b/(a+b)$, see Eq. (4.8). That this relation works indeed well is shown in the inset of Fig. 4.16. Since the exponent κ is less than unity, we see that τ_2 is smaller than τ_4 , as expected [10]. This can also be concluded from Fig. 4.3 where we have added in panels (a)-(c) the values of τ_4 (downward arrows), in that one recognizes that at low T , these are indeed to the right of the arrows presenting τ_2 . These graphs also show that, interestingly, the (logarithmic) slope of the MSD at $t = \tau_4$ is independent of T but weakly dependent on k .

4.3 Conclusion

Due to the presence of the pseudo neighbors, the relaxation dynamics shows a very strong dependence on k in that the onset temperature as well as the critical temperature of mode-coupling theory increase with increasing k . However, once the relaxation times are expressed in terms of the critical temperature of MCT one finds only a mild k -dependence, indicating that for this class of systems T_c is the most relevant parameter for the dynamics, at least in the T -range investigated here. We note that the range in temperature in which MCT seems to give a good description of the relaxation dynamics increases systematically with increasing k , thus indicating that in the mean-field limit, the theory becomes exact. This is also confirmed by the observation that the dynamical heterogeneities, characterized by the dynamic susceptibility $\chi_4(t)$, decrease with increasing k .

It is often believed that the fragility of the glass-former is directly related to the presence of dynamical heterogeneities (or more precisely to the value of the stretching parameter β in the Kohlrausch-Williams-Watts function used to fit the time-correlation functions) [44, 45, 46]. Since we find that the fragility of the system increases with k while the dynamic heterogeneity decreases we conclude that there is no such (strict) connection between these two quantities, although we do not want to exclude the possibility that in practice there might be a certain correlation. This result is in qualitative agreement with the findings in earlier studies [12, 47]. Sengupta *et. al.* have, e.g., reported that compared to a three-dimensional system, the corresponding four-dimensional system was less heterogeneous but more fragile [12]. This is also corroborated by experimental data analyzed by Dyre, which indicate that there is no direct connection between fragility and heterogeneity [47].

The possibility to tune the mean-field character of the system without changing the structure also allows elucidating the relation between the non-Gaussian parameter $\alpha_2(t)$ and $\chi_4(t)$. While previous studies have often considered both functions to be indicators for the dynamical heterogeneities, our analysis shows that this is not the case at all since their dependence on k is very different. Therefore our work clearly shows that these two observables convey information that is very different, a conclusion that is in line with previous results that showed that the peak in $\alpha_2(t)$ has a temperature dependence which differs from the one of χ_4^p [12]. Furthermore, we also recall that for the MK-model, Ref. mari-kurchan, one finds that χ_4^p decreases with increasing mean-field character of the system, i.e. the same behavior as we have found here, but that also the value of α_2^p decreases, while in our case we find that α_2^p is independent of k . Also in the case of the Gaussian core model, it was found that its $\alpha_2(t)$ peak is lower than the one for the Kob-Andersen model, whereas the χ_4 peak is much higher [9, 8]. The authors of these papers justified this results by stating that α_2 provides a measure of the degree of dynamic heterogeneity and thus its peak value should be lower for more mean-field like models and χ_4 provides a measure of the size of the domains and systems which have larger domains should have higher value of χ_4 . Although this interpretation might apply to the Gaussian core model, it is not in agreement for the system studied here and hence not general. This suggests that further studies are required to understand the exact information provided by χ_4 and α_2 and if these two quantities are indeed related to each other.

Finally, we also note that the decrease of χ_4 with increasing k can be due to the fact that the fluctuations in the overlap function do indeed decrease, i.e. the relaxation dynamics of the system becomes more homogeneous, as expected for

a mean-field-like system. However, since with increasing k the characteristic temperatures of the system also increase, the fluctuations should decrease. So for the moment, it is not clear which one of the two mechanisms is the main cause for the decrease of χ_4^p that we observe in the present work.

The range of k that we were able to access in the present simulation is relatively modest since for larger k the relaxation dynamics became too slow to equilibrate the system within a reasonable amount of computer time. It is, however, of interest to make an educated guess on what will happen if k is increased further. Our analytical results for the structure, Fig. 3.5, shows that with increasing k the main peak in the effective radial distribution function becomes very high. In this limit one can thus expect that the contribution from the pseudo neighbors will start to dominate the one from the real nearest neighbors and hence will make the system mean-field like. However, from the graph we recognize that this increase becomes strong only once k is larger than $O(10^2)$, i.e., a value that is at present somewhat beyond the reach of standard computer simulations. It can be expected, however, that in the near future improved algorithms will allow to deal with this bottleneck. In that case our approach will thus allow to make more stringent investigations on how the properties of a normal three dimensional glass-former can be connected to the corresponding system in the mean field limit.

Bibliography

- [1] W. Kob and K. Binder, *Glassy Materials and Disordered Solids: An Introduction to Their Statistical Mechanics* (World Scientific, 2011).
- [2] W. Götze, *Journal of Physics: Condensed Matter* **11**, A1 (1999).
- [3] W. Götze, *Complex Dynamics of Glass-Forming Liquids: A Mode-Coupling Theory* (Oxford Science Publication, 2008).
- [4] W. Kob and H. C. Andersen, *Phys. Rev. E* **51**, 4626 (1995).
- [5] W. Kob and H. C. Andersen, *Phys. Rev. E* **52**, 4134 (1995).
- [6] S.-H. Chong, *Phys. Rev. E* **78**, 041501 (2008).
- [7] R. Mari and J. Kurchan, *The Journal of Chemical Physics* **135**, 124504 (2011).
- [8] D. Coslovich, A. Ikeda, and K. Miyazaki, *Phys. Rev. E* **93**, 042602 (2016).
- [9] A. Ikeda and K. Miyazaki, *The Journal of Chemical Physics* **135**, 054901 (2011).
- [10] A. Ikeda and K. Miyazaki, *Phys. Rev. Lett.* **106**, 015701 (2011).
- [11] M. K. Nandi and S. M. Bhattacharyya, *The Journal of Chemical Physics* **148**, 034504 (2018).
- [12] S. Sengupta, S. Karmakar, C. Dasgupta, and S. Sastry, *The Journal of Chemical Physics* **138**, 12A548 (2013).
- [13] P. Charbonneau, A. Ikeda, G. Parisi, and F. Zamponi, *Proceedings of the National Academy of Sciences* **109**, 13939 (2012).
- [14] J. P. Hansen and I. R. McDonald, *Theory of Simple Liquids* (Elsevier, Amsterdam, 1986).
- [15] D. Coslovich, M. Ozawa, and W. Kob, *The European Physical Journal E* **41**, 62 (2018).

- [16] A. Banerjee, M. K. Nandi, S. Sastry, and S. Maitra Bhattacharyya, *The Journal of Chemical Physics* **147**, 024504 (2017).
- [17] P. Chaudhuri, L. Berthier, P. I. Hurtado, and W. Kob, *Phys. Rev. E* **81**, 040502 (2010).
- [18] S. Sastry, *Nature* **409**, 164 (2001).
- [19] S. Sastry, *PhysChemComm* **3**, 79 (2000).
- [20] U. K. Nandi, S. Sengupta, W. Kob, and S. M. Bhattacharyya, manuscript in preparation (2020).
- [21] C. A. Angell, *Science* **267**, 1924 (1995).
- [22] R. Das, C. Dasgupta, and S. Karmakar, *Frontiers in Physics* **8**, 210 (2020).
- [23] W. Kob and H. C. Andersen, *Phys. Rev. Lett.* **73**, 1376 (1994).
- [24] A. Cavagna, I. Giardinà, and G. Parisi, *Journal of Physics A: Mathematical and General* **34**, 5317 (2001).
- [25] T. R. Kirkpatrick and P. G. Wolynes, *Phys. Rev. A* **35**, 3072 (1987).
- [26] T. R. Kirkpatrick and D. Thirumalai, *Phys. Rev. Lett.* **58**, 2091 (1987).
- [27] C. Brangian, W. Kob, and K. Binder, *Europhysics Letters (EPL)* **53**, 756 (2001).
- [28] M. D. Ediger, *Annual Review of Physical Chemistry* **51**, 99 (2000).
- [29] W. Kob, C. Donati, S. J. Plimpton, P. H. Poole, and S. C. Glotzer, *Phys. Rev. Lett.* **79**, 2827 (1997).
- [30] W. Kob, C. Donati, S. J. Plimpton, P. H. Poole, and S. C. Glotzer, *Phys. Rev. Lett.* **79**, 2827 (1997).
- [31] B. Doliwa and A. Heuer, *Phys. Rev. Lett.* **80**, 4915 (1998).
- [32] M. M. Hurley and P. Harrowell, *The Journal of Chemical Physics* **105**, 10521 (1996).
- [33] K. Kim and S. Saito, *The Journal of Chemical Physics* **138**, 12A506 (2013).
- [34] T. Odagaki and Y. Hiwatari, *Phys. Rev. A* **43**, 1103 (1991).
- [35] F. W. Starr, J. F. Douglas, and S. Sastry, *The Journal of Chemical Physics* **138**, 12A541 (2013).

-
- [36] G. Buchalla, U. Dersch, W. Götze, and L. Sjögren, *Journal of Physics C: Solid State Physics* **21**, 4239 (1988).
- [37] T. Gleim, W. Kob, and K. Binder, *Phys. Rev. Lett.* **81**, 4404 (1998).
- [38] M. Nauroth and W. Kob, *Phys. Rev. E* **55**, 657 (1997).
- [39] R. Das, I. Tah, and S. Karmakar, *The Journal of Chemical Physics* **149**, 024501 (2018).
- [40] L. Berthier *et al.*, *The Journal of Chemical Physics* **126**, 184503 (2007).
- [41] L. Berthier *et al.*, *The Journal of Chemical Physics* **126**, 184504 (2007).
- [42] C. Brangian, W. Kob, and K. Binder, *Journal of Physics A: Mathematical and General* **35**, 191 (2002).
- [43] E. Flenner and G. Szamel, *Phys. Rev. E* **72**, 011205 (2005).
- [44] R. Böhmer, K. L. Ngai, C. A. Angell, and D. J. Plazek, *The Journal of Chemical Physics* **99**, 4201 (1993).
- [45] X. Xia and P. G. Wolynes, *Phys. Rev. Lett.* **86**, 5526 (2001).
- [46] K. Niss, C. Dalle-Ferrier, G. Tarjus, and C. Alba-Simionesco, *Journal of Physics: Condensed Matter* **19**, 076102 (2007).
- [47] J. C. Dyre, *Journal of Physics: Condensed Matter* **19**, 205105 (2007).
- [48] G. M. Hocky, D. Coslovich, A. Ikeda, and D. R. Reichman, *Phys. Rev. Lett.* **113**, 157801 (2014).

Chapter 5

Connecting real glasses to mean-field models: A study of thermodynamics

5.1 Introduction:

The slowing down of the dynamics in supercooled liquids and its correlation with the thermodynamics of the system have been topics of intense research. There are several characteristic temperatures where both the thermodynamic and dynamic properties of the system change in a significant manner. At the onset temperature (T_{onset}), the relaxation dynamics of the system start to differ from that of a typical liquid because due to the lowering of temperature, the system begins to explore the underlying free energy landscape [1]. This onset temperature can also be identified as the temperature where the pair part of the excess entropy becomes less than the total excess entropy of the system [2, 3]. Below T_{onset} , the temperature dependence of the dynamics can be described reasonably well by the so-called mode-coupling theory (MCT), which predicts a power-law divergence of the relaxation times at a dynamic transition temperature T_c . [4] However, experimental and numerical studies found [5, 6, 7, 8, 9, 10] that the relaxation time does not diverge at T_c as predicted by the MCT, but instead shows a smooth crossover to weaker temperature dependence. This crossover scenario is consistent with the predictions of the so-called random first-order transition (RFOT) theory [11, 12] and it has been related to the properties of the underlying potential energy landscape [13].

According to the RFOT theory and the phenomenological Adam-Gibbs (AG) theory [14], the low-temperature dynamics of supercooled liquid is controlled by its configurational entropy (S_c), which measures the number of possible dis-

tinct states accessible to the system. The AG theory predicts the following relationship between the α relaxation time (τ) and the configurational entropy (S_c): $\tau = \tau_0 \exp(-A/TS_c)$ where τ_0 is a microscopic timescale and A is a system-dependent constant. Thus according to the AG theory, the temperature T_0 where the relaxation time diverges is the same as the Kauzmann temperature T_K where the configurational entropy goes to zero [15]. For a large number of systems the AG relationship is found to hold [14, 16, 17, 18, 19, 20, 21, 22, 23, 24, 25]. There has been a recent study which showed that it is the diffusion coefficient which follows the AG relationship for the widest temperature range [26].

The validity of the AG theory in the form presented above has recently been challenged [16]. It has been argued that according to the RFOT theory, the reduction in the configurational entropy is related to the growth of a static correlation length over which the activation happens, giving rise to the relaxation process. This theory predicts a generalized AG relation given by $\tau = \tau_0 \exp(-A/TS_c^\alpha)$, where α can be different from unity. It was further shown that the generalized AG relation holds [16] both in experiments and in simulations. Note that even according to the generalized AG relationship, the relaxation timescale should diverge below $T = T_K$ when the configurational entropy vanishes.

In a recent study, some of us have developed a novel of glass-forming liquid where we can switch between a 3-dimensional liquid and a fully connected mean-field system in a continuous manner [9]. The parameter that is introduced to achieve this is k added pseudo neighbours for each particle. The structure, dynamics, and dynamical heterogeneity of this model have been studied as a function of k . It was shown that the structure given by the radial distribution function (rdf) of the usual neighbours remains almost unchanged with k . However, the pseudo neighbours do contribute to the total rdf that shows a weaker modulation with distance, a typical mean-field like behaviour [9, 28]. With increase in k , the dynamics also slows down and the transition temperatures (T_0, T_c, T_{onset}) move to higher values. The range over which a system follows the MCT power-law behaviour becomes wider with an increase in k . The heterogeneity decreases with an increase in k . Thus it was shown that with an increase in k the system becomes more mean-field like.

The goal of the present work is to study the thermodynamic properties of this system and its correlation with the dynamics. In order to do so, we employ the well-known thermodynamic integration (TI) method to calculate the total entropy and the configurational entropy of the system [29]. We find that with an increase in k , the Kauzmann temperature becomes higher which is similar to that found for T_0 . However, we also find a violation of the AG relation. As

discussed before, the breakdown of the AG relationship is a possibility but for larger k systems we find that close to the onset temperature where the dynamics continues and is reasonably fast, the configurational entropy disappears. In our opinion, this is an unphysical result not even supported by the generalized AG relationship. This implies that the TI method of entropy calculation needs to be re-examined.

We thus employ a completely different method to calculate the entropy of the system, namely the two-phase thermodynamics (2PT) method. It is another conventional method [30, 31]. It has provided accurate entropy values over a wide range of thermodynamic state points for the LJ fluid and different water models [30, 32]. We first test this model for a regular Kob-Anderson model system which is the $k = 0$ system in the mean-field model. We compare the entropy values obtained *via* the TI and the 2PT methods and find them to be close to each other. We then employ the 2PT method for different mean-field systems and compare with the results obtained by the TI method. We find that with an increase in k the difference in entropy obtained by the two methods increases. We also find that using the entropy calculated via the 2PT method, the AG relationship holds in the range of temperature studied here.

In the discussion of the possible failure points of the TI method, we note that for usual systems in the TI method we assume that particles are indistinguishable. On the other hand, in this mean-field system, each particle has a distinct set of pseudo neighbours. Thus the particles might appear to be distinguishable. We also find that for the mean-field system not only the AG relation but the Rosenfeld relationship between the excess entropy and the dynamics fails.

The rest of this chapter is organized as follows: The system and simulation details are described in Sec. 5.2. In Sec. 5.3, we describe different methods for the calculation of entropy. In Sec.5.4, we present the result of our analysis for the mean-field system. We discuss the implication of the results in Sec. 5.5 and conclude in Sec. 5.7.

5.2 Details of system and simulations

The system details are given elaborately in the 'Details of system and simulations' section in Chapter3.

5.3 Different methods to calculate entropy

We have calculated entropy of the systems using two different methods one is thermodynamic integration method and another one is two phase thermo-

dynamics method. The details are discussed in section 2.3 (Thermodynamic properties) in chapter. 2.

5.4 Results for Mean-field system

In this section, we will discuss the entropy of the mean-field system and its correlation with the dynamics. We will first discuss the results obtained using the TI method and its shortcomings and then discuss the results obtained from the 2PT method.

5.4.1 Entropy using thermodynamic integration method

In the estimation of the entropy using the TI method, we need to calculate the excess entropy and the vibrational entropy. The configurational entropy is then obtained from Eq.2.37.

Excess entropy

Note that in the calculation of the excess entropy via the TI method, we need the information of the internal energy (Eq.2.19). For the mean-field systems, the internal energy has two parts, one is the contribution from the regular neighbor (NN) and the other is the contribution from the pseudo-neighbor (PN). A similar decomposition is present for the entropy, where we can write $S_{ex} = S_{ex}^{NN} + S_{ex}^{PN}$. The first term on the r.h.s refers to the contribution from the regular neighbours and the second term from that of the pseudo neighbours. These are given by,

$$S_{ex}^{NN}(\beta^*, k) = \beta^* \langle U \rangle - \int_0^{\beta^*} d\beta \langle U \rangle \quad (5.1)$$

and

$$S_{ex}^{PN}(\beta^*, k) = \beta^* \langle U_k^{pseudo} \rangle - \int_0^{\beta^*} d\beta \langle U_k^{pseudo} \rangle \quad (5.2)$$

In Fig.5.1, we plot the temperature dependence of S_{ex} from the TI method for different k systems. In the TI method, we assume the particles to be indistinguishable. We find that the excess entropy decreases with increasing k . Our earlier study showed that with an increasing k the structure of the system remains unchanged [9]. Thus the contribution of the regular neighbours to the entropy does not change with k . However, with an increase in the number of pseudo neighbours and thus U_k^{pseudo} , the total excess entropy decreases. Thus

the decrease in excess entropy obtained via the TI method can be attributed to the increase in the pseudo neighbour interactions.

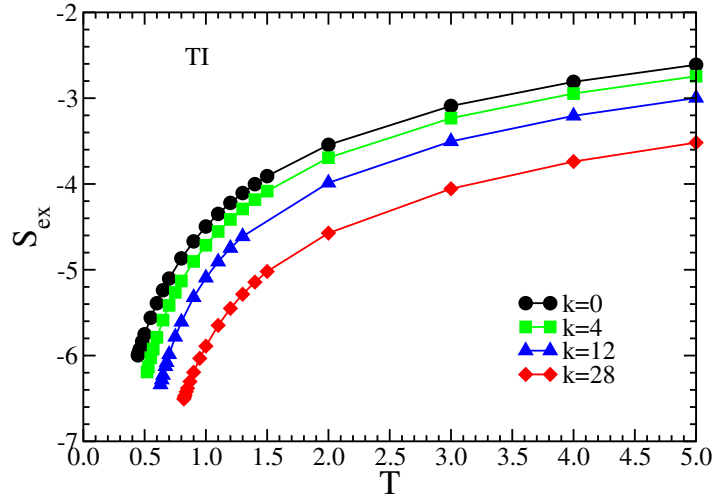


Figure 5.1: Plot of per particle excess entropy S_{ex} vs. T for $k = 0, 4, 12$ and 28 systems. S_{ex} is estimated using the TI method. With increase in k , the excess entropy becomes more negative.

Vibrational entropy

We next calculate the vibrational density of states (VDOS) for different k values. We find that with an increase in pseudo neighbours, there is a suppression of the low-frequency modes, and the whole spectrum moves to a higher frequency range as shown in Fig.5.2. A similar effect was also seen in the high-temperature dynamics where it was shown that with the increase in the pseudo neighbours, the cage becomes stiffer and the dynamics inside the cage becomes faster [9].

The temperature dependence of the vibrational entropy S_{vib} (obtained from the VDOS) is plotted in Fig.5.3. We find that with increasing k , as the vibrational spectrum shifts to higher frequencies, the vibrational entropy decreases.

Configurational entropy

Next, we study the configurational entropy of the system. For all the systems the data is plotted below their respective onset temperatures (see Table.5.1)[9]. The systems follow the expected linear relationship between TS_c and T (Fig.5.4). The Kauzmann temperature T_K^{TI} is obtained by fitting to $TS_c = K_T(\frac{T}{T_K} - 1)$. We find that T_K^{TI} increases with k . This is expected as in the earlier study it was found that with an increase in pseudo neighbours, the α relaxation time of the system appears to diverge at a higher temperature [9]. However, the unphysical part of the result is the vanishing of the configurational entropy for larger k systems ($k=12$ and 28) at comparatively high temperatures where the

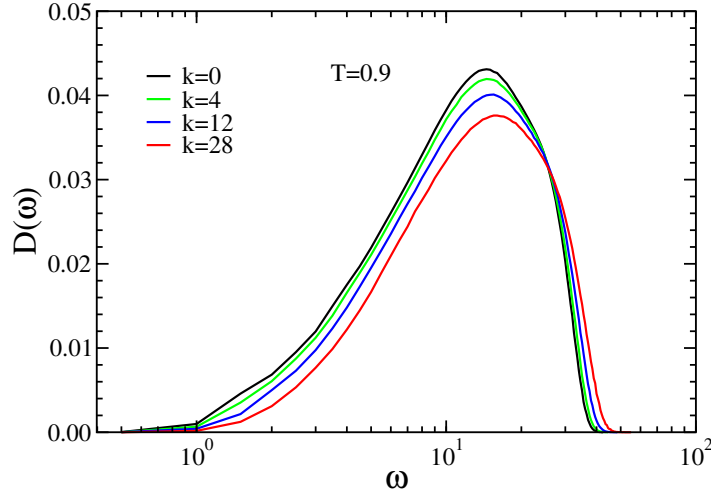


Figure 5.2: Vibrational density of states (VDOS), $D(\omega)$ vs. ω , for $k = 0, 4, 12, 28$ systems. With the increase in k , the low-frequency modes are suppressed and the whole spectrum shifts to higher frequencies.

system can be equilibrated in simulations. Especially for the $k = 28$ system, the temperature where the configurational entropy vanishes is close to the onset temperature of glassy dynamics[9]. The T_K^{TI} values are listed in the Table.5.1. In the same Table, we also list the respective T_0 values. For many systems, it is found that $T_K \simeq T_0$ which suggests that the slowing down of dynamics is driven by thermodynamics [14]. On the contrary, in Table 5.1 we find that the difference between the T_K^{TI} and T_0 increases with increase in k . The correlation between the dynamics and thermodynamics is also given by the Adam-Gibbs (AG) relation, $\tau = \tau_0 \exp(-\frac{A}{TS_c})$. Note that this expression implies that the divergence of the relaxation time is an effect of the vanishing of the configurational entropy and if we replace the expression of TS_c in terms of T_K then we get back the VFT expression provided we assume $T_K = T_0$. If the system follows the AG relation then the semi-log plot of τ vs $\frac{1}{TS_c}$ should follow a linear behaviour which it does for most systems [14, 17, 18, 19, 20, 21, 22, 23, 24, 25] In Fig.5.5, we study the validity of the AG relationship and find that with an increase in k there is a departure from the linearity. We next show that for the $k = 28$ system at $T = 0.82$ which is much below the $T_K^{TI} = 1.19$, both the collective overlap function and the intermediate scattering function decay with time and reach their respective longtime values ($Q^{tot}(t \rightarrow \infty) = 0.135$ and $F(q, t \rightarrow \infty) = 0$). Note that because of the introduction of the pseudo neighbours at a distance “ L_{ij} ”, the system has more than one length scale. Thus to make sure that the relaxation persists at length scale that are larger and smaller than the nearest neighbor distance, we plot the Intermediate scattering function at wave numbers larger and smaller than $q_{max} = \frac{2\pi}{\sigma_{max}}$ where σ_{max} is the position of the first peak in the radial distribution function. We find that the intermediate scattering

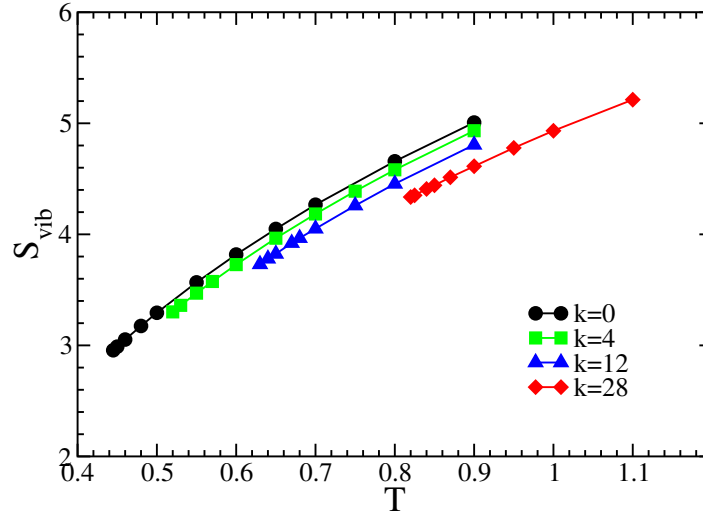


Figure 5.3: The vibrational entropy S_{vib} vs. T for $k = 0, 4, 12$ and 28 systems. With an increase in k , the DOS shifts to higher frequencies leading to a decrease in the vibrational entropy.

function relax to zero at all length scales. Note that more than the breakdown of the AG relation which has been suggested to be a possibility [16], the fact that the dynamics shows full relaxation where the configurational entropy vanishes suggests that we need to revisit the TI method of calculating the entropy. In the TI method, we need information about the ideal gas entropy, the excess entropy, and the vibrational entropy. The vibrational entropy calculation was cross-checked by calculating it from the Fourier transform of the velocity autocorrelation function which matched the data obtained from the Hessian (See Appendix I).

5.5 Possible reasons for the failure of the TI method

Let us first summarize the main observations made here when the entropy is calculated using TI method (i) Negative values of S_c at low temperatures for large values of k ; (ii) Full relaxation of the dynamical quantities at temperatures lower than the temperature at which S_c goes to zero; (iii) Breakdown of the AG relation. In this section, we discuss the possible failure points of the TI method.

5.5.1 Ideal gas entropy

In the calculation of the configurational entropy (Eq.2.37), we need the information of the ideal gas entropy. To make the entropy an extensive quantity we calculate the ideal gas entropy (Eq.2.16) by assuming the particles to be indis-

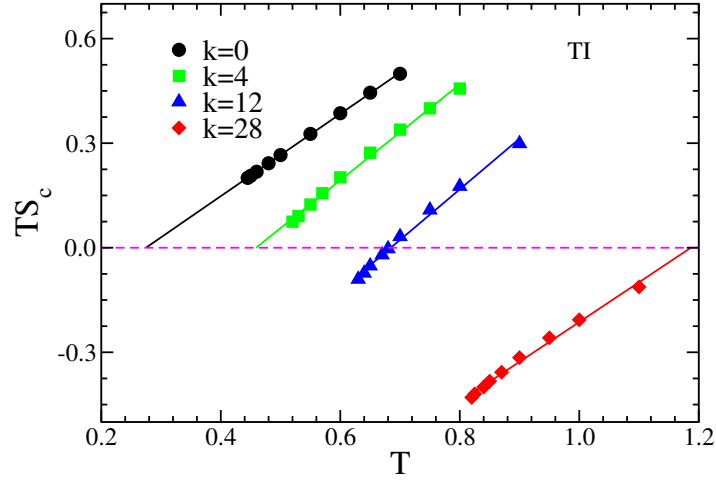


Figure 5.4: TS_c vs. T for $k = 0, 4, 12$ and 28 systems where the S_c is calculated using the TI method. The value of the Kauzmann temperature T_K^{TI} increases with increasing k . The value of T_K^{TI} (see Table.5.1) for $k = 28$ system is close to its onset temperature. For $k = 12, 28$ systems, T_K^{TI} values are high enough such that temperatures below T_K^{TI} are accessible in simulation. Consequently, S_c becomes negative for temperatures below.

tinguishable. However, in the mean-field system, each particle has a different set of pseudo neighbours with different L values. Thus one might argue that the particles are distinguishable.

If we assume all particles to be distinguishable *i.e.* $m = N$, then the entropy in the thermodynamic limit will diverge (Eq.2.16). However, for finite N , we can estimate the entropy which will increase by a factor that is proportional to $\log(N)$ but independent of k . From our analysis, it appears that with an increase in 'k' the error in the entropy calculation increases. This implies that the correction term should depend on 'k'. Apart from the distinguishability factor, there is one other issue that can affect the ideal gas term. Here the way the interaction between a particle and its pseudo neighbour is designed restricts the particle to access a certain part of the total volume. Per pseudo neighbour this volume is a spherical region of radius L_{ij} . Thus in the ideal gas limit, the whole volume of the system is not accessible to a particle. The per particle inaccessible volume should increase with 'k' which will lower the entropy of the system. Thus the distinguishability factor will increase the entropy whereas inaccessible volume will decrease the entropy, the former is independent of 'k' but the latter depends on 'k'. This might appear to solve the 'k' dependence of the correction term. However, if we combine the distinguishability and inaccessible volume part then we will find that for systems with small values of 'k' the volume correction is really small and the distinguishability factor which is independent of 'k' increases the entropy by a large amount. Thus the dynamics for these systems will be

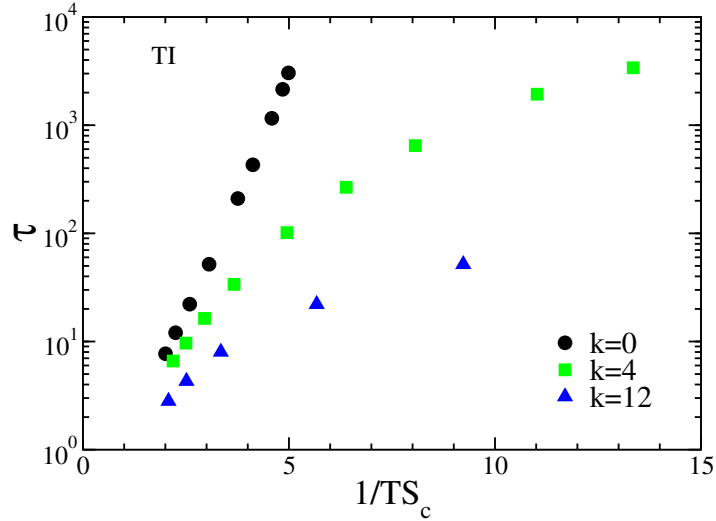


Figure 5.5: Testing the Adam-Gibbs relation between the relaxation time τ and $1/TS_c$, for the $k = 0, 4$ and 12 systems. The AG relation is obeyed for the $k = 0$ system, but is violated for non-zero k systems. The relaxation time τ is estimated from the self-part of the overlap function.

similar to the $k=0$ system but the entropy calculated in this way will be much higher.

Another possibility is that the distinguishability is not a binary function but is a function 'k'. When we have these extra connections with the pseudo neighbours replacing particles with another one while keeping the identity of pseudo contacts the same can increase the energy of the system, and the larger the number of pseudo contacts the higher is the increase in the energy. This appears quite similar to the case of polydisperse systems with continuous polydispersity where depending on the size range of the two particles the replacement may or may not keep the system in the same minimum [42]. It was argued that after particle swapping if the system remains in the same inherent structure minima then the two particles are indistinguishable and if not then they belong to different species. Thus to find the number of species we need to swap particle positions. Swapping particles while keeping the identity of the pseudo neighbours the same is not straightforward. The swap should make sure that in the new position of the particle none of the pseudo neighbours are within the interaction range r_c . With the increase in the number of pseudo neighbours these swaps will be mostly rejected thus making it impossible to quantify the number of species and thus the entropy.

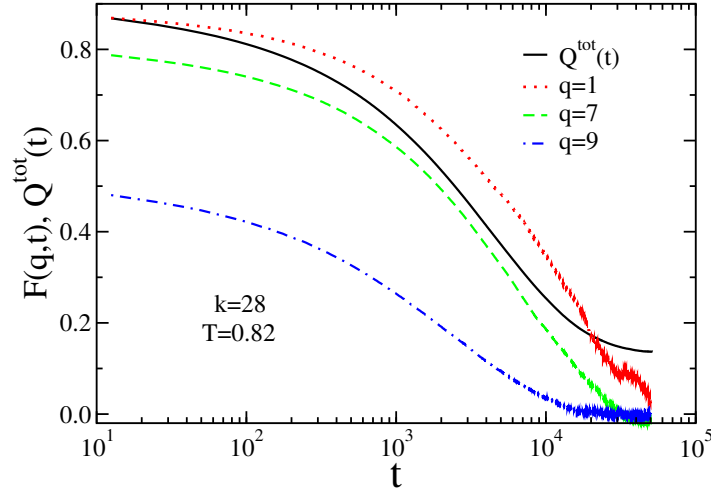


Figure 5.6: Time dependence of the intermediate scattering function and the collective overlap function for the $k = 28$ system at a temperature $T = 0.82$ which is lower than T_K^{TI} (see Table.5.1). It shows that even when the configurational entropy vanishes the self and the collective dynamics continues.

5.5.2 Excess entropy and the validity of the Rosenfeld relationship

We next test the accuracy of the excess entropy value calculated via the TI method. Apart from the AG relationship which is valid in the low-temperature regime and connects the configurational entropy to the dynamics, there is another phenomenological relationship, namely the Rosenfeld relation between the excess entropy and the dynamics [43, 44]. According to the Rosenfeld relation, any dimensionless transport property will follow the excess entropy scaling. For the relaxation time it can be written as, $\tau^* = R \exp(-K S_{ex})$ where $\tau^* = \tau \rho^{-1/3} T^{1/2} m^{-1/2}$. For simple liquids, it has been found that $R \simeq 0.6$ and $K \simeq 0.8$, and this relationship is valid in the high-temperature regime showing a data collapse between scaled diffusion and S_{ex} [45] and also scaled relaxation time and S_{ex} [46, 47]. A recent study has also shown that scaled viscosity and diffusion coefficient for a large number of systems show a quasi universal excess entropy scaling extending over both high and low temperature regimes [48]. In Fig. 5.7 we plot τ^* vs. S_{ex} for the different mean-field systems and do not find any data collapse. Thus we find a breakdown of the Rosenfeld relation and also the quasi universal excess entropy scaling [48]. The deviation from the Rosenfeld relationship might appear quite weak. However note that, unlike the AG relationship where we deal with the configurational entropy which has a very small value, in the Rosenfeld relationship we deal with the excess entropy which has a large value. Thus the Rosenfeld relation is not sensitive to small errors in the calculation of the entropy.

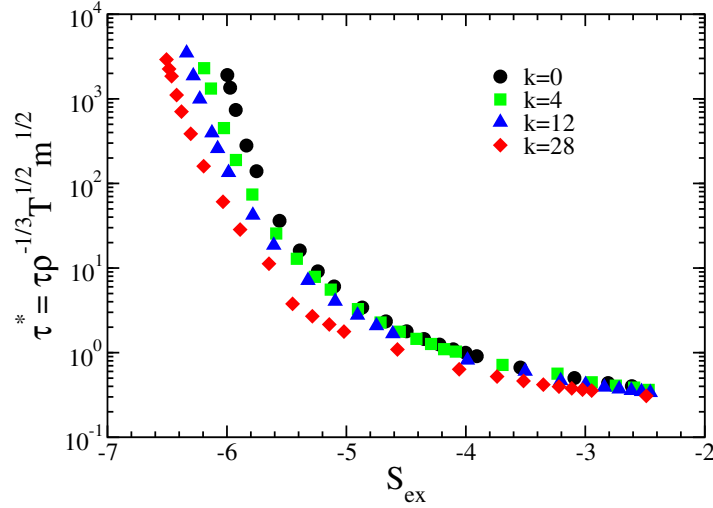


Figure 5.7: Scaled relaxation time vs. excess entropy. Rosenfeld scaling relation does not show universal scaling for all k systems. It deviates more from the universal scaling with increasing k .

In the mean-field system, we find that the excess entropy has a strong dependence on the number of pseudo neighbours. On the other hand, the study of the dynamics of the mean-field system showed that the interaction with the pseudo neighbours slows down the overall dynamics of the system, but has a weak effect on the structural relaxation [9]. Thus it appears that the role of the pseudo neighbours is not the same for the TI entropy and the dynamics.

5.5.3 Entropy using the 2PT method

In this section, we present the results of the calculation of entropy using a completely different technique. In the 2PT method (discussed in chapter 2), we primarily use the information of the dynamics, namely the velocity to determine the entropy. We know that the TI method works well for a regular KA model. Thus to validate the 2PT method we compare it with the TI method for a regular KA system ($k = 0$). As shown in Appendix I, the 2PT method works well. At temperatures close to the mode-coupling transition temperature, the 2PT method shows some deviation which is identified as an averaging issue. Thus we use the results from the 2PT method in the temperature range where the upper bound is the onset temperature and the lower bound is above the respective mode-coupling theory transition temperature [9]. In this section, we will first compare the total entropy obtained using the 2PT (Eq. 2.32) and the TI (Eq. 2.17) methods for the different mean-field systems. In the TI method, we assume the particles to be indistinguishable. As shown in Fig. 5.8 the difference in total entropy between TI and 2PT method increases systematically with increasing k . This suggests that for this system the TI method of calculating the

entropy is not correct. We next study the configurational entropy as predicted by the 2PT method and also its correlation with the dynamics. To calculate the configurational entropy, we need the information of the vibrational entropy which is the same as that used in the TI method. In Fig.5.9 we show the TS_c vs T plots. We find that for all the systems T_K^{2PT} is smaller than T_k^{TI} and close to T_0 (see Table.5.1). In Fig.5.10 we have a semi-log plot of τ against $\frac{1}{TS_c}$. It clearly shows the validity of the AG relation for all the systems in the temperature range studied.

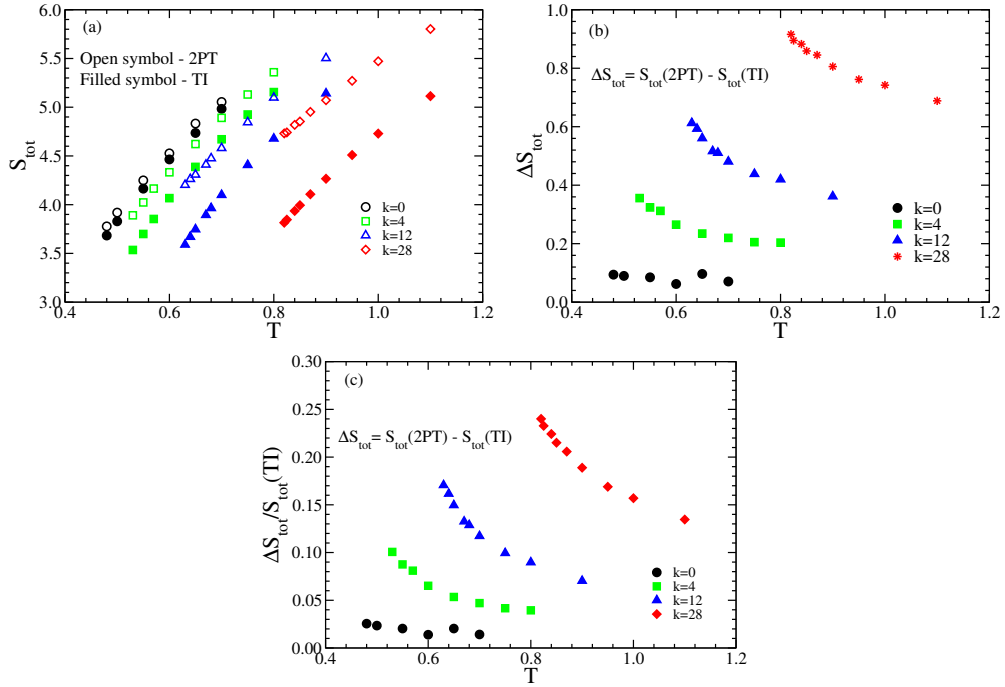


Figure 5.8: Comparison of the TI and 2PT method of calculation of entropy: (a) S_{tot} vs. T . Filled symbols represent the TI method and open symbols represent the 2PT method. S_{tot} computed by the 2PT method is higher than that by the TI method. (b) The difference in total entropy, ΔS_{tot} between 2PT and TI method increases with increasing k . (c) The relative difference in the total entropy, $\frac{\Delta S_{tot}}{S_{tot}(TI)}$ between 2PT and TI shows similar behavior as Fig.5.8b.

5.6 Pair and higher order entropy terms

Following Kirkwood expansion the per particle excess entropy of a liquid can be written in terms of two body and higher order correlations as,

$$S_{ex} = S_2 + S_3 + \dots + S_n \quad (5.3)$$

Where S_n is the entropy due to n -body correlation. S_{ex} can also be calculated via thermodynamic integration as the pair part of the excess entropy is expressed

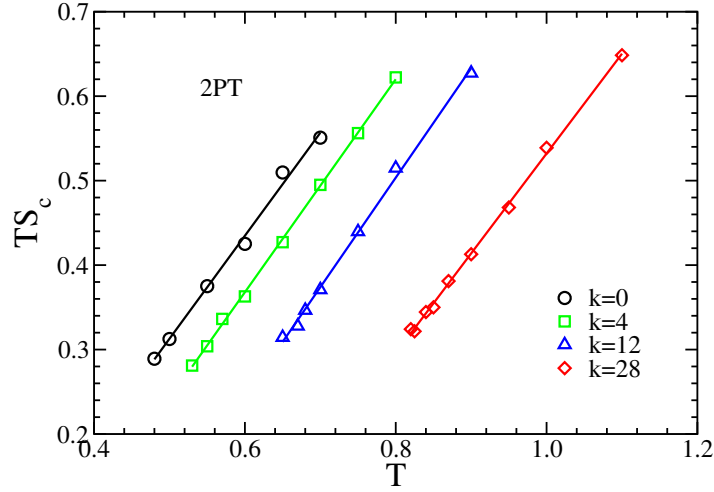


Figure 5.9: TS_c vs. T for $k = 0, 4, 12,$ and 28 systems using 2PT method. Values of T_K^{2PT} , which are in the same range as T_0 , are given in Table.5.1.

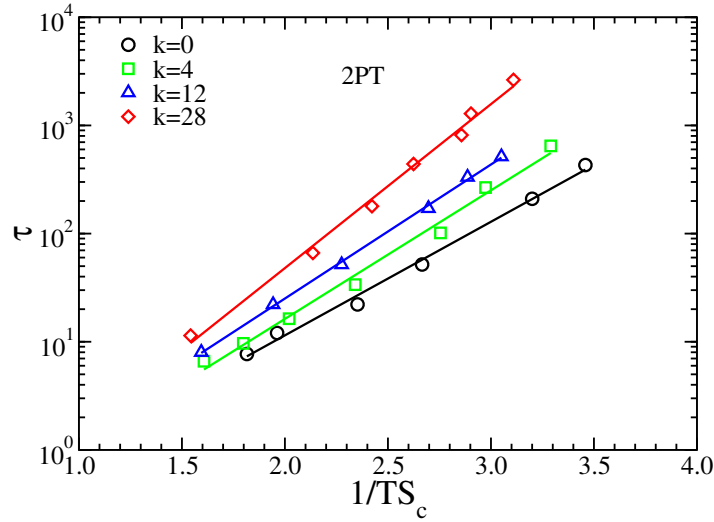


Figure 5.10: Testing the AG relation τ vs. $\frac{1}{TS_c}$ for $k = 0, 4, 12,$ and 28 systems with entropy computed by the 2PT method. All the systems follow the AG relation in the range of temperature studied here.

in terms of the rdf as

$$S_2 = -2\pi \int_0^\infty \rho [g(r) \ln g(r) - (g(r) - 1)] r^2 dr \quad (5.4)$$

The higher order contributions are clubbed together, $S_3 + S_4 + \dots = \Delta S$ and ΔS is the residual multiparticle entropy (RMPE).

5.6.1 MCT power law behavior

In earlier studies it has been found that there is an overlap between the MCT and the AG regime and S_c follows MCT like behaviour over the same temperature regime as the relaxation time [56, 11]. It was also shown that the vanishing of

Table 5.1: The value of all characteristic temperatures for systems with different k values. T_0 is the VFT temperature where the dynamics of the systems diverges. T_K^{TI} is the Kauzmann temperature estimated from TI. T_K^{2PT} is the Kauzmann temperature estimated from the 2PT method. T_K^{TI} (distinguishable) is the Kauzmann temperature when we consider all particles in the pseudo neighbor system are distinguishable.

k	T_{onset}	T_0	T_K^{TI}	T_K^{2PT}	T_{K_2}
0	0.74 ± 0.04	0.28	0.28	0.24	0.465
4	0.83 ± 0.08	0.36	0.46	0.31	0.572
12	1.03 ± 0.07	0.46	0.68	0.41	0.734
28	1.28 ± 0.22	0.61	1.19	0.55	0.1.07

the pair configurational entropy, S_{c2} at T_c is the origin of this predicted disappearance of the total configurational entropy which is avoided due to positive values of RMPE. For the S_c to follow MCT power-law behaviour a prerequisite is the validity of the AG relationship. In the MCT regime $\tau \propto (\frac{T-T_c}{T_c})^{-\gamma}$ and according to the AG relation $\ln \tau \propto \frac{1}{TS_c}$. Thus $\frac{1}{TS_c} \propto \frac{T-T_c}{T_c}$ plot. In the Fig.5.11, we plot $\frac{1}{TS_c}$ vs $\frac{T-T_c}{T_c}$ for $k=0, 4,$ and 12 systems where the entropy is calculated using the TI method. As expected we find that for systems which do not follow the AG relationship the entropy follows the MCT power-law behaviour in a narrower regime. The reason is for these systems the pair configurational entropy disappears at temperatures higher than T_C as shown in Fig.5.12 and also tabulated in Table.5.1. Thus we can say that the error in the entropy value obtained via the TI method appears even at the pair level. Note that if the problem is in the excess entropy calculation as suggested from the breakdown of the Rosenfeld scaling then most likely the error is in the pair part. This is because the PN interaction has only two body correlation as seen from the rdf ($g(r) = \exp(-\beta u(r))$) (Chapter3).

Here we show that when there is only two body correlation, excess entropy calculated via thermodynamic integration is exactly equal to the two body excess entropy expressed via the radial distribution function.

$$S_{ex}(\beta^*) = \beta^* \langle U \rangle - \int_0^{\beta^*} d\beta \langle U \rangle \quad (5.5)$$

Where $\langle U \rangle$ is the per particle potential energy written as,

$$\langle U \rangle = 2\pi\rho \int_0^\infty u(r)g(r)r^2 dr \quad (5.6)$$

Here $u(r)$ is the interaction energy between two particles situated at distance

r and $g(r)$ is the radial distribution function. Let us now assume that the system is such that there are only two body correlation. This will imply that $g(r) = \exp(-\beta u(r))$. The average potential energy per particle level can now be written as

$$\langle U \rangle = 2\pi\rho \int_0^\infty u(r) \exp(-\beta u(r)) r^2 dr \quad (5.7)$$

Using Eq.5.7, we will go from Eq.5.5 to Eq.5.4. First we will put the value of $\langle U \rangle$ from Eq.5.7 into Eq.5.5.

$$\begin{aligned} S_{ex} = & 2\pi\rho \left[\int_0^\infty \beta^* u(r) \exp(-\beta^* u(r)) r^2 dr \right. \\ & \left. - \int_0^{\beta^*} d\beta \int_0^\infty u(r) \exp(-\beta u(r)) r^2 dr \right] \end{aligned} \quad (5.8)$$

First term of Eq.5.8 can be written as

$$\begin{aligned} & \int_0^\infty \beta^* u(r) \exp(-\beta^* u(r)) r^2 dr \\ & = \int_0^\infty (-) \ln[\exp(-\beta^* u(r))] \exp(-\beta^* u(r)) r^2 dr \\ & = - \int_0^\infty \ln[g(r)] g(r) r^2 dr \\ & = - \int_0^\infty g(r) \ln[g(r)] r^2 dr \end{aligned} \quad (5.9)$$

as $\exp(-\beta^* u(r)) = g(r)$

If we integrate the second term of Eq.5.8 for the β variable then we get as

$$\begin{aligned} & - \int_0^{\beta^*} d\beta \int_0^\infty u(r) \exp(-\beta u(r)) r^2 dr \\ & = - \int_0^\infty \left[u(r) \frac{-1}{u(r)} \exp(-\beta u(r)) \right]_0^{\beta^*} r^2 dr \\ & = \int_0^\infty [\exp(-\beta u(r))]_0^{\beta^*} r^2 dr \\ & = \int_0^\infty [\exp(-\beta^* u(r)) - 1] r^2 dr \\ & = \int_0^\infty [g(r) - 1] r^2 dr \end{aligned} \quad (5.10)$$

as $\exp(-\beta^* u(r)) = g(r)$

Now Eq.5.8 can be rewritten using Eq.5.9 and Eq.5.10 as

$$\begin{aligned}
S_{ex} &= 2\pi\rho \left[- \int_0^\infty g(r) \ln[g(r)] r^2 dr + \int_0^\infty [g(r) - 1] r^2 dr \right] \\
&= -2\pi\rho \left[\int_0^\infty g(r) \ln[g(r)] r^2 dr - \int_0^\infty [g(r) - 1] r^2 dr \right] \quad (5.11) \\
&= -2\pi\rho \int_0^\infty [g(r) \ln g(r) - (g(r) - 1)] r^2 dr
\end{aligned}$$

We find Eq.5.4 and Eq.5.11 are exactly same i.e. $S_{ex} = S_2$. Thus we know that the PN interaction only contributes to the pair excess entropy.

Next we show in Fig.5.13 that the entropy calculated via the 2PT method follows the MCT power-law behavior. Similar to that observed for the relaxation time the temperature range over which the power-law behaviour is valid is wider for higher 'k' systems. In the 2PT method we cannot separately calculate the contribution of the pair and higher order terms. Thus we cannot comment on the T_{K2} value and compare it with T_C . However it appears that if the AG relationship is valid and if $T_K \simeq T_0$ then S_c follows a power law behavior and appears to vanish at T_C . However this is an avoided transition and at low temperatures there is a departure from this power-law behaviour. The power-law range for the entropy increases with 'k'.

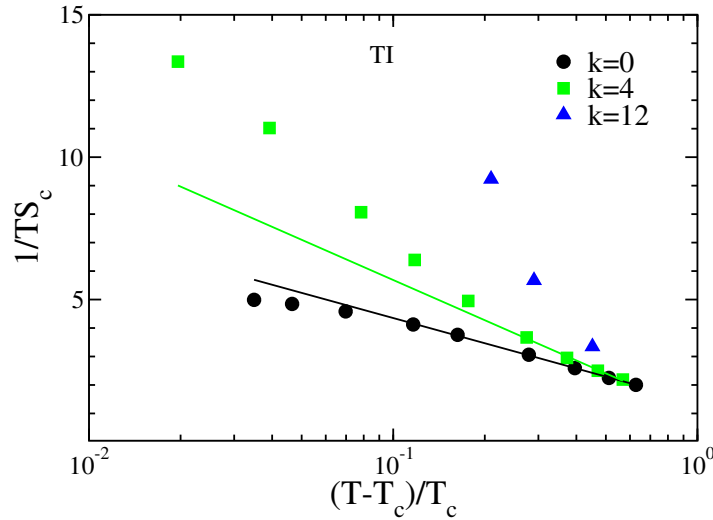


Figure 5.11: $\frac{1}{TS_c}$ vs. $\frac{T-T_c}{T_c}$ for $k=0, 4$ and 12 systems. Except $k=0$, no system follows the linear relationship like AG fit. As the S_c becomes negative for $k=28$ system, we could not plot here and for the same reason the most state points are absent in the plot for $k=12$ system.

5.6.2 Residual multiparticle entropy

In this section, we discuss 'k' dependence of the residual multiparticle entropy. RMPE denotes the contribution of the many body correlation in the entropy. In

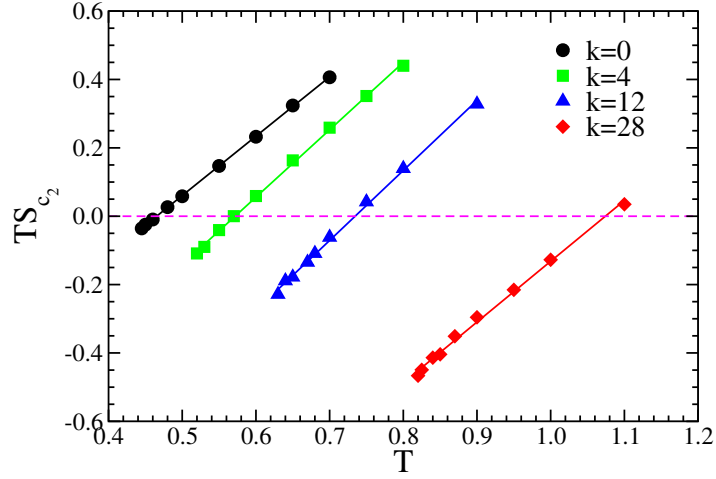


Figure 5.12: TS_{c_2} vs. T for $k=0, 4, 12$ and 28 systems. The value of T_{K_2} increases with increasing k . The values of T_{K_2} for $k=0, 4, 12$ and 28 systems are $0.465, 0.572, 0.734$ and 1.07 respectively.

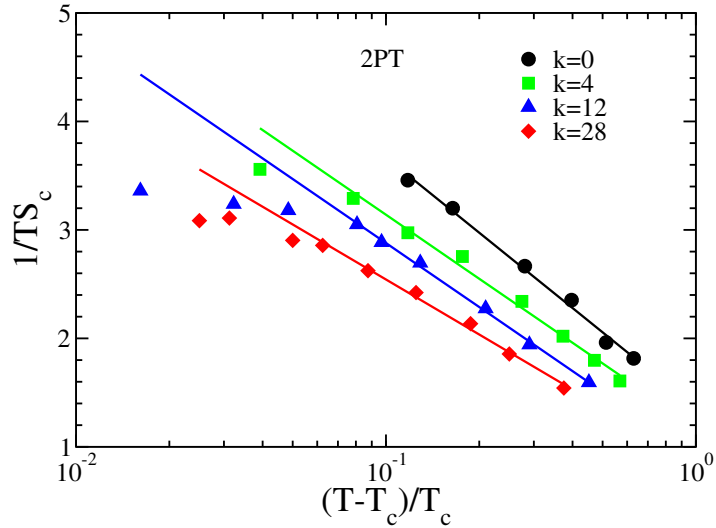


Figure 5.13: $\frac{1}{TS_c}$ vs. $\frac{T-T_c}{T_c}$ for $k=0, 4, 12$ and 28 systems. Here, the value of S_c have been estimated using the 2PT method. All systems follows the linear relationship like AG fit within the range.

a large number of systems it was shown that with decrease in temperature the RMPE undergoes a change in sign and the temperature where RMPE vanishes is similar to the freezing or the onset temperature [54, 55, 2, 11]. At higher temperatures, the RMPE has a negative value suggesting that due to many body interaction the entropy decreases. However at lower temperatures it has a positive value and it appears that many body interaction increases the entropy of the system. It has been suggested that this increase in entropy is akin to the hopping mechanism [2, 11, 56] and we can see that below the MCT transition temperature where the pair configurational entropy disappears the RMPE becomes the only source of entropy [56]. However, another study has shown

that it is only for three dimensional systems that vanishing of ΔS happens at the onset/freezing temperature/density. For higher dimensional systems RMPE disappears at a density higher than the freezing density [57]. Thus it can be assumed that mean field systems will show similar behaviour as these higher dimensional system.

As discussed earlier the TI method overestimates the entropy for the mean field system. Thus the question arises that can we calculate the RMPE accurately in this system. Since the PN correlation is only two body in nature it only affects the pair excess entropy and not the RMPE. Thus the RMPE is independent of 'k'. We have shown in chapter4 that the onset temperature increases with increasing k. Thus we show in Fig.5.14 that ΔS changes sign at a temperature which is lower than the onset temperature and with increase in 'k', the difference between these two temperatures increases. This result is similar to that observed by Truskett *et al.*[57]. This is another proof that higher 'k' system shows more mean-field like behaviour.

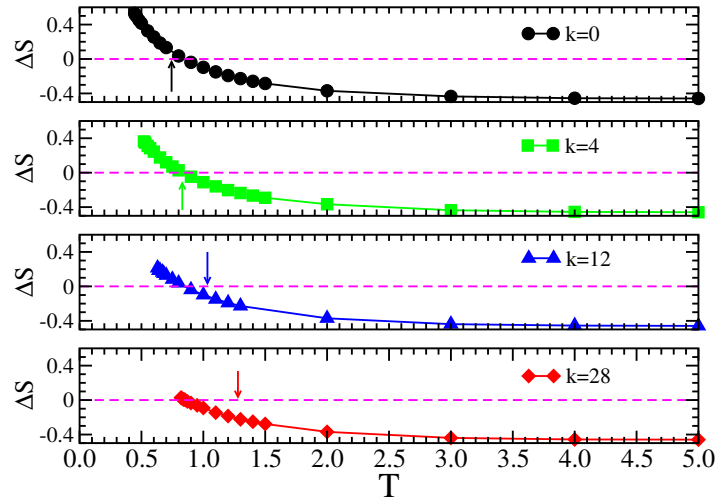


Figure 5.14: ΔS vs. T for all k . Arrows show the onset temperature.

As discussed before in earlier studies the positive value of ΔS was associated with activated hopping dynamics [2, 11, 56]. Since with increase in 'k' the ΔS remains constant but the temperature range of the supercooled liquids shifts to higher temperatures the dominance of the activated dynamics reduces. Eventually we expect that for higher 'k' systems the supercooled temperature range will shift completely in the range where RMPE is negative. In Fig.5.15 we plot the 'k' dependence of the different transition temperatures and extrapolate the dependence to higher 'k' values. We also show the temperature where RMPE=0 by magenta dashed line. Above this temperature, RMPE is negative and below this temperature, it is positive. We find that around 'k=60' the T_K value becomes equal to the temperature where RMPE vanishes. This implies that for

systems $k > 60$ RMPE will be always negative even in the supercooled regime, there will be no activated dynamics and the system will behave like a mean field system.

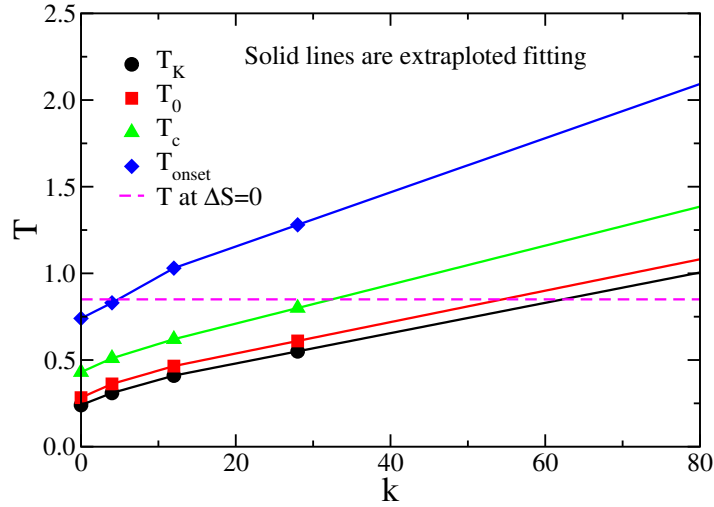


Figure 5.15: All characteristic temperatures vs. k plot. Solid lines are fitted graph. Dashed horizontal line is the temperature at which ΔS become zero.

5.7 Conclusion

In chapter 3 and chapter 4, we have described the development of the model for glass-forming liquid whereby changing a parameter the system can continuously switch from a standard three-dimensional liquid to a fully connected mean-field like system [9]. The parameter is k , the number of additional particle-particle interactions that are introduced per particle on top of the regular interactions in the system. With increasing k , the structure and the dynamics were studied which showed more mean-field like behaviour at higher k values. The present work aims to study the thermodynamics of the system and understand its correlation with the dynamics. To study thermodynamics, we first calculate the entropy using the well-known TI method [29]. We then study the correlation of the entropy with the dynamics. This model shows super-Arrhenius dynamics similar to conventional glassy liquids [9], suggesting that the RFOT description should apply. However, we find that the relaxation times calculated from both single-particle and collective dynamics remain finite at temperatures where the configurational entropy vanishes. This is different from the prediction of RFOT and the behavior seen in conventional glass-forming liquids for which the (extrapolated) values of T_K and T_0 are found to be close to each other [14, 16, 53]. We discuss the possible source of error in the TI method of calculation of the entropy for the mean-field system. However, at this point, we do not know

how to modify the TI method to correctly calculate the entropy of these model systems.

We thus use another technique namely the 2PT method to calculate the entropy. The 2PT method assumes that a liquid can be represented as partially a gas and partially a solid and this fraction is a function of the thermodynamic parameters of the system and also of the size of the particles. The 2PT method has been extensively used to calculate the entropy for many systems, mostly in the high-temperature regime [38, 30]. In recent work, this method was also extended to lower temperatures [32]. We find that for the KA system at $k = 0$, both the 2PT method and the TI method provide similar results. We then compare the total entropy calculated by the 2PT method with that by the TI method for different mean-field systems. We find that the difference between the entropy values obtained in the two methods systematically increases with increasing k . We also find that the entropy calculated via the 2PT method describes the dynamics quite well and confirms the RFOT prediction. The results of the mean-field systems appear quite similar to that of the pinned particle system studied earlier [33]. Thus our analysis suggests that for a certain class of systems, the TI method in its current form fails to predict the correct value of the entropy. At this point, we are unable to comment exactly why the TI method which has a microscopic basis fails whereas the 2PT method which is in a way heuristic in nature succeeds in predicting the dynamics. Also, the possible source of error in the TI method of entropy calculation for the two different systems may or may not be the same. In the mean-field system the source of error in the entropy calculation using the TI method can be the ideal gas term as the particles due to their fixed set of pseudo neighbours can appear to be distinguishable and also the total volume of the system might not be accessible to the particles even at infinite temperature limit. The mean-field system shows a breakdown of the Rosenfeld scaling when the excess entropy is calculated using the TI method. A recent study has shown that for the pinned system the correlation between the local pair excess entropy and the dynamics breaks down [52]. These two results appear similar in spirit. The excess entropy calculation only depends on the interaction between particles. Thus for the mean-field system, we may be overestimating the interaction between the particle. This conjecture needs to be tested and more such systems need to be studied to understand the role of interaction in the estimation of entropy using the TI method.

Appendix I: Comparison of 2PT and TI method for KA model

For a binary system in the 2PT method of entropy calculation, we need to provide the information of the partial volume fraction which can be calculated

as [38],

$$\bar{V}_i = \frac{\sigma_i^3}{\sum_j x_j \sigma_j^3} \frac{V}{N} \quad (5.12)$$

where, $V_i = \bar{V}_i N_i$.

Partial volume fraction depends on the radii of the particles. In the KA system, the diameter of the A and B particles are 1 and 0.88. However, the potential in the KA model is designed in such a way that it allows interpenetration between the A and the B particles ($\sigma_{AB} < (\sigma_A + \sigma_B)/2$). Thus if we assume that the B particles are surrounded by all A particles then the effective diameter of a B particle will be 0.6. To understand the role of partial volume fraction on the entropy we calculated S_{tot} from the 2PT method, assuming the B particle diameter to be 0.8 and 0.6. We find that at high temperatures the 0.6 value provides a better result but at low temperatures, the entropy is almost independent of the small changes in the partial volume fraction. Thus for these systems, we assume the diameter of the B particles to be 0.6.

We compare the total entropy of the system as estimated from the TI [39] and from the 2PT [30] methods. Fig.5.16 shows that the S_{tot} obtained TI and 2PT methods have similar values. The error bar for the 2PT data is estimated from a set of ten runs at each temperature. We find some deviation in the low temperature. At low temperatures as the dynamics become slow, we need longer runs to get a converged DOS. Fig.5.17 shows the effect the time step has on the value of total entropy at lower temperatures. Initially, with an increase in time step the entropy value faster approaches the value calculated using the TI method. However, at longer times, the slope of the curve reduces.

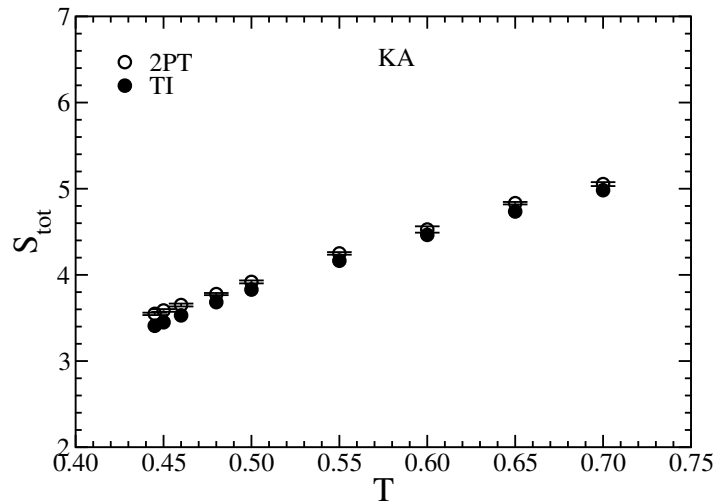


Figure 5.16: S_{tot} vs. T for the KA model using the TI and the 2PT method. The two methods agree reasonably well. A small systematic deviation in the low-temperature regime is due to limited averaging possible for the 2PT method, see Fig.5.17.

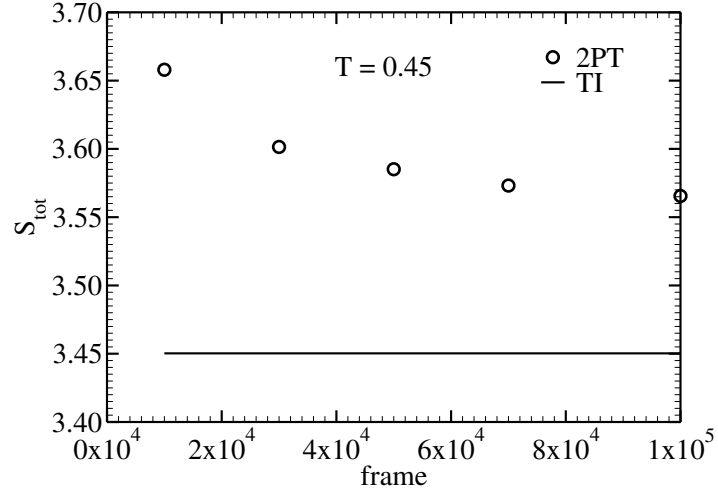


Figure 5.17: The total entropy via the 2PT method as a function of the number of time frames over which the velocity autocorrelation function is integrated to obtain the spectral density at a low temperature $T = 0.45$. For comparison, we also plot the entropy value obtained using the TI method. The difference decreases with increasing time interval, but the rate of convergence becomes slower at longer times.

Configurational entropy, S_c obtained in the two different methods is plotted in Fig.5.18 We find that the values of Kauzmann temperature (T_K) using two different methods are close which validates the applicability of the 2PT method for the calculation of the configurational entropy.

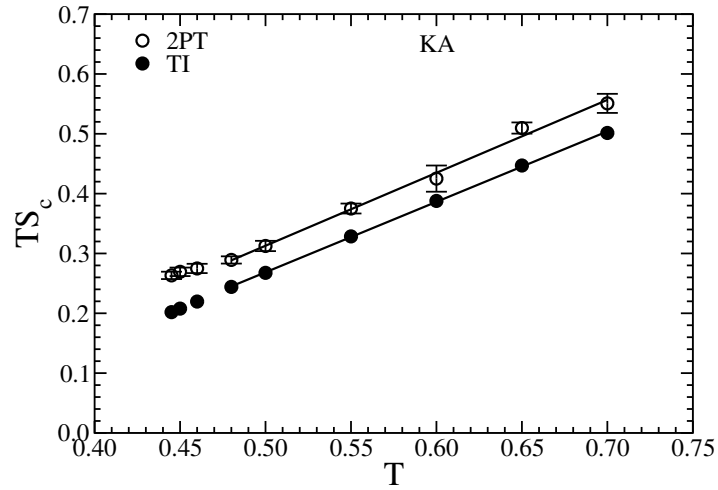


Figure 5.18: TS_c vs. T for the KA model using the TI and the 2PT methods. The value of T_K estimated by the two methods are similar ($T_K^{TI}=0.27$, $T_K^{2PT}=0.24$).

Bibliography

- [1] F. H. S. Srikanth Sastry, Pablo G. Debenedetti, *Nature* **393**, 554 (1998).
- [2] A. Banerjee, M. K. Nandi, S. Sastry, and S. Maitra Bhattacharyya, *The Journal of Chemical Physics* **147**, 024504 (2017).
- [3] P. Patel, M. K. Nandi, U. K. Nandi, and S. Maitra Bhattacharyya, *The Journal of Chemical Physics* **154**, 034503 (2021).
- [4] W. Götze, *Journal of Physics: Condensed Matter* **11**, A1 (1999).
- [5] W. M. Du *et al.*, *Phys. Rev. E* **49**, 2192 (1994).
- [6] P. Lunkenheimer, A. Pimenov, and A. Loidl, *Phys. Rev. Lett.* **78**, 2995 (1997).
- [7] K. Kim and S. Saito, *The Journal of Chemical Physics* **138**, 12A506 (2013).
- [8] W. Kob and H. C. Andersen, *Phys. Rev. E* **51**, 4626 (1995).
- [9] E. Flenner and G. Szamel, *Phys. Rev. E* **72**, 031508 (2005).
- [10] E. Flenner and G. Szamel, *Phys. Rev. E* **72**, 011205 (2005).
- [11] V. Lubchenko and P. G. Wolynes, *The Journal of Chemical Physics* **119**, 9088 (2003).
- [12] T. R. Kirkpatrick and P. G. Wolynes, *Phys. Rev. A* **35**, 3072 (1987).
- [13] A. Cavagna, *Physics Reports* **476**, 51 (2009).
- [14] G. Adam and J. H. Gibbs, *The Journal of Chemical Physics* **43**, 139 (1965).
- [15] W. Kauzmann, *Chemical Reviews* **43**, 219 (1948).
- [16] M. Ozawa, C. Scalliet, A. Ninarello, and L. Berthier, *The Journal of Chemical Physics* **151**, 084504 (2019).
- [17] C. A. Angell, *J Res Natl Inst Stand Technol.* **102**, 171 (1997).

- [18] R. Richert and C. A. Angell, *The Journal of Chemical Physics* **108**, 9016 (1998).
- [19] J. H. Magill, *The Journal of Chemical Physics* **47**, 2802 (1967).
- [20] T. M. Shuichi Takahara, Osamu Yamamuro, *The Journal of Physical Chemistry* **99**, 9589 (1995).
- [21] K. L. Ngai, *The Journal of Physical Chemistry B* **103**, 5895 (1999).
- [22] C. Alba-Simionesco, *Comptes Rendus de l'Académie des Sciences - Series IV - Physics-Astrophysics* **2**, 203 (2001).
- [23] C. M. Roland, S. Capaccioli, M. Lucchesi, and R. Casalini, *The Journal of Chemical Physics* **120**, 10640 (2004).
- [24] D. Cangialosi, A. Alegría, and J. Colmenero, *Europhysics Letters (EPL)* **70**, 614 (2005).
- [25] E. Masiewicz *et al.*, *Scientific Reports* **5**, 2045 (2015).
- [26] A. D. S. Parmar, S. Sengupta, and S. Sastry, *Phys. Rev. Lett.* **119**, 056001 (2017).
- [27] U. K. Nandi, W. Kob, and S. Maitra Bhattacharyya, *The Journal of Chemical Physics* **154**, 094506 (2021).
- [28] R. Mari and J. Kurchan, *The Journal of Chemical Physics* **135**, 124504 (2011).
- [29] S. Sastry, *PhysChemComm* **3**, 79 (2000).
- [30] S.-T. Lin, M. Blanco, and W. A. Goddard, *The Journal of Chemical Physics* **119**, 11792 (2003).
- [31] S.-T. Lin, P. K. Maiti, and W. A. Goddard, *The Journal of Physical Chemistry B* **114**, 8191 (2010).
- [32] M. Moid, S. Sastry, C. Dasgupta, T. A. Pascal, and P. K. Maiti, *The Journal of Chemical Physics* **154**, 164510 (2021).
- [33] M. Ozawa, W. Kob, A. Ikeda, and K. Miyazaki, *Proceedings of the National Academy of Sciences* **112**, 6914 (2015).
- [34] M. Ozawa, W. Kob, A. Ikeda, and K. Miyazaki, *Proceedings of the National Academy of Sciences* **112**, E4821 (2015).

- [35] S. Chakrabarty, S. Karmakar, and C. Dasgupta, *Scientific Reports* **5**, 12577 (2015).
- [36] S. Sengupta, F. Vasconcelos, F. Affouard, and S. Sastry, *The Journal of Chemical Physics* **135**, 194503 (2011).
- [37] D. A. McQuarrie, *Statistical Mechanics book* (1975).
- [38] P.-K. Lai, C.-M. Hsieh, and S.-T. Lin, *Phys. Chem. Chem. Phys.* **14**, 15206 (2012).
- [39] S. Sastry, *Nature* **409**, 164 (2001).
- [40] F. Sciortino, *Journal of Statistical Mechanics: Theory and Experiment* **2005**, P05015 (2005).
- [41] B. Doliwa and A. Heuer, *Phys. Rev. Lett.* **80**, 4915 (1998).
- [42] M. Ozawa and L. Berthier, *The Journal of Chemical Physics* **146**, 014502 (2017).
- [43] Y. Rosenfeld, *Phys. Rev. A* **15**, 2545 (1977).
- [44] Y. Rosenfeld, *Journal of Physics: Condensed Matter* **11**, 5415 (1999).
- [45] M. Singh, M. Agarwal, D. Dhabal, and C. Chakravarty, *The Journal of Chemical Physics* **137**, 024508 (2012).
- [46] A. Banerjee, S. Sengupta, S. Sastry, and S. M. Bhattacharyya, *Phys. Rev. Lett.* **113**, 225701 (2014).
- [47] A. Banerjee, M. K. Nandi, and S. M. Bhattacharyya, *Journal of Chemical Sciences* **129**, 793 (2017).
- [48] I. H. Bell, J. C. Dyre, and T. S. Ingebrigtsen, *Nature Communications* **11**, 4300 (2020).
- [49] M. Ozawa, A. Ikeda, K. Miyazaki, and W. Kob, *Phys. Rev. Lett.* **121**, 205501 (2018).
- [50] S. Chakrabarty, S. Karmakar, and C. Dasgupta, *Proceedings of the National Academy of Sciences* **112**, E4819 (2015).
- [51] S. Chakrabarty, R. Das, S. Karmakar, and C. Dasgupta, *The Journal of Chemical Physics* **145**, 034507 (2016).
- [52] I. Williams *et al.*, *Journal of Physics: Condensed Matter* **30**, 094003 (2018).

- [53] L. Berthier, M. Ozawa, and C. Scalliet, *The Journal of Chemical Physics* **150**, 160902 (2019).
- [54] L.V. Giaquinta, and G. Guinta, *Physica A* **187**, 145 (1992).
- [55] M. Singh, M. Agarwal, D. Dhabal, and C. Chakravarty, *The Journal of Chemical Physics* **137**, 024508 (2012).
- [56] M. Nandi, A. Banerjee, S. Sengupta, S. Sastry, and S. M. Bhattacharyya, *The Journal of Chemical Physics* **143**, 174504 (2015).
- [57] W.P. Krekelberg, V.K. Shen, J.R. Errington, and T.M. Truskett, *The Journal of Chemical Physics* **128**, 161101 (2008).

Chapter 6

Connecting real glasses to mean-field models: A study on jamming

6.1 Introduction:

Jamming is the transition of the disordered matter to rigidity. Different systems like Emulsions, foams, colloidal suspensions, pastes, granular media and glasses can jam in rigid, disordered states, and they respond essentially elastically to small applied shear stresses. However, these jammed states can easily be made to yield (unjam) and flow by tuning various control parameters. The jamming transition can be influenced by varying thermodynamic variables, such as temperature or density also by mechanical variables such as the stress applied to the sample.

It is impossible to compress a disordered assembly of rigid particles beyond a maximal packing fraction. In the idealized case of hard, spherical, frictionless particles, a critical value of the volume fraction is defined in the thermodynamic limit[1, 2], beyond which the system cannot be compressed, and this critical point is called the jamming point. The jammed system corresponds to a critical point (“point J”) with remarkable scaling properties observed when J is approached from either side[1, 3, 2]. Although the different initial state points show different jamming points when we plot pressure(P) *vs* $(\phi - \phi_J)$, it shows a universal scaling behaviour, and similarly, the energy of the system also shows the universal scaling behaviour with different exponent[4, 1]. Below the jamming transition, the average number of particles in contact jumps from a finite value(Z_J) to zero. Z_J is the number of particles in contact at the jamming point. Maxwell’s estimate for the rigidity transition is compatible with the value of Z_J .

It states that each particle has minimum contacts to exist the rigid state, which is called the isotactic state[5, 6]. less spheres. We consider a packing of N soft particles in the d dimensions. The average number of contacts at a particle, equals to Z and the total number of contacts equals to $\frac{ZN}{2}$ because each contact is shared by two particles. Thus the system needs $\frac{ZN}{2}$ contact forces balance on all the particles, which yields dN number of constraints on $\frac{ZN}{2}$ force degrees of freedom. The isotactic stability occurs when $\frac{Z_c N}{2}$ becomes equal to Nd . Thus Z_c becomes $2d$. The additional contacts are added when the system reaches above the jamming transition. This additional contacts ($\Delta Z = Z - Z_J$) follow a universal scaling law with the change of volume fraction ($\Delta\phi = \phi - \phi_J$) as $\Delta Z \propto \Delta\phi^\delta$ (where $\delta = 0.5$ for harmonic sphere system)[4, 1].

There are lots of similarities between the glass transition and the jamming transition. The glass transition is reached by cooling the equilibrium liquid fast, whereas the jamming transition is achieved by compressing systems rapidly. One argument is that the jamming transition is the zero-temperature limit of glass transition[7]. However, the numerical study[8] show that these two transitions are distinct and complicated in nature. We do not know how the jamming transition occurs and the scaling behavior in the vicinity of the jamming transition in the mean-field systems. In earlier work[9], we have added k number of pseudo neighbor (k) with each particle, and we have found the systems become more mean-field like as we go to higher k systems. Our aim is to find the jamming point and to see the scaling properties near the jamming transition for mean-field systems with the different pseudo neighbors.

In this chapter, we numerically investigate jamming transition and the scaling properties for different mean-field systems. We find the for higher k systems the jamming transition occurs at lower volume fraction. Energy and pressure show a good scaling behavior near the the jamming state. Total coordination number increases rapidly with increase in k . However the increase in coordination number as a function of volume fraction do not show the same scaling behavior for all the systems, we find the exponent increases with increase in k . The contribution of the nearest neighbor in Z_J decreases with increase in k and on the other hand, the contribution of the pseudo neighbor in Z_J increase with increase in k and we predict that around $k=136$ the jamming will be dominated by the pseudo neighbours. The local structure of the system estimated from the radial distribution function (rdf) show a diverging behaviour near the contact distance and a double second peak for both $k=0$ and large k systems. RDF also shows a power-law behavior near the contact distance, where the exponent is k dependent.

The rest of this chapter is organized as follows: The system and simulation

details are described in Sec. 6.2. In Sec. 6.3, we describe system details. In Sec.6.4, we have discussed energy minimization technique and the algorithm. We show the results and its implications in Sec. 6.5 and conclude in Sec. 6.6.

6.2 Simulation details

We have performed molecular dynamics simulations for three-dimensional binary mixtures using soft repulsive harmonic potential.

$$U_{ij}(r) = \begin{cases} (1 - \frac{r}{\sigma})^2, & r \leq \sigma \\ 0, & r > \sigma \end{cases} \quad (6.1)$$

The system contains total N number of particles with density $\rho = \frac{N}{V}$, where V is the volume of the system. The system is under periodic boundary conditions. For binary mixtures total N contains N_A particles of type A (50%) and N_B particles of type B (50%). We have performed constant volume and constant temperature (velocity rescaling) simulation (NVT) using time step $\Delta t = 0.002$. We use σ_{AA} and ϵ_{AA} as the unit of length and energy, setting the Boltzmann constant $k_B = 1$. We have used reduced time unit in terms of $\sqrt{\frac{m_{AA}\sigma_{AA}^2}{\epsilon_{AA}}}$ and mass of both type of particles are same ($m_A = m_B$). We have used 50% of A particles and 50% of B particles with the diameter $\sigma_{AA}=1.0$, $\sigma_{AB}=1.2$ and $\sigma_{BB}=1.4$. The interaction strength between the particles are $\epsilon_{AA}=1.0$, $\epsilon_{AB}=1.0$ and $\epsilon_{BB}=1.0$.

6.3 System details

The mean-field system is given by N particles that interact with each other via a standard short-range potential. In addition, each particle also interacts with ‘‘pseudo neighbors’’, i.e. particles that are not necessarily close in space. Hence, the total interaction potential of the system is given by,

$$U_{\text{tot}}(r_1, \dots, r_N) = \sum_{i=1}^N \sum_{j>i}^N u(r_{ij}) + \frac{1}{2} \sum_{i=1}^N \sum_{j=1}^k u^{\text{pseudo}}(r_{ij}) \quad (6.2)$$

$$= U + U_k^{\text{pseudo}} \quad (6.3)$$

The first term on the right-hand side is the regular interaction between particles, while the second term is the interaction each particle has with its pseudo neighbours. Here we consider the case that the regular interaction as described

by the Eq.6.1.

The interaction potential with the pseudo neighbours is modelled in terms of a modified LJ potential,

$$u^{\text{pseudo}}(r_{ij}) = u(r_{ij} - L) \quad (6.4)$$

$$= \left(1 - \frac{r_{ij} - L}{\sigma_{ij}}\right)^2 \quad (6.5)$$

where L is a fixed value defined below. In our simulations we impose the restriction that any two particles interact either via $u(r_{ij})$ or via $u^{\text{pseudo}}(r_{ij})$. We have chosen fixed L values for all the systems and all the pairs of particles. This condition determines how for a given configuration equilibrated with the potential u the pseudo neighbors and the values L are chosen: $L \leq L_{\text{box}}/2 - r_c$, with L_{box} the size of the simulation box. Subsequently we choose k distinct particles j with $r_{ij} > r_c$ and use the L to fix *permanently* the interaction between particles i and j . This procedure thus makes that each particle i interacts not only with the particles that are within the cutoff distance but in addition to k particles that can be far away. Note that once the particle j is chosen as a pseudo neighbour of particle i , automatically particle i becomes a pseudo neighbour of particle j . The system, as defined here, can then be simulated using standard simulation algorithms.

NVT molecular dynamics (MD) simulation is performed in a cubic box using velocity rescaling method for $N = 1000$ particles at $\rho = 0.51$ ($L_{\text{box}} = 12.515$), using a time integration step of $\Delta t = 0.002$. We have taken $L=1.5$. We have simulated four different systems with the number of pseudo neighbours, $k = 0, 10, 20, 30, 40, 50, 60, 70, 80, 90$ and 100 .

6.4 Inherent structure

One of the most common tasks in computational material science is to find mechanically stable equilibrium configurations in the atomistic system, which corresponds to find the minimum potential energy starting from an initial configuration. Here we have used a simple but powerful MD scheme for structural relaxation. This method relies on inertia. Thus it is called a Fast Inertia Relaxation engine (FAST) algorithm[10]. It searches the fastest way to reach the bottom of the potential energy landscape ($E(x)$) of a state point using the following equation

$$\dot{\mathbf{v}}(t) = \mathbf{F}(t)/m - \gamma(t)|\mathbf{v}(t)|[\hat{\mathbf{v}}(t) - \hat{\mathbf{F}}(t)] \quad (6.6)$$

where m is the mass, $\mathbf{v} = \dot{\mathbf{x}}$, the force $\mathbf{F} = -\Delta E(x)$ and hat signifies the corresponding unit vector. The strategy for searching the energy surface is to introduce an acceleration in the direction that is steeper than the current direction of motion via the function $\gamma(t)$ if the power $P(t) = \mathbf{F}(t) \cdot \mathbf{v}(t)$ is positive and it stops the velocity as soon as power becomes negative to avoid the uphill motion. FIRE can be calculated using any Molecular Dynamics integrator.

Practically FIRE algorithm can be performed using few steps. Two kinds of velocity are required to adjust the MD trajectories continuously. (1) immediate stop the velocity upon uphill motion (2) a mixing of the global velocity (3N dimensional) and force vectors $\mathbf{v} \rightarrow (1 - \alpha)\mathbf{v} + \alpha\hat{\mathbf{F}}|\mathbf{v}|$, resulting from an Euler-discretization of the last term in Eq.6.6 with time step Δt and $\alpha = \gamma\Delta t$ are treated as dynamically adaptive quantities. Δt and α are dynamically adaptive quantities. FIRE algorithm follows some propagation rules

1. Initialize the values of Δt , $\alpha = \alpha_{start}$, global vector $\mathbf{x} = \mathbf{0}$ and $\mathbf{v} = \mathbf{0}$.
2. Calculate \mathbf{x} , $\mathbf{F} = -\Delta\mathbf{E}(\mathbf{x})$ and \mathbf{v} needs to calculate using any MD integrator.
3. Calculate $P = \mathbf{F} \cdot \mathbf{v}$
4. set $\mathbf{v} \rightarrow (1 - \alpha)\mathbf{v} + \alpha\hat{\mathbf{F}}|\mathbf{v}|$
5. if $P \rightarrow 0$ and the number of steps since P was negative is larger than N_{min} , increase the time step $\Delta t \rightarrow \min(\Delta t_{f_{inc}}, \Delta t_{max})$ and decrease $\alpha \rightarrow \alpha f_{\alpha}$
6. if $P \leftarrow 0$, decrease time step $\Delta t \rightarrow \Delta t \alpha_{dec}$, freeze the system $v \rightarrow 0$ and set α back to α_{start} .
7. Return to MD

6.5 Result and discussion

To generate configurations near the jamming point, we take high-temperature configurations with low volume fraction (ϕ) and quench them at zero temperature using the FIRE algorithm (see section 6.4) with that fixed volume fraction. Then we increase the diameter of the particle by 10^{-5} , and again do the

minimization using the FIRE algorithm in the higher volume fraction, and we continue this process. During the compression, the system reaches the jammed state and go beyond the jamming volume fraction (ϕ_J) on further compression. When the system reaches a volume fraction higher than ϕ_J , we decompress the system by decreasing the diameter of the particle with the same amount as compression, and again we come across the jamming transition. In this chapter, we have analysed and present all the data which is obtained during the decompression cycle.

The jamming point is not fixed, it exists over a continuous window, and it depends on the protocol to generate the jammed state. Many studies have shown that if the initial equilibrium system has a higher density or lower temperature, then the jamming point shifts towards higher volume fraction [4, 11, 12, 13]. This effect is not the same as the mean-field system. We have found that as we go to higher k system the jamming transition happens at lower volume fractions as shown in Fig.6.1. Thus with increasing k the jamming point shifts towards lower volume. We obtain ϕ_J by fitting $E \propto (\phi - \phi_J)^\alpha$ and the values of ϕ_J and α are given in Table6.1. We find that the pressure also diverges at the same ϕ_J as shown in Fig.6.1.

In Fig.6.2 we plot the 'k' dependence of ϕ_J . In our system, when we increase the number of pseudo neighbors, the network of the interaction increases. Since the pseudo neighbours also contribute to the jamming transition this lowering of jamming volume fraction is expected. This is similar to the observation made in the earlier study [9] where we found that with an increase in k, the transition temperatures increase. Note that these pseudo neighbours effectively increase the density of the system. In the earlier study [9], we have explained the effective density of the system as $\rho_{eff} = \rho + \rho_k$, where ρ is the regular density of the system and ρ_k is the pseudo neighbor density. In a similar manner that we have used to define the regular volume fraction (ϕ) we can define the volume fraction due to the pseudo neighbours as ($\phi_k = \frac{\frac{k}{2} \frac{4}{3} \pi [(\sigma_{AA}/2)^3 + (\sigma_{BB}/2)^3]}{BOX^3 - \frac{4}{3} \pi L^3}$) and thus we define an effective volume fraction in the system $\phi^{eff} = \phi + \phi_k$. We estimate the effective jamming volume fraction (ϕ_J^{eff}) for all the systems, and we find ϕ_J^{eff} does not change much with increase in k as shown with red symbols in Fig.6.2. Also the E vs. ϕ^{eff} and the P vs. ϕ^{eff} show a near data collapse (see Fig.6.3).

Although ϕ_J is different for different k systems, the scaling properties near the jamming transition are not different. Fig.6.4(a) shows that all the systems follow the power-law behaviour for energy *vs* $\phi - \phi_J$ plot, and the exponent is near 2. Fig.6.4(b) shows that pressure *vs* $\phi - \phi_J$ follow the similar universal power-law behavior for all k systems with an exponent close to 1. We also find

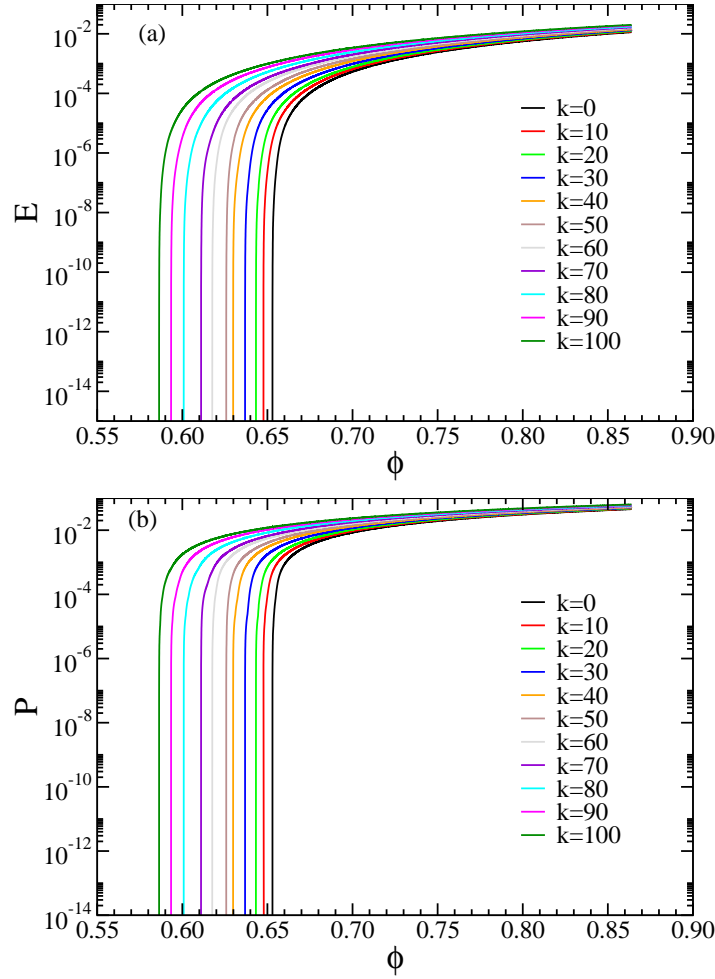


Figure 6.1: (a) Energy vs. Volume fraction plot for different k systems. Jamming point goes to lower volume fraction with increasing k . (b) Pressure vs. Volume fraction plot for different k systems. Jamming point goes to lower volume fraction with increasing k .

that in the energy *vs* $\phi^{eff} - \phi_J^{eff}$ and pressure *vs* $\phi^{eff} - \phi_J^{eff}$ plots the power-law behaviour remains quite similar (see Fig.6.4). In Fig.6.5, we plot the $\phi - \phi_J$ *vs* $\phi^{eff} - \phi_J^{eff}$. We find that as we increase k the slope of the line deviates from 1. However the deviation is weak and even for $k=100$ the slope is 0.91. This is the reason both $\phi - \phi_J$ and $\phi^{eff} - \phi_J^{eff}$ appear to be good parameters in describing the behaviour of energy and pressure near the jamming point. Right now, we are unable to comment on which volume fraction, ϕ and ϕ^{eff} should better describe the system. This will require further study.

The geometry at the jamming point is nontrivial, and the systems at a jamming point are isotactic [14] which is the sharply defined minimum required of the average contact number to stabilize the jamming state. The contact number at a jamming point can be argued from the number of degrees of freedom and the constraints in the system [5, 6] and the coordination number at the

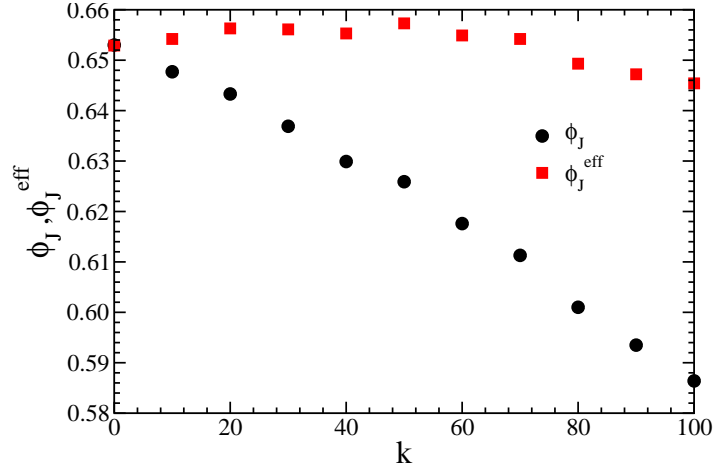


Figure 6.2: ϕ_J or ϕ_J^{eff} vs k plot. ϕ_J goes to lower volume fraction as we go to the higher k system. But ϕ_J^{eff} almost remains same with increase in k .

Table 6.1: The values of jamming volume fraction, coordination number at jamming point and their corresponding exponents are given here. ϕ_J is the volume fraction at jamming point and α is the corresponding exponent. Z_J and Z_J^{NN} are the total coordination number and coordination number with only normal neighbor respectively. β and β^{NN} are the corresponding exponents.

k	ϕ_J	α	Z_J	β	Z_J^{NN}	β^{NN}
0	0.6530	1.99	5.46	0.490	5.46	0.490
10	0.6477	1.99	5.41	0.496	5.28	0.490
20	0.6433	1.98	5.40	0.506	5.15	0.492
30	0.6369	2.00	5.46	0.529	5.09	0.514
40	0.6299	2.00	5.51	0.550	4.95	0.521
50	0.6259	1.97	5.64	0.569	4.90	0.541
60	0.6176	1.98	5.60	0.579	4.75	0.540
70	0.6113	1.99	5.51	0.578	4.52	0.530
80	0.6010	2.02	5.35	0.576	4.14	0.519
90	0.5935	1.99	5.48	0.604	4.15	0.550
100	0.5864	1.98	5.50	0.614	4.05	0.563

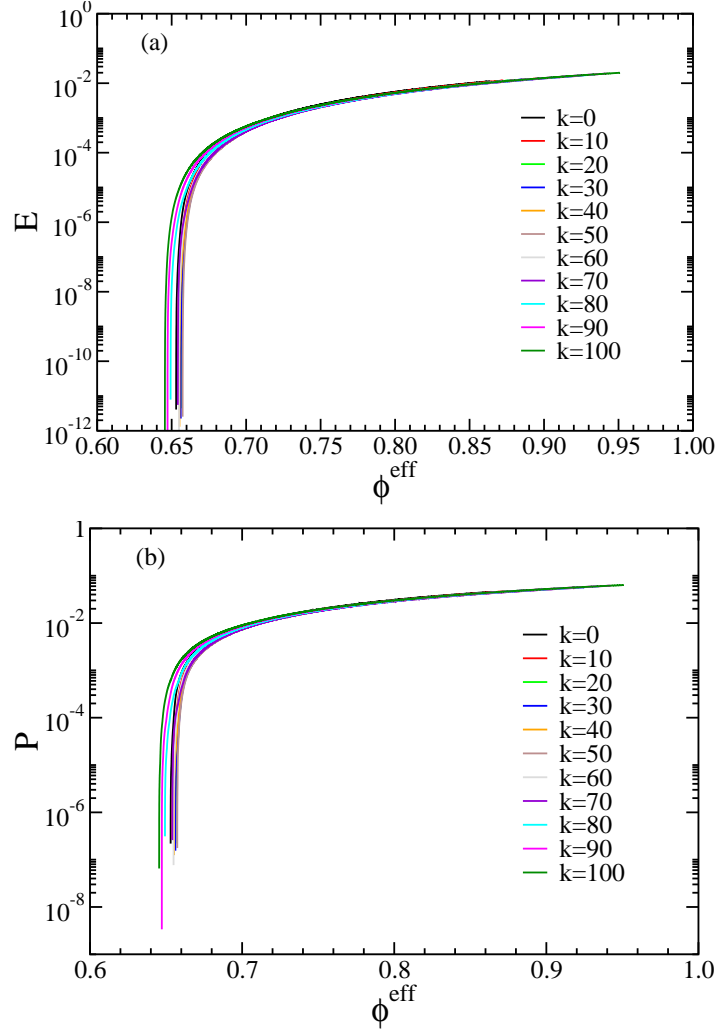


Figure 6.3: (a)Energy vs. effective Volume fraction plot for different k systems. Jamming point does not change much with increase in k . It shows close to master plot. (b) Pressure vs. effective Volume fraction plot for different k systems. It shows the similar behavior as energy plot.

jamming point in the 3-dimensional system should be 6. Another nontrivial property of the geometry in the jamming state is that the $g(r)$ diverges at the contact distance when the system is in the jammed state. $g(r)$ shows a power-law behavior near contact distance. Next, we discuss the geometry of our systems at the jamming point. Similar to the energy and pressure, we find a sudden jump in the coordination number of the particle near the jamming transition. In our systems, two types of coordination numbers are present in the system; one is the nearest neighbor coordination number (Z^{NN}), and another is the pseudo neighbor coordination number (Z^{PN}). The total coordination number in the system is defined as $Z = Z^{NN} + Z^{PN}$. Interestingly we find (Fig.6.6) that all three coordination numbers (Z, Z^{NN}, Z^{PN}) jump near ϕ_J . We estimate the total coordination number at jamming point by fitting the equation $Z - Z_J = (\phi - \phi_J)^\beta$

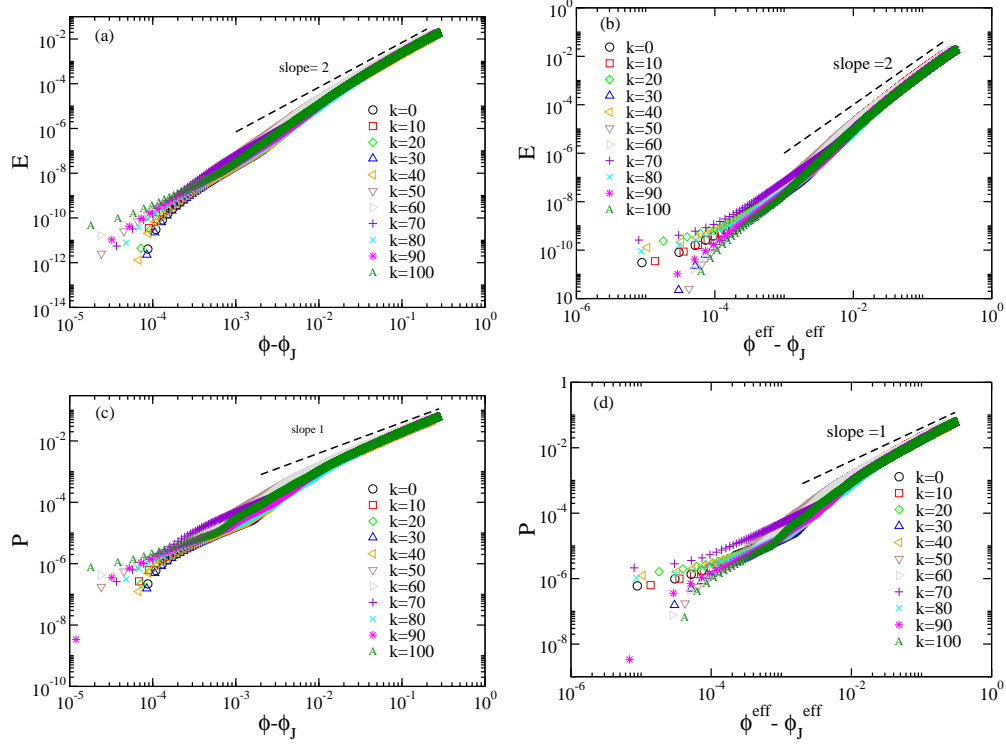


Figure 6.4: (a) Energy vs. $(\phi - \phi_J)$ plot which shows power law scaling for all k . (b) Energy vs. $(\phi - \phi_J^{\text{eff}})$ plot which shows power law scaling for all k . (c) Pressure vs. $(\phi - \phi_J)$ plot which shows power law scaling for all k . The exponent is near 1. (d) Pressure vs. $(\phi - \phi_J^{\text{eff}})$ plot which shows power law scaling for all k . The exponent is near 1

where ϕ_J is taken from the E vs ϕ fitting, Z_J and β are treated as the fitting parameter and their values are given in Table 6.1. We also plot Z against ϕ^{eff} which shows a near overlap of the lines. We find that the value of Z_J for all the systems is below 6, which is the coordination number at the isotactic condition. It is well known that at the jamming point there are rattlers in the system. Rattlers are those particles that do not have any contact. When we calculate the coordination number, we have not neglected the rattlers, and this might be the reason we get a lower coordination number at the jamming point than the coordination number at the isotactic condition, which is 6. Unlike pressure and energy, the total coordination number as shown in Fig. 6.7 does not follow the master plot. The value of the exponent increases with increasing k . Note that in a regular 3D system the coordination number can increase from 6 at the jamming point to around 13. However for mean field system due to the contribution of the pseudo neighbours this upper limit is a function of k . This leads to a sharper rise in the Z value as a function of ϕ .

We need to investigate more to find out the source of increasing the values of exponents.

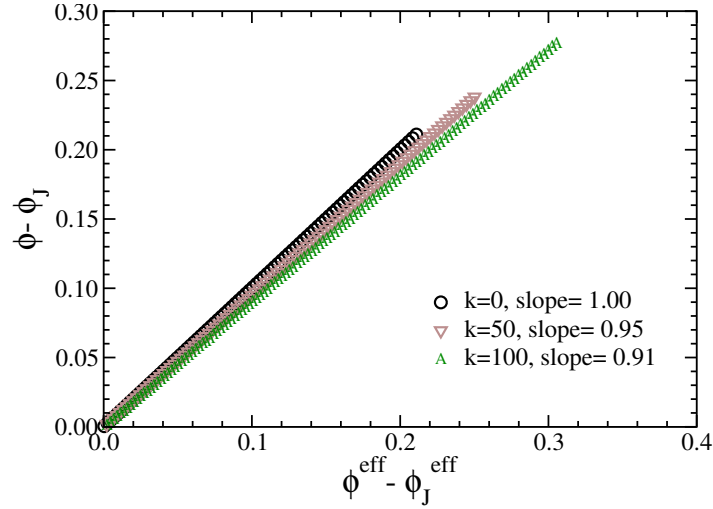


Figure 6.5: $(\phi - \phi_J)$ vs. $(\phi^{eff} - \phi_J^{eff})$ plot which shows the slope decreases with increase in k .

We have already shown (see Fig.6.2) that as the number of pseudo neighbors increases, the jamming happens at a lower volume fraction. We next analyse the role of PN in the jamming transition. To do that we obtain the Z_J^{NN} and Z_J^{PN} as a function of 'k'. Fig.6.8 shows that the contribution of regular neighbor in the coordination number at jamming point decreases with increasing k , and the contribution of the pseudo neighbor increases with increasing k . When we extrapolate the plot we get a cross over at a value of $k \simeq 136$. This implies that beyond this value of 'k', the jamming will be dominated by the pseudo neighbours.

Next we analyze the effective radial distribution function which is calculated in the same way as discussed in Chapter4. Near the jamming point we find a sharp peak of the $g_{AA}^{eff}(r)$ at the contact distance (see Fig.6.10). This $g(r)$ is plotted just below the jamming point. We also find the characteristic double peak structure near the second peak for both the $k=0$ and $k=100$ systems. In Fig.6.9 we find that all the systems show the power-law singularity near the contact distance. However the exponent appears to be k dependent. For the $k=0$ system the exponent as found earlier is 0.5 but it decreases with k . We need better statistical averaging for the $g^{eff}(r)$ analysis.

6.6 Conclusion

We investigate the jamming transition in the mean-field system using the soft repulsive harmonic potential where each particle in the system is allocated a fixed set of pseudo neighbors in addition to the normal neighbor. Pseudo particles are present outside the normal interaction range, and by design they do not interact

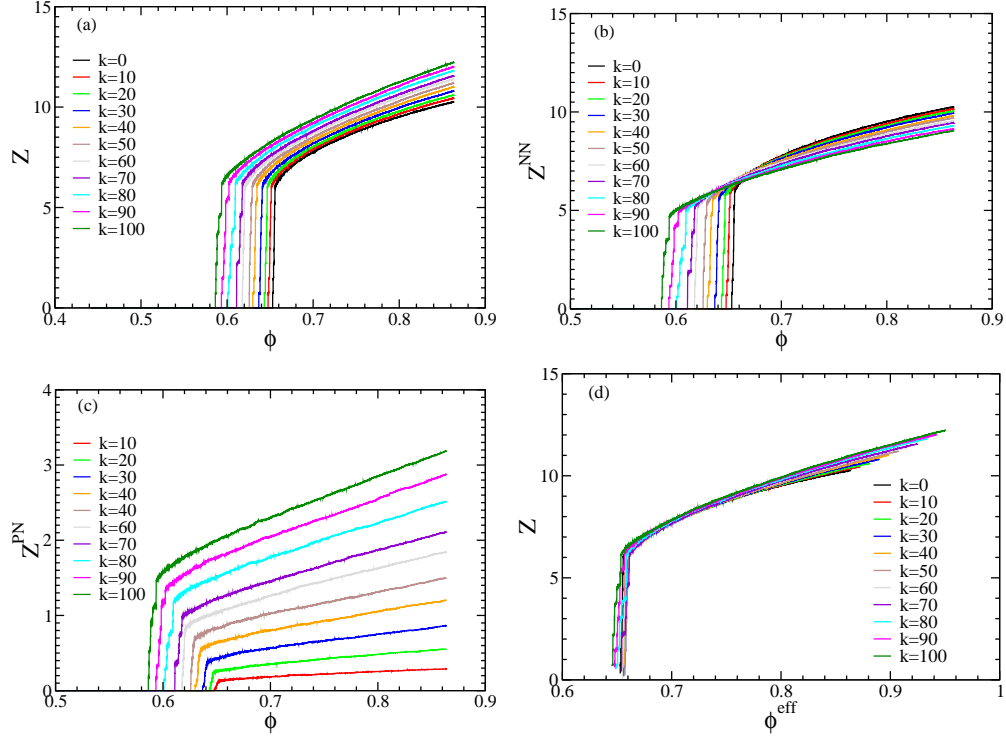


Figure 6.6: (a) Z vs. ϕ plot for all k systems. (b) Z_{NN} vs. ϕ plot for all k systems. (c) Z_{pseudo} vs. ϕ plot for all k systems. (d) Z vs. ϕ^{eff} plot for all k systems. All kinds of coordination number show jump at their respective jamming points.

with each other. We have made ten such mean-field systems with $k=10, 20, 30, 40, 50, 60, 70, 80, 90, 100$. The aim of the present study is to find how these pseudo interaction affect the jamming transition. We find that at the jamming point both energy and pressure show a jump. The value of ϕ_J is determined from the scaling behavior between energy and volume fraction. The pressure and the volume fraction also show the same ϕ_J values. We find that with increase in k ϕ_J decreases. This can be connected to the network formation because of the pseudo neighbors. When we calculate the effective volume fraction which takes into consideration the PN interaction we find that the effective jamming volume fraction remains almost constant for all the systems.

We also find that the power-law behavior of E vs $\phi - \phi_J$ and P vs $\phi - \phi_J$ remains same for all the systems. The total coordination number at the jamming point remains almost constant for all the mean-field systems. We find that at the jamming point both NN and PN contribute and with increase in the k the contribution from the former decreases whereas from the latter increases. We extrapolate the NN and PN contacts as a function of k and it appears that above $k=136$ the pseudo neighbours will dominate the jamming transition. Apart from the coordination number, another important quantity which provides the

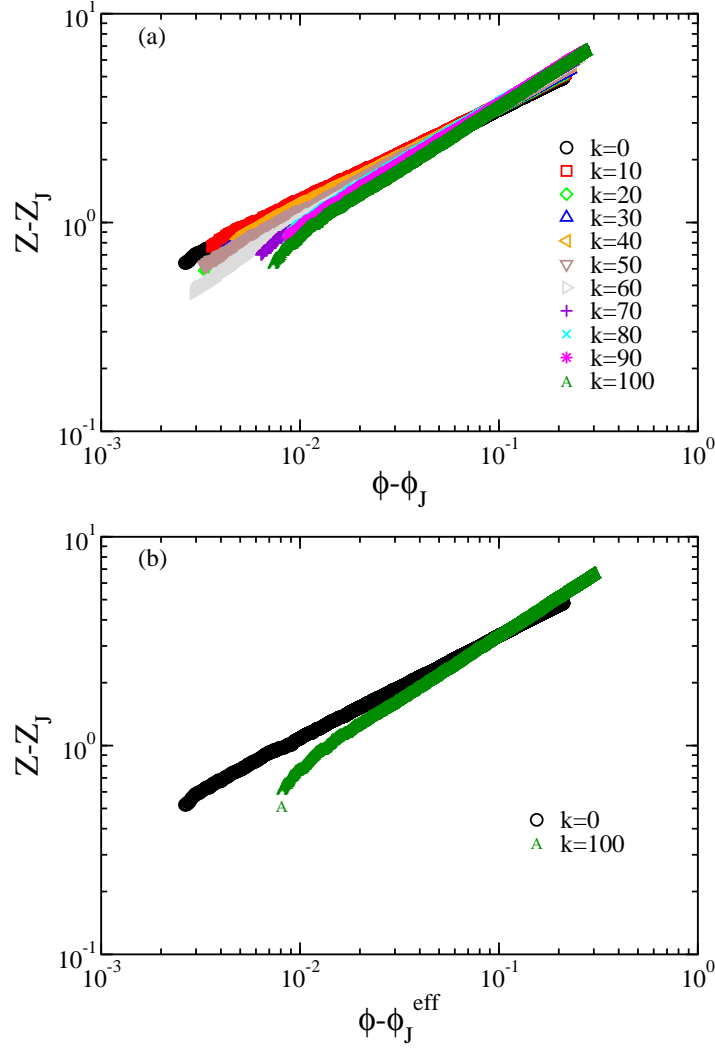


Figure 6.7: Both (a) $Z - Z_J$ vs $\phi - \phi_J$ plot and (b) $Z - Z_J$ vs $\phi - \phi_J^{\text{eff}}$ for all k systems do not show any collapse into the master plot.

information of the geometry is the $g(r)$. Near the jamming point the effective radial distribution function for both the $k=0$ and $k=100$ systems show a sharp peak at contact distance. Near the contact distance all the systems show a power-law behavior of g_{AA}^{eff} , however the exponent is a function of k . Thus we find that although most of the properties near the jamming transition is similar for all the systems the pseudo neighbours do affect values of certain exponents. We will need further investigation and better averaging to better understand the role of pseudo neighbours in the jamming transition.

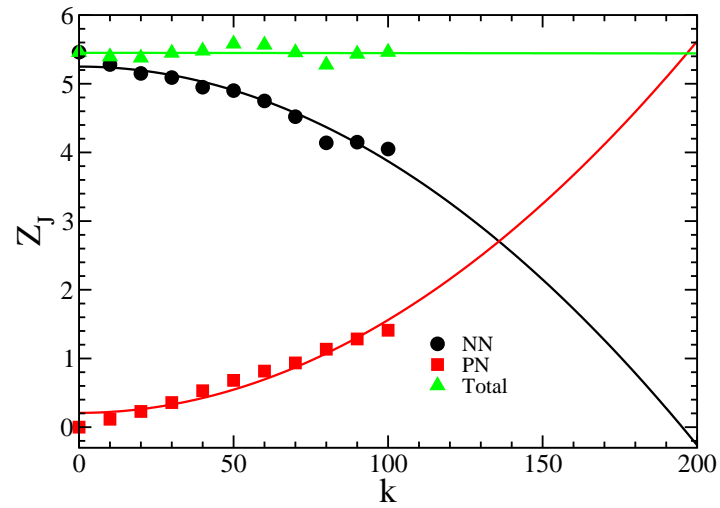


Figure 6.8: Z_J vs k plot. Regular neighbor and pseudo neighbor contributions in Z_J have been shown separately. The contribution of the regular neighbor decreases with increasing k and the contribution of the pseudo neighbor increases with increasing k .

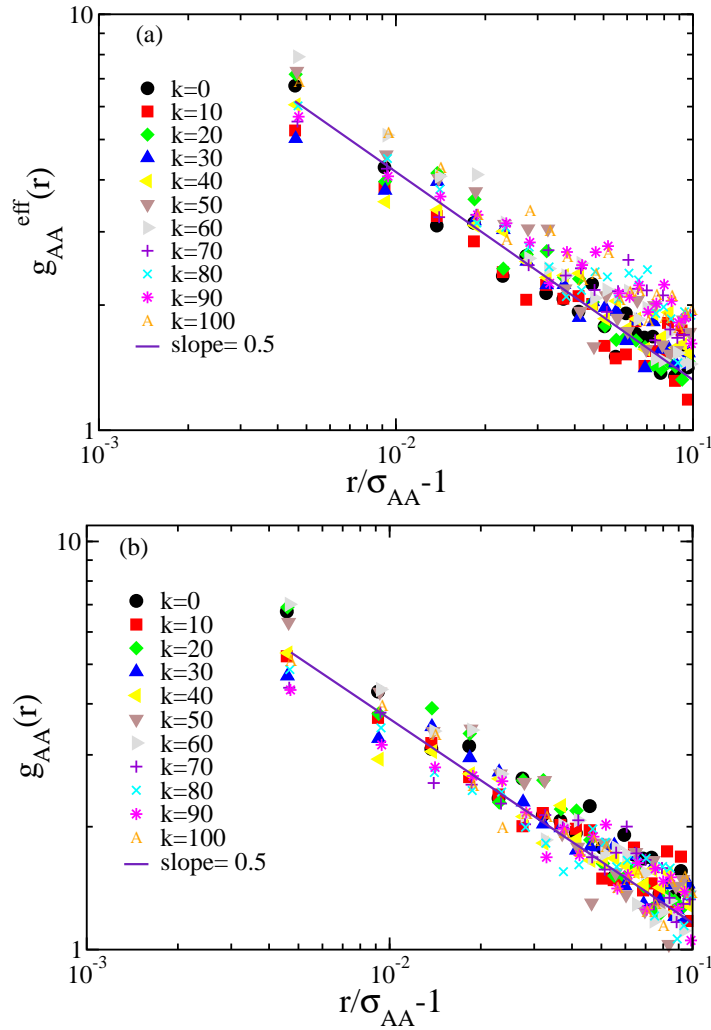


Figure 6.9: The pair correlation shows a power-law singularity near contact at jamming transition. Pair correlation function of type A particles has been considered here. It shows a spread in the data. (a) It shows the power-law in the effective radial distribution function. (b) It shows the power-law in the regular radial distribution function.

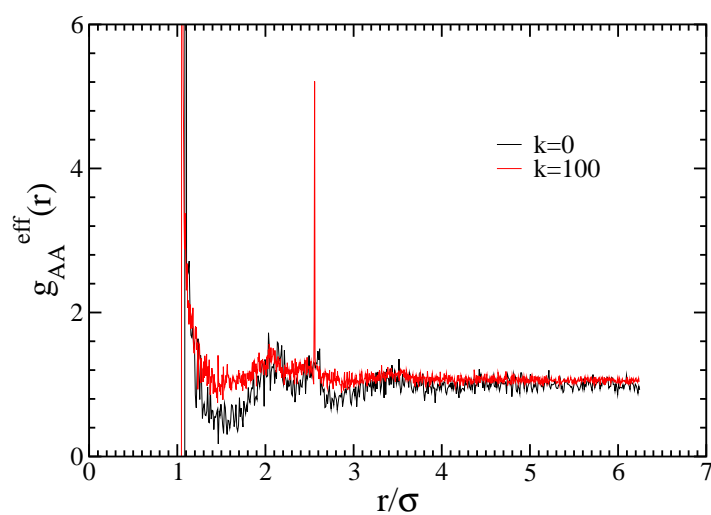


Figure 6.10: The effective radial distribution function at jamming point for $k=0$ and $k=100$ systems.

Bibliography

- [1] C. S. O'Hern, S. A. Langer, A. J. Liu, and S. R. Nagel, *Phys. Rev. Lett.* **88**, 075507 (2002).
- [2] C. Song, P. Wang, A. J. Liu, and H. A. Makse, *Nature* **453**, 629 (2008).
- [3] C. S. O'Hern, L. E. Silbert, A. J. Liu, and S. R. Nagel, *Phys. Rev. E* **68**, 011306 (2003).
- [4] P. Chaudhuri, L. Berthier, and S. Sastry, *Phys. Rev. Lett.* **104**, 165701 (2010).
- [5] C. F. Moukarzel, *Phys. Rev. Lett.* **81**, 1634 (1998).
- [6] A. V. Tkachenko and T. A. Witten, *Phys. Rev. E* **60**, 687 (1999).
- [7] A. J. Liu and S. R. Nagel, *Nature* **396**, 21 (1998).
- [8] A. Ikeda, L. Berthier, and P. Sollich, *Phys. Rev. Lett.* **109**, 018301 (2012).
- [9] U. K. Nandi, W. Kob, and S. Maitra Bhattacharyya, *The Journal of Chemical Physics* **154**, 094506 (2021).
- [10] E. Bitzek, P. Koskinen, F. Gähler, M. Moseler, and P. Gumbsch, *Phys. Rev. Lett.* **97**, 170201 (2006).
- [11] M. Pica Ciamarra, A. Coniglio, and A. de Candia, *Soft Matter* **6**, 2975 (2010).
- [12] C. F. Schreck, C. S. O'Hern, and L. E. Silbert, *Phys. Rev. E* **84**, 011305 (2011).
- [13] M. Ozawa, T. Kuroiwa, A. Ikeda, and K. Miyazaki, *AIP Conference Proceedings* **1518**, 128 (2013).
- [14] S. Alexander, *Physics Reports* **296**, 65 (1998).

Chapter 7

Composition dependence of the glass forming ability in binary mixtures: The role of demixing entropy

7.1 Introduction

A liquid upon cooling undergoes first order phase transition and forms a crystal. However if the cooling rate is increased it cannot crystallize and forms an amorphous glassy material [1]. In addition to fast supercooling, there are other methods to favor glass formation over crystallization. In bulk metallic glass community the usual rules of thumb are to at least have a two component mixture with negative enthalpy of mixing and a 12% size ratio between the components [2]. Single component systems are known to crystallize in a fcc+hcp structure [3], thus multi-component systems are commonly used for making glasses. The negative enthalpy of mixing makes sure that the components remain in a mixed state and do not demix to form single component crystals, whereas the size ratio provides frustration in packing. Although there is an array of experimental systems which form glasses, in computer simulation studies there is only a handful of systems known to be good glass formers [4, 5, 6, 7, 8]. Note that most of the glass forming systems have global crystalline minima [9, 10]. Thus depending on the barrier to crystallization it is just a matter of time for the systems to crystallize. With the increase in the available computational power some of the well known glass formers like Kob-Anderson (KA) model and Wahnstrom (WA) model are now found to partially crystallize [11, 12]. Thus in order to design better glass formers we need to be able to estimate the glass forming ability

(GFA) of these systems.

In order to quantify GFA, first we need to understand the origin of the stability against crystallization. This is an active field of research and different studies have attributed the GFA to different phenomena [13, 14, 15, 16, 17, 10, 18]. The most popular among them is the theory of frustration first proposed by Frank [13]. According to him, the local liquid ordering is different from the crystalline order and this frustrates the system and decreases the rate of crystallization. It has also been argued that regions with locally favored structures (LFS) give rise to domains and are connected to the slow dynamics in the supercooled liquids [14, 15]. Sometimes the LFS can also be related to the underlying crystalline structure [16, 17, 10]. In some cases the LFS which is connected to crystal structure grows more than the one connected to the liquid structure [17]. The LFS can vary in different dimensions. There are LFS, like the icosahedral ordering, which can cause frustration in the Euclidean space but tile the curved space [15]. Frustrations are not always structural but can also be energetic in nature [18].

Most binary equimolar mixtures form crystalline structures [19], where the crystal structure may vary according to the size ratio of the components. There are also some exceptions like the equimolar CuZr structure which is found to be a good glass former [8]. However, when the compositions of the mixtures are changed then it is usually found that close to the deep eutectic point many of them form glasses. One of the argument in favor of the deep eutectic point being a good glass forming zone is that the viscosity is highest at this point so kinetically it takes a longer time to form a crystal nucleus. However it has also been shown that the structural frustration between two different crystal structures can make this region a good glass former. This kind of phase diagram (in temperature vs. composition space) is often referred to as V-shaped phase diagram where the bottom of the V is the glass forming region [20, 21, 22, 23, 25].

In a recent work by some of us we have shown that even though all the systems at equimolar mixture undergo crystallization, as the composition of the larger size particles increases, the zone which forms CsCl crystal at equimolar composition does not crystallize any more [25]. It is already known from the study of energetics that the global free energy minima of these systems are CsCl+fcc crystals [9]. The well known KA glass former is one of the systems present in this more generic CsCl zone. So far only in one study it has been reported to crystallize but in a structure which is different from that of the global minimum [11]. In the earlier study we have shown that in the CsCl+fcc crystal structure the bigger “A” particles need to have two different populations where there is a large difference in the order parameter (coordination number

and bond orientational order parameter) of these two populations. According to us, this large difference in order parameter creates frustration. Note that in this system the LFS is bicapped square anti prism which is structurally quite close to CsCl[24]. Thus unlike systems discussed earlier where the geometric frustration is between icosahedral and fcc structure [14, 15, 17], in this system it is between CsCl and fcc structure which stabilizes it against crystallization [25].

In this present work we study a similar series of binary systems by changing the composition and also the inter species interaction length. Many of the binary systems studied here are good glass formers and have a global minima which is CsCl+fcc structure. Thus according to our earlier study the structural frustration for these systems are similar. However, these systems are expected to have different glass forming ability. The goal of this work is to get a relative estimate of the GFA of different systems and then explore the origin of their differences. Our study shows that the free energy cost for CsCl crystallization increases with the composition of the smaller particles. The system with lowest free energy cost also shows a pre-crystalline demixing in the liquid phase near the liquid/crystal interface. The demixing takes place due to the structural frustration between the CsCl and fcc structures. Upto a certain composition, the composition dependence of the free energy cost to create a crystal nucleus can be related to the composition dependence of this demixing entropy. Our study of energetics shows that although in the whole range of composition the global minima is CsCl+fcc crystal the driving force of crystallization in a certain region is the CsCl crystal and in another region is fcc crystal. In the former region the system tends to demix and form CsCl+fcc crystal and demixing frustrates the crystallization process. However, in the latter region we show that demixing does not play a crucial role. It is primarily the slow dynamics near eutectic point and LFS around the smaller “B” particles which frustrate the crystallization process.

The simulation details are given in the next section. In section III we present the definition and method for evaluating different quantities, in section IV we have the results and discussion, and section V ends with a brief summary.

7.2 Simulation Details

The atomistic models which are simulated are two component mixtures of classical particles (larger “A” and smaller “B” type), where particles of type i interact with those of type j with pair potential, $U_{ij}(r)$, where r is the distance between the pair. $U_{ij}(r)$ is described by a shifted and truncated Lennard-Jones (LJ)

potential, as given by:

$$U_{ij}(r) = \begin{cases} U_{ij}^{(LJ)}(r; \sigma_{ij}, \epsilon_{ij}) - U_{ij}^{(LJ)}(r_{ij}^{(c)}; \sigma_{ij}, \epsilon_{ij}), & r \leq r_{ij}^{(c)} \\ 0, & r > r_{ij}^{(c)} \end{cases} \quad (7.1)$$

where $U_{ij}^{(LJ)}(r; \sigma_{ij}, \epsilon_{ij}) = 4\epsilon_{ij}[(\sigma_{ij}/r)^{12} - (\sigma_{ij}/r)^6]$ and $r_{ij}^{(c)} = 2.5\sigma_{ij}$. Subsequently, we'll denote A and B types of particles by indices 1 and 2, respectively.

The different models are distinguished by different choices of lengths and composition parameters. Length, temperature and time are given in units of σ_{11} , $k_B T/\epsilon_{11}$ and $\sqrt{(m_1\sigma_{11}^2/\epsilon_{11})}$, respectively. Here we have simulated various binary mixtures with the interaction parameters $\sigma_{11} = 1$, $\sigma_{22} = 0.88$, $\epsilon_{11} = 1$, $\epsilon_{12} = 1.5$, $\epsilon_{22} = 0.5$, $m_1 = m_2 = 1$ and the inter-species interaction length $\sigma_{12} = 0.7, 0.8$. In some cases we have used the symbol S , where $S = \sigma_{12}/\sigma_{11}$. We have simulated systems with different compositions, varying x_B from 0.50 to 0.0, where x_B is the mole fraction of the smaller B type particles [11, 26].

The molecular dynamics (MD) simulations have been carried out using the LAMMPS package [27]. We have performed MD simulations in the isothermal isobaric ensemble (NPT) using Nosé-Hoover thermostat and Nosé-Hoover barostat with integration timestep 0.005τ . The time constants for Nosé-Hoover thermostat and barostat are taken to be 100 and 1000 timesteps, respectively. Except for the liquid/crystal interface study where we use a rectangular box, all of the other studies are performed in a cubic box with periodic boundary condition. The free energy barrier calculations are done via biased Monte Carlo method. All the studies are performed at $P = 0.5$.

7.3 Definitions

7.3.1 Bond Orientational Order Parameter

Bond Orientational Order (BOO) parameter was first prescribed by Steinhardt *et al.* to characterize specific crystalline structures [28]. To characterize specific crystal structures we have calculated the locally averaged BOO parameters (\bar{q}_{lm}) of l -fold symmetry as a $2l+1$ vector, [29]

$$\bar{q}_l = \sqrt{\frac{4\pi}{2l+1} \sum_{m=-l}^l |\bar{q}_{lm}|^2} \quad (7.2)$$

where

$$\bar{q}_{lm}(i) = \frac{1}{\tilde{N}_i} \sum_0^{\tilde{N}_i} q_{lm}(k). \quad (7.3)$$

Here \tilde{N}_i is the number of neighbours of the i -th particle and the particle i itself. $q_{lm}(i)$ is the local BOO of the i -th particle.

$$q_{lm}(i) = \frac{1}{N_i} \sum_0^{N_i} Y_{lm}(\theta(r_{ij}), \phi(r_{ij})) \quad (7.4)$$

where Y_{lm} are the spherical harmonics, $\theta(r_{ij})$ and $\phi(r_{ij})$ are spherical coordinates of a bond r_{ij} in a fixed reference frame, and N_i is the number of neighbours of the i -th particles. Two particles are considered neighbours if $r_{ij} < r_{min}$, where r_{min} is the first minimum of the radial distribution function (RDF). For the liquids and the crystals the r_{min} has been chosen as the first minima of the respective partial RDF of the ‘‘A’’ type of particles. For the pure CsCl crystal this comprises of 14 neighbours and for fcc 12 neighbours.

In Fig.7.1 we plot the probability distribution of \bar{q}_6 of the liquid at three different composition and also the same for pure CsCl and fcc crystals. We note that at the level of this parameter all the three liquids can be clearly separated from the two different crystal forms.

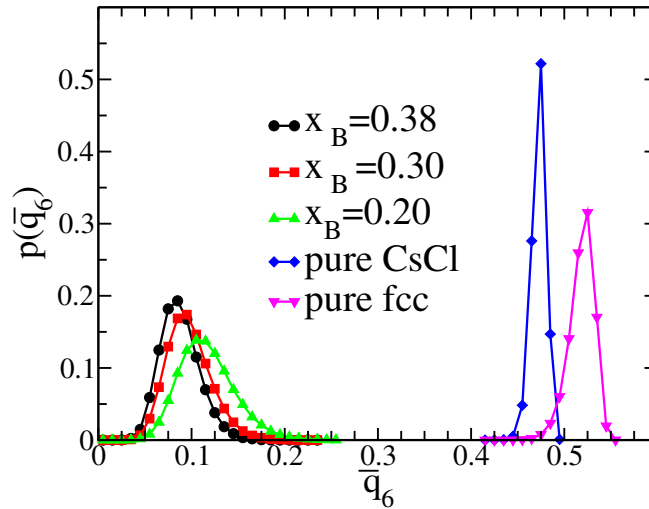


Figure 7.1: The probability distribution of the locally averaged BOO, \bar{q}_6 for the liquid at three different compositions $x_B = 0.38, 0.3, 0.2$ at $T = 0.5$. We also plot the same for the CsCl crystal made up of ‘‘A’’ and ‘‘B’’ type of particles and pure fcc made up of ‘‘A’’ particles.

7.3.2 Relaxation Time

We have calculated the relaxation times obtained from the decay of the overlap function $q(t)$, where $q(t = \tau_\alpha, T)/N = 1/e$ which is explained in chapter 2.

7.4 Results

7.4.1 Melting Temperatures

In order to calculate the crystallization rate and thus the glass forming ability we first determine the melting temperatures of the different crystals. The melting temperature is studied by calculating the temperature dependent growth/melting rate of the crystal and fitting them to a straight line. The temperature at which the growth rate cuts the temperature axis is the predicted melting temperature where the growth rate goes to zero [10]. The simulations are done at $P = 0.5$. With the crystal at the center of the box and the crystal particles being pinned the liquid of 8000 particles is equilibrated at $T=1.5$. The system is then quenched to the target lower temperatures and the crystal particles are unpinned. We then run a short equilibration of 1000 steps for the quenched system. Depending on the temperature and the composition of the liquid the central seed either grows or melts. In the $x_B = 0.38$ and 0.3 systems we study the melting temperature of CsCl crystal with an initial crystal seed of 432 particles. In the $x_B = 0.2$ mixture we study the melting temperature of the pure fcc crystal comprising of 500 ‘‘A’’ particles. The growth of the seed is monitored by cluster analysis where the \bar{q}_6 is calculated for each particle and if the value of $\bar{q}_6 > 0.3$ (Fig.7.1) and it has a neighbour which is part of the existing cluster then it is included in the cluster. The cluster growth is monitored for about 100-500 τ_α , where τ_α is the temperature dependent α relaxation time that varies across different systems. 5-10 independent runs are generated at each temperature by starting from the same initial configuration but randomized initial velocity. The growth rate is calculated by scaling the time w.r.t the corresponding τ_α . From the average growth/decay rate we approximate the melting temperature as the temperature where the predicted growth or decay rate is zero (Fig.7.2). The melting points obtained from Fig.7.2 is used to construct the composition dependent phase diagram reported in Fig.7.3.

We find that the $x_B = 0.38$ mixture phase separates and forms a CsCl+fcc crystal structure (Fig.7.4a). The $x_B = 0.3$ mixture also shows similar tendency however the crystal growth rate is slower and within our simulation timescale the demixing is not complete. We also try to grow the CsCl crystal in the $x_B = 0.2$ mixture but we find that instead of CsCl, fcc structure of ‘‘A’’ particles grow

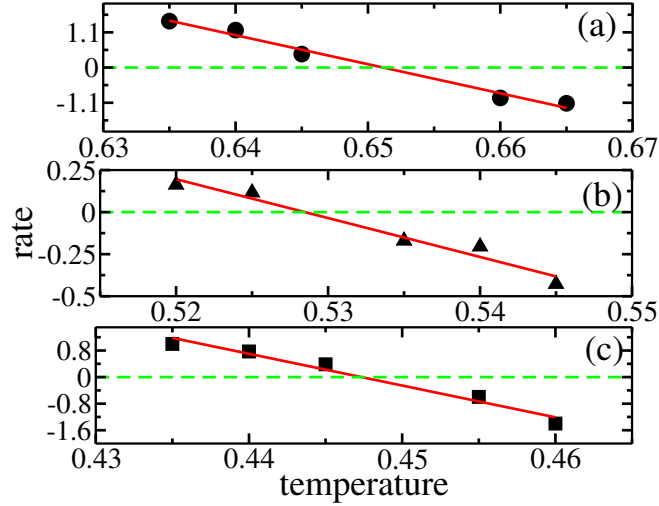


Figure 7.2: The growth rate (negative for melting) of the pure CsCl/fcc crystal as a function of temperature for different compositions: (a) CsCl in $x_B = 0.38$ system, the predicted melting temperature (T_m) is 0.651. (b) CsCl in $x_B = 0.3$, $T_m = 0.528$. (c) fcc in $x_B = 0.2$, $T_m = 0.447$.

around the initial seed (Fig.7.4b). This is similar to the observation reported earlier [31]. When a fcc seed is inserted in the same mixture it continues to grow.

In the above mentioned method it is not possible to calculate the melting temperature of the mixed CsCl+fcc crystal as the growth of such crystal never happens within our simulation timescale. For this calculation at each composition ($x_B = 0.05 - 0.5$) we heat the mixed crystal (CsCl+fcc) starting from temperature 0.2-0.3 and increase it up to 0.59-1.0 (depending on the melting temperature of the crystal) with temperature interval of 0.05. Closer to the melting temperature heating is done with 0.01 temperature interval. At each temperature equilibration is done for 10^7 steps. The size of the initial crystal structure is in the range of 468-612. The total number of particles are chosen in such a way that a perfect mixed crystal can be created. Periodic boundary condition is applied in all directions. Similar study is done for the pure and distorted fcc crystal for $x_B = 0.0, 0.1, 0.2$ systems. For $x_B = 0.0$ we get pure fcc and for $x_B = 0.05$ and 0.1 the “A” particles form fcc crystal but with distortion due to presence of the “B” particles. In the $x_B = 0.2$ system within our simulation run we do not observe the formation of the fcc crystal. However as reported earlier in a MKA2 model, if the interaction between the two species is reduced, then the system forms crystal [11]. In a similar method by keeping the $\epsilon_{12} = 0.96$ we first form a distorted fcc crystal of the $x_B = 0.2$ system. Once the crystal is formed we switch back to the larger inter species interaction of $\epsilon_{12} = 1.5$ and study its melting. The melting of all the crystals happens instantaneously. The

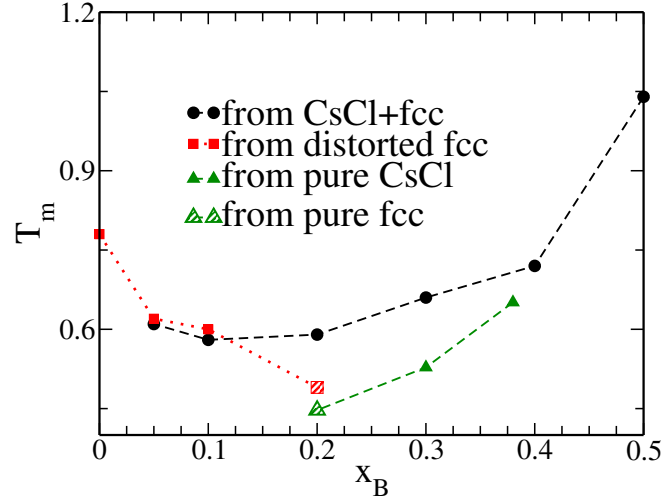


Figure 7.3: The melting temperatures of different crystal forms in different binary mixtures. The melting temperature for the pure fcc and CsCl crystal is obtained by studying the growth/melt rate of the crystal. The melting temperature is where the predicted rate disappears (see Fig 7.2). The melting temperature of the mixed CsCl+fcc crystal and the distorted fcc crystal are obtained by step wise heating the system.

melting temperatures are reported in Fig.7.3.

7.4.2 Free Energy of Nucleation and Role of Demixing

In this section we perform a comparative study of the Gibbs free energy (potential of mean force) of crystalline nucleation/growth in different binary mixtures using umbrella sampling technique with the reaction coordinate being the size of the largest crystalline cluster present in the system. The studies are performed at the same degree of undercooling at $0.8T_m$, where the melting temperatures used are those calculated by studying the temperature dependent growth/melting rate for the pure CsCl and fcc crystals. A crystalline cluster is defined by a neighborhood criteria (within a cut-off distance determined by the first minimum of the partial radial distribution of function of “A”-type particles for respective systems) of “crystal-like” particles (with the criterion of $\bar{q}_6 > 0.3$). To grow the clusters we use a biased Monte Carlo approach, where we apply an external harmonic potential of the form $\frac{1}{2}k(n - n_c)^2$, where k is the force constant, n is the number of particles in the largest cluster, and n_c is the position of the bias window. We use $k = 0.1$ for $x_B = 0.38$, and $k = 0.2$ for $x_B = 0.30$ and $x_B = 0.20$. We have used 5-7 umbrella windows (depending on the system) in the cluster size range of 15-35. After equilibration, the data is collected for 10^4 Monte Carlo steps per window and Weighted Histogram Analysis method (WHAM)[32] is then used to compute the free energy as a function of the size

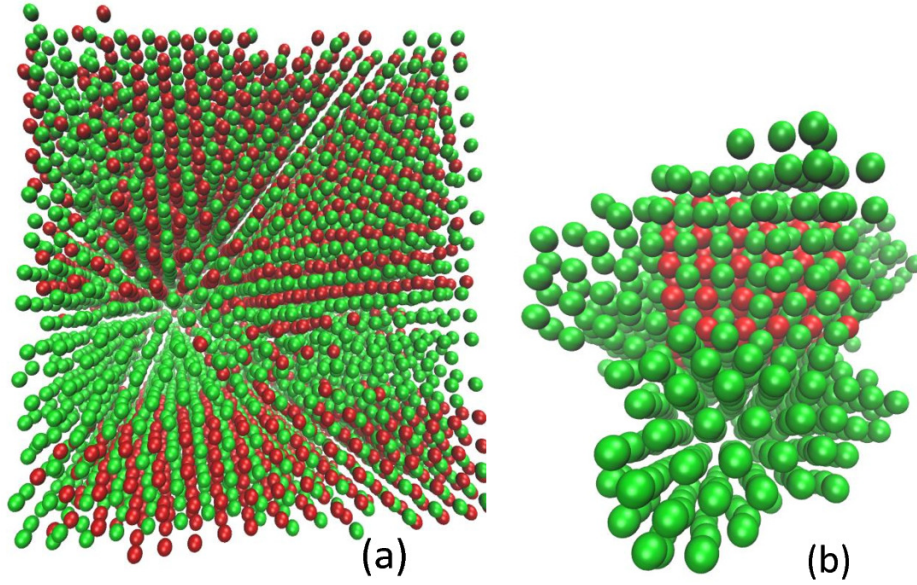


Figure 7.4: (a) Snapshot of the $x_B = 0.38$ system after 10^7 steps post quench at temperature 0.52. The system shows clear demixing and grows into CsCl+fcc crystal. (b) Snapshot of the initial seed and the cluster that has grown around it for $x_B = 0.2$ system after 2×10^7 steps post quench at temperature 0.4. Around the CsCl seed we find the growth of fcc crystal of “A” particles. For both the systems the initial CsCl crystal seed consists of 432 particles which is inserted in a liquid of 8000 particles.

of the largest cluster as reported in Fig.7.5.

While our calculations focus on the pre-critical region of the free energy surfaces, we can compare the relative free energy cost to form a crystalline nucleus of certain size as the composition of the system is varied. We observe that the free energy cost to grow a nucleus from 15 to 35 for all the systems are quite high (in the range of $10-20 k_B T$), which explains why all these systems are good glass formers. A comparative study of the cost of free energy shows that $x_B = 0.38$ has a lower cost to grow a CsCl crystal compared to $x_B = 0.3$. This explains the slow growth of the CsCl crystal in the latter system which is observed during the melting study. We also try to grow CsCl crystal for $x_B = 0.2$, which we do not observe during our simulation time. This implies that the free energy cost for CsCl crystal growth in this system is even larger. However, similar to the melting study the crystal that grows around the initial CsCl cluster in the $x_B = 0.2$ system is made up of only “A” particles. Next we study the free energy cost for fcc crystallization in $x_B = 0.2$ system. We find that the free energy cost to grow a fcc crystal from 15-35 cluster size in $x_B = 0.2$ system is lower than the free energy cost to grow a similar size range CsCl crystal for $x_B = 0.3$. This implies that in the $x_B = 0.2$ system the free

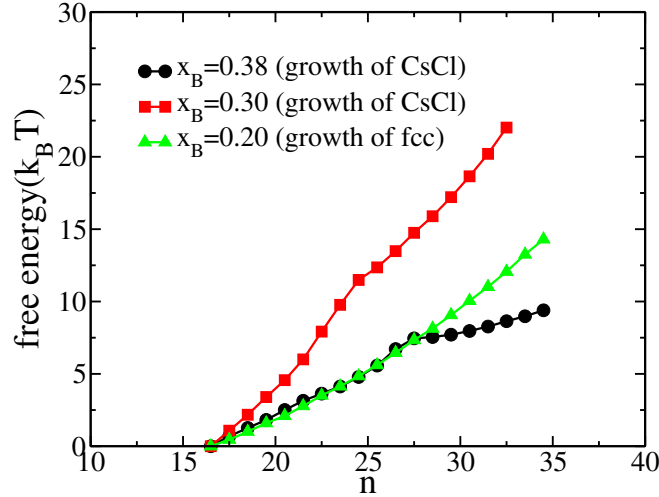


Figure 7.5: Gibbs free energy for crystallization as obtained from the umbrella sampling simulations as a function of the largest cluster size for the three systems. For $x_B = 0.38$ and 0.3 we can grow the CsCl cluster, whereas for $x_B = 0.2$ we can only grow the fcc cluster. Even with a initial small CsCl seed the cluster that grows consists of “A” particles forming fcc lattice which is similar to that we find for melting study.

energy cost for fcc crystallization is lower than the CsCl crystallization. Note that although we make this comparative statement we are unable to determine the free energy cost for growing a CsCl crystal in the $x_B = 0.2$ which leads us to believe that the cost must be very high.

We next analyze the origin of the difference in the free energy cost to grow a CsCl crystal in different systems. In a recent study of crystallization in $Pd - Ag$ mixture it has been found that the barrier to crystallization for the mixed system is about $10K_B T$ higher than the pure system [33]. The Pd and the Ag have a small difference in their sizes and form fcc crystal structure. Thus unlike structural frustration between the CsCl and fcc crystal present in the systems studied here [31, 25] there exists no structural frustration in the $Pd - Ag$ system. However due to higher $Pd - Pd$ interaction the crystal nucleus for the $Pd - Ag$ system has a higher concentration of the Pd molecules compared to that in the bulk. This leads to demixing in the system and the authors have concluded that this demixing leads to higher barrier. In a separate study it is shown that the phase that nucleates easily is the one which has composition closer to the liquid [34]. In this present study we note that in the CsCl crystallization process, except for the equimolar mixture the composition of the nucleus is different from that of the liquid. The difference increases as we go towards smaller x_B values. Thus it is obvious that the growth of CsCl crystal leads to demixing in the system. However, we would like to investigate if signature of demixing is present in the liquid which surrounds the crystal.

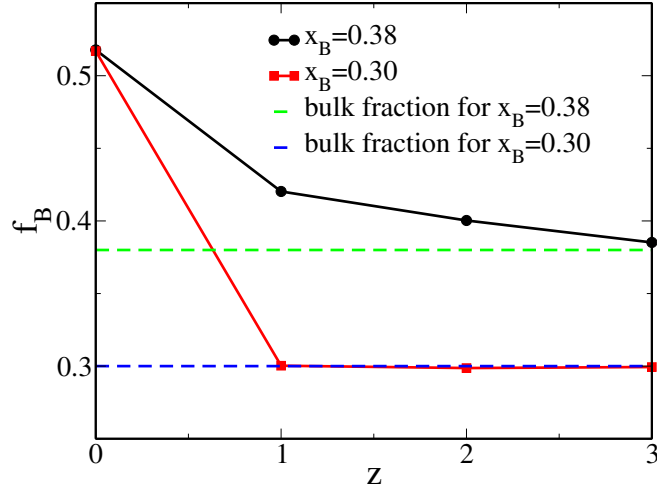


Figure 7.6: Distance dependence of the composition from the liquid/crystal interface along the perpendicular direction. We plot the fraction of “B” particles, f_B , as obtained within each slab of width one σ_{11} as a function of the distance from the interface. The interface that has “A” particles is taken and the plot is done for $x_B = 0.38$ and $x_B = 0.3$. We find that for the former system where the initial rate of crystallization is higher the interface has higher concentration of “B” particles compared to the bulk. Thus there is pre-crystalline demixing in the liquid phase.

In a recent study it has been shown that the liquid in the crystal/liquid interface shows some compositional ordering [8]. In a similar spirit we now look at the crystal/liquid interface and investigate if the demixing takes place in the pre-crystalline liquid. For this study we perform NP_ZT calculation in a rectangular box where $P_Z = 0.5$. Initially the system consists of 432 CsCl crystal particles (equal amount of “A” and “B” particles) and 864 liquid particles. The 010 layer of the crystal faces the liquid where the last layer of the crystal on one side has “A” particles and on the other side has “B” particles. The box length in the x and y direction is $6.92\sigma_{11}$. The box length in the z direction is $20.76\sigma_{11}$. Periodic boundary condition is applied in all directions. Since we want to study the interface property it is important not to have a rugged interface. Thus the study is performed above the melting temperature of the pure CsCl crystal in the respective liquid ($1.2T_m$) by pinning the crystal particles. Although performed above the melting temperature while equilibrating the $x_B = 0.38$ system we find the growth of a layer of particles on both sides of the crystal. In the analysis we consider these two layers, which are not pinned, to be part of the crystal. Thus for this system after equilibration there are 504 crystal particles and 792 liquid particles. The liquid particles span over more than $13\sigma_{11}$ distance which makes it possible to study both the interfacial and bulk properties of the liquid. For the $x_B = 0.3$ system an extra layer of “A” particles grow on the surface which has “B” particles facing the liquid. Due to the scarcity of “B” particles no extra “B”

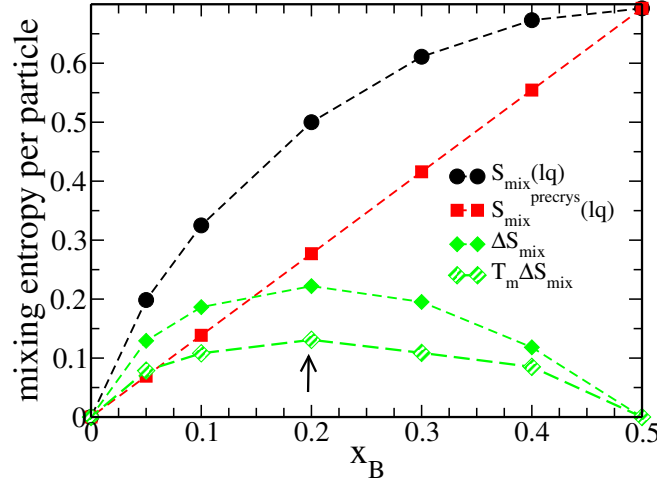


Figure 7.7: The mixing entropy of the liquid, $S_{mix}(lq)$, that of the partially demixed pre-crystalline liquid $S_{mix}^{precryst}(lq)$ and the difference between them ΔS_{mix} plotted at different compositions. We also plot the $T_m \Delta S_{mix}$ where T_m is the melting temperature of the mixed CsCl+fcc crystal. The ΔS_{mix} shows a non monotonic composition dependence with a maximum around $x_B = 0.2$.

layer grows on the other side. In this analysis we consider the surface where the extra layer of “A” particle has grown. We calculate the fraction of “B” particles, f_B , within each slab of width $1\sigma_{11}$, as a function of distance from the interface (Fig.7.6). The first point ($z=0$) in this plot is taken within the crystal which for the both the systems show same value of f_B . Interestingly we find that for the $x_B = 0.38$ system the concentration of the “B” particles are higher at the interface and it gradually reaches the bulk value around $z=4$. However for $x_B = 0.3$ system the concentration of the “B” particles are same at the interface and at the bulk. Thus we show that the liquid which has a lower free energy cost for crystal growth also undergoes a pre-crystalline demixing in the liquid phase. Similar to the earlier study [8] we find that the liquid/crystal interface properties differ for apparently similar systems with different glass forming ability.

Thus we show that the process of crystallization requires demixing which takes place in the pre-crystalline liquid. We now analyze the role of demixing in the free energy barrier. Note that the per particle mixing entropy in a liquid can be written as,

$$S_{mix}(lq) = - \sum x_i \ln x_i \quad (7.5)$$

where x_i is the mole fraction of the components. To form CsCl+fcc crystal the liquid needs to demix. We show here that the demixing takes place in a liquid state (refer to Fig.7.6). Although the demixing process happens step wise here we calculate the total effect of demixing. Thus we consider that to form a CsCl+fcc crystal, part of the liquid needs to form a equimolar mixture and the

other part should have pure ‘‘A’’ particles. Thus the per particle mixing entropy in the pre-crystalline partially demixed liquid should be,

$$S_{mix}^{precryst}(lq) = -2.0x_B \sum x_i \ln x_i \quad (7.6)$$

The difference between these two entropies, $\Delta S_{mix} = S_{mix}(lq) - S_{mix}^{precryst}(lq)$, is the mixing entropy at per particle level that a liquid will loose in the process of partial demixing. ΔS_{mix} as a function of x_B is shown in Fig.7.7 which shows a non-monotonic behaviour with a maximum around $x_B \simeq 0.2$. Note that this kind of non monotonic behaviour is obtained in the free energy barrier to crystallization for the *Pd – Ag* mixture which as discussed earlier is attributed to the demixing process[33]. Thus our demixing entropy study can explain the increase in the free energy cost for CsCl crystal growth with decrease in x_B till it reaches a value of 0.2. However this study does not explain why in the $x_B = 0.2$ system where CsCl+fcc is the global minima, the free energy cost for fcc crystallization is much lower than the cost for CsCl crystallization, the latter being so high that an estimation of it is beyond the scope of the present study.

7.4.3 Analysis from Energetics

In order to understand the origin of lower free energy cost for fcc crystallization we analyze the role of different crystal structures in crystallization by studying the energetics. In Fig.7.8a we plot the energy per particle of the liquid, the mixed crystal, the fcc crystal and the CsCl crystal for different compositions at 0.8 times the melting temperature of their respective mixed crystals (given in Fig.7.3). This is the melting temperature which has been obtained by step wise heating the mixed crystal. We find that the energy of the mixed crystal is always lower than the supercooled liquid, which implies that the liquid is in a metastable state. The energy of the CsCl crystal is always lower than the liquid. However for higher x_B values the energy of the fcc crystal is above the liquid and at lower x_B values although it becomes less than the liquid it is always higher than the CsCl value. This would imply that the CsCl crystal always drives the crystallization process. However this does not explain why both in the melting study and the free energy barrier calculation at $x_B = 0.2$ although we can not grow CsCl crystal we can grow fcc crystals. Our subsequent analysis will explain this discrepancy.

Next we make an estimation of energy of the mixed crystal, $E_{CsCl+fcc}(est)$, at the per particle level, at different compositions by assuming that $2x_B$ of the crystal forms CsCl and the rest forms fcc.

$$\begin{aligned}
E_{CsCl+fcc}(est) &= E_{CsCl}(est) + E_{fcc}(est) \\
&= 2x_B E_{CsCl} + (x_A - x_B) E_{fcc}
\end{aligned} \tag{7.7}$$

Here E_{CsCl} and E_{fcc} are the energy of the CsCl and fcc crystal respectively, at per particle level calculated for each system at their respective $0.8T_m$. $E_{CsCl}(est)$ and $E_{fcc}(est)$ are the estimated contribution from the respective CsCl and fcc crystal part of the mixed crystal again presented at the per particle level. Note that the values of $E_{CsCl}(est)$ and $E_{fcc}(est)$ take into account the fraction of the system which is in different crystal form. In this calculation we of course make certain approximations by neglecting the surface energy. However we find that the value of energy per particle of the mixed crystal thus calculated is not too different from the value of the actual crystal (Fig.7.8b). These are again calculated at the same temperatures as reported in Fig.7.8a. We now break up the contribution of the two components, the contribution from CsCl and that from fcc and plot them separately. Once we do that we find that although at higher x_B values the CsCl formation drives the crystallization, at lower x_B values it is the fcc formation which drives the crystallization. Although the energy per particle of the fcc crystal is still lower than that of the CsCl, the larger fraction of the fcc crystal wins over. A cross over happens just above $x_B = 0.2$. This explains why the system at $x_B = 0.2$, whose global minima is the mixed crystal, shows higher tendency towards fcc formation.

However, this does not explain why the the crystallization process when driven by fcc formation has a lower free energy cost than when driven by CsCl formation. In order to understand this, we study the coordination number between the “B” particles, CN_{BB} in the $x_B = 0.2$ system, before and after crystallization. Since we cannot crystallize the $x_B = 0.2$ system we study the crystallization of the MKA2 model (referred earlier in the melting temperature study) which according to Dyre and coworkers is similar in structure as the KA model but with a lower viscosity [11]. Confirming their conclusion we find that the LFS of the MKA2 model appears quite similar to the KA model however the dynamics is orders of magnitude faster. We now analyze the CN_{BB} as obtained in the MKA2 system when it is in liquid form at $T = 0.4$ and when it forms distorted fcc crystal around $T = 0.35$. These are plotted in Fig.7.9. For comparison we also plot the CN_{BB} for the pure CsCl+fcc crystal at $T = 0.4$. Note that the probability distribution of CN_{BB} in the CsCl+fcc crystal should ideally have a peak at 6 but the peak is shifted to smaller value due to the presence of a large number of surface layer of “B” particles. The study shows

that to form distorted fcc crystal although there is an increase in the CN_{BB} it is not as much as required for the CsCl+fcc crystal. Thus demixing in the distorted fcc is much weaker than CsCl+fcc. Analysis of the same kind for the $x_B = 0.9$ system (not shown here) shows similar behaviour.

Thus on the right hand side of the crossover where CsCl drives the crystallization there should be free energy barriers due to demixing. However on the left hand side the system can avoid or reduce the loss of mixing entropy by paying some energetic penalty to form distorted crystals. The lower energetic stability of the distorted fcc is evident from Fig.7.3. We find that for $x_B = 0.2$ the disordered fcc structure melts at a lower temperature compared to the mixed CsCl+fcc structure.

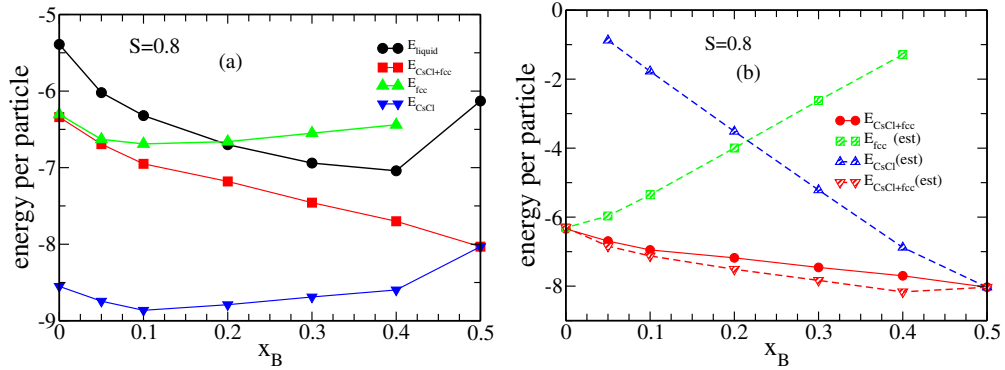


Figure 7.8: (a) The energy per particle of the liquid, mixed crystal (CsCl+fcc), CsCl crystal and fcc crystal for different compositions. The calculations are done at $0.8T_m$ of each composition, where T_m is the melting temperature obtained by heating the different mixed crystals. (b) The energy of the mixed crystal, the estimated energy of the mixed crystal, $E_{CsCl+fcc}(est)$, the estimated contribution from the CsCl part, $E_{CsCl}(est)$, and that from the fcc part, $E_{fcc}(est)$, as a function of composition. The calculations are done at same temperature as in (a).

In order to strengthen our argument that it is indeed the demixing that frustrates the CsCl driven crystallization process and leads to high free energy cost, we present a study of a similar system. Reported in an earlier study by some of us we have shown that for the NaCl system ($\sigma_{12} = 0.7$) the crystallization takes place not only at equimolar composition but also at smaller value of x_B forming mixed NaCl+fcc crystal [25]. A similar energetic study of the $\sigma_{12} = 0.7$ system is shown in Fig.7.10a. We find that energy of the NaCl crystal is always lower than the fcc crystal (Fig.7.10a). A similar crossover is also obtained for this system where at higher x_B values the crystallization is driven by NaCl and at lower x_B values it is driven by fcc (Fig.7.10b). Thus we should expect a similar crystallization problem in this system which appears not to be the case.

Although the NaCl and CsCl systems appear quite similar there are some

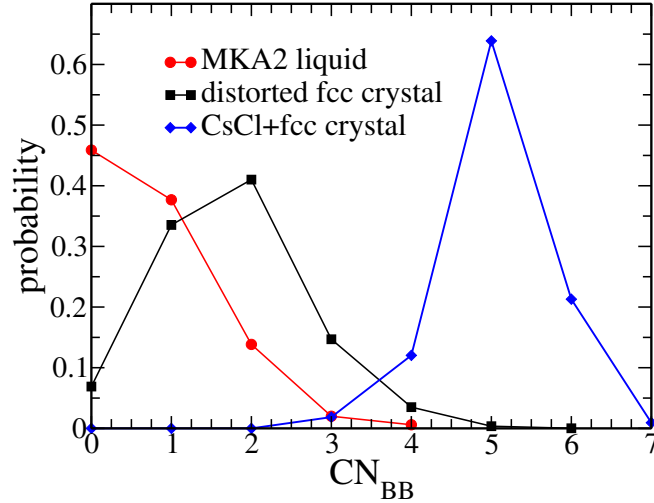


Figure 7.9: The probability distribution of the CN_{BB} as obtained in the MKA2 liquid at $T = 0.4$, the distorted fcc crystal formed by the MKA2 liquid at $T = 0.35$ and CsCl+fcc crystal at $T = 0.4$. The CsCl+fcc is formed at the same composition as the MKA2 liquid. The demixing required by the CsCl+fcc liquid is much higher than the distorted fcc.

basic differences. The CsCl crystal is made up of two interpenetrating sc structures of “A” and “B” type of particles. Thus in the CsCl+fcc crystal the “A” particles have two different populations, namely one which forms sc and the other which forms fcc structure. In an earlier work we had mentioned that this wide difference in the order parameter of the two population causes the frustration between the two structures[25]. If we are away from the equimolar mixture the growth of a CsCl will deplete the population of the “B” particles in the neighbourhood which should promote the formation of fcc structure between the “A” particles. However a unit cell of fcc is not compatible with the CsCl structure thus to reduce the structural frustration the system sacrifices the mixing entropy and increase the concentration of the “B” particles in the liquid near the cluster as seen in Fig.7.6 to form more CsCl structures till finally it is devoid of any more “B” particles in the liquid. This is the reason we find “AB” and “A” rich zone separated in Fig.7.4a. The NaCl crystal on the other hand is compatible with a fcc crystal as both require the “A” particles to form fcc structure with same lattice spacing. Thus unlike CsCl and fcc the NaCl and fcc can grow in a seamless fashion and the system does not require any demixing which reduces the free energy barrier. A snapshot of the NaCl+fcc structure is shown in Fig.7.11 which shows that there is no specific “A” rich zone.

The study of the energetics can also explain the glass forming ability of some systems which has been previously proposed by Dyre and coworkers [11]. In the above calculation if we decrease the interaction between the “AB” particles then the contribution from the CsCl in lowering the system energy will decrease and

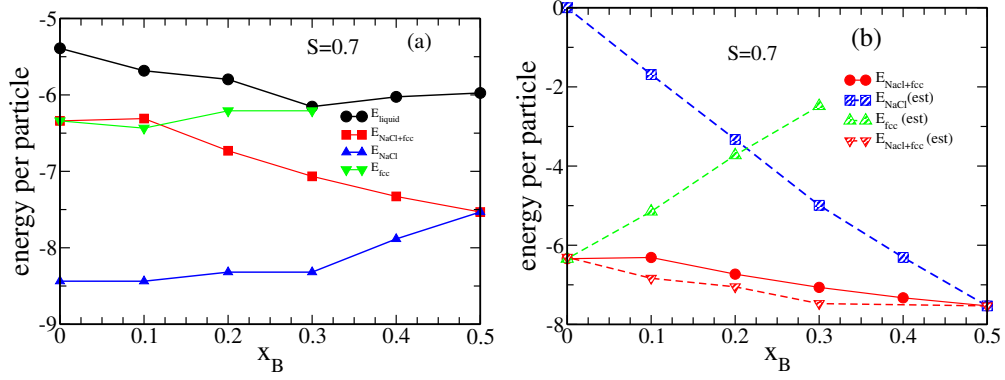


Figure 7.10: (a) The energy per particle of the liquid, mixed crystal (NaCl+fcc), NaCl crystal and fcc crystal for different compositions. The calculations are done at $0.8T_m$ of each composition, where T_m is the melting temperature obtained by heating the different mixed crystals. (b) The energy of the mixed crystal, the estimated energy of the mixed crystal, $E_{NaCl+fcc}(est)$, the estimated contribution from the NaCl part, $E_{NaCl}(est)$, and that from the fcc part, $E_{fcc}(est)$, as a function of composition. The calculations are done at same temperature as in (a).

the crossover will happen at a higher x_B value. Thus the $x_B = 0.2$ will show higher tendency of fcc crystallization as has been reported earlier [11]. In the same system if we make the interaction between the “A” particles repulsive then in a similar fashion the crossover will shift to lower x_B values and this will imply that the $x_B = 0.2$ system will still be driven by the CsCl crystallization. Since this will also require demixing thus the system will be a better glass former as reported earlier [11].

7.4.4 Glass Forming Ability- Role of Demixing and Eutectic Point

We find that the loss of mixing entropy is maximum for $x_B = 0.2$. In the free energy study within the scope of our calculation we can not grow a CsCl crystal and thus can not estimate the free energy cost to grow a CsCl crystal in this system. Which implies that free energy cost is high and w.r.t CsCl formation the $x_B = 0.2$ system is most frustrated and a better glass former. However in the free energy calculation and the study of energetics this system shows a tendency towards fcc crystallization. The fcc crystallization also has a free energy cost because although without clear demixing the system can crystallize in fcc structure the presence of the LFS centered around “B” particles can frustrate this crystallization process. However the cost of free energy to form a fcc crystal in $x_B = 0.2$ system is lower than the cost of free energy to form a CsCl crystal in $x_B = 0.3$ system. Thus it is tempting to comment that the

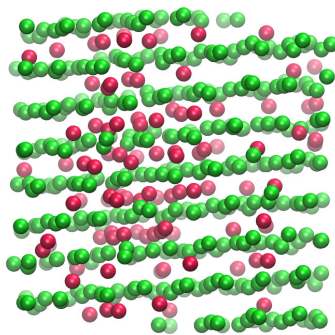


Figure 7.11: Snapshot of a NaCl+fcc crystal structure at $x_B = 0.2$. The simulation is done at $T=0.6$. The snapshot shows seamless formation of NaCl and fcc structure with no demixing.

$x_B = 0.3$ system is a better glass former. However the process of crystallization is not only dependent on the free energy barrier but also on the dynamics of the system. This is the reason the eutectic point is expected to be a better glass forming region and our study of dynamics shows that indeed the $x_B = 0.2$ system is the slowest. For the study of the dynamics we calculate τ_α from overlap function at the respective $0.8T_m$. Note these are the temperatures where the free energy calculations are done. We find that for the $x_B = 0.38$ system $\tau_\alpha = 17.5$ at $T = 0.52$, for the $x_B = 0.3$ system, $\tau_\alpha = 1350$ at $T = 0.42$ and for $x_B = 0.2$ system $\tau_\alpha = 4954$ at $T = 0.36$. Thus according to the study of the dynamics the $x_B = 0.2$ system is a better glass former. Note that the MKA2 model which undergoes crystallization differs from the KA model not in terms of the structure of the liquid but in terms of dynamics. The local structure around the smaller “B” particles which actually frustrates the fcc crystallization is present even in the MKA2 model. However the relaxation timescale of the MKA2 model is orders of magnitude faster than the KA model. Thus our study confirms that as stated earlier[11] it is indeed the dynamics/viscosity of the system which makes KA model a good glass former.

7.5 Conclusion

In this article we study the comparative glass forming ability of different binary systems. In an earlier study by some of us we have shown that binary systems which form CsCl crystals in a equimolar mixture fails to crystallize if the mole fraction of the larger particles are increased [25]. The well known KA model is one of the systems. Thus the KA model’s stability against crystallization is more generic and is similar to systems which form equimolar CsCl crystal.

The global structure for these systems are a mixed form of CsCl+fcc crystal [9]. In the CsCl+fcc crystal the bigger “A” particles need to create two different populations, namely one which contributes towards the CsCl formation and the other which contributes towards the fcc formation. The order parameters such as BOO and coordination number of the “A” particles are quite different in these two crystal forms. Thus the failure in the crystallization has been attributed to the frustration between the CsCl and fcc crystal structures. Note that there is an array of systems which have similar frustration. However the glass forming ability of these systems although have not been calculated but is believed to be different. Thus there should be more factors contributing to the glass forming ability.

In this article we perform a comparative study of binary glass forming liquids all having good glass forming ability and similar global minima. The study has been performed by changing the composition. We find that the free energy cost to grow a CsCl nucleus increases as we move away from an equimolar mixture. The study of the liquid at the liquid/crystal interface shows that the system which has lowest free energy cost to form a nucleus also shows a demixing near the crystal surface. We believe that the structural frustration between the CsCl and fcc structure makes this demixing a prerequisite for crystallization. Our calculation of the partial demixing entropy in the liquid state shows a non monotonic dependence on composition. It shows a maxima for $x_B = 0.2$ system. We could show a connection between the change in free energy cost to create a crystal nucleus and the change in demixing entropy as a function of composition. Our study shows that although the $x_B = 0.2$ system is strongly frustrated against CsCl crystallization, it has tendency towards fcc growth. We can justify this tendency of fcc growth from the study of the energetics. We show that in the composition range studied here there are two regions, one which is driven by the CsCl crystallization and the other at lower x_B values is driven by fcc crystallization. It is primarily in the former region that the structural frustration between the CsCl and fcc structure leads to the requirement of demixing which eventually increases the free energy barrier and provides stability against crystallization. This point has been confirmed by studying a NaCl+fcc system which naturally undergoes crystallization at all compositions. The study of the energetics of this system also shows two similar region. However unlike the CsCl+fcc system, in the region where crystallization is driven by NaCl, due to the compatibility of the NaCl and fcc structure no demixing has been observed and the crystal grows in a seamless fashion. In the second region driven by fcc crystallization we show that demixing is not a stringent criteria and the stability against crystallization comes from the frustration caused by the presence of the

“B” particles with well defined LFS and also the system’s proximity to eutectic point where the dynamics is slow. Thus although we study three very similar glass formers, which ideally belong to the same class of system and differ only in composition, we find that they do not share the same origin of stability against crystallization.

We should also comment that our search of crystal structures is not exhaustive and the system which we claim to be a better glass former can crystallize in a different crystal form like the Al_2Cu structure is found to be a low energy state of a system belonging to the same class where $x_B = 0.33$ [10]. This system is also known to show resistance towards crystallization. The CuZr liquid which has a low energy CsCl like structure is also a good glass former [8]. Note that in these two systems the composition of the crystal is identical to that of the liquid. Thus even above $x_B > 0.2$ it is not always demixing which provides stability against crystallization.

Bibliography

- [1] K. VOLLMAYR, W. KOB, and K. BINDER, *J. Chem. Phys.* **105**, 4714 (1996).
- [2] A. INOUE, *Acta Mater.* **48**, 279 (2000).
- [3] W. G. HOOVER and F. H. REE, *J. Chem. Phys.* **49**, 3609 (1968).
- [4] W. KOB and H. C. ANDERSEN, *Phys. Rev. E* **51**, 4626 (1995).
- [5] G. WAHNSTRÖM, *Phys. Rev. A* **44**, 3752 (1991).
- [6] D. COSLOVICH and G. PASTORE, *J. Phys.: Cond. Mat.* **21**, 285107 (2009).
- [7] K. ZHANG, Y. LIU, J. SCHROERS, M. D. SHATTUCK, and C. S. O'HERN, *J. Chem. Phys.* *044503* **142**, 104504 (2015).
- [8] C. TANG and P. HARROWELL, *Nat Mater* **12**, 507 (2013).
- [9] J. R. FERNANDEZ and P. HARROWELL, *J. Chem. Phys.* **120**, 9222 (2004).
- [10] P. CROWTHER, F. TURCI, and C. P. ROYALL, *J. Chem. Phys.* **143**, 044503 (2015).
- [11] S. TOXVAERD, U. R. PEDERSEN, T. B. SCHRODER, and J. C. DYRE, *J. Chem. Phys.* **130**, 224501 (2009).
- [12] U. R. PEDERSON, N. P. BAILEY and T. B. SCHRODER and J. C. DYRE, *arXiv:0706.0813v2*.
- [13] F. C. FRANK, *Proc. R. Soc. A* **215**, 43 (1952).
- [14] D. KIVELSON, S. A. KIVELSON, X. ZHAO, Z. NUSSINOV, and G. TARJUS, *Physica A* **219**, 27 (1995).
- [15] F. M. C. SAUSSET, G. TARJUS, and P. VIOT, *Phys. Rev. Lett.* **101**, 155701 (2008).
- [16] H. TANAKA, *J. Non-Crys. Solids* **351**, 3371 (2005).

- [17] M. LEOCMACH and H. TANAKA, *Nat Commun* **3**, 974 (2012).
- [18] H. TANAKA, *J. Non-Cryst. Solids* **351**, 3385 (2005).
- [19] M. J. VLOT, H. E. A. HUITEMA, A. DE VOOYS, and J. P. VAN DER EERDEN, *J. Chem. Phys.* **107**, 4345 (1997).
- [20] H. TANAKA, *Eur. Phys. J. E* **35**, 113 (2012).
- [21] M. KOBAYASHI and H. TANAKA, *Phys. Rev. Lett.* **106**, 125703 (2011).
- [22] V. MOLINERO, S. SASTRY, and C. A. ANGELL, *Phys. Rev. Lett.* **97**, 075701 (2006).
- [23] D. NAYAR and C. CHAKRAVARTY, *Phys. Chem. Chem. Phys.* **15**, 14162 (2013).
- [24] D. COSLOVICH, and G. PASTORE, *J. Chem. Phys.* **127**, 124504 (2007).
- [25] A. BANERJEE, S. CHAKRABARTY, and S. M. BHATTACHARYYA, *J. Chem. Phys.* **139**, 104501 (2013).
- [26] L. C. VALDES, F. AFFOUARD, M. DESCAMPS, and J. HABASAKI, *J. Chem. Phys.* **130**, 154505 (2009).
- [27] S. J. PLIMPTON, *J. Comput. Phys.* **117**, 1 (1995).
- [28] P. J. STEINHARDT, D. R. NELSON, and M. RONCHETTI, *Phys. Rev. B* **28**, 784 (1983).
- [29] W. LECHNER and C. DELLAGO, *J. Chem. Phys.* **129**, 114707 (2008).
- [30] M. K. NANDI, A. BANERJEE, S. SENGUPTA, S. SASTRY, and S. M. BHATTACHARYYA, *J. Chem. Phys.* **143**, 174504 (2015).
- [31] J. R. FERNÁNDEZ and P. HARROWELL, *Phys. Rev. E* **67**, 011403 (2003).
- [32] S. KUMAR, J. M. ROSENBERG, D. BOUZIDA, R. H. SWENDSEN, and P. A. KOLLMAN, *J. Comp. Chem.* **13**, 1011 (1992).
- [33] C. DESGRANGES and J. DELHOMMELLE, *JACS* **136**, 8145 (2014).
- [34] S. PUNNATHANAM and P. A. MONSON, *J. Chem. Phys.* **125**, 024508 (2006).

Chapter 8

Summary and future work

8.1 Summary

The dynamics and thermodynamics in the glass-forming system are still not completely understood. Many experiments, simulations and theories have explained a lot about the glass transition and the glass-forming systems. Most of the theories in the glass community are mean-field in nature. It can not fully explain the experiments and simulations results, and thus it is very important to understand theories better, which will give more insights into the glass transition. We have found an innovative way where a 3 dimensional system develops mean-field like properties. We have also studied the glass-forming ability in the different systems. We summarize all our achievements of the thesis in this chapter, and we also discuss further aspects and possible work for the future, which is worth studying.

We have discussed important concepts of the glass transition and the most popular theories, which explains many properties of the glass transition in chapter1. In chapter2, we have explained many properties of the glass transition and discussed the relevant definition and the detailed computational techniques.

After setting up the basic knowledge of the glass and direction of the thesis, in chapter3, we propose a novel model for a glass-forming liquid which allows to switch in a continuous manner from a standard three-dimensional liquid to a fully connected mean-field model. This is achieved by introducing k additional particle-particle interactions which thus augments the effective number of neighbors of each particle. Our computer simulations of this system show that the structure of the liquid does not change with the introduction of these pseudo neighbours and by means of analytical calculations, we determine the structural properties related to these additional neighbors.

In chapter.4, we show that the relaxation dynamics of the system slows down

very quickly with increasing k and that the onset and the mode-coupling temperatures increase. The systems with high values of k follow the MCT power law behaviour for a larger temperature range compared to the ones with lower values of k . The dynamic susceptibility indicates that the dynamic heterogeneity decreases with increasing k whereas the non-Gaussian parameter is independent of it. Thus we conclude that with the increase in the number of pseudo neighbours the system becomes more mean-field like. By comparing our results with previous studies on mean-field like system we come to the conclusion that the details of how the mean-field limit is approached are important since they can lead to different dynamical behavior in this limit.

In chapter5, we presents an extensive study of the thermodynamics of the above-mentioned model for several values of k and its correlation with the dynamics. We surprisingly find that the usual thermodynamic integration (TI) method of calculating the entropy provides unphysical results for this model. It predicts the vanishing of configurational entropy at state points at which both the collective and the single-particle dynamics of the system show complete relaxation. We then employ a new method known as the two-phase thermodynamics (2PT) method to calculate the entropy. We find that with an increase in k the difference in the entropy computed using the two methods (2PT and TI) increases. We also find that in the temperature range studied, the entropy calculated via the 2PT method satisfies the Adam-Gibbs (AG) relationship between the relaxation time and the configurational entropy, whereas the entropy calculated via the TI method shows a strong violation of the same. Finally, we discuss the possible reasons for the failure of the TI method of entropy calculation.

In chapter6, we show the behavior of the mean-field system near the jamming transition. We find the jamming transition happens at lower volume fraction with increase in k and it shows a power-law behavior of pressure and energy of the system with volume fraction in the vicinity of the jamming transition. The contribution of the nearest neighbor in the coordination number at the jamming state decreases with increasing in k and the contribution of the pseudo neighbor increases with k .

In chapter7, we have discussed a comparative study of the glass forming ability of binary systems with varying composition, where the systems have similar global crystalline structure (CsCl+fcc). Biased Monte Carlo simulations using umbrella sampling technique shows that the free energy cost to create a CsCl nucleus increases as the concentration of the smaller particles are decreased. We find that systems with comparatively lower free energy cost to form CsCl nucleus exhibit more pronounced pre-crystalline demixing near the liquid/crystal interface. The structural frustration between the CsCl and fcc crystal demands this

demixing. We show that closer to the equimolar mixture the entropic penalty for demixing is lower and a glass forming system may crystallize when seeded with a nucleus. This entropic penalty as a function of composition shows a non-monotonic behavior with a maximum at a composition similar to the well known Kob-Anderson (KA) model. Although the KA model shows the maximum entropic penalty and thus maximum frustration against CsCl formation, it also shows a strong tendency towards crystallization into fcc lattice of the larger “A” particles which can be explained from the study of the energetics. Thus for systems closer to the equimolar mixture although it is the requirement of demixing which provides their stability against crystallization, for KA model it is not demixing but slow dynamics and the presence of the “B” particles which makes it a good glass former. The locally favoured structure around “B” particles is quite similar to the CsCl structure and the incompatibility of CsCl and fcc hinders the fcc structure growth in the KA model. Although the glass forming binary systems studied here are quite similar, differing only in composition, we find that their glass forming ability cannot be attributed to a single phenomenon.

8.2 Future work

This summary clearly indicates that the details of how the mean-field limit is approached are important, and future studies are needed to clarify this point. Finally, we note that the approach we propose here on how the mean-field character is tuned can be applied to any system. Hence it will be interesting to study whether other types of interaction potentials, such as the Coulomb potentials used to describe oxide glass-formers, will give qualitatively the same behavior, or in other words, whether the approach to the mean-field limit depends on the nature of the local structure of the system. In an earlier study involving different glass-formers, evidence was given that the locally preferred structures (LPS) are connected to the dynamics only for systems that are not mean-field like. The ability of the present model to continuously tune the mean-field behaviour makes it thus an ideal system to check the validity of this observation. Since we find that with the increasing number of pseudo neighbours, the LPS remains unchanged whereas the dynamics slow down, this suggests that with an increase in the mean-field nature, the correlation between the LPS and the dynamics decreases, a result that corroborates the earlier findings.

Recent work on polymeric systems showed that systems that demonstrated higher sub nanosecond anharmonic motions are more ductile and tough [21]. Note that similar to our mean field system, each monomer in a polymeric system

has both short range nearest neighbour interaction and long range connections. In our study, we find that although the pseudo neighbours (PN) slow down the overall dynamics of the system, the structural relaxation has a weak dependence on this long range connectivity with the pseudo neighbours and strongly depends on the nearest neighbours (NN). This suggests that the mobility will probably depend more on the nearest neighbours. The calculation of softness parameter depends on the radial distribution function. In our model system we find that the effective rdf has two components, one coming from the contribution of the nearest neighbours (NN) and the other from the pseudo neighbours (PN). We will study the role of both NN and PN in the confining potential and also its softness. We will then study the correlation of the different components of the softness and the mobility. This will also give us an idea about the role of connectivity in the sub nanosecond dynamics in polymeric systems.

Note that according to classical nucleation theory, the free energy barrier is determined by both surface tension and the difference in free energy between the two phases. Moreover, the surface free energy would also include an entropic term, which is likely to be influenced by the demixing entropy cost as discussed in the text. Thus surface tension may play an important role in lowering the free energy cost of fcc nucleation. However, an estimation of this is beyond the scope of the present thesis and will be addressed in the future.

ABSTRACT

Name of the Student: Ujjwal Kumar Nandi

Faculty of Study: Physical Sciences (PS)

CSIR Lab: CSIR-NCL, Pune

Registration No.: 10PP17J26052

Year of Submission: 2021

Name of the Supervisor: Dr. Sarika Maitra
Bhattacharyya

Title of the thesis: Connecting real glasses to mean-field models: A study of structure, dynamics and thermodynamics

The dynamics and thermodynamics in the glass-forming system are still not completely understood. Most of the theories in the glass community are mean-field in nature. It cannot fully explain the experiments and simulations results, and thus we have found an innovative way where a 3 dimensional system develops mean-field like properties. We propose a novel model for a glass-forming liquid which allows to switch in a continuous manner from a standard three-dimensional liquid to a fully connected mean-field model. This is achieved by introducing k additional particle-particle interactions which thus augments the effective number of neighbors of each particle. Our computer simulations of this system show that the structure of the liquid does not change with the introduction of these pseudo neighbors and by means of analytical calculations, we determine the structural properties related to these additional neighbors. The relaxation dynamics of the system slows down very quickly with increasing k and that the onset and the mode-coupling temperatures increase. The systems with high values of k follow the MCT power law behavior for a larger temperature range compared to the ones with lower values of k and the heterogeneity of the system decreases with increase in k .

To study the thermodynamic properties of the mean-field model, we surprisingly find that the usual thermodynamic integration (TI) method of calculating the entropy provides unphysical results. It predicts the vanishing of configurational entropy at state points at which both the collective and the single-particle dynamics of the system show complete relaxation. We then employ a new method known as the two-phase thermodynamics (2PT) method to calculate the entropy. We find that in the temperature range studied, the entropy calculated via the 2PT method satisfies the Adam-Gibbs (AG) relationship between the relaxation time and the configurational entropy, whereas the entropy calculated via the TI method shows a strong violation of the same.

Behavior of the mean-field system near the jamming transition is very interesting to study. We find the jamming transition happens at lower volume fraction with increase in k and it shows a power-law behavior of pressure and energy of the system with volume fraction in the vicinity of the jamming transition. The contribution of the nearest neighbor in the coordination number at the jamming state decreases with increasing in k and the contribution of the pseudo neighbor increases with k .

Most of the systems which show glassy behavior have global crystalline order. Glass forming ability (GFA) depends on the barrier to crystallize in the system. It can easily crystallize if the system crosses the barrier. With the increase of the computational facility, it has been found some glass forming systems show partial crystallinity. In this thesis, we have tried to estimate the glass forming ability of some glass forming systems. We have shown which systems are best glass former. We have found some system shows higher free energy barrier because of the loss of demixing entropy but for some other system it has lower free energy barrier for different crystalline structure which does not allow this system to be a good glass former.

LIST OF PUBLICATIONS

Publications emanating from Thesis work

1. **Ujjwal Kumar Nandi**, Atreyee Banerjee, Suman Chakrabarty And and Sarika Maitra Bhattacharyya, *Composition dependence of the glass forming ability in binary mixtures: The role of demixing entropy*, *The Journal of Chemical Physics*, 145, 034503 (2016), DOI:<http://dx.doi.org/10.1063/1.4958630>
2. **Ujjwal Kumar Nandi**, Walter Kob And Sarika Maitra Bhattacharyya, *Connecting real glasses to mean-field models*, *Journal of Chemical Physics*, 154, 094506 (2021), DOI:<https://doi.org/10.1063/5.0038749>
3. **Ujjwal Kumar Nandi**, Palak Patel, Mohd Moid, Manoj Kumar Nandi, Shiladitya Sengupta, Smarajit Karmakar, Prabal K Maiti, Chandan Dasgupta And Sarika Maitra Bhattacharyya, *Thermodynamics and its correlation with dyanmcis in a mean-field model and pinned systems: A comparative study using two different methods of entropy calculation (Submitted)*
4. **Ujjwal Kumar Nandi**, Manoj Kumar Nandi, Walter Kob And Sarika Maitra Bhattacharyya, *Connecting real glasses to mean-field models: A study of jamming (Under Preparation)*

Other Publications

1. Sayantan Acharya, **Ujjwal Kumar Nandi** And and Sarika Maitra Bhattacharyya, *Fickian yet non-Gaussian behaviour: A dominant role of the intermittent dynamics*, *The Journal of Chemical Physics*, 146, 134504 (2017), DOI:<http://dx.doi.org/10.1063/1.4979338>
2. Sayantan Acharya, **Ujjwal Kumar Nandi** Bhattacharyya, *Comparative Study of Anomalous Size Dependence of Charged and Neutral Solute Diffusion in Water*, *The Journal of Physical Chemistry B*, 123, 10275 - 10285 (2019), DOI:[10.1021/acs.jpcc.9b08023](https://doi.org/10.1021/acs.jpcc.9b08023)

-
3. Palak Patel, Manoj Kumar Nandi, **Ujjwal Kumar Nandi** And Sarika Maitra
Bhattacharyya, *Effective structure of a system with continuous polydispersity,*
Journal of Chemical Physics., 154, 034503 (2021),
DOI:<https://doi.org/10.1063/5.0038812>

***THESIS RELATED
PUBLICATIONS***

Composition dependence of the glass forming ability in binary mixtures: The role of demixing entropy

Ujjwal Kumar Nandi, Atreyee Banerjee, Suman Chakrabarty, and Sarika Maitra Bhattacharyya

Citation: *The Journal of Chemical Physics* **145**, 034503 (2016); doi: 10.1063/1.4958630

View online: <http://dx.doi.org/10.1063/1.4958630>

View Table of Contents: <http://aip.scitation.org/toc/jcp/145/3>

Published by the [American Institute of Physics](#)

Articles you may be interested in

[The nature of geometric frustration in the Kob-Andersen mixture](#)

The Journal of Chemical Physics **143**, 044503 (2015); 10.1063/1.4927302

[Interplay between crystallization and glass transition in binary Lennard-Jones mixtures](#)

The Journal of Chemical Physics **139**, 104501 (2013); 10.1063/1.4820402

[Effect of total and pair configurational entropy in determining dynamics of supercooled liquids over a range of densities](#)

The Journal of Chemical Physics **145**, 034502 (2016); 10.1063/1.4958627

[Multiple length and time scales of dynamic heterogeneities in model glass-forming liquids: A systematic analysis of multi-point and multi-time correlations](#)

The Journal of Chemical Physics **138**, 12A506 (2013); 10.1063/1.4769256

[Unraveling the success and failure of mode coupling theory from consideration of entropy](#)

The Journal of Chemical Physics **143**, 174504 (2015); 10.1063/1.4934986

[Identification of long-lived clusters and their link to slow dynamics in a model glass former](#)

The Journal of Chemical Physics **138**, 12A535 (2013); 10.1063/1.4790515



**COMPLETELY
REDESIGNED!**

**PHYSICS
TODAY**

Physics Today Buyer's Guide
Search with a purpose.

Composition dependence of the glass forming ability in binary mixtures: The role of demixing entropy

Ujjwal Kumar Nandi,¹ Atreyee Banerjee,¹ Suman Chakrabarty,²
and Sarika Maitra Bhattacharyya^{1,a)}

¹Polymer Science and Engineering Division, CSIR-National Chemical Laboratory, Pune-411008, India

²Physical and Materials Chemistry Division, CSIR-National Chemical Laboratory, Pune-411008, India

(Received 30 March 2016; accepted 28 June 2016; published online 18 July 2016)

We present a comparative study of the glass forming ability of binary systems with varying composition, where the systems have similar global crystalline structure (CsCl+fcc). Biased Monte Carlo simulations using umbrella sampling technique show that the free energy cost to create a CsCl nucleus increases as the composition of the smaller particles is decreased. We find that systems with comparatively lower free energy cost to form CsCl nucleus exhibit more pronounced pre-crystalline demixing near the liquid/crystal interface. The structural frustration between the CsCl and fcc crystal demands this demixing. We show that closer to the equimolar mixture, the entropic penalty for demixing is lower and a glass forming system may crystallize when seeded with a nucleus. This entropic penalty as a function of composition shows a non-monotonic behaviour with a maximum at a composition similar to the well known Kob-Anderson (KA) model. Although the KA model shows the maximum entropic penalty and thus maximum frustration against CsCl formation, it also shows a strong tendency towards crystallization into fcc lattice of the larger “A” particles which can be explained from the study of the energetics. Thus for systems closer to the equimolar mixture although it is the requirement of demixing which provides their stability against crystallization, for KA model it is not demixing but slow dynamics and the presence of the “B” particles make it a good glass former. The locally favoured structure around “B” particles is quite similar to the CsCl structure and the incompatibility of CsCl and fcc hinders the fcc structure growth in the KA model. Although the glass forming binary systems studied here are quite similar, differing only in composition, we find that their glass forming ability cannot be attributed to a single phenomenon. *Published by AIP Publishing.* [<http://dx.doi.org/10.1063/1.4958630>]

I. INTRODUCTION

A liquid upon cooling undergoes first order phase transition and forms a crystal. However if the cooling rate is increased it cannot crystallize and forms an amorphous glassy material.¹ In addition to fast supercooling, there are other methods to favor glass formation over crystallization. In bulk metallic glass community, the usual rules of thumb are to at least have a two component mixture with negative enthalpy of mixing and a 12% size ratio between the components.² Single component systems are known to crystallize in a fcc+hcp structure,³ thus multi-component systems are commonly used for making glasses. The negative enthalpy of mixing makes sure that the components remain in a mixed state and do not demix to form single component crystals, whereas the size ratio provides frustration in packing. Although there is an array of experimental systems which form glasses, in computer simulation studies there is only a handful of systems known to be good glass formers.^{4–8} Note that most of the glass forming systems have global crystalline minima.^{9,10} Thus depending on the barrier to crystallization it is just a matter of time for the systems to crystallize. With the increase in the available computational power, some of the well known glass formers

like Kob-Anderson (KA) model and Wahnstrom (WA) model are now found to partially crystallize.^{11,12} Thus in order to design better glass formers we need to be able to estimate the glass forming ability (GFA) of these systems.

In order to quantify GFA, first we need to understand the origin of the stability against crystallization. This is an active field of research and different studies have attributed the GFA to different phenomena.^{10,13–18} The most popular among them is the theory of frustration first proposed by Frank.¹³ According to him, the local liquid ordering is different from the crystalline order and this frustrates the system and decreases the rate of crystallization. It has also been argued that regions with locally favored structures (LFSs) give rise to domains and are connected to the slow dynamics in the supercooled liquids.^{14,15} Sometimes the LFS can also be related to the underlying crystalline structure.^{10,16,17} In some cases the LFS which is connected to crystal structure grows more than the one connected to the liquid structure.¹⁷ The LFS can vary in different dimensions. There are LFSs, like the icosahedral ordering, which can cause frustration in the Euclidean space but tile the curved space.¹⁵ Frustrations are not always structural but can also be energetic in nature.¹⁸

Most binary equimolar mixtures form crystalline structures,¹⁹ where the crystal structure may vary according to the size ratio of the components. There are also some

^{a)}Electronic mail: mb.sarika@ncl.res.in

exceptions like the equimolar CuZr structure which is found to be a good glass former.⁸ However, when the compositions of the mixtures are changed, it is usually found that close to the deep eutectic point many of them form glasses. One of the arguments in favor of the deep eutectic point being a good glass forming zone is that the viscosity is highest at this point so kinetically it takes a longer time to form a crystal nucleus. However it has also been shown that the structural frustration between two different crystal structures can make this region a good glass former. This kind of phase diagram (in temperature vs. composition space) is often referred to as V-shaped phase diagram where the bottom of the V is the glass forming region.^{20-23,25}

In a recent work by some of us we have shown that even though all the systems at equimolar mixture undergo crystallization, as the composition of the larger size particles increases, the zone which forms CsCl crystal at equimolar composition does not crystallize any more.²⁵ It is already known from the study of energetics that the global free energy minima of these systems are CsCl+fcc crystals.⁹ The well known KA glass former is one of the systems present in this more generic CsCl zone. So far only in one study it has been reported to crystallize but in a structure which is different from that of the global minimum.¹¹ In the earlier study we have shown that in the CsCl+fcc crystal structure the bigger “A” particles need to have two different populations where there is a large difference in the order parameter (coordination number and bond orientational order parameter) of these two populations. According to us, this large difference in order parameter creates frustration. Note that in this system the LFS is biccapped square anti-prism which is structurally quite close to CsCl.²⁴ Thus unlike systems discussed earlier where the geometric frustration is between icosahedral and fcc structure,^{14,15,17} in this system it is between CsCl and fcc structure which stabilizes it against crystallization.²⁵

In this present work we study a similar series of binary systems by changing the composition and also the inter-species interaction length. Many of the binary systems studied here are good glass formers and have a global minima which is CsCl+fcc structure. Thus according to our earlier study the structural frustration for these systems is similar. However, these systems are expected to have different glass forming ability. The goal of this work is to get a relative estimate of the GFA of different systems and then explore the origin of their differences. Our study shows that the free energy cost for CsCl crystallization increases with the composition of the smaller particles. The system with lowest free energy cost also shows a pre-crystalline demixing in the liquid phase near the liquid/crystal interface. The demixing takes place due to the structural frustration between the CsCl and fcc structures. Up to a certain composition, the composition dependence of the free energy cost to create a crystal nucleus can be related to the composition dependence of this demixing entropy. Our study of energetics shows that although in the whole range of composition the global minima is CsCl+fcc crystal, the driving force of crystallization in a certain region is the CsCl crystal and in another region is fcc crystal. In the former region the system tends to demix and form CsCl+fcc crystal and demixing frustrates the

crystallization process. However, in the latter region we show that demixing does not play a crucial role. It is primarily the slow dynamics near eutectic point and LFS around the smaller “B” particles which frustrate the crystallization process.

The simulation details are given in Sec. II. In Section III we present the definition and method for evaluating different quantities, in Section IV we have the results and discussion, and Section V ends with a brief summary.

II. SIMULATION DETAILS

The atomistic models which are simulated are two component mixtures of classical particles (larger “A” and smaller “B” type), where particles of type i interact with those of type j with pair potential, $U_{ij}(r)$, where r is the distance between the pair. $U_{ij}(r)$ is described by a shifted and truncated Lennard-Jones (LJ) potential, as given by

$$U_{ij}(r) = \begin{cases} U_{ij}^{(LJ)}(r; \sigma_{ij}, \epsilon_{ij}) - U_{ij}^{(LJ)}(r_{ij}^{(c)}; \sigma_{ij}, \epsilon_{ij}), & r \leq r_{ij}^{(c)} \\ 0, & r > r_{ij}^{(c)} \end{cases}, \quad (1)$$

where $U_{ij}^{(LJ)}(r; \sigma_{ij}, \epsilon_{ij}) = 4\epsilon_{ij}[(\sigma_{ij}/r)^{12} - (\sigma_{ij}/r)^6]$ and $r_{ij}^{(c)} = 2.5\sigma_{ij}$. Subsequently, we will denote A and B types of particles by indices 1 and 2, respectively.

The different models are distinguished by different choices of lengths and composition parameters. Length, temperature, and time are given in units of σ_{11} , $k_B T / \epsilon_{11}$, and $\sqrt{(m_1 \sigma_{11}^2 / \epsilon_{11})}$, respectively. Here we have simulated various binary mixtures with the interaction parameters $\sigma_{11} = 1$, $\sigma_{22} = 0.88$, $\epsilon_{11} = 1$, $\epsilon_{12} = 1.5$, $\epsilon_{22} = 0.5$, $m_1 = m_2 = 1$ and the inter-species interaction length $\sigma_{12} = 0.7, 0.8$. We have simulated systems with different compositions, varying x_B from 0.50 to 0.0, where x_B is the mole fraction of the smaller B type particles.^{11,26}

The molecular dynamics (MD) simulations have been carried out using the LAMMPS package.²⁷ We have performed MD simulations in the isothermal isobaric ensemble (NPT) using Nosé-Hoover thermostat and Nosé-Hoover barostat with integration timestep 0.005τ . The time constants for Nosé-Hoover thermostat and barostat are taken to be 100 and 1000 timesteps, respectively. Except for the liquid/crystal interface study where we use a rectangular box, all of the other studies are performed in a cubic box with periodic boundary condition. The free energy barrier calculations are done via biased Monte Carlo method. All the studies are performed at $P = 0.5$.

III. DEFINITIONS

A. Bond Orientational Order parameter

Bond Orientational Order (BOO) parameter was first prescribed by Steinhardt *et al.* to characterize specific crystalline structures.²⁸ To characterize specific crystal structures, we have calculated the locally averaged BOO

parameters (\bar{q}_{lm}) of l -fold symmetry as a $2l + 1$ vector,²⁹

$$\bar{q}_l = \sqrt{\frac{4\pi}{2l+1} \sum_{m=-l}^l |\bar{q}_{lm}|^2}, \quad (2)$$

where

$$\bar{q}_{lm}(i) = \frac{1}{\tilde{N}_i} \sum_0^{\tilde{N}_i} q_{lm}(k). \quad (3)$$

Here \tilde{N}_i is the number of neighbours of the i -th particle and the particle i itself. $q_{lm}(i)$ is the local BOO of the i -th particle,

$$q_{lm}(i) = \frac{1}{N_i} \sum_0^{N_i} Y_{lm}(\theta(r_{ij}), \phi(r_{ij})) \quad (4)$$

where Y_{lm} are the spherical harmonics, $\theta(r_{ij})$ and $\phi(r_{ij})$ are spherical coordinates of a bond r_{ij} in a fixed reference frame, and N_i is the number of neighbours of the i th particles. Two particles are considered neighbours if $r_{ij} < r_{min}$, where r_{min} is the first minimum of the radial distribution function (RDF). For the liquids and the crystals the r_{min} has been chosen as the first minima of the respective partial RDF of the ‘‘A’’ type of particles. For the pure CsCl crystal, this comprises of 14 neighbours and for fcc 12 neighbours.

In Fig. 1 we plot the probability distribution of \bar{q}_6 of the liquid at three different composition and also the same for pure CsCl and fcc crystals. We note that at the level of this parameter all the three liquids can be clearly separated from the two different crystal forms.

B. Relaxation time

We quench the system from a random configuration to each temperature and equilibrate the system at that temperature for approximately $100\tau_\alpha$, where τ_α is the alpha relaxation time. It is calculated from the decay of the overlap function, $q(t = \tau_\alpha, T)/N = 1/e$, obtained from the equilibrated

simulations and is defined as

$$\begin{aligned} \langle q(t) \rangle &\equiv \left\langle \int dr \rho(r, t_0) \rho(r, t + t_0) \right\rangle \\ &= \left\langle \sum_{i=1}^N \sum_{j=1}^N \delta(\mathbf{r}_j(t_0) - \mathbf{r}_i(t + t_0)) \right\rangle \\ &= \left\langle \sum_{i=1}^N \delta(\mathbf{r}_i(t_0) - \mathbf{r}_i(t + t_0)) \right\rangle \\ &\quad + \left\langle \sum_i \sum_{j \neq i} \delta(\mathbf{r}_i(t_0) - \mathbf{r}_j(t + t_0)) \right\rangle. \end{aligned} \quad (5)$$

The overlap function is a two-point time correlation function of local density $\rho(r, t)$. It has been used in many recent studies of slow relaxation.³⁰ In this work, we consider only the self-part of the total overlap function (i.e., neglecting the $i \neq j$ terms in the double summation). Earlier it has been shown to be a good approximation to the full overlap function. So, the self-part of the overlap function can be written as

$$\langle q(t) \rangle \approx \left\langle \sum_{i=1}^N \delta(\mathbf{r}_i(t_0) - \mathbf{r}_i(t + t_0)) \right\rangle. \quad (6)$$

Again, the δ function is approximated by a window function $\omega(x)$ which defines the condition of overlap between two particle positions separated by a time interval t ,

$$\begin{aligned} \langle q(t) \rangle &\approx \left\langle \sum_{i=1}^N \omega(|\mathbf{r}_i(t_0) - \mathbf{r}_i(t + t_0)|) \right\rangle, \\ \omega(x) &= 1, x \leq a \text{ implying ‘‘overlap’’} \\ &= 0, \text{ otherwise.} \end{aligned} \quad (7)$$

The time dependent overlap function thus depends on the choice of the cutoff parameter a , which we choose to be 0.3. This parameter is chosen such that particle positions separated due to small amplitude vibrational motion are treated as the same or that a^2 is comparable to the value of the MSD in the plateau between the ballistic and diffusive regimes.

IV. RESULTS

A. Melting temperatures

In order to calculate the crystallization rate and thus the glass forming ability we first determine the melting temperatures of the different crystals. The melting temperature is studied by calculating the temperature dependent growth/melting rate of the crystal and fitting them to a straight line. The temperature at which the growth rate cuts the temperature axis is the predicted melting temperature where the growth rate goes to zero.¹⁰ The simulations are done at $P = 0.5$. With the crystal at the center of the box and the crystal particles being pinned, the liquid of 8000 particles is equilibrated at $T = 1.5$. The system is then quenched to the target lower temperatures and the crystal particles are unpinned. We then run a short equilibration of 1000 steps for the quenched system. Depending on the temperature and the composition of the liquid, the central seed either grows or melts. In the $x_B = 0.38$ and 0.3 systems, we study the melting temperature of CsCl crystal with an initial crystal

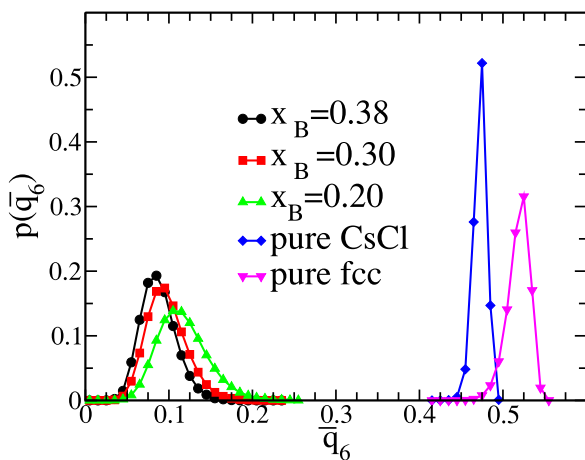


FIG. 1. The probability distribution of the locally averaged BOO, \bar{q}_6 , for the liquid at three different compositions $x_B = 0.38, 0.3, 0.2$ at $T = 0.5$. We also plot the same for the CsCl crystal made up of ‘‘A’’ and ‘‘B’’ type of particles and pure fcc made up of ‘‘A’’ particles.

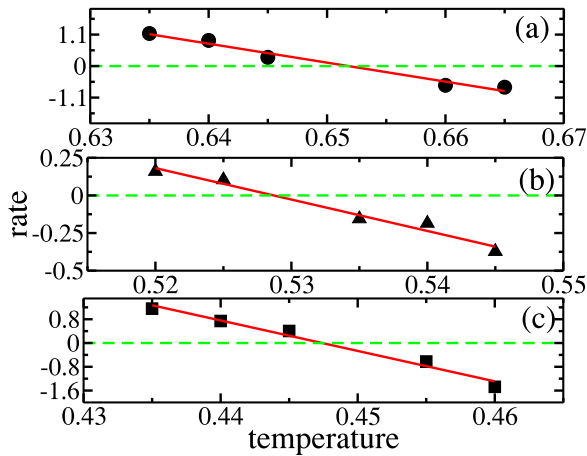


FIG. 2. The growth rate (negative for melting) of the pure CsCl/fcc crystal as a function of temperature for different compositions: (a) CsCl in $x_B = 0.38$ system, the predicted melting temperature (T_m) is 0.652. (b) CsCl in $x_B = 0.3$, $T_m = 0.528$. (c) fcc in $x_B = 0.2$, $T_m = 0.447$.

seed of 432 particles. In the $x_B = 0.2$ mixture we study the melting temperature of the pure fcc crystal comprising of 500 “A” particles. The growth of the seed is monitored by cluster analysis where the \bar{q}_6 is calculated for each particle and if the value of $\bar{q}_6 > 0.3$ (Fig. 1) and it has a neighbour which is part of the existing cluster, then it is included in the cluster. The cluster growth is monitored for about 100–500 τ_α , where τ_α is the temperature dependent α relaxation time that varies across different systems. 5–10 independent runs are generated at each temperature by starting from the same initial configuration but randomized initial velocity. The growth rate is calculated by scaling the time with respect to the corresponding τ_α . From the average growth/decay rate we approximate the melting temperature as the temperature where the predicted growth or decay rate is zero (Fig. 2). The melting points obtained from Fig. 2 is used to construct the composition dependent phase diagram reported in Fig. 3.

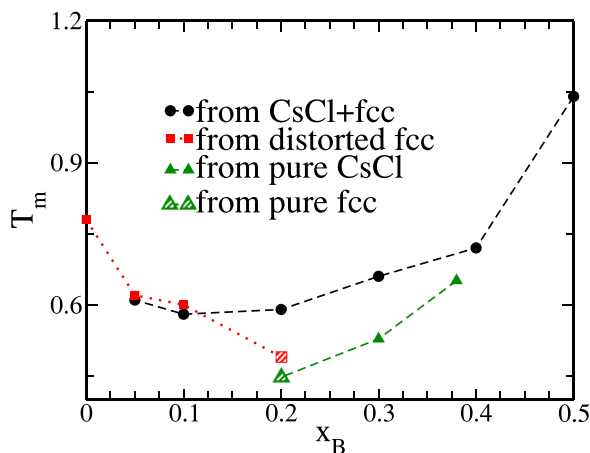


FIG. 3. The melting temperatures of different crystal forms in different binary mixtures. The melting temperature for the pure fcc and CsCl crystal is obtained by studying the growth/melt rate of the crystal. The melting temperature is where the predicted rate disappears (see Fig. 2). The melting temperature of the mixed CsCl+fcc crystal and the distorted fcc crystal are obtained by stepwise heating the system.

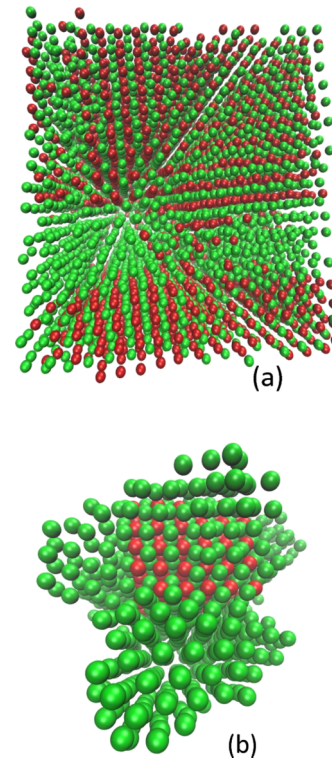


FIG. 4. (a) Snapshot of the $x_B = 0.38$ system after 10^7 steps post-quench at temperature 0.52. The system shows clear demixing and grows into CsCl+fcc crystal. (b) Snapshot of the initial seed and the cluster that has grown around it for $x_B = 0.2$ system after 2×10^7 steps post-quench at temperature 0.4. Around the CsCl seed we find the growth of fcc crystal of “A” particles. For both the systems the initial CsCl crystal seed consists of 432 particles which is inserted in a liquid of 8000 particles.

We find that the $x_B = 0.38$ mixture phase separates and forms a CsCl+fcc crystal structure (Fig. 4(a)). The $x_B = 0.3$ mixture also shows similar tendency; however, the crystal growth rate is slower and within our simulation time scale the demixing is not complete. We also try to grow the CsCl crystal in the $x_B = 0.2$ mixture but we find that instead of CsCl, fcc structure of “A” particles grow around the initial seed (Fig. 4(b)). This is similar to the observation reported earlier.³¹ When a fcc seed is inserted in the same mixture it continues to grow.

In the above mentioned method it is not possible to calculate the melting temperature of the mixed CsCl+fcc crystal as the growth of such crystal never happens within our simulation time scale. For this calculation at each composition ($x_B = 0.05$ – 0.5) we heat the mixed crystal (CsCl+fcc) starting from temperature 0.2–0.3 and increase it up to 0.59–1.0 (depending on the melting temperature of the crystal) with temperature interval of 0.05. Closer to the melting temperature, heating is done with 0.01 temperature interval. At each temperature equilibration is done for 10^7 steps. The size of the initial crystal structure is in the range of 468–612. The total number of particles is chosen in such a way that a perfect mixed crystal can be created. Periodic boundary condition is applied in all directions. Similar study is done for the pure and distorted fcc crystals for $x_B = 0.0, 0.1, 0.2$ systems. For $x_B = 0.0$ we get pure fcc and for $x_B = 0.05$ and 0.1 the “A” particles form fcc crystal but with distortion due to

presence of the “B” particles. In the $x_B = 0.2$ system within our simulation run, we do not observe the formation of the fcc crystal. However as reported earlier in a MKA2 model, if the interaction between the two species is reduced, then the system forms crystal.¹¹ In a similar method by keeping the $\epsilon_{12} = 0.96$, we first form a distorted fcc crystal of the $x_B = 0.2$ system. Once the crystal is formed, we switch back to the larger inter-species interaction of $\epsilon_{12} = 1.5$ and study its melting. The melting of all the crystals happens instantaneously. The melting temperatures are reported in Fig. 3.

B. Free energy of nucleation and role of demixing

In this section we perform a comparative study of the Gibbs free energy (potential of mean force) of crystalline nucleation/growth in different binary mixtures using umbrella sampling technique with the reaction coordinate being the size of the largest crystalline cluster present in the system. The studies are performed at the same degree of undercooling at $0.8T_m$, where the melting temperatures used are those calculated by studying the temperature dependent growth/melting rate for the pure CsCl and fcc crystals. A crystalline cluster is defined by a neighborhood criteria (within a cutoff distance determined by the first minimum of the partial radial distribution function of “A”-type particles for respective systems) of “crystal-like” particles (with the criterion of $\bar{q}_6 > 0.3$). To grow the clusters, we use a biased Monte Carlo approach, where we apply an external harmonic potential of the form $\frac{1}{2}k(n - n_c)^2$, where k is the force constant, n is the number of particles in the largest cluster, and n_c is the position of the bias window. We use $k = 0.1$ for $x_B = 0.38$, and $k = 0.2$ for $x_B = 0.30$ and $x_B = 0.20$. We have used 5-7 umbrella windows (depending on the system) in the cluster size range of 15–35. After equilibration, the data are collected for 10^4 Monte Carlo steps per window and Weighted Histogram Analysis Method (WHAM)³² is then used to compute the free energy as a function of the size of the largest cluster as reported in Fig. 5.

While our calculations focus on the pre-critical region of the free energy surfaces, we can compare the relative free energy cost to form a crystalline nucleus of certain size as the composition of the system is varied. We observe that the free energy cost to grow a nucleus from 15 to 35 for all the systems is quite high (in the range of 10–20 $k_B T$), which explains why all these systems are good glass formers. A comparative study of the cost of free energy shows that $x_B = 0.38$ has a lower cost to grow a CsCl crystal compared to $x_B = 0.3$. This explains the slow growth of the CsCl crystal in the latter system which is observed during the melting study. We also try to grow CsCl crystal for $x_B = 0.2$, which we do not observe during our simulation time. This implies that the free energy cost for CsCl crystal growth in this system is even larger. However, similar to the melting study, the crystal that grows around the initial CsCl cluster in the $x_B = 0.2$ system is made up of only “A” particles. Next we study the free energy cost for fcc crystallization in $x_B = 0.2$ system. We find that the free energy cost to grow a fcc crystal from 15-35 cluster size in $x_B = 0.2$ system is lower than the free energy cost to grow a similar size range CsCl crystal for $x_B = 0.3$. This

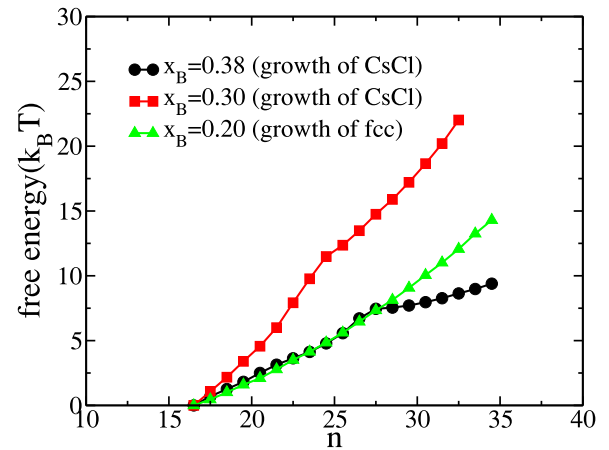


FIG. 5. Gibbs free energy for crystallization as obtained from the umbrella sampling simulations as a function of the largest cluster size for the three systems. For $x_B = 0.38$ and 0.3 we can grow the CsCl cluster, whereas for $x_B = 0.2$ we can only grow the fcc cluster. Even with a initial small CsCl seed the cluster that grows consists of “A” particles forming fcc lattice which is similar to that we find for melting study.

implies that in the $x_B = 0.2$ system the free energy cost for fcc crystallization is lower than the CsCl crystallization. Note that although we make this comparative statement we are unable to determine the free energy cost for growing a CsCl crystal in the $x_B = 0.2$ which leads us to believe that the cost must be very high.

We next analyze the origin of the difference in the free energy cost to grow a CsCl crystal in different systems. In a recent study of crystallization in Pd–Ag mixture it has been found that the barrier to crystallization for the mixed system is about $10K_B T$ higher than the pure system.³³ The Pd and the Ag have a small difference in their sizes and form fcc crystal structure. Thus unlike structural frustration between the CsCl and fcc crystal present in the systems studied here,^{25,31} there exists no structural frustration in the Pd–Ag system. However due to higher Pd–Pd interaction the crystal nucleus for the Pd–Ag system has a higher concentration of the Pd molecules compared to that in the bulk. This leads to demixing in the system and the authors have concluded that this demixing leads to higher barrier. In a separate study it is shown that the phase that nucleates easily is the one which has composition closer to the liquid.³⁴ In this present study we note that in the CsCl crystallization process, except for the equimolar mixture, the composition of the nucleus is different from that of the liquid. The difference increases as we go towards smaller x_B values. Thus it is obvious that the growth of CsCl crystal leads to demixing in the system. However, we would like to investigate if signature of demixing is present in the liquid which surrounds the crystal.

In a recent study it has been shown that the liquid in the crystal/liquid interface shows some compositional ordering.⁸ In a similar spirit we now look at the crystal/liquid interface and investigate if the demixing takes place in the pre-crystalline liquid. For this study we perform $NP_Z T$ calculation in a rectangular box where $P_Z = 0.5$. Initially the system consists of 432 CsCl crystal particles (equal amount of “A” and “B” particles) and 864 liquid particles. The 010 layer

of the crystal faces the liquid where the last layer of the crystal on one side has “A” particles and on the other side has “B” particles. The box length in the x and y directions is $6.92\sigma_{11}$. The box length in the z direction is $20.76\sigma_{11}$. Periodic boundary condition is applied in all directions. Since we want to study the interface property, it is important not to have a rugged interface. Thus the study is performed above the melting temperature of the pure CsCl crystal in the respective liquid ($1.2T_m$) by pinning the crystal particles. Although performed above the melting temperature while equilibrating the $x_B = 0.38$ system, we find the growth of a layer of particles on both sides of the crystal. In the analysis we consider these two layers, which are not pinned, to be part of the crystal. Thus for this system after equilibration, there are 504 crystal particles and 792 liquid particles. The liquid particles span over more than $13\sigma_{11}$ distance which makes it possible to study both the interfacial and bulk properties of the liquid. For the $x_B = 0.3$ system an extra layer of “A” particles grow on the surface which has “B” particles facing the liquid. Due to the scarcity of “B” particles no extra “B” layer grows on the other side. In this analysis we consider the surface where the extra layer of “A” particle has grown. We calculate the fraction of “B” particles, f_B , within each slab of width $1\sigma_{11}$, as a function of distance from the interface (Fig. 6). The first point ($z = 0$) in this plot is taken within the crystal which for the both the systems show same value of f_B . Interestingly we find that for the $x_B = 0.38$ system the concentration of the “B” particles is higher at the interface and it gradually reaches the bulk value around $z = 4$. However for $x_B = 0.3$ system the concentration of the “B” particles is same at the interface and at the bulk. Thus we show that the liquid which has a lower free energy cost for crystal growth also undergoes a pre-crystalline demixing in the liquid phase. Similar to the earlier study⁸ we find that the liquid/crystal interface properties differ for apparently similar systems with different glass forming ability.

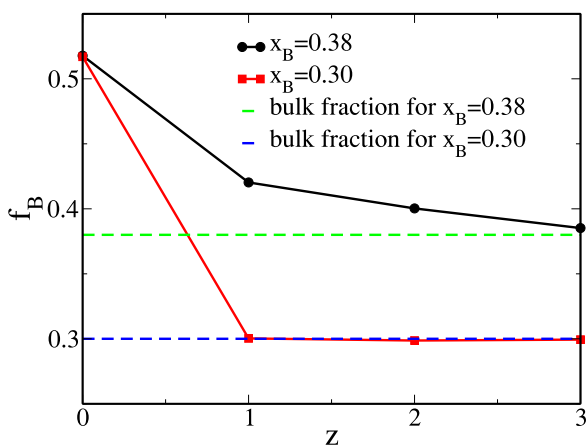


FIG. 6. Distance dependence of the composition from the liquid/crystal interface along the perpendicular direction. We plot the fraction of “B” particles, f_B , as obtained within each slab of width one σ_{11} as a function of the distance from the interface. The interface that has “A” particles is taken and the plot is done for $x_B = 0.38$ and $x_B = 0.3$. We find that for the former system where the initial rate of crystallization is higher, the interface has higher concentration of “B” particles compared to the bulk. Thus there is pre-crystalline demixing in the liquid phase.

Thus we show that the process of crystallization requires demixing which takes place in the pre-crystalline liquid. We now analyze the role of demixing in the free energy barrier. Note that the per particle mixing entropy in a liquid can be written as

$$S_{mix}(lq) = - \sum x_i \ln x_i, \quad (8)$$

where x_i is the mole fraction of the components. To form CsCl+fcc crystal, the liquid needs to demix. We show here that the demixing takes place in a liquid state (refer to Fig. 6). Although the demixing process happens stepwise here, we calculate the total effect of demixing. Thus we consider that to form a CsCl+fcc crystal, part of the liquid needs to form an equimolar mixture and the other part should have pure “A” particles. Thus the per particle mixing entropy in the pre-crystalline partially demixed liquid should be

$$S_{mix}^{precryst}(lq) = -2.0x_B \sum x_i \ln x_i. \quad (9)$$

The difference between these two entropies, $\Delta S_{mix} = S_{mix}(lq) - S_{mix}^{precryst}(lq)$, is the mixing entropy at per particle level that a liquid will lose in the process of partial demixing. ΔS_{mix} as a function of x_B is shown in Fig. 7 which shows a non-monotonic behavior with a maximum around $x_B \approx 0.2$. Note that this kind of non-monotonic behaviour is obtained in the free energy barrier to crystallization for the Pd–Ag mixture which as discussed earlier is attributed to the demixing process.³³ Thus our demixing entropy study can explain the increase in the free energy cost for CsCl crystal growth with decrease in x_B till it reaches a value of 0.2. However this study does not explain why in the $x_B = 0.2$ system where CsCl+fcc is the global minima, the free energy cost for fcc crystallization is much lower than the cost for CsCl crystallization; the latter being so high than an estimation of it is beyond the scope of the present study.

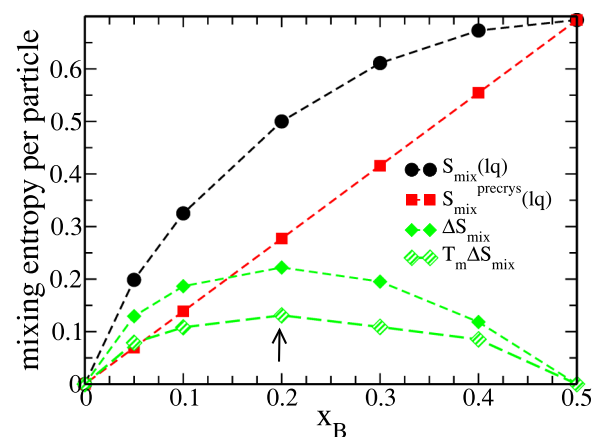


FIG. 7. The mixing entropy of the liquid, $S_{mix}(lq)$, that of the partially demixed pre-crystalline liquid $S_{mix}^{precryst}(lq)$, and the difference between them ΔS_{mix} plotted at different compositions. We also plot the $T_m \Delta S_{mix}$ where T_m is the melting temperature of the mixed CsCl+fcc crystal. The ΔS_{mix} shows a non-monotonic composition dependence with a maximum around $x_B = 0.2$.

C. Analysis from energetics

In order to understand the origin of lower free energy cost for fcc crystallization, we analyze the role of different crystal structures in crystallization by studying the energetics. In Fig. 8(a) we plot the energy per particle of the liquid, the mixed crystal, the fcc crystal, and the CsCl crystal for different compositions at 0.8 times the melting temperature of their respective mixed crystals (given in Fig. 3). This is the melting temperature which has been obtained by stepwise heating the mixed crystal. We find that the energy of the mixed crystal is always lower than the supercooled liquid, which implies that the liquid is in a metastable state. The energy of the CsCl crystal is always lower than the liquid. However for higher x_B values the energy of the fcc crystal is above the liquid and at lower x_B values although it becomes less than the liquid, it is always higher than the CsCl value. This would imply that the CsCl crystal always drives the crystallization process. However this does not explain why both in the melting study and the free energy barrier calculation at $x_B = 0.2$, although we cannot grow CsCl crystal, we can grow fcc crystals. Our subsequent analysis will explain this discrepancy.

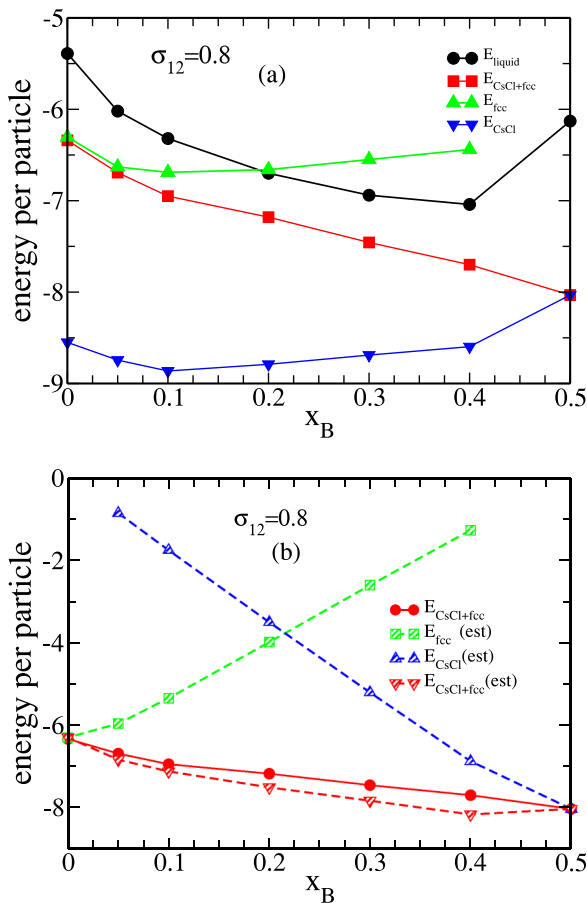


FIG. 8. (a) The energy per particle of the liquid, mixed crystal (CsCl+fcc), CsCl crystal, and fcc crystal for different compositions. The calculations are done at $0.8T_m$ of each composition, where T_m is the melting temperature obtained by heating the different mixed crystals. (b) The energy of the mixed crystal, the estimated energy of the mixed crystal, $E_{\text{CsCl+fcc}}(\text{est})$, the estimated contribution from the CsCl part, $E_{\text{CsCl}}(\text{est})$, and that from the fcc part, $E_{\text{fcc}}(\text{est})$, as a function of composition. The calculations are done at same temperature as in (a).

Next we make an estimation of energy of the mixed crystal, $E_{\text{CsCl+fcc}}(\text{est})$, at the per particle level, at different compositions by assuming that $2x_B$ of the crystal forms CsCl and the rest forms fcc,

$$\begin{aligned} E_{\text{CsCl+fcc}}(\text{est}) &= E_{\text{CsCl}}(\text{est}) + E_{\text{fcc}}(\text{est}) \\ &= 2x_B E_{\text{CsCl}} + (x_A - x_B) E_{\text{fcc}}. \end{aligned} \quad (10)$$

Here E_{CsCl} and E_{fcc} are the energy of the CsCl and fcc crystal, respectively, at per particle level calculated for each system at their respective $0.8T_m$. $E_{\text{CsCl}}(\text{est})$ and $E_{\text{fcc}}(\text{est})$ are the estimated contribution from the respective CsCl and fcc crystal part of the mixed crystal again presented at the per particle level. Note that the values of $E_{\text{CsCl}}(\text{est})$ and $E_{\text{fcc}}(\text{est})$ take into account the fraction of the system which is in different crystal form. In this calculation we of course make certain approximations by neglecting the surface energy. However we find that the value of energy per particle of the mixed crystal thus calculated is not too different from the value of the actual crystal (Fig. 8(b)). These are again calculated at the same temperatures as reported in Fig. 8(a). We now break up the contribution of the two components, the contribution from CsCl and that from fcc and plot them separately. Once we do that we find that although at higher x_B values the CsCl formation drives the crystallization, at lower x_B values it is the fcc formation which drives the crystallization. Although the energy per particle of the fcc crystal is still lower than that of the CsCl, the larger fraction of the fcc crystal wins over. A cross over happens just above $x_B = 0.2$. This explains why the system at $x_B = 0.2$, whose global minima is the mixed crystal, shows higher tendency towards fcc formation.

However, this does not explain why the crystallization process when driven by fcc formation has a lower free energy cost than when driven by CsCl formation. In order to understand this, we study the coordination number between the “B” particles, CN_{BB} in the $x_B = 0.2$ system, before and after crystallization. Since we cannot crystallize the $x_B = 0.2$ system we study the crystallization of the MKA2 model (referred earlier in the melting temperature study) which according to Dyre and co-workers is similar in structure as the KA model but with a lower viscosity.¹¹ Confirming their conclusion we find that the LFS of the MKA2 model appears quite similar to the KA model; however, the dynamics is orders of magnitude faster. We now analyze the CN_{BB} as obtained in the MKA2 system when it is in liquid form at $T = 0.4$ and when it forms distorted fcc crystal around $T = 0.35$. These are plotted in Fig. 9. For comparison we also plot the CN_{BB} for the pure CsCl+fcc crystal at $T = 0.4$. Note that the probability distribution of CN_{BB} in the CsCl+fcc crystal should ideally have a peak at 6 but the peak is shifted to smaller value due to the presence of a large number of surface layer of “B” particles. The study shows that to form distorted fcc crystal although there is an increase in the CN_{BB} it is not as much as required for the CsCl+fcc crystal. Thus demixing in the distorted fcc is much weaker than CsCl+fcc. Analysis of the same kind for the $x_B = 0.9$ system (not shown here) shows similar behaviour.

Thus on the right hand side of the crossover where CsCl drives the crystallization there should be free energy barriers

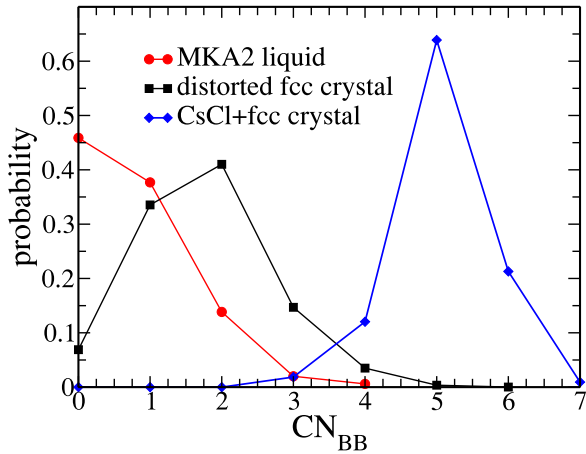


FIG. 9. The probability distribution of the CN_{BB} as obtained in the MKA2 liquid at $T=0.4$, the distorted fcc crystal formed by the MKA2 liquid at $T=0.35$, and CsCl+fcc crystal at $T=0.4$. The CsCl+fcc is formed at the same composition as the MKA2 liquid. The demixing required by the CsCl+fcc liquid is much higher than the distorted fcc.

due to demixing. However on the left hand side the system can avoid or reduce the loss of mixing entropy by paying some energetic penalty to form distorted crystals. The lower energetic stability of the distorted fcc is evident from Fig. 3. We find that for $x_B = 0.2$ the disordered fcc structure melts at a lower temperature compared to the mixed CsCl+fcc structure.

In order to strengthen our argument that it is indeed the demixing that frustrates the CsCl driven crystallization process and leads to high free energy cost, we present a study of a similar system. Reported in a earlier study by some of us we have shown that for the NaCl system ($\sigma_{12} = 0.7$) the crystallization takes place not only at equimolar composition but also at smaller value of x_B forming mixed NaCl+fcc crystal.²⁵ A similar energetic study of the $\sigma_{12} = 0.7$ system is shown in Fig. 10(a). We find that energy of the NaCl crystal is always lower than the fcc crystal (Fig. 10(a)). A similar crossover is also obtained for this system where at higher x_B values the crystallization is driven by NaCl and at lower x_B values it is driven by fcc (Fig. 10(b)). Thus we should expect a similar crystallization problem in this system which appears not to be the case.

Although the NaCl and CsCl systems appear quite similar there are some basic differences. The CsCl crystal is made up of two interpenetrating sc structures of ‘‘A’’ and ‘‘B’’ type of particles. Thus in the CsCl+fcc crystal the ‘‘A’’ particles have two different populations, namely, one which forms sc and the other which forms fcc structure. In an earlier work we had mentioned that this wide difference in the order parameter of the two population causes the frustration between the two structures.²⁵ If we are away from the equimolar mixture the growth of a CsCl will deplete the population of the ‘‘B’’ particles in the neighbourhood which should promote the formation of fcc structure between the ‘‘A’’ particles. However a unit cell of fcc is not compatible with the CsCl structure thus to reduce the structural frustration the system sacrifices the mixing entropy and increase the concentration of the ‘‘B’’ particles in the liquid near the cluster as seen in Fig. 6 to form more CsCl structures till finally it is devoid of any more ‘‘B’’

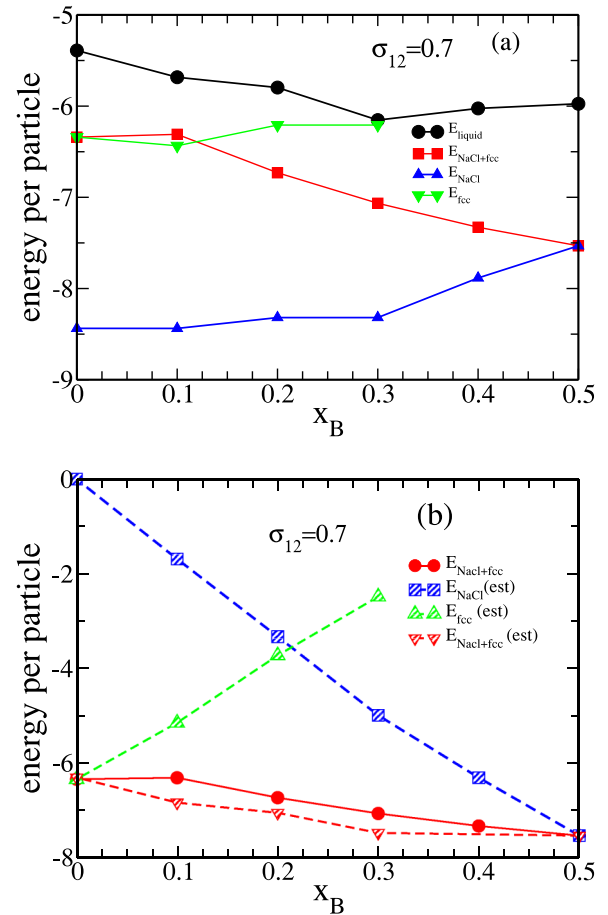


FIG. 10. (a) The energy per particle of the liquid, mixed crystal (NaCl+fcc), NaCl crystal and fcc crystal for different compositions. The calculations are done at $0.8T_m$ of each composition, where T_m is the melting temperature obtained by heating the different mixed crystals. (b) The energy of the mixed crystal, the estimated energy of the mixed crystal, $E_{NaCl+fcc}(est)$, the estimated contribution from the NaCl part, $E_{NaCl}(est)$, and that from the fcc part, $E_{fcc}(est)$, as a function of composition. The calculations are done at same temperature as in (a).

particles in the liquid. This is the reason we find ‘‘AB’’ and ‘‘A’’ rich zone separated in Fig. 4(a). The NaCl crystal on the other hand is compatible with a fcc crystal as both require the ‘‘A’’ particles to form fcc structure with same lattice spacing. Thus unlike CsCl and fcc the NaCl and fcc can grow in a seamless fashion and the system does not require any demixing which reduces the free energy barrier. A snapshot of the NaCl+fcc structure is shown in Fig. 11 which shows that there is no specific ‘‘A’’ rich zone.

Since in the $x_B = 0.2$ system the free energy cost for fcc formation is lower than CsCl formation and also we find growth of fcc structure around a CsCl nucleus (Fig. 4(b)), we expect the fcc nucleus to be energetically more stable than the CsCl nucleus. However, our preliminary study of the surface interaction energy calculation between the crystal and the solvent suggests that the CsCl nucleus is more stable. Note that the surface tension has both energetic and entropic contributions. Thus this counter-intuitive result obtained in the surface interaction energy calculation along with the observed fcc growth suggests that the entropic part, and in this particular case the demixing entropy part plays an even bigger role. In the

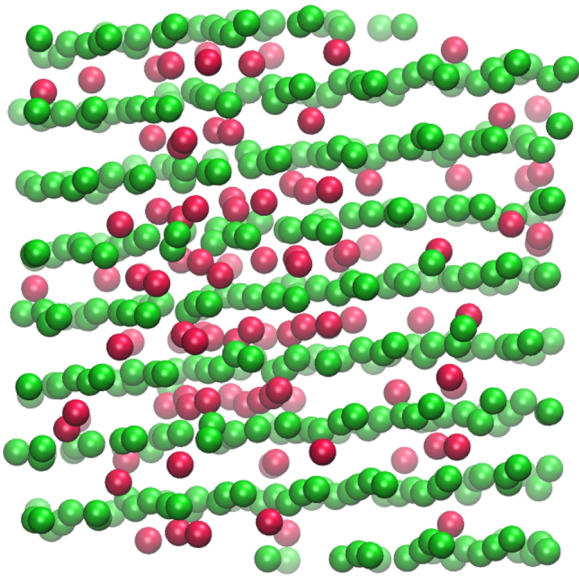


FIG. 11. Snapshot of a NaCl+fcc crystal structure at $x_B = 0.2$. The simulation is done at $T = 0.6$. The snapshot shows seamless formation of NaCl and fcc structure with no demixing.

$x_B = 0.2$ system the less stringent requirement of demixing makes the fcc a more stable nucleus.

The study of the energetics can also explain the glass forming ability of some systems which has been previously proposed by Dyre and co-workers.¹¹ In the above calculation if we decrease the interaction between the “AB” particles then the contribution from the CsCl in lowering the system energy will decrease and the crossover will happen at a higher x_B value. Thus the $x_B = 0.2$ will show higher tendency of fcc crystallization as has been reported earlier.¹¹ In the same system if we make the interaction between the “A” particles repulsive then in a similar fashion the crossover will shift to lower x_B values and this will imply that the $x_B = 0.2$ system will still be driven by the CsCl crystallization. Since this will also require demixing thus the system will be a better glass former as reported earlier.¹¹

D. Glass forming ability-role of demixing and eutectic point

We find that the loss of mixing entropy is maximum for $x_B = 0.2$. In the free energy study within the scope of our calculation we cannot grow a CsCl crystal and thus cannot estimate the free energy cost to grow a CsCl crystal in this system, which implies that free energy cost is high and with respect to CsCl formation, the $x_B = 0.2$ system is most frustrated and a better glass former. However in the free energy calculation and the study of energetics this system shows a tendency towards fcc crystallization. The fcc crystallization also has a free energy cost because although without clear demixing the system can crystallize in fcc structure the presence of the LFS centered around “B” particles can frustrate this crystallization process. However the cost of free energy to form a fcc crystal in $x_B = 0.2$ system is lower than the cost of free energy to form a CsCl crystal in $x_B = 0.3$ system. Thus it is tempting to comment that the $x_B = 0.3$ system is

a better glass former. However the process of crystallization is not only dependent on the free energy barrier but also on the dynamics of the system. This is the reason the eutectic point is expected to be a better glass forming region and our study of dynamics shows that indeed the $x_B = 0.2$ system is the slowest. For the study of the dynamics we calculate τ_α from overlap function at the respective $0.8T_m$. Note these are the temperatures where the free energy calculations are done. We find that for the $x_B = 0.38$ system $\tau_\alpha = 13.12$ at $T = 0.52$, for the $x_B = 0.3$ system, $\tau_\alpha = 507$ at $T = 0.42$, and for $x_B = 0.2$ system $\tau_\alpha = 26450$ at $T = 0.36$. Thus according to the study of the dynamics the $x_B = 0.2$ system is a better glass former. Note that the MKA2 model which undergoes crystallization differs from the KA model not in terms of the structure of the liquid but in terms of dynamics. The local structure around the smaller “B” particles which actually frustrates the fcc crystallization is present even in the MKA2 model. However the relaxation time scale of the MKA2 model is orders of magnitude faster than the KA model. Thus our study confirms that as stated earlier¹¹ it is indeed the dynamics/viscosity of the system which makes KA model a good glass former.

V. CONCLUSION

In this article we study the comparative glass forming ability of different binary systems. In an earlier study by some of us we have shown that binary systems which form CsCl crystals in a equimolar mixture fails to crystallize if the mole fraction of the larger particles is increased.²⁵ The well known KA model is one of the systems. Thus the KA model’s stability against crystallization is more generic and is similar to systems which form equimolar CsCl crystal. The global structure for these systems are a mixed form of CsCl+fcc crystal.⁹ In the CsCl+fcc crystal the bigger “A” particles need to create two different populations, namely one which contributes towards the CsCl formation and the other which contributes towards the fcc formation. The order parameters such as BOO and coordination number of the “A” particles are quite different in these two crystal forms. Thus the failure in the crystallization has been attributed to the frustration between the CsCl and fcc crystal structures. Note that there is an array of systems which have similar frustration. However the glass forming ability of these systems, although has not been calculated, is believed to be different. Thus there should be more factors contributing to the glass forming ability.

In this article we perform a comparative study of binary glass forming liquids, all having good glass forming ability and similar global minima. The study has been performed by changing the composition. We find that the free energy cost to grow a CsCl nucleus increases as we move away from an equimolar mixture. The study of the liquid at the liquid/crystal interface shows that the system which has lowest free energy cost to form a nucleus also shows a demixing near the crystal surface. We believe that the structural frustration between the CsCl and fcc structure makes this demixing a prerequisite for crystallization. Our calculation of the partial demixing entropy in the liquid state shows a non-monotonic dependence

on composition. It shows a maxima for $x_B = 0.2$ system. We could show a connection between the change in free energy cost to create a crystal nucleus and the change in demixing entropy as a function of composition. Our study shows that although the $x_B = 0.2$ system is strongly frustrated against CsCl crystallization, it has tendency towards fcc growth. We can justify this tendency of fcc growth from the study of the energetics. We show that in the composition range studied here there are two regions, one which is driven by the CsCl crystallization and the other at lower x_B values is driven by fcc crystallization. It is primarily in the former region that the structural frustration between the CsCl and fcc structure leads to the requirement of demixing which eventually increases the free energy barrier and provides stability against crystallization. This point has been confirmed by studying a NaCl+fcc system which naturally undergoes crystallization at all compositions. The study of the energetics of this system also shows two similar region. However unlike the CsCl+fcc system, in the region where crystallization is driven by NaCl, due to the compatibility of the NaCl and fcc structure, no demixing has been observed and the crystal grows in a seamless fashion. In the second region driven by fcc crystallization we show that demixing is not stringent criteria and the stability against crystallization comes from the frustration caused by the presence of the “B” particles with well defined LFS and also the system’s proximity to eutectic point where the dynamics is slow. Thus although we study three very similar glass formers, which ideally belong to the same class of system and differ only in composition, we find that they do not share the same origin of stability against crystallization. Note that according to classical nucleation theory the free energy barrier is determined by both surface tension and the difference in free energy between the two phases. Moreover, the surface free energy would also include an entropic term, which is likely to be influenced by the demixing entropy cost as discussed in the text. Thus surface tension may play an important role in lowering the free energy cost of fcc nucleation. However an estimation of this is beyond the scope of the present study and will be addressed in the future.

We should also comment that our search of crystal structures is not exhaustive and the system which we claim to be a better glass former can crystallize in a different crystal form like the Al_2Cu structure is found to be a low energy state of a system belonging to the same class where $x_B = 0.33$.¹⁰ This system is also known to show resistance towards crystallization. The CuZr liquid which has a low energy CsCl like structure is also a good glass former.⁸ Note that in these two systems the composition of the crystal is identical to that of the liquid. Thus even above $x_B > 0.2$

it is not always demixing which provides stability against crystallization.

ACKNOWLEDGMENTS


This work has been supported by the Department of Science and Technology (DST), India and CSIR-Multi-Scale Simulation and Modeling project. U.K.N thanks DST for fellowship and A.B. thanks CSIR for fellowship. S.C. thanks DST for the Ramanujan Fellowship. S.M.B thanks Srikanth Sastry, Peter Harowell, Ulf Pederson, Jeppe Dyre, Paddy Royall, Hajime Tanaka, and Daan Frenkel for discussions.

- ¹K. Vollmayr, W. Kob, and K. Binder, *J. Chem. Phys.* **105**, 4714 (1996).
- ²A. Inoue, *Acta Mater.* **48**, 279 (2000).
- ³W. G. Hoover and F. H. Ree, *J. Chem. Phys.* **49**, 3609 (1968).
- ⁴W. Kob and H. C. Andersen, *Phys. Rev. E* **51**, 4626 (1995).
- ⁵G. Wahnström, *Phys. Rev. A* **44**, 3752 (1991).
- ⁶D. Coslovich and G. Pastore, *J. Phys.: Condens. Matter* **21**, 285107 (2009).
- ⁷K. Zhang, Y. Liu, J. Schroers, M. D. Shattuck, and C. S. O'Hern, *J. Chem. Phys.* **142**, 104504 (2015).
- ⁸C. Tang and P. Harowell, *Nat. Mater.* **12**, 507 (2013).
- ⁹J. R. Fernandez and P. Harowell, *J. Chem. Phys.* **120**, 9222 (2004).
- ¹⁰P. Crowther, F. Turci, and C. P. Royall, *J. Chem. Phys.* **143**, 044503 (2015).
- ¹¹S. Toxvaerd, U. R. Pedersen, T. B. Schroder, and J. C. Dyre, *J. Chem. Phys.* **130**, 224501 (2009).
- ¹²U. R. Pederson, N. P. Bailey, T. B. Schroder, and J. C. Dyre, “Crystallization of the Wahnström Binary Lennard-Jones Liquid,” e-print [arXiv:0706.0813v2](https://arxiv.org/abs/0706.0813v2).
- ¹³F. C. Frank, *Proc. R. Soc. A* **215**, 43 (1952).
- ¹⁴D. Kivelson, S. A. Kivelson, X. Zhao, Z. Nussinov, and G. Tarjus, *Physica A* **219**, 27 (1995).
- ¹⁵F. M. C. Sausset, G. Tarjus, and P. Viot, *Phys. Rev. Lett.* **101**, 155701 (2008).
- ¹⁶H. Tanaka, *J. Non-Cryst. Solids* **351**, 3371 (2005).
- ¹⁷M. Leocmach and H. Tanaka, *Nat. Commun.* **3**, 974 (2012).
- ¹⁸H. Tanaka, *J. Non-Cryst. Solids* **351**, 3385 (2005).
- ¹⁹M. J. Vlot, H. E. A. Huitema, A. de Vooy, and J. P. van der Eerden, *J. Chem. Phys.* **107**, 4345 (1997).
- ²⁰H. Tanaka, *Eur. Phys. J. E* **35**, 113 (2012).
- ²¹M. Kobayashi and H. Tanaka, *Phys. Rev. Lett.* **106**, 125703 (2011).
- ²²V. Molinero, S. Sastry, and C. A. Angell, *Phys. Rev. Lett.* **97**, 075701 (2006).
- ²³D. Nayar and C. Chakravarty, *Phys. Chem. Chem. Phys.* **15**, 14162 (2013).
- ²⁴D. Coslovich and G. Pastore, *J. Chem. Phys.* **127**, 124504 (2007).
- ²⁵A. Banerjee, S. Chakrabarty, and S. M. Bhattacharyya, *J. Chem. Phys.* **139**, 104501 (2013).
- ²⁶L. C. Valdes, F. Affouard, M. Descamps, and J. Habasaki, *J. Chem. Phys.* **130**, 154505 (2009).
- ²⁷S. J. Plimpton, *J. Comput. Phys.* **117**, 1 (1995).
- ²⁸P. J. Steinhardt, D. R. Nelson, and M. Ronchetti, *Phys. Rev. B* **28**, 784 (1983).
- ²⁹W. Lechner and C. Dellago, *J. Chem. Phys.* **129**, 114707 (2008).
- ³⁰M. K. Nandi, A. Banerjee, S. Sengupta, S. Sastry, and S. M. Bhattacharyya, *J. Chem. Phys.* **143**, 174504 (2015).
- ³¹J. R. Fernández and P. Harowell, *Phys. Rev. E* **67**, 011403 (2003).
- ³²S. Kumar, J. M. Rosenberg, D. Bouzida, R. H. Swendsen, and P. A. Kollman, *J. Comput. Chem.* **13**, 1011 (1992).
- ³³C. Desgranges and J. Delhommelle, *J. Am. Chem. Soc.* **136**, 8145 (2014).
- ³⁴S. Punnathanam and P. A. Monson, *J. Chem. Phys.* **125**, 024508 (2006).

Connecting real glasses to mean-field models

Cite as: J. Chem. Phys. **154**, 094506 (2021); <https://doi.org/10.1063/5.0038749>

Submitted: 30 November 2020 . Accepted: 01 February 2021 . Published Online: 03 March 2021

Ujjwal Kumar Nandi,  Walter Kob, and  Sarika Maitra Bhattacharyya



View Online



Export Citation



CrossMark

ARTICLES YOU MAY BE INTERESTED IN

[Ordering, phase behavior, and correlations of semiflexible polymers in confinement](#)

The Journal of Chemical Physics **154**, 090901 (2021); <https://doi.org/10.1063/5.0038052>

[Single-parameter aging in a binary Lennard-Jones system](#)

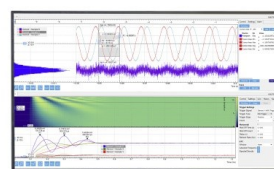
The Journal of Chemical Physics **154**, 094504 (2021); <https://doi.org/10.1063/5.0039250>

[Classical molecular dynamics](#)

The Journal of Chemical Physics **154**, 100401 (2021); <https://doi.org/10.1063/5.0045455>

Challenge us.

What are your needs for
periodic signal detection?



Zurich
Instruments

Connecting real glasses to mean-field models

Cite as: J. Chem. Phys. 154, 094506 (2021); doi: 10.1063/5.0038749

Submitted: 30 November 2020 • Accepted: 1 February 2021 •

Published Online: 3 March 2021



View Online



Export Citation



CrossMark

Ujjwal Kumar Nandi,^{1,2} Walter Kob,^{3,a)}  and Sarika Maitra Bhattacharyya^{1,2,b)} 

AFFILIATIONS

¹Polymer Science and Engineering Division, CSIR-National Chemical Laboratory, Pune 411008, India

²Academy of Scientific and Innovative Research (AcSIR), Ghaziabad 201002, India

³Laboratoire Charles Coulomb and CNRS, University of Montpellier, Montpellier F-34095, France

^{a)}Electronic mail: walter.kob@umontpellier.fr

^{b)}Author to whom correspondence should be addressed: mb.sarika@ncl.res.in

ABSTRACT

We propose a novel model for a glass-forming liquid, which allows us to switch in a continuous manner from a standard three-dimensional liquid to a fully connected mean-field model. This is achieved by introducing k additional particle-particle interactions, which thus augments the effective number of neighbors of each particle. Our computer simulations of this system show that the structure of the liquid does not change with the introduction of these pseudo-neighbors and by means of analytical calculations, and we determine the structural properties related to these additional neighbors. We show that the relaxation dynamics of the system slows down very quickly with the increase in k and that the onset and the mode-coupling temperatures increase. The systems with high values of k follow the mode-coupling theory power law behavior for a larger temperature range compared to the ones with lower values of k . The dynamic susceptibility indicates that the dynamic heterogeneity decreases with the increase in k , whereas the non-Gaussian parameter is independent of it. Thus, we conclude that with the increase in the number of pseudo-neighbors, the system becomes more mean-field-like. By comparing our results with previous studies on mean-field-like systems, we come to the conclusion that the details of how the mean-field limit is approached are important since they can lead to different dynamical behavior in this limit.

Published under license by AIP Publishing. <https://doi.org/10.1063/5.0038749>

I. INTRODUCTION

The details of the relaxation dynamics of the glassy system and the properties of the glass have been and continue to be in the focus of intense research activity.¹ These investigations are motivated by the fact that glasses are not only important for many daily and technological applications but are also an intellectual challenge for fundamental studies, since so far, there is no theoretical framework that is able to give a satisfactory description of the unusual properties of glassy systems and glasses. Although there are sophisticated mean-field (MF) theories, such as the mode-coupling theory (MCT) of the glass transition^{2–5} or the random first order transition theory,^{6–8} that are able to give in some cases a surprisingly good description of the real glass former,^{9–14} these approaches still have many flaws since they fail to give a reliable description of many features of glass-forming systems, thus opening the door to other approaches that attempt to describe glassy systems.^{15–20} Note that these theories are mean-field in nature, whereas the experiments

and computer simulation studies are three or lower dimensional systems. Moreover, it has been found that MCT, although expected to be mean-field in nature, does not become exact even at high dimensions,^{21,22} a flaw that might, however, be related to the approximations used to describe the structure of the liquid in high dimensions. Thus, it is important to understand how these theories are connected to real glass-forming systems and how the properties change as the mean-field character of the system is modified. To establish such a connection, it is useful to study systems whereby varying a parameter, one can go from a d dimensional system to a mean-field system. In the past, various possibilities have been proposed to take this limit (see Ref. 23 for an overview), but most of them do have some drawbacks that prevent us from reaching a solid understanding how three-dimensional (3D) and MF systems are related to each other.²³

One interesting model that allows approaching the MF limit in a continuous manner has been proposed by Mari and Kurchan (MK).²³ The MK model is a hard-sphere system in which the

interaction range between two particles i and j is a random variable with a variance that allows switching from a standard three-dimensional system to a MF-like system. For this model, it is found that with the increase in the interaction range, the Stokes–Einstein relation holds down to lower temperatures and that the dynamic heterogeneity of the system, measured by the four-point susceptibility and non-Gaussian parameter (NGP), decreases. The increase in the interaction range also makes the system follow MCT-like behavior for a larger range in temperature. Although all these results indicate that the MK model can indeed be used to study the transition from 3D to MF, there are certain features of the model that are disturbing. First of all, the structural properties of the system become very different from the one of a normal liquid if the MF limit is approached in that the radial distribution function becomes gas-like. Related to this is the fact that the three-point correlation functions vanish. As a consequence, one loses the property that nearest neighbors can cage a tagged particle, a notion that is fundamental for the slowing down of the dynamics in real glass-forming systems.¹ Second, the maximum attainable packing fraction diverges in the MF limit, a behavior that is very different from the one found in finite dimensions. Some of these oddities are avoided if one considers models on a lattice.²⁴ However, lattice models, notably kinetic Ising models with non-conserved particle density, do have the drawback that it is not obvious to what extent their relaxation dynamics is related to any off-lattice systems. As a consequence, one has to be cautious when applying results from lattice models to describe the dynamics of real systems.

Another approach to connect the properties of 3D systems with the MF behavior has been proposed in a series of papers by Miyazaki and co-workers who have studied the properties of the Gaussian-Core Model (GCM).^{25–27} Due to the long interaction range, each particle has a large number of neighbors, and hence, the system can be expected to be MF-like. These authors showed that compared to the (short-ranged) Kob–Andersen (KA) model,⁹ in the GCM, the Stokes–Einstein relation is followed until a lower temperature regime and that the relaxation dynamics shows a qualitatively better agreement with the MCT predictions.²⁶ Furthermore, it was found that the GCM shows less dynamic fluctuation and that activated processes are suppressed,²⁵ in agreement with the recent studies of the thermodynamic properties of this system.²⁸

A further possibility to connect the properties of low dimensional systems with the MF predictions is to consider systems with increasingly higher dimensions. Sengupta *et al.* have studied the properties of some standard glass formers in two, three, and four dimensions and found that with the increase in dimensionality, the breakdown of the Stokes–Einstein relation becomes less pronounced and that the dynamical heterogeneity decreases.²⁹ Charbonneau *et al.* have studied systems up to six dimensions and found that the shape of the cage does not become Gaussian-like, as expected from MF,³⁰ showing that the approach to this limit might be more complex than expected.

In the present paper, we introduce a simple approach that allows crossing over in a continuous manner from a normal 3D liquid to a MF system. In practice, we do this by increasing for each particle the number of particles it can interact with, thus increasing the effective interaction of the particle with the rest of the system. In contrast to the studies discussed above, our method does not modify in a significant manner the local structure of the liquid even when

the MF limit is reached, i.e., the structure is always similar to the one of the 3D system. Hence, this allows us to study how increasing the connectivity affects the relaxation dynamics, without modifying in a noticeable manner the structure, and hence to probe the dynamics upon approaching the MF limit.

The rest of this paper is organized as follows: The system and simulation details are described in Sec. II. In Sec. III, we present the result, while in Sec. IV, we summarize and conclude.

II. DETAILS OF SYSTEM AND SIMULATIONS

As mentioned in the Introduction, our system is given by N particles that interact with each other via a standard short-range potential. In addition, each particle interacts also with “pseudo-neighbors,” i.e., particles that are not necessarily close in space. Hence, the total interaction potential of the system is given by

$$U_{\text{tot}}(r_1, \dots, r_N) = \sum_{i=1}^N \sum_{j>i}^N u(r_{ij}) + \frac{1}{2} \sum_{i=1}^N \sum_{j=1}^k u^{\text{pseudo}}(r_{ij}) \quad (1)$$

$$= U + U_k^{\text{pseudo}}. \quad (2)$$

The first term on the right-hand side is the regular interaction between particles, while the second term is the interaction each particle has with its pseudo-neighbors. Here, we consider the case that the regular interaction describes a binary Lennard-Jones (LJ) system, with 80% of the particles of type A and 20% of the particles of type B. Thus, the interaction between the particles i and j is given by

$$u(r_{ij}) = 4\epsilon_{ij} \left[\left(\frac{\sigma_{ij}}{r_{ij}} \right)^{12} - \left(\frac{\sigma_{ij}}{r_{ij}} \right)^6 \right], \quad (3)$$

where r_{ij} is the distance between the particles, σ_{ij} is the effective diameter of the particle, and ϵ_{ij} is the interaction strength. We use σ_{AA} and ϵ_{AA} as the unit of length and energy, setting the Boltzmann constant $k_B = 1$. The values of the other parameters are given in Ref. 9, i.e., $\sigma_{AB} = 0.8$, $\sigma_{BB} = 0.88$, $\epsilon_{AB} = 1.5$, and $\epsilon_{BB} = 0.5$, a choice that makes this binary system to be a good glass former. This potential is cut and shifted at $r_c = 2.5\sigma_{ij}$. The masses are $m_A = m_B = 1$ and time is expressed in units of $\sqrt{m_A \sigma_{AA}^2 / \epsilon_{AA}}$.

The interaction potential with the pseudo-neighbors is modeled in terms of a modified LJ potential,

$$u^{\text{pseudo}}(r_{ij}) = u(r_{ij} - L_{ij}) \quad (4)$$

$$= 4\epsilon_{ij} \left[\left(\frac{\sigma_{ij}}{r_{ij} - L_{ij}} \right)^{12} - \left(\frac{\sigma_{ij}}{r_{ij} - L_{ij}} \right)^6 \right], \quad (5)$$

where L_{ij} is a random variable defined below. In our simulations, we impose the restriction that any two particles interact either via $u(r_{ij})$ or via $u^{\text{pseudo}}(r_{ij})$. This condition determines how for a given configuration equilibrated with the potential u , the pseudo-neighbors and

the values L_{ij} are chosen: Taking this configurations, we select for each particle, i , k random numbers L_{ij} in the range $r_c \leq L_{ij} \leq L_{\max}$, where $L_{\max} \leq L_{\text{box}}/2 - r_c$, with L_{box} being the size of the simulation box. (The distribution of these random variables will be denoted by $\mathcal{P}(L_{ij})$, and in the following, we will consider the case that the distribution is uniform.) Subsequently, we choose k distinct particles j with $r_{ij} > r_c$ and use the L_{ij} to fix *permanently* the interaction between particles i and j . This procedure thus makes that each particle i interacts not only with the particles that are within the cutoff distance but in addition to k particles that can be far away. Note that once the particle j is chosen as a pseudo-neighbor of particle i , automatically particle i becomes a pseudo-neighbor of particle j which gives rise with the 1/2 factor in the second term of Eq. (1). The system, as defined here, can then be simulated using standard simulation algorithms.

The molecular dynamics (MD) simulation have been done using $N = 2744$ particles. We have performed constant volume, constant temperature simulations (velocity rescaling) at density $\rho = 1.2$, thus $L_{\text{box}} = 13.1745$, using a time integration step of $\Delta t = 0.005$. For L_{\max} , we have taken 4.0, slightly below the maximum value of 4.09. We have simulated four different systems with the number of pseudo-neighbors $k = 0, 4, 12$, and 28.

III. RESULTS

A. Structure of the liquid

To start, we discuss the effect of the pseudo-neighbors on the structure of the liquid. In Fig. 1, we show the three partial radial distribution function, $g_{\alpha\beta}(r)$, with $\alpha, \beta \in \{A, B\}$,³¹ for the $k = 0$ and the $k = 28$ systems. The temperature is $T = 0.9$, which for the $k = 0$ system is slightly above the onset temperature (see Ref. 9), while for the $k = 28$ system, it corresponds to a state at which the system is already rather viscous (see below). The graph shows that the radial distribution functions for the two systems overlap perfectly well, i.e., the structure is independent of k for this value of k . Thus, this indicates

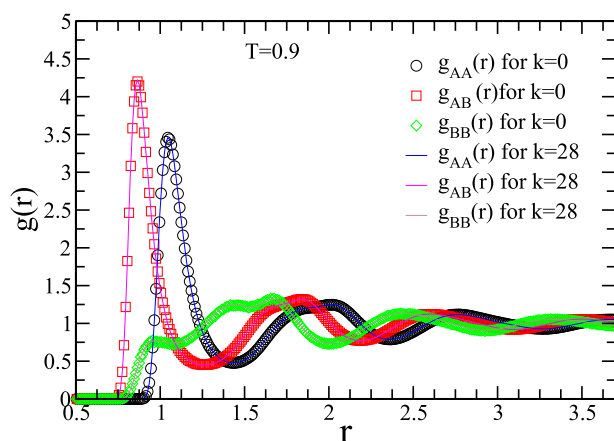


FIG. 1. The partial radial distribution functions for $k = 0$ and $k = 28$ at $T = 0.9$. The structure remains invariant under the introduction of the pseudo-neighbors.

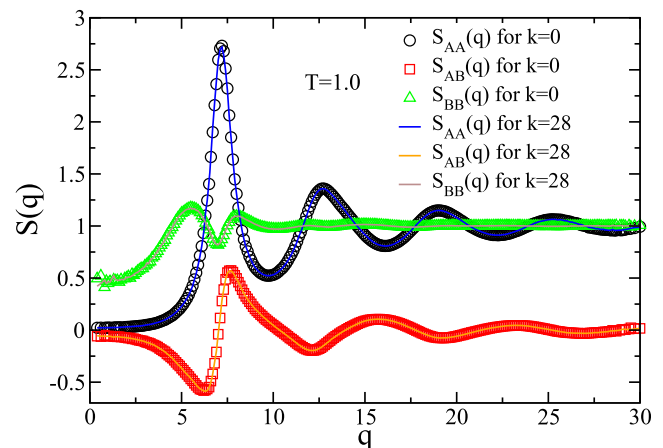


FIG. 2. The partial structure factors for $k = 0$ and $k = 28$ at $T = 1.0$. Similar to what we have obtained in the radial distribution function, the structure remains invariant under the introduction of the pseudo-neighbors.

that the interactions due to the pseudo-neighbors do not affect the local structure of the system, one of the reasons for our choice of the interactions of the model.

To probe whether the structure of the liquid on a large scale is influenced by the introduction of the pseudo-neighbors, we have calculated the partial static structure factors and show them in Fig. 2 for the case of $k = 0$ and $k = 28$. Since the two sets of curves match each other perfectly well, we can conclude that also the large scale structure is not influenced by the additional neighbors.

B. Static properties of the pseudo-neighbors

In this subsection, we characterize some of the structural properties of the pseudo-neighbors with respect to a tagged particle.

To start, we first calculate the probability P_L that a given pseudo-neighbor j interacts with the tagged particle i , where $L = L_{ij}$. Neglecting the indirect interactions (via the direct neighbors) between the tagged particle and the pseudo-neighbor, one can express P_L as

$$P_L = \frac{\int_{V_{\text{acc}}} d\mathbf{r} e^{-\beta u(r-L)} y(r)}{\int_{V_{\text{acc}}} d\mathbf{r} e^{-\beta u(r-L)}}. \quad (6)$$

Here, $\beta = 1/k_B T$, V_{acc} is the volume accessible to the pseudo-neighbor, and $y(r)$ is a step function that takes into account that the potential is cut off at $2.5\sigma_{\alpha\beta}$, i.e., $y(r) = 1$ if $L \leq r \leq L + 2.5\sigma_{\alpha\beta}$ and $y(r) = 0$ for all other values of r . The volume integrals in Eq. (6) can be decomposed into a spherical part that is contained inside the cubic box and the rest. The latter volume is given by

$$\Delta V = L_{\text{box}}^3 - \frac{4}{3}\pi \left(\frac{L_{\text{box}}}{2}\right)^3 \quad (7)$$

$$= L_{\text{box}}^3 \left(1 - \frac{\pi}{6}\right). \quad (8)$$

A spherical integration in Eq. (6) then gives

$$P_L = \frac{\int_L^{L+r_c} dr r^2 e^{-\beta u(r-L)}}{\int_L^{L_{\text{box}}/2} dr r^2 e^{-\beta u(r-L)} + \Delta V}. \quad (9)$$

Note that in Eq. (9), $L = L_{ij}$ is fixed. Hence, for a distribution of L , the probability of finding a pseudo-neighbor within the interaction range of the tagged particle is given by

$$P = \int_{r_c}^{L_{\text{max}}} dL \mathcal{P}(L) \frac{\int_L^{L+r_c} dr r^2 e^{-\beta u(r-L)}}{\int_L^{L_{\text{box}}/2} dr r^2 e^{-\beta u(r-L)} + \Delta V}. \quad (10)$$

In the numerator, we make the substitution $r' = r - L$, which allows us to interchange the two integrals,

$$P = \int_0^{r_c} dr' \int_{r_c}^{L_{\text{max}}} dL \mathcal{P}(L) \frac{(r' + L)^2 e^{-\beta u(r')}}{\int_L^{L_{\text{box}}/2} dr r^2 e^{-\beta u(r-L)} + \Delta V}. \quad (11)$$

We thus find that this probability is independent of k , a result that is reasonable since we have neglected any correlations between the pseudo-neighbors. Also note that P depends on the interaction potential via $u(r)$ and r_c . For a binary system, we can generalize this calculation to obtain the partial probabilities $P_{\alpha\beta}$, and then the total probability is given by

$$P = x_A^2 P_{AA} + 2x_A x_B P_{AB} + x_B^2 P_{BB}, \quad (12)$$

where x_α is the concentration of species α . In the simulation, this probability can be obtained by calculating the ratio k_e/k , where k_e is the number of pseudo-neighbors that have a non-zero interaction with the tagged particle. In Fig. 3, we show the temperature dependence of P as obtained from Eqs. (11) and (12) (solid line) and compare it with the corresponding quantity k_e/k determined from the simulations (symbols). One recognizes that k_e/k is as expected independent of k and that the simulation data match perfectly well the theoretical prediction given by Eqs. (11) and (12). Note that at the lowest temperatures at which we could equilibrate the systems for the different value of k , the probability is around 0.3, i.e., for the glassy dynamics, we will discuss below that only a relatively small part of the pseudo-neighbors actually interacts with the tagged particle. The inset of the figure shows that P becomes 0.5 at around $T = 0.4$, a temperature at which already the $k = 0$ system is very viscous,³² and for $T \rightarrow 0$, the probability becomes 1, as expected.

To characterize the relative position of a pseudo-neighbor j with respect to a tagged particle i , we can consider the corresponding radial distribution function,

$$g^{\text{pseudo}}(r') = \frac{\rho_k}{4\pi r'^2} \sum_{i=1}^N \sum_{j(i)}^k \langle \delta(r' - |\mathbf{r}_i - \mathbf{r}_j| + L_{ij}) \rangle, \quad (13)$$

where in the second sum, the index runs over the pseudo-neighbors of the tagged particle i and ρ_k is the average pseudo-neighbor density,

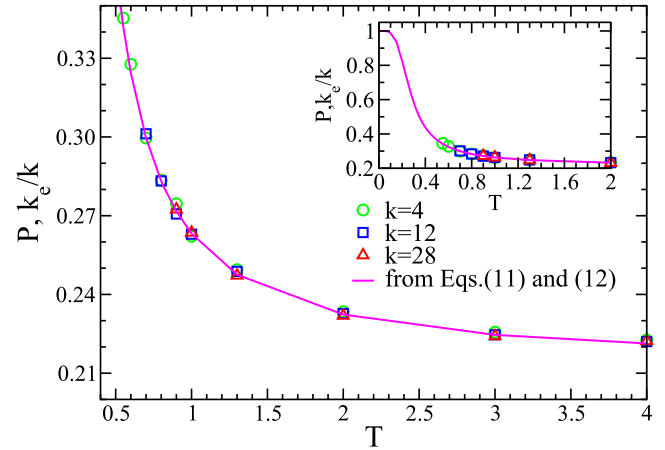


FIG. 3. Probability that a pseudo-neighbor is within the interaction range as a function of temperature. The pink line is the theoretical prediction from Eqs. (11) and (12). Inset: same quantities extending the temperature range to $T = 0$. The theoretical curve shows a sigmoidal shape.

$$\rho_k = \int_{r_c}^{L_{\text{max}}} \frac{k \mathcal{P}(L)}{V - \frac{4}{3}\pi L^3} dL, \quad (14)$$

where V is the total volume of the system.

To calculate $g^{\text{pseudo}}(r)$ analytically, we can make use of our result for P given by Eqs. (11) and (12). The number k_e of pseudo-neighbors within the interaction range can be expressed in terms of $g^{\text{pseudo}}(r')$ as

$$k_e = \rho_k \int_0^{r_c} dr' g^{\text{pseudo}}(r') \int_{r_c}^{L_{\text{max}}} dL \mathcal{P}(L) 4\pi (r' + L)^2. \quad (15)$$

Since k_e can also be written as $k_e = k \times P$, we get, using Eqs. (11) and (15),

$$\begin{aligned} g^{\text{pseudo}}(r') \rho_k \int_{r_c}^{L_{\text{max}}} dL \mathcal{P}(L) 4\pi (r' + L)^2 \\ = k \int_{r_c}^{L_{\text{max}}} dL \mathcal{P}(L) \frac{(r' + L)^2 e^{-\beta u(r')}}{\int_L^{L_{\text{box}}/2} dr r^2 e^{-\beta u(r-L)} + \Delta V} \end{aligned} \quad (16)$$

from which one obtains directly $g^{\text{pseudo}}(r')$. Note that $g^{\text{pseudo}}(r')$ is independent of k , since ρ_k is directly proportional to k [see Eq. (14)].

Figure 4 shows the radial distribution function $g^{\text{pseudo}}(r')$ from the simulations of three different values of k (symbols), and we recognize that, as predicted by Eq. (16), the function is indeed independent of k . We have also included the analytical result from Eq. (16), and we see that the theory describes perfectly well the simulation data, thus demonstrating that the approximation that the structure of the pseudo-neighbors can be obtained well by the bare interaction with the tagged particle is very accurate, at least for the k values considered in the present work. We also note that since one has the relation $g^{\text{pseudo}}(r') = \exp(-\beta u(r'))$, which can be derived from

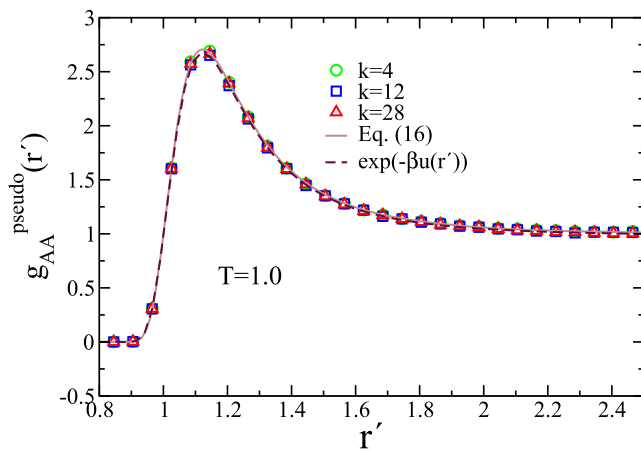


FIG. 4. Radial distribution function for pseudo-neighbors from simulations at $T = 1.0$ for $k = 4, 12,$ and 28 . The distribution function of the pseudo-neighbors is independent of k . The solid line is the result from the theoretical expression given by Eq. (16). The dashed line is the theoretical prediction from the bare potential.

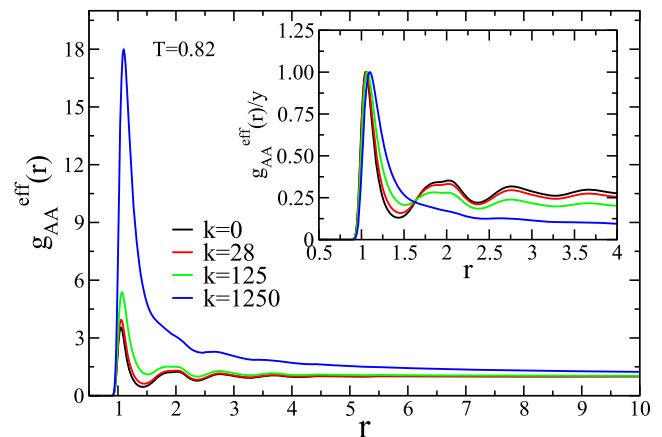


FIG. 5. The effective A–A particle radial distribution function for $k = 0, 28, 125,$ and 1250 . With the increase in k , the multi-peak structure disappears. Inset: $g_{AA}^{\text{eff}}(r)/y(k)$ vs r , where $y(k)$ is the height of the main peak. The smoothing of the undulation with the increase in k is clearly seen.

Eq. (16), the function $g^{\text{pseudo}}(r')$ can also be obtained directly from the bare interaction potential $u(r')$, as shown in Fig. 4.

Within the standard theory of liquids, the radial distribution function allows us to obtain the potential energy.³¹ Due to the presence of the pseudo-neighbors this is no longer possible, and thus the usual expression has to be modified as follows. (Note that in the following, we give the expressions for a one-component system. For the binary system considered here, one will have to do the sum over the various partials.) Since the potential energy of the system has two contributions, one is the regular neighbor and the other is the pseudo-neighbor [see Eq. (1)], the total potential energy U_{tot} is given by

$$\frac{U_{\text{tot}}}{N} = \frac{\rho}{2} \int_0^\infty u(r)g(r)4\pi r^2 dr + \frac{\rho k}{2} \int_0^\infty u(r)g^{\text{pseudo}}(r) \times \int_{r_c}^{L_{\text{max}}} \mathcal{P}(L)4\pi(r+L)^2 dL dr. \quad (17)$$

At this stage, it is useful to introduce an “effective radial distribution” function $g^{\text{eff}}(r)$ by defining

$$\rho_{\text{eff}}g^{\text{eff}}(r) = \rho g(r) + \rho_k g^{\text{pseudo}}(r) \frac{\int_{r_c}^{L_{\text{max}}} \mathcal{P}(L)(r+L)^2 dL}{r^2}, \quad (18)$$

where the effective particle density is given by

$$\rho_{\text{eff}} = \rho + \rho_k. \quad (19)$$

Note that since ρ_k increases linearly with k , for large k , the density ρ_{eff} is dominated by ρ_k , and hence in that limit, g^{eff} will be directly proportional to $g^{\text{pseudo}}(r)$.

Using $g^{\text{eff}}(r)$, we now can express the total potential energy of the system as a function of the radial distribution function $g^{\text{eff}}(r)$,

$$\frac{U_{\text{tot}}}{N} = \frac{\rho_{\text{eff}}}{2} \int_0^\infty u(r)g^{\text{eff}}(r)4\pi r^2 dr. \quad (20)$$

In Fig. 5, we present $g^{\text{eff}}(r)$ for the A–A correlation for different values of k . Since the regular radial distribution function $g(r)$ is independent of k (see Fig. 1) and $g^{\text{pseudo}}(r)$ can be calculated analytically from Eq. (16), it is possible to obtain g^{eff} for arbitrary values of k . The graph shows that with the increase in k , the radial distribution function loses its characteristic structure with the multiple peaks and converges toward a distribution that has a single peak at $r = 1$. This result can be understood directly from Eq. (18) since for large k , the first term on the right-hand side vanishes (if divided by ρ_{eff}), while the second term is $g^{\text{pseudo}}(r)$ multiplied by an r -dependent factor that is independent of k . Hence, we see that in the large k limit, the effective radial distribution function develops a dominant sharp peak at a finite distance. With the decrease in temperature, this peak increases since most of the pseudo-neighbors will condensate at the optimal distance L_{ij} . It is this growing peak that signals the increasing number of constraints in the system, which induce the slowdown of the relaxation dynamics. This loss of structure of the radial distribution function is a typical signature of mean-field-like systems, such as the hard-sphere system of Ref. 23. (However, unlike the results in the present study, in the hard-sphere system, there is no peak at $r = 1$.)

C. Relaxation dynamics

We now analyze how the presence of the pseudo-neighbors affects the relaxation dynamics. To characterize this dynamics, we consider the self-part of the overlap function $Q(t)$ and the mean

squared displacement (MSD) of a tagged particle, $\Delta r^2(t)$. The former observable is defined as

$$Q(t) = \frac{1}{N} \sum_{i=1}^N \langle \omega(|\mathbf{r}_i(t) - \mathbf{r}_i(0)|) \rangle, \quad (21)$$

where the function $\omega(x)$ is 1 if $0 \leq x \leq a$ and $\omega(x) = 0$ otherwise. The parameter a is chosen to be 0.3, a value that is slightly larger than the size of the cage (determined from the height of the plateau in the MSD at intermediate times.⁹) Thus, the quantity $Q(t)$ tells whether or not at time t , a tagged particle is still inside the cage it occupied at $t = 0$.

In Fig. 6, we show the time dependence of $Q(t)$ for different values of k . The temperature is $T = 0.9$, which corresponds for $k = 0$ to a T that is around the onset temperature.^{9,33} The graph demonstrates that with the increase in k , the relaxation dynamics slows down quickly in that the correlator for $k = 28$ decays on a time scale that is about two orders of magnitude larger than the one for $k = 0$. Also note that for the largest k , we clearly see a two-step relaxation, i.e., the hallmark of glassy dynamics in which the particles are temporally trapped by their neighbors,¹ while for $k = 0$, one has just a simple one-step relaxation, i.e., a normal liquid state relaxation. These results demonstrate that the presence of the pseudo-neighbors does have the sought after effect of strongly slowing down the relaxation dynamics of the system, although, as demonstrated above, the overall structure of the liquid is not changed. Interestingly, the shape of the time correlation function in the α -relaxation regime does not seem to have a noticeable dependence on k , indicating that the relaxation mechanism is weakly dependent on k . However, this conclusion only holds for length scales on the order of “ a ,” while it could be noticeable on larger length scales. Here, we also note that for other mean-field-like models, such as the one introduced by Mari and Kurchan,²³ an increase in the interaction range leads to an *acceleration* of the dynamics, i.e., the sought slowing down of the dynamics is not necessarily guaranteed.

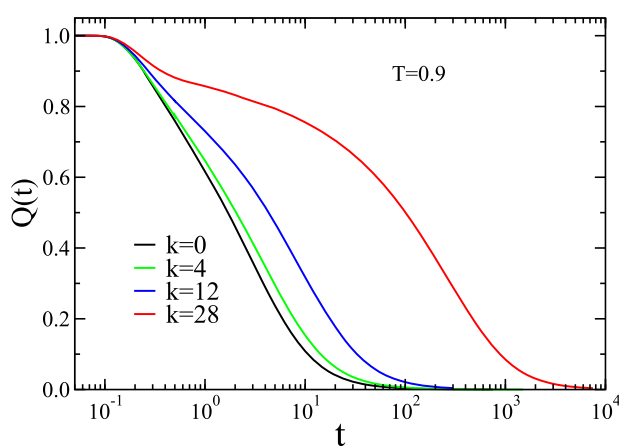


FIG. 6. Time dependence of the self overlap function $Q(t)$ for systems with different values of k at $T = 0.9$. With the increase in k , the relaxation dynamics quickly slows down.

Next, we compare the time dependence of the mean squared displacement, averaged over all the particles, of two systems: $k = 0$ and $k = 28$ (Fig. 7). For the $k = 0$ system, we show the MSD for $T = 0.82$, i.e., a temperature close to the onset T , and as a consequence one sees that the curve shows between the ballistic regime at short times, $\Delta r^2(t) \propto t^2$, and the diffusive regime at long times, $\Delta r^2(t) \propto t^1$, a weak shoulder. Qualitatively, the same time dependence is found for the $k = 28$ system, but this time at the higher temperature, $T = 1.5$, indicating that the increase in k leads to an increase in the onset temperature. If for the $k = 0$ system, the temperature is lowered to 0.445, the MSD shows at intermediate times a very pronounced plateau that is due to the temporary caging of the particles.¹ The same behavior is found in the $k = 28$ system at $T = 0.82$ with a plateau height and length that is very close to the one of the $k = 0$ system. (This similarity is due to our choice of the temperature $T = 0.82$.) Since we have seen above that the local structure of the system at fixed temperature hardly depends on k (see Fig. 1), the pronounced caging for the $k = 28$ system (at $T = 0.82$) is thus due to the pseudo-neighbors, i.e., the non-local interactions. From these curves, we hence can conclude that the presence of the additional interactions leads to a substantial slowing down of the relaxation dynamics, while the details of the MSD, such as the height of the plateau or its width, at the same effective temperature (discussed below) are modified only mildly, at least in the parameter regime probed here.

At sufficiently long times, the motion of the particles is expected to be diffusive, and hence the MSD should increase linearly in time. Figure 7 shows that for the $k = 0$ system, this is indeed the case and that this diffusion sets in once the MSD has reached a value around 1.0. Interestingly, one observes for the $k = 28$ system even at the longest times a sub-diffusive behavior, with an exponent that is around 0.8, and even for values of the MSD that are on the order of 10. This behavior can be noticed better by calculating the slope of the MSD in the log-log presentation (see Fig. 8). For $k = 0$, panel (a),

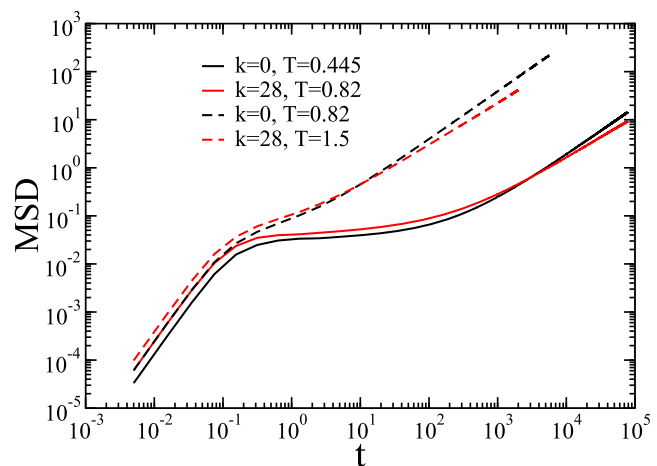


FIG. 7. Time dependence of the mean squared displacement for the $k = 0$ and $k = 28$ systems in the high and low temperature regimes. The curves are for similar values of the relaxation time. The $k = 28$ system shows a weak sub-diffusive behavior at high and low temperatures.

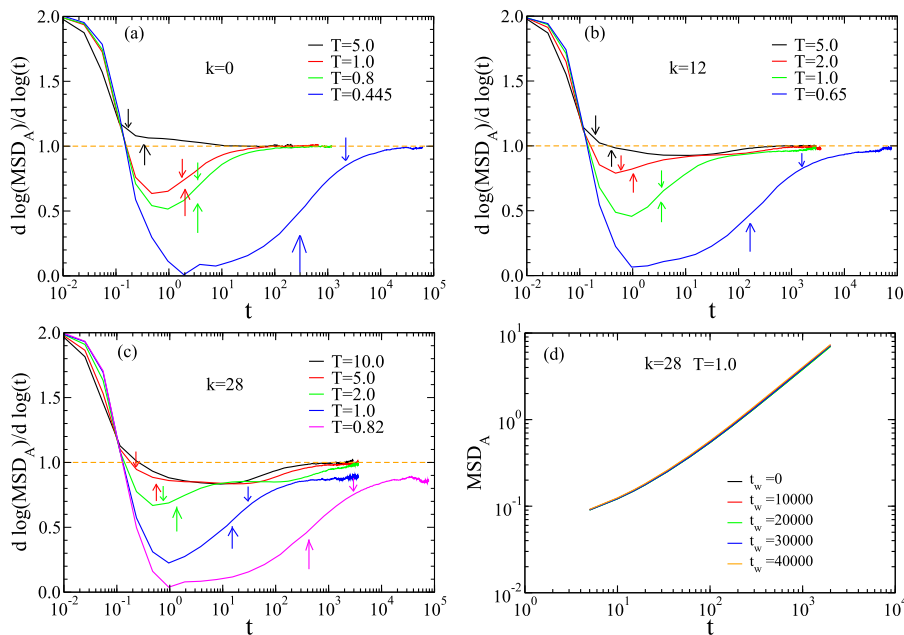


FIG. 8. Double-logarithmic derivative of the MSD of the A particles as a function of time. (a) System for $k = 0$. If temperature is decreased, the derivative shows at low T a local minimum, indicating the presence of caging. (b) System for $k = 12$. Qualitatively, the same time dependence as in panel (a) but now at higher temperatures. (c) System for $k = 28$. One sees that the curves show at intermediate times a plateau that is due to the caging caused by the pseudo-neighbors. The arrows pointing upward [downward] in panels (a)–(c) indicate τ_2 [τ_4], the location of the peak in the non-Gaussian parameter $\alpha_2(t)$ [in the dynamic susceptibility $\chi_4(t)$]. (d) MSD of the A particles for different waiting times t_w (see the legend). No waiting time dependence is noticeable.

we see that at short times, the slope is 2.0, as expected for a ballistic motion. At high temperatures, the slope crosses over to 1.0 at around $t = 3$, i.e., the system becomes diffusive. If T is lowered, the slope starts to show a dip with a depth and width that increase rapidly with the decrease in temperature. For long times, we see, however, that the curves again attain the value of 1.0, i.e., the system is diffusive. Qualitatively, the same behavior is found for $k = 4$ (not shown) and $k = 12$ [panel (b)]. However, a closer inspection of the curve for $T = 2.0$ reveals that after the first dip in the slope, the curve does not rise immediately to the value 1.0 but shows instead a plateau at a height of around 0.9 in the time window, $5 \leq t \leq 200$. The asymptotic value 1.0 is thus reached only at longer times, i.e., the MSD shows a sub-diffusive regime. Qualitatively, the same behavior is found for $k = 28$ [panel (c)], but now, the mentioned plateau at intermediate times becomes more visible since its height has decreased to 0.8, i.e., the deviation from the diffusive regime becomes more pronounced. We now clearly see that if the temperature is lowered, the curves reach this second plateau at a later time, but its height is unchanged (see the curves for $T = 1.0$ and 0.82). Note that this plateau at long times is indeed a distinct dynamic regime and not just a brief transient during which the system approaches the diffusive limit. We also exclude the possibility that this new plateau is just an out-of-equilibrium phenomenon since [see panel (d)] the MSD for different waiting times shows no waiting time dependence. We interpret this new regime as a consequence of the interaction of the tagged particle with its pseudo-neighbors. These interactions will vanish only if all the involved pairs have moved by a radial distance of around r_c , and, because of geometrical reasons (the volume of the spherical cap increases with L_{ij}) and the fact that $L_{ij} > r_c$, this takes certainly more time than cutting just the interactions between the tagged particle and its nearest neighbors, which explains the long time tail in the MSD. Note, however, that for sufficiently long times, the MSD can

be expected to become diffusive for all values of k [see the curve for $T = 2.0$ in panel (c)]. This behavior is thus similar to that observed earlier in systems where there are two length scales.³⁴ In order to distinguish in the following the two mentioned processes, we will refer to the one corresponding to the particles leaving their nearest neighbor (NN) cage as the “NN- α process,” while the dynamics in which the pseudo-neighbors (PN) leave the interaction range of the tagged particle will be referred to as the “PN- α process.” Note that although Fig. 8 clearly indicates that there are two processes, we will see in the following that not all observables reveal this in a direct manner. For example, the time dependence of $Q(t)$, presented in Fig. 6, does not indicate an obvious presence of two different α -processes, although the pseudo-neighbors can be expected to affect not only the relaxation time but also the details of the correlator.

Since the onset temperature is an important point on the energy scale of the system, we now have a closer look at the k -dependence of T_{onset} . As mentioned above, this temperature can be identified from the first occurrence of a plateau in the MSD. Alternatively, one can study the inherent structure energy, E_{IS} , which shows at T_{onset} a marked change in its T -dependence.^{35,36} (We recall that E_{IS} of a configuration is the potential energy evaluated at the local minimum of the energy reached from the configuration via the steepest descent procedure.) In Fig. 9(a), we show E_{IS} as a function of T , with the different curves corresponding to different values of k . From the graph, one recognizes that with the increase in k , the energy decreases, an effect that is due to the presence of the pseudo-neighbors, which can lower the energy by occupying the well in the interaction potential. Less trivial is the fact that the temperature at which the curve starts to decrease rapidly, i.e., the onset temperature, increases with the increase in k . Thus, the increase in T_{onset} with k can be seen directly from this static observable. In order

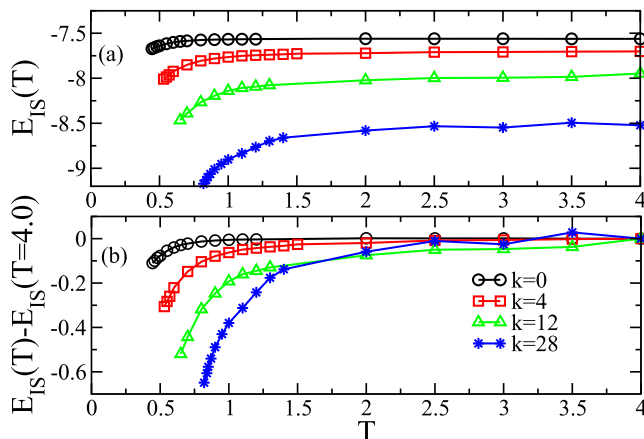


FIG. 9. (a) Inherent structure energy, E_{IS} , as a function of temperature for the $k = 0, 4, 12,$ and 28 systems. (b) Shifted [by $E_{IS}(T = 4.0)$] inherent structure energy vs T . Near T_{onset} , the energy starts to deviate from its high temperature value, allowing us to determine T_{onset} . With the increase in k , T_{onset} moves to higher temperatures.

to see better the k -dependence of T_{onset} , we plot in Fig. 9(b) the inherent structure energy shifted by $E_{IS}(T = 4.0)$. (The choice of $T = 4.0$ for this normalization is not crucial.) The resulting graph clearly shows that the bend in the inherent structure energy occurs at higher temperatures with growing k , demonstrating the increase in the onset temperature. Fitting two straight lines to the data for $T > T_{\text{onset}}$ and $T < T_{\text{onset}}$, their intersection point can be used to determine T_{onset} . As we will show elsewhere,⁵⁷ only for the $k = 0$ system, the so obtained values are compatible with the values of onset temperature, as determined from the entropy.³³ In Table I, we list the values of T_{onset} obtained from these curves, and one sees that for $k = 28$, this temperature is about 90% higher than T_{onset} for $k = 0$.

A further important quantity to characterize the relaxation dynamics of a glass-former is the α -relaxation time τ . Here, we define this time scale via $Q(\tau) = 1/e$. This definition is reasonable since we have seen in Fig. 6 that the shape of the time correlation functions is basically independent of k . (Note that with this definition of τ , we

do not distinguish between the NN- α process and the PN- α process discussed in the context of Fig. 6. For the values of k considered here, this is justified since the final decay of $Q(t)$ involves both processes.) Figure 10(a) is an Arrhenius plot of τ for the different systems. One clearly sees that with the increase in k , the dynamics quickly slows down and that the bending of the curve seems to increase, i.e., the system becomes more fragile. To quantify this trend as a function of k , we have fitted $\tau(T, k)$ at intermediate and low temperatures to a Vogel-Fulcher-Tammann (VFT) law,

$$\tau(T) = \tau_0 \exp\left[\frac{1}{K(T/T_0 - 1)}\right]. \quad (22)$$

Here, T_0 is the so-called VFT temperature at which the relaxation time of the system is predicted to diverge. The parameter K describes the curvature of the data in an Arrhenius plot and hence can be considered as a measure for the fragility of the glass former. The figure demonstrates that this functional form gives a good fit to the data (solid lines) and hence allows us to estimate T_0 and K .

The values of T_0 are included in Table I as well and one sees that T_0 changes by about a factor of 2 if k is increased from 0 to 28, i.e., a factor that is comparable to the one found for T_{onset} . In contrast to this, we find that the parameter K occurring in the Vogel-Fulcher-Tammann law [Eq. (22)] increases by about 30% in the considered k -range (see Table I). This indicates that the introduction of the pseudo-neighbors renders the system increasingly more fragile. Another way to see this is to define an effective glass transition temperature T_g via $\tau(T_g) = 10^3$ and to plot the relaxation time as a function of T_g/T .^{1,38} This is done in Fig. 10(b), and one sees that the curves for large k are indeed more bent than the ones for small k , i.e., the fragility of the system increases with k . This trend is thus qualitatively similar to the observation of Ref. 29 in which it was found that increasing the dimensionality of a glass former gives rise to a higher fragility.

Since the MSD has shown that the system has two kinds of α -processes, it is useful to study how the corresponding relaxation times relate to each other. For the $k > 0$ systems, particles are caged by their nearest neighbors as well as by their pseudo-neighbors. When a particle leaves its NN cage, the overlap function decays and this timescale is captured by τ . We now define a relaxation time τ_D

TABLE I. The value of the characteristic temperatures and the kinetic fragility parameter for systems with different values of k . T_{onset} is the onset temperature at which the inherent structure energy starts to deviate significantly from its high temperature value. T_c is the MCT transition temperature. T_0 is the singular temperature of the Vogel-Fulcher-Tammann equation [Eq. (22)]. All characteristic temperatures increase with the increase in k . Also included are the normalized differences between various temperatures. K is the kinetic fragility defined in Eq. (22). $x(k)$ is the prefactor needed for the scaling plot shown in Fig. 11(b).

k	T_{onset}	T_c	T_0	$\frac{T_{\text{onset}} - T_c}{T_c}$	$\frac{T_{\text{onset}} - T_c}{T_{\text{onset}}}$	$\frac{T_{\text{onset}} - T_0}{T_0}$	$\frac{T_c - T_0}{T_0}$	K	$x(k)$
0	0.74 ± 0.04	0.43	0.283	0.72	0.42	1.61	0.52	0.184	1.0
4	0.83 ± 0.08	0.51	0.362	0.63	0.38	1.29	0.41	0.237	1.55
12	1.03 ± 0.07	0.62	0.465	0.66	0.40	1.22	0.33	0.286	2.0
28	1.28 ± 0.22	0.80	0.610	0.60	0.38	1.10	0.31	0.297	2.1

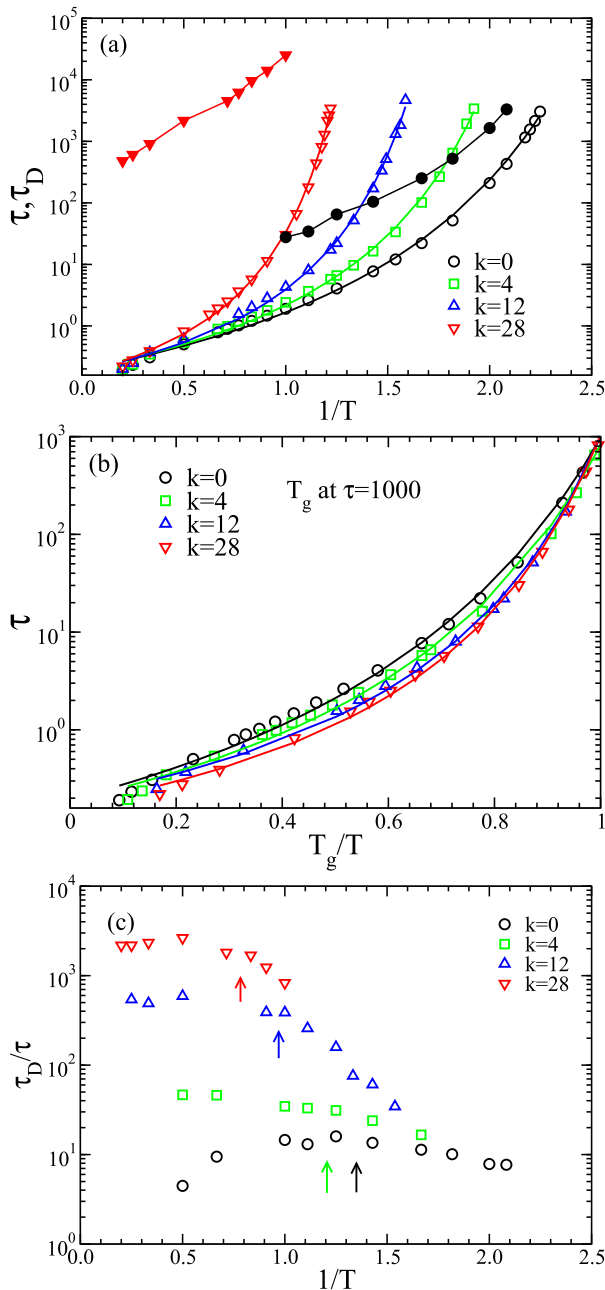


FIG. 10. (a) Arrhenius plot of the α -relaxation time, τ , and the relaxation time obtained from the MSD, τ_D , for systems with different values of k . Open and full symbols are for τ and τ_D , respectively. The lines are fits to τ with the Vogel–Fulcher–Tammann expression [Eq. (22)]. (b) Same data as in (a) but now as a function of the scaled temperature T_g/T , with $\tau(T_g) = 10^3$. (c) Temperature dependence of the ratio τ_D/τ for different values of k . The arrows indicate T_{onset} .

for the PN process as the time scale at which the system becomes diffusive, i.e., the time where the logarithmic derivative of the MSD goes to 1.³⁹ In practice, we consider $t = \tau_D$ for which $\frac{d \log(\text{MSD})}{d \log(t)} = 0.97$. In Fig. 10(a), we have included the T -dependence of τ_D for the

$k = 0$ and the $k = 28$ systems and one recognizes that τ_D is significantly larger than τ but that its T -dependence is weaker. To see the latter in a clearer way, we show in panel (c) the T -dependence of the ratio τ_D/τ for all values of k considered. We recognize that the ratio starts to decrease quickly for temperatures that are below T_{onset} , i.e., once the systems start to show glassy dynamics. Since this decrease is very pronounced for $k > 0$, we conclude that the slowing down of the overall dynamics of the system is mainly governed by the NN- α process (which is strongly influenced by the presence of the pseudo-neighbors).

These results show that the pseudo-neighbors strongly influence the relaxation dynamics of a tagged particle in that the leaving of the cage formed by the nearest neighbors is strongly slowed down, as indicated by $\tau(T)$. In addition, the pseudo-neighbors also induce a new slow process, the PN- α process, which is related to the motion of the pseudo-neighbors with respect to the tagged particle. However, this slow process does not depend very strongly on T , since there is no structural correlation between the pseudo-neighbors of a given tagged particle (this is in contrast to the nearest neighbors that are correlated because of the local steric hindrance). As a consequence, this slow PN- α process is *not* the mechanism responsible for the slowing down of the overall dynamics of the system. The relevant mechanism for this is thus given by the NN- α process.

D. MCT power law

Having presented our findings regarding the relaxation dynamics of the system, we now probe whether this dynamics can be described by means of mode coupling theory. MCT predicts that close to the critical temperature T_c of the theory, the relaxation times show a power law divergence,

$$\tau(T) = \tau_{\text{MCT}}(T - T_c)^{-\gamma}. \quad (23)$$

Using this functional form to fit the temperature dependence of the relaxation time, we obtain $T_c(k)$ (values are given in Table I). In Fig. 11(a), we present a log–log plot of the relaxation time as a function of the normalized temperature $(T - T_c)/T_c$. One recognizes that for $k = 0$, the increase in τ with the decrease in T is described well by a power law (dashed line), in agreement with previous simulations.^{9,40} However, at the lowest T 's, deviations are observed, and the increase in τ is weaker than the power law predicted by MCT. This deviation is usually attributed to the existence of “hopping processes,” i.e., a component in the relaxation dynamics that is not taken into account in the *idealized* version of the MCT. The two arrows in the plot delimit the T -range in which the power law gives a good description to the data.

For the system with $k = 28$, the temperature dependence of τ is qualitatively very similar to the one for the $k = 0$ system, if one plots the data as a function of the reduced temperature $(T - T_c)/T_c$. The highest temperature at which the data follows the power law (dashed line), marked by an arrow, is around $2 T_c$ and very close to the corresponding reduced temperature for the $k = 0$ system. However, the lower (reduced) temperature at which τ starts to deviate from this power law (see the arrow) is smaller for the $k = 28$ system than the corresponding T for the $k = 0$ system, showing that for the former system, the mentioned hopping processes are less important, i.e., the system is more mean-field-like. For the $k = 28$ system, this lower

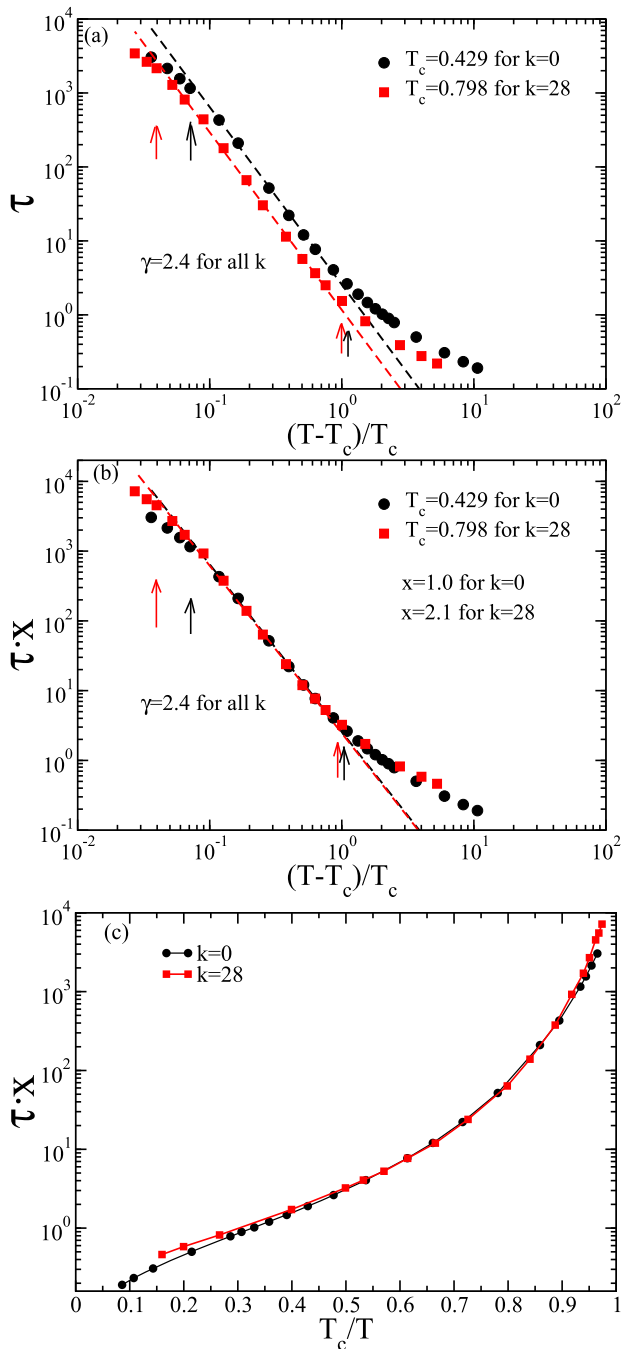


FIG. 11. (a) The relaxation time obtained from the overlap function as a function of the scaled temperature $(T - T_c)/T_c$ for the $k = 0$ and the $k = 28$ systems. (b) Same data as in (a) but now with τ multiplied with a scaling factor $x(k)$. (c) Same data as in (b) as a function of $T_c(k)/T$.

limit is about a factor of 3 smaller than the limit for $k = 0$; thus, the T -range in which the idealized MCT can be expected to be reliable has increased significantly by the introduction of the pseudo-neighbors. In Table I, we have also included the value of T_c and one

recognizes that the critical temperature for $k = 28$ is about 90% higher than the one for $k = 0$, i.e., the k -dependence of T_c is very similar to the one of T_{onset} .

According to the analytical calculations for the mean-field p -spin model, for which there is no activated dynamics, the onset temperature coincides with the MCT temperature, which is also the temperature at which the dynamics diverges.^{41–43} (Note that this is only true in the thermodynamic limit, while for finite systems, one has very strong finite-size effects that completely wash out these transitions, see Ref. 44.) For the GCM it was found that the relative distance between the three temperatures T_{onset} , T_c , and T_0 is much smaller than the one we find here for the $k = 0$ system.^{26,28} Thus, the reduction of this relative distance with the increase in k , given in Table I, can also be taken as a signature of increasing mean-field-like behavior.

From Fig. 11(a), we recognize that the relaxation times for the $k = 28$ system are shorter than the ones for the $k = 0$ system if compared at the same reduced temperature. In fact, as plotted in Fig. 11(b) on an intermediate time scale, the two datasets can be superimposed with high accuracy by applying a multiplicative factor $x(k)$ (see Table I for values). Thus, we conclude that the main difference in the two datasets is the prefactor τ_{MCT} in Eq. (23). A decrease in τ_{MCT} implies a faster motion inside the cage, and this is, in fact, very reasonable since with the increase in k , the tagged particle interacts with more particles, thus making its effective cage stiffer. Another way to present this result is to plot the time scale $\tau \cdot x(k)$ as a function of T_c/T [see Fig. 11(c)]. We find that this representation of the data gives rise to a collapse of the curves for the different values of k , demonstrating that the T -dependence is indeed very similar at intermediate temperatures. Hence, we conclude that the introduction of the pseudo-neighbors does not only increase the α -relaxation time strongly but also increase somewhat the attempt frequency with which the particle tries to leave the cage.

E. Wave-vector dependence of relaxation process

The relaxation time of glass-forming systems depends on the observable considered. Within MCT, this dependence is, however, encoded in a prefactor, τ_{MCT} , in Eq. (23), while T_c and the exponent γ are expected to be independent of the observable. While for many glass-forming systems, this is indeed the case (see Ref. 10), the present system has at least two relevant length scales, the nearest neighbor distance and the mean distance between the particles and their pseudo-neighbors, and hence it is of interest whether the mention factorization works here as well. To probe this, we consider the self-intermediate scattering function $F_s(q, t)$, where q is the wave-vector,³¹

$$F_s(q, t) = \frac{1}{N} \sum_{j=1}^N \langle \exp[-iq \cdot (\mathbf{r}_j(t) - \mathbf{r}_j(0))] \rangle. \quad (24)$$

We define the relaxation time $\tau(q)$ via $F_s(q, \tau(q)) = 1/e$ and thus can study its dependence on the length scale. In Fig. 12, we show the q -dependence of $\tau(q)$ for three values of k . Since one expects that at small wave-vectors $\tau(q)$ is proportional to q^{-2} , i.e., the hydrodynamic behavior, we plot directly $q^2 \tau(q)$. Panel (a) is for a fixed reduced temperature slightly below the onset temperature, while panel (b) corresponds to a significantly supercooled state. In

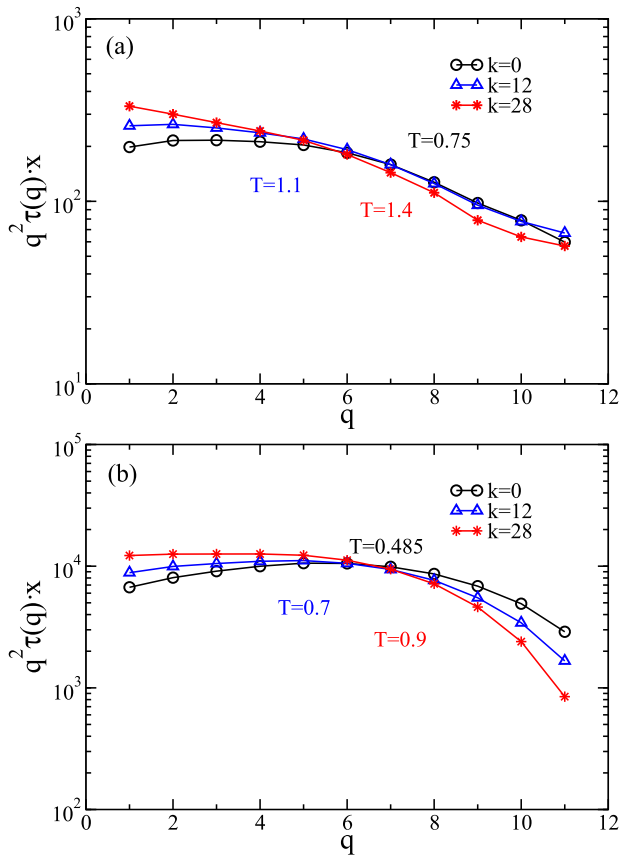


FIG. 12. $q^2 \tau(q) \cdot x(k)$ as a function of the wave-vector q . Panels (a) and (b) are for two different reduced temperatures. The values of $x(k)$ are given in Table I.

the context of Fig. 11(b), we have seen that, at a fixed reduced temperature, the relaxation time τ , obtained from the decay of the overlap function, shows a weak dependence on k , leading to the introduction of the factor $x(k)$. In order to take into account this k -dependence, we have multiplied also in Fig. 12 the relaxation times $\tau(q)$ with the *same* factor $x(k)$. The graphs show that for $q \approx 6.5$, i.e., close to the peak of the static structure factor, the relaxation times for the different systems coincide perfectly, which demonstrates that for this wave-vector, the overlap and $F_s(q, t)$ probe the same type of dynamics. For the other wave-vectors considered, the $\tau(q)$ curves for the different systems show a q -dependence that depends on k , but this dependence is relatively weak. Hence, we conclude that the presence of the pseudo-neighbors does not introduce a new length scale that influences the relaxation dynamics in a significant manner.

F. Dynamic heterogeneity

One of the hallmarks of glassy dynamics is that time correlation functions are stretched in time. The reason for this non-Debye relaxation has been a long-standing puzzle with the contrasting views that each small domain of the sample shows the same stretched

time dependence or, alternatively, that the stretching is related to dynamical heterogeneities (DHs).⁴⁵ Experiments and simulations have shown that the homogeneous scenario is not compatible with the observations, i.e., glass-forming systems do have a significant amount of dynamical heterogeneities (DH).^{46–50} In this final section, we therefore discuss the existence of these DHs and probe whether with the increase in k , one does indeed find a decrease in these fluctuations, the behavior expected for a mean-field system.

One first step to probe the DH is to look at the so-called non-Gaussian parameter (NGP) $\alpha_2(t)$, which is defined by

$$\alpha_2(t) = \frac{3 \langle r^4(t) \rangle}{5 \langle r^2(t) \rangle^2} - 1, \quad (25)$$

where $r(t)$ is the displacement of a tagged particle within a time t . Thus, $\alpha_2(t)$ measures whether or not the distribution of the particle displacement is Gaussian.^{9,46,51,52}

In Fig. 13(a), we plot the NGP for the $k = 28$ system. Interestingly, one finds that at high temperatures, $\alpha_2(t)$ has *two* peaks:

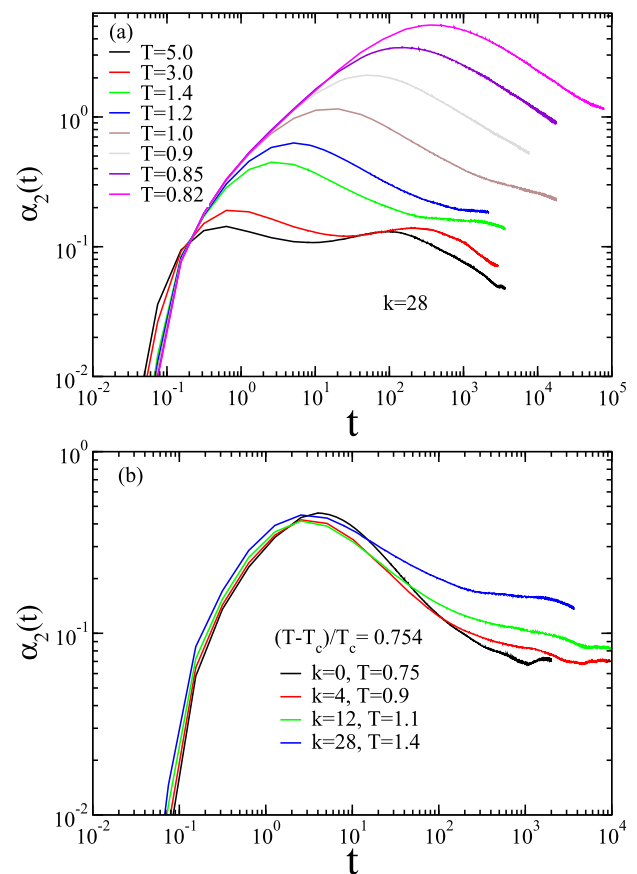


FIG. 13. (a) The time dependence of the non-Gaussian parameter, α_2 , at different temperatures for the $k = 28$ system. $\alpha_2(t)$ shows a double peak structure. (b) $\alpha_2(t)$ at fixed reduced temperature and different values of k . The peak at short times is independent of k , while the one at long times grows with the increase in k .

A first one at t around 0.6 and a second one at $t \approx 150$. The first time is close to the timescale at which the MSD crosses over from the ballistic regime to the diffusive one and thus corresponds to the start of the NN- α process, in agreement with earlier studies.⁹ The second peak has so far not been seen in the glass-forming systems considered before and is likely due to the breaking of the bonds with the pseudo-neighbors, i.e., the PN- α relaxation. Note that the presence of this second peak is coherent with our findings for the MSD [see Fig. 8(c)], for which we observed a plateau in the slope that, for $T = 2.0$, ended at around $t = 10^2$ and we had argued that this is due to the motion of the pseudo-neighbors. If T is lowered, the first peak in $\alpha_2(t)$ rises quickly and dominates the second peak, i.e., overall, the time dependence of the NGP becomes again quite similar to the one that has been observed in the previous studies of glass-forming systems. The main difference is that in our case, the second peak will make the decay of $\alpha_2(t)$ slow since at long times, the dynamics will be influenced by the pseudo-neighbors, which decorrelate only slowly (see the data for the MSD in Fig. 8).

The influence of the pseudo-neighbors on $\alpha_2(t)$ is shown in Fig. 13(b) where we plot this function for different values of k but keep $(T - T_c)/T_c$ constant. One sees that at short and intermediate times, i.e., around the peak, the curves are independent of k , which shows that the NN- α process is not affected by the presence of the pseudo-neighbors. Only at longer times, the curves for large k are higher than the ones for small k , showing that the pseudo-neighbors affect the NGP only at time scales that are beyond the time scale of the first maximum in the NGP. Since with the decrease in temperature, the peak corresponding to the NN- α relaxation grows quicker than the second peak, we can conclude that the dominant feature in $\alpha_2(t)$ is due to the NN- α process, except if k becomes much larger than the values we consider here.

In Fig. 14, we show α_2^p , the height of the peak in $\alpha_2(t)$, as a function of the reduced temperature $(T - T_c)/T_c$. Surprisingly, we find that this quantity is completely independent of k , i.e., the strength of the non-Gaussianity of the relaxation dynamics does not depend on whether or not the system is mean-field-like. In other words, the

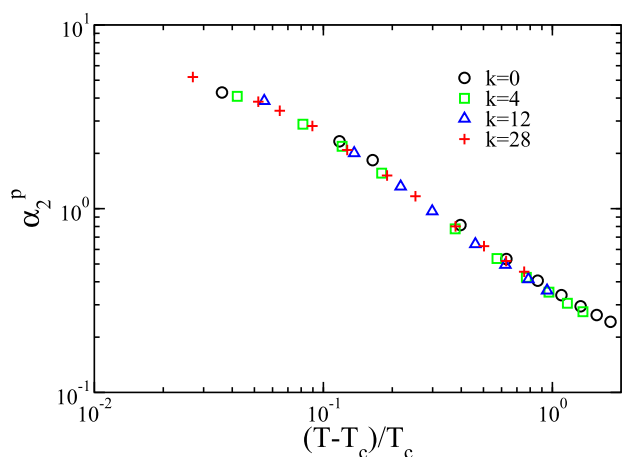


FIG. 14. The peak height of $\alpha_2(t)$ as a function of the reduced temperature $(T - T_c)/T_c$ for different values of k .

statistics of the displacement of a tagged particle is independent of the number of pseudo-neighbors, if measured at the same reduced temperature. This result reflects the fact that the first peak in $\alpha_2(t)$ is dominated by the dynamics in which the tagged particle leaves the cage formed by its nearest neighbors.

Note that α_2^p shows a bend at around $(T - T_c)/T_c \approx 0.1$. Although we did not investigate the origin of this change in the T -dependence, we expect it to be the signature of the onset of the hopping processes mentioned above. The bend indicates that these processes start to become prominent at around 10% above T_c , a value that seems to be coherent with the observation from Fig. 11 regarding the T -dependence of the relaxation times.

One might wonder whether the master curve in Fig. 14 is just due to the choice of the scaling factor of the temperatures, i.e., T_c . To test this possibility, we show in Fig. 15 the same data as a function of the relaxation time τ multiplied by the same factor $x(k)$ that was used to obtain a master curve in Fig. 11(b). We recognize that this representation leads to a very nice collapse of the data onto a master curve, which, for intermediate and long relaxation times, can be described well with a power law with an exponent close to 0.36 (see solid line in the figure). It is remarkable that the hopping processes discussed above, which lead to the bends in the different curves if the temperature approaches T_c , do not seem to affect the validity of the power law. At present, it is not clear up to which value of τ this power law will hold, in particular, whether it will be observed at temperatures below T_c . Future studies on this point will certainly be of interest to understand better the relaxation dynamics of glass-forming liquids.

In Fig. 16, we plot τ_2 , the time at which $\alpha_2(t)$ peaks, as a function of the α -relaxation time τ . Surprisingly, we find that the two quantities show a simple relation with each other in the form of a power law with an exponent $\kappa = 0.70$ (solid line). This result can be rationalized within the framework of MCT as follows: $\alpha_2(t)$ is related to the shape of the self-part of the van Hove function in that it measures its deviation from a Gaussian.^{9,51} At the end of the caging regime, i.e., the β -relaxation, some of the particles will have already left their cage,

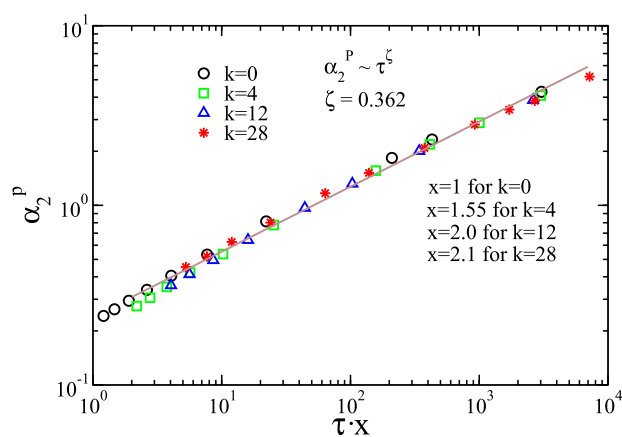


FIG. 15. The peak height of α_2 as a function of the α -relaxation time τ multiplied by $x(k)$ for different values of k . Also included is a fit to the data with a power law.

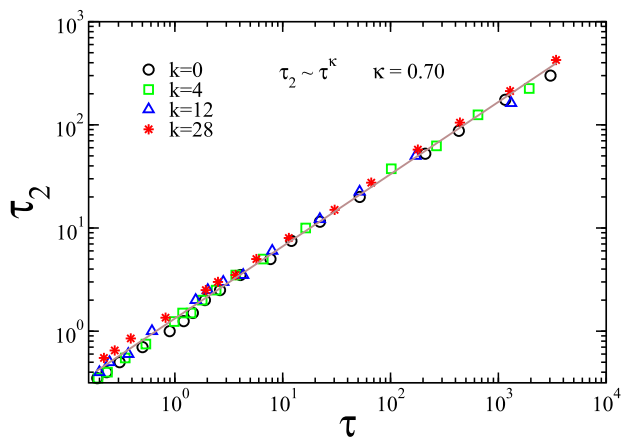


FIG. 16. The time scale τ_2 at which $\alpha_2(t)$ peaks as a function of the α -relaxation time τ . The solid line is a power law with an exponent $\kappa = 0.70$.

thus giving rise to a tail to the right of the main peak of the van Hove function. It is this tail that is responsible for the non-Gaussian shape of the van Hove function and hence leads to an increase in $\alpha_2(t)$. Thus, it is reasonable to assume that τ_2 is directly related to the time scale of the β -relaxation τ_β . MCT predicts that the latter time scale increases like

$$\tau_\beta \propto (T - T_c)^{-1/(2a)}. \quad (26)$$

The α -relaxation time τ is instead predicted by MCT to increase like

$$\tau \propto (T - T_c)^{-1/(2a)-1/(2b)} = (T - T_c)^{-\gamma}. \quad (27)$$

In Eqs. (26) and (27), the parameters a and b can, in principle, be calculated from the T -dependence of the static structure factor or, exploiting Eq. (27), determined from the T -dependence of the relaxation time.^{1,2,53} For the $k = 0$ system, it has been found that a is around 0.324 and b is around 0.627.^{9,53-55} Combining these last two equations gives, under the assumption that $\tau_2 \propto \tau_\beta$,

$$\tau_2 \propto \tau^{b/(a+b)}. \quad (28)$$

Thus, we find a power law dependence with an exponent of 0.66 (using the mentioned values of a and b), which is indeed very close to our exponent κ from the fit (0.7). We mention here that the observed power law extends over the whole accessible range of τ , i.e., it also includes the temperature regime in which we expect hopping processes to be present. To the best of our knowledge, this simple connection between τ_2 and τ has not been reported before. Since, however, we find it to hold for all values of k , we expect it to be valid for other glass-forming systems as well, and hence, it will be of interest to check this in the future.

To get Eq. (28), we have made the assumption that τ_2 is proportional to τ_β . As argued above, this hypothesis is reasonable since

it can be expected that the non-Gaussian parameter peaks at a time at which a substantial number of particles start to leave their cage and MCT defines τ_β as the time at which the correlator starts to drop below the plateau at intermediate times.³ Previous studies have therefore made the assumption that τ_β can be determined from the minimum in the slope of the MSD.⁵⁶ However, we argue that such an identification might be misleading: For the case of a system with Newtonian dynamics, the phonons that govern the short-time dynamics mask the critical decay of the time correlation functions, thus also masking the correlation between the above-mentioned minimum and τ_β . (This effect is, however, absent if the system has a Brownian dynamics.⁵⁴) Therefore, we think it is more appropriate to determine τ_β from a quantity that is not directly influenced by these vibrational modes, such as the $\alpha_2(t)$ considered here. In Figs. 8(a)–8(c), we have also included for the various curves the times τ_2 , arrows pointing upward, and one sees that they do not correspond to the location of the minimum in the curves but that they are located at somewhat larger times, as expected because of the mentioned effect of the phonons. Although at present, we do not have any solid proof why τ_2 does indeed correspond to τ_β , our finding that the relation between τ_2 and τ given by Eq. (28) is obeyed by our data does speak in favor of this identification. More tests on this using a system with Brownian dynamics would certainly be useful to clarify this point further.

Finally, we show in Fig. 17 the time at which $\alpha_2(t)$ peaks, τ_2 , as a function of $(T - T_c)/T_c$. Since we have argued in the context of Fig. 11 that the k -dependence of τ will include a factor $x(k)$ that is related to the short time dynamics and we also showed that $\tau_2 \propto \tau^\kappa$ (Fig. 16), we plot directly $\tau_2 \cdot x(k)^\kappa$, with the values of $x(k)$ obtained from Fig. 11 and κ from Fig. 16. We recognize that the data for the different values of k fall nicely on a master curve, which follows a power law with an exponent around -1.54 . Also this result can be understood within the framework of MCT since Eq. (26) predicts that the slope should be given by $-1/(2a)$, which for $a = 0.324$ results in an exponent of -1.54 , in excellent agreement with the data from the fit in Fig. 17.

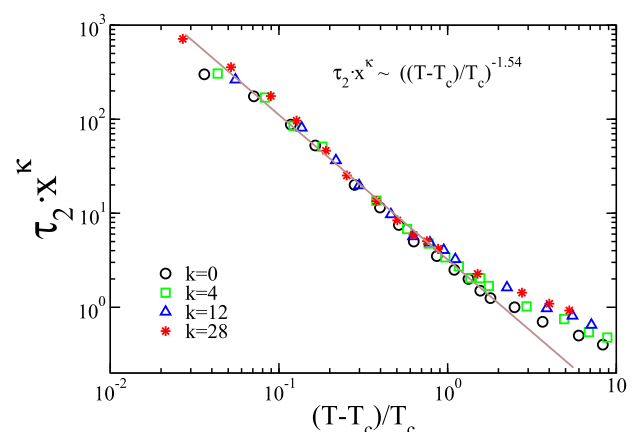


FIG. 17. $\tau_2 x(k)^\kappa$ as a function of the reduced temperature $(T - T_c)/T_c$. The solid line is a power law with an exponent of -1.54 .

Next, we discuss the other parameter that is often related to the dynamic heterogeneity, the dynamic susceptibility. The fluctuations of the overlap function $Q(t)$ are related to a dynamic susceptibility, which indicates whether or not the system relaxes in a cooperative manner, i.e., shows dynamical heterogeneities.^{32,57,58} Thus, one defines

$$\chi_4(t) = \frac{1}{N} [\langle Q^2(t) \rangle - \langle Q(t) \rangle^2] \quad (29)$$

as a measure to quantify this cooperativity. In Fig. 18(a), we show the time dependence of χ_4 for the system with $k = 28$ at different temperatures. In agreement with earlier studies,²⁹ we find that χ_4 shows a marked peak, the height of which increases with the decrease in temperature and also its position shifts to larger times upon decreasing T , i.e., the cooperativity becomes more pronounced and occurs at later times. In panel (b) of the figure, we present χ_4 for different values of k while keeping the normalized temperature $(T - T_c)/T_c$ constant. The graph demonstrates that with the increase in k , the height of the peak decreases quickly, indicating that

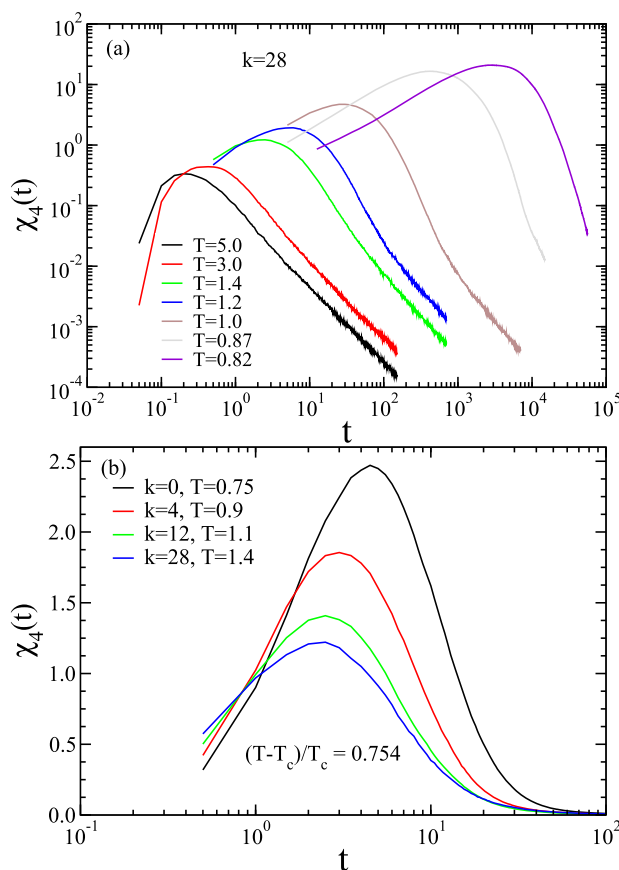


FIG. 18. (a) The time dependence of the dynamical susceptibility $\chi_4(t)$ for different temperatures for the $k = 28$ system. $\chi_4(t)$ increases with the decrease in temperature. (b) Time dependence of χ_4 at a fixed reduced temperature $(T - T_c)/T_c$ for different values of k .

the system does indeed become more mean-field-like, as expected, and in agreement with previous simulations of mean-field-like models.^{23,29} This k -dependence is thus very different from the one seen for the height of the peak in α_2 , highlighting the difference between the two quantities, despite their (apparently) similar time dependence. We also note that with the increase in k , the location of the peak in $\chi_4(t)$ shifts to shorter times, in qualitative agreement with the fact that, at fixed reduced temperature, the α -relaxation time decreases somewhat [see Fig. 11(a)].

To probe in more detail how the height of the peak in $\chi_4(t)$, χ_4^p , depends on T and k , we show in Fig. 19 this height as a function of the reduced temperature. We see immediately that this representation of the data does not give rise to a master curve. With the increase in k , the curves move downwards, a k -dependence that is in contrast to the one we found for α_2^p shown in Fig. 14. Thus, we conclude that with the increase in k , the dynamical heterogeneities decrease, i.e., the system becomes more mean-field-like. However, we point out that even in the mean-field limit, these heterogeneities cannot be expected to vanish completely,^{23,59} which shows that this aspect of the dynamics is a delicate feature that is highly non-trivial.

From the figure, one can conclude that for reduced temperatures higher than around 0.1, the height of the peak shows a power law dependence on the reduced temperature and we find an exponent of -1.2 that is independent of k , which implies that the dependence of χ_4^p on the number of pseudo-neighbors is encoded in the prefactor of the power law.

The presence of power laws in χ_4^p can be rationalized by means of MCT. This theory predicts that the dynamical susceptibility in the NVT ensemble is given by

$$\chi_4^{\text{NVT}}(t) = \chi_4^{\text{NVE}}(t) + \frac{T^2}{c_V} \left(\frac{dQ(t)}{dT} \right)^2, \quad (30)$$

where c_V is the specific heat at constant volume.^{32,57,58} Evaluating this expression at $t = \tau$, thus giving the height of the peak, χ_4^p ,

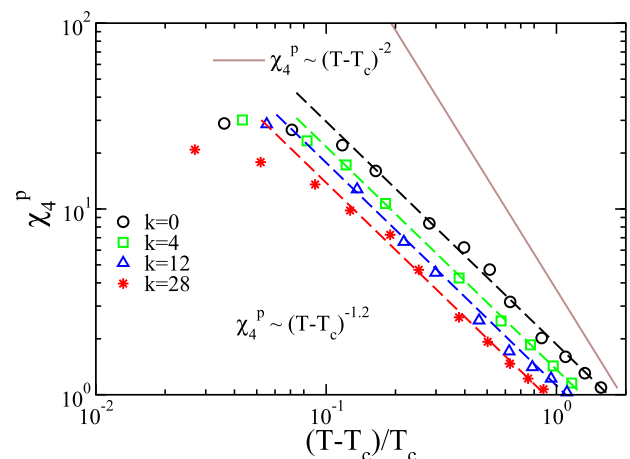


FIG. 19. Height of the peak in $\chi_4(t)$ as a function of the reduced temperature for different values of k . The dashed lines are power laws with an exponent of -1.2 and the solid line is a power law with an exponent of -2 .

one finds that the first term on the right-hand side of the equation increases like $(T - T_c)^{-1}$, while the second one is found to be proportional to $(T - T_c)^{-2}$. Hence, the power law with an exponent of -1.2 we found at intermediate and higher temperatures can be interpreted to be due to the power law from the first term, i.e., with an exponent -1.0 , which is somewhat augmented by the presence of the second term, thus giving rise to a power law with an effective exponent smaller than -1 . Thus, if the mentioned hopping processes would be absent, one would expect that at sufficiently low temperatures, the power law crosses over to one with an exponent -2 . Whether this is indeed the case will have to be tested for systems in which one is able to suppress these hopping processes, a work that is left for the future.

Since the representation of the data in Fig. 19 depends on the choice of T_c , it is also useful to look at the k -dependence of χ_4^p in a more direct manner. This is done in Fig. 20 where we plot this quantity as a function of the α -relaxation time τ . [Also here, we use $\tau \cdot x(t)$ as abscissa in order to take into account the trivial k dependence of the relaxation time.] We see that the shape of the curves for the different k is basically independent of k , but that the absolute value of χ_4^p at fixed $\tau \cdot x(k)$ decreases with the increase in k . (The same conclusion is reached if one uses just τ as the abscissa.) Hence, we confirm the conclusion from Fig. 18(b) that the heterogeneity of the system decreases with the increase in k . For small and intermediate values of τ , the data fall approximately on a straight line, and a power law fit gives an exponent of 0.51 (solid line). Expressing the T -dependence on the right hand side of Eq. (30) as a function of $\tau = (T - T_c)^{-\gamma}$ [see Eq. (23)], we obtain for the height of the peak

$$\chi_4^p = A\tau^{1/\gamma} + B\tau^{2/\gamma}, \quad (31)$$

where A and B are expressions that have only a weak T -dependence. Using our value $\gamma = 2.4$ gives for the exponent of the first and second term 0.42 and 0.83, respectively. These values are thus upper

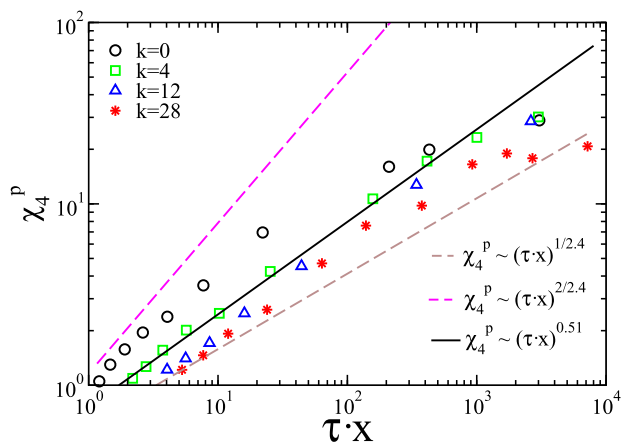


FIG. 20. The height of the peak in χ_4 as a function of $\tau \cdot x(k)$ for different values of k . The solid line is a power law fit to the data for $k = 4$. The two dashed lines are power laws with exponents that correspond to the theoretical upper and lower bounds from Eq. (31).

and lower bounds (included in Fig. 20 as well) and the exponent we extract from our data, 0.51, is thus not too far from the lower limit. Hence, although our data do not allow us to make strong statements about the validity of Eq. (31) because of the lack of sufficiently large window in the dynamics, we can at least say that our findings are compatible with the theoretical prediction, in agreement with the results from Ref. 32.

Finally, we note that for large τ , we find clear deviations of our data from the predicted power law in that the growth of χ_4^p is weaker than predicted. Hence, in this regime, we can again invoke the argument that hopping processes decrease the cooperativity of the relaxation dynamics.

Figure 18(a) shows that the location of the peak in $\chi_4(t)$, τ_4 , quickly moves to larger times if the temperature is lowered. To determine the connection between the α -relaxation time τ and the time scale τ_4 , we plot in Fig. 21 τ_4 as a function of τ . Also included in the graph is the line $\tau_4 = \tau$ (solid line), and one recognizes that all the data points fall on this line with high accuracy. Hence, we can conclude that the time scale at which the system shows maximum cooperativity is on the time scale of the α -process, which is in agreement with earlier results.⁵² Also note that this conclusion is independent of k , i.e., the strength of the mean-field character does not play a role for this result. This result demonstrates that the α -relaxation process is tightly related to the presence of the dynamical heterogeneities, and hence, it is useful to study the latter in order to understand the slowdown of the relaxation dynamics. Finally, we mention that the direct proportionality of τ_4 to τ and the power law connection between τ_2 and τ (see Fig. 16) implies that we have the simple connection $\tau_2 \propto \tau_4^\kappa$, with an exponent κ given by $b/(a + b)$ [see Eq. (28)]. That this relation works indeed well is shown in the inset of Fig. 21. Since the exponent κ is less than unity, we see that τ_2 is smaller than τ_4 , as expected.⁶⁰ This can also be concluded from Fig. 8 where we have added in panels (a)–(c) the values of τ_4 (downward arrows) in that one recognizes that at low T , these are indeed to the right of the arrows presenting τ_2 . These graphs also show

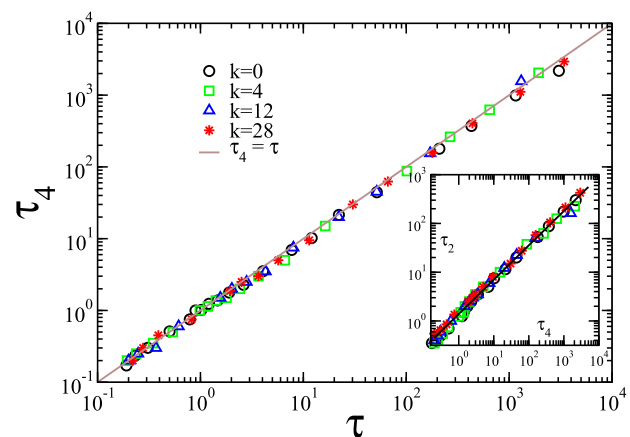


FIG. 21. The location of the peak in $\chi_4(t)$ as a function of the α -relaxation time τ . The symbols are for different values of k and different T , and the solid line is a power law with exponent 1.0. Inset: τ_2 as a function of τ_4 showing a power law connection between the two quantities. The straight line has a slope of 0.70.

that, interestingly, the (logarithmic) slope of the MSD at $t = \tau_4$ is independent of T but weakly dependent on k .

IV. SUMMARY AND CONCLUSION

We have introduced a simple glass-forming system that allows us to tune in a smooth manner its mean-field character. This is achieved by introducing additional k “pseudo-neighbors” with which a particle can interact. These additional interactions are long-ranged, and hence with the increase in k , each particle becomes increasingly connected with the rest of the system. However, since we also keep the original interaction between nearest-neighbor particles, our model has the advantage of maintaining a liquid-like structure even in the mean-field limit, i.e., the nearest neighbor distances are always of the order of the particle diameter, which is in contrast to other models that allow tuning their mean-field character.²³

We find that the structure of the system, as characterized by the radial distribution function or the static structure factor, remains unchanged with the addition of the K pseudo-neighbors, also in contrast to previous models. Due to the way the model is set up, it is possible to analytically calculate all the static structural properties of the system from the knowledge of the $k = 0$ system. This allows us to understand that the additional interactions give rise to an effective potential that increases with k , thus influencing the relevant temperature scale of the system.

Due to the presence of the pseudo-neighbors, the relaxation dynamics shows a very strong dependence on k in that the onset temperature and the critical temperature of mode-coupling theory increase with the increase in k . However, once the relaxation times are expressed in terms of the critical temperature of MCT, one finds only a mild k -dependence, indicating that for this class of systems, T_c is the most relevant parameter for the dynamics, at least in the T -range investigated here. We note that the range in temperature in which MCT seems to give a good description of the relaxation dynamics increases systematically with the increase in k , thus indicating that in the mean-field limit, the theory becomes exact. This is also confirmed by the observation that the dynamical heterogeneities, characterized by the dynamic susceptibility $\chi_4(t)$, decrease with the increase in k .

It is often believed that the fragility of the glass former is directly related to the presence of dynamical heterogeneities (or more precisely to the value of the stretching parameter β in the Kohlrausch–Williams–Watts function used to fit the time-correlation functions).^{61–63} Since we find that the fragility of the system increases with k , while the dynamic heterogeneity decreases, we conclude that there is no such (strict) connection between these two quantities, although we do not want to exclude the possibility that in practice, there might be a certain correlation. This result is in qualitative agreement with the findings in earlier studies.^{29,64} Sengupta *et al.* have reported that compared to a three-dimensional system, the corresponding four-dimensional system was less heterogeneous but more fragile.²⁹ This is also corroborated by the experimental data analyzed by Dyre, which indicate that there is no direct connection between fragility and heterogeneity.⁶⁴

The possibility to tune the mean-field character of the system without changing the structure also allows elucidating the relation between the non-Gaussian parameter $\alpha_2(t)$ and $\chi_4(t)$. While

previous studies have often considered both functions to be indicators for the dynamical heterogeneities, our analysis shows that this is not the case at all since their dependence on k is very different. Therefore, our work clearly shows that these two observables convey information that is very different, a conclusion that is in line with previous results that showed that the peak in $\alpha_2(t)$ has a temperature dependence that differs from the one of χ_4^p .²⁹ Furthermore, we also recall that for the MK model,²³ one finds that χ_4^p decreases with the increase in mean-field character of the system, i.e., the same behavior as we have found here, but that also the value of α_2^p decreases, while in our case, we find that α_2^p is independent of k . Also, in the case of the Gaussian core model, it was found that its $\alpha_2(t)$ peak is lower than the one for the Kob–Andersen model, whereas the χ_4 peak is much higher.^{25,26} The authors of these papers justified these results by stating that α_2 provides a measure of the degree of dynamic heterogeneity and, thus, its peak value should be lower for more mean-field-like models and χ_4 provides a measure of the size of the domains and systems that have larger domains and should have higher value of χ_4 . Although this interpretation might apply to the Gaussian core model, it is not in agreement with the system studied here and hence not general. This suggests that further studies are required to understand the exact information provided by χ_4 and α_2 and how these two quantities are related to each other.

Finally, we also note that the decrease in χ_4 with the increase in k can be due to the fact that the fluctuations in the overlap function do indeed decrease, i.e., the relaxation dynamics of the system becomes more homogeneous, as expected for a mean-field-like system. However, since with the increase in k , the characteristic temperatures of the system also increase, the fluctuations should decrease. Hence, for the moment, it is not clear which one of the two mechanisms is the main cause for the decrease in χ_4^p that we observe in the present work.

In an earlier study involving different glass-formers, evidence was given that the locally preferred structures (LPSs) are connected to the dynamics only for systems that are not mean-field-like.⁶⁵ The ability of the present model to continuously tune the mean-field behavior makes it thus an ideal system to check the validity of this observation. Since we find that with the increase in the number of pseudo-neighbors, the LPS remains unchanged, whereas the dynamics slows down, this suggests that with an increase in the mean field nature, the correlation between the LPS and the dynamics decreases, a result that corroborates the earlier findings from Ref. 65.

The range of k that we were able to access in the present simulation is relatively modest, since for larger k , the relaxation dynamics became too slow to equilibrate the system within a reasonable amount of computer time. It is, however, of interest to make an educated guess on what will happen if k is increased further. Our analytical results for the structure, Fig. 5, show that with the increase in k , the main peak in the effective radial distribution function becomes very high. In this limit, one can thus expect that the contribution from the pseudo-neighbors will start to dominate the one from the real nearest neighbors and hence will make the system mean-field-like. However, from the graph, we recognize that this increase becomes strong only when k is larger than $O(10^2)$, i.e., a value that is at present somewhat beyond the reach of standard computer simulations. It can be expected, however, that in the near future, improved algorithms will allow us to deal with this bottleneck. In that case, our

approach will thus allow us to make more stringent investigations on how the properties of a normal three dimensional glass-former can be connected to the corresponding system in the mean field limit.

This summary clearly indicates that the details of how the mean-field limit is approached are important and future studies are needed to clarify this point. Finally, we note that the approach we propose here on how the mean-field character is tuned can be applied to any system. Hence, it will be interesting to study whether other types of interaction potentials, such as the Coulomb potentials used to describe oxide glass formers, will give qualitatively the same behavior or, in other words, whether the approach to the mean-field limit depends on the nature of the local structure of the system.

ACKNOWLEDGMENTS

W.K. is a member of the Institut Universitaire de France. S.M.B. thanks SERB for funding. U.K.N. thanks the CSIR for his fellowship. The authors thank C. Dasgupta, D. Coslovich, M. K. Nandi, and M. Sharma for discussions. U.K.N. thanks S. Sengupta, A. Banerjee, and Md. Alamgir for the help with the initial setup of the system.

DATA AVAILABILITY

The data that support the findings of this study are available from the corresponding author upon reasonable request.

REFERENCES

- W. Kob and K. Binder, *Glassy Materials and Disordered Solids: An Introduction to Their Statistical Mechanics* (World Scientific, 2011).
- W. Götze, *J. Phys.: Condens. Matter* **11**, A1 (1999).
- W. Götze, *Complex Dynamics of Glass-Forming Liquids: A Mode-Coupling Theory* (Oxford Science Publication, 2008).
- L. M. C. Janssen, *Front. Phys.* **6**, 97 (2018).
- S. P. Das, *Statistical Physics of Liquids at Freezing and Beyond* (Cambridge University Press, 2011).
- T. R. Kirkpatrick and P. G. Wolynes, *Phys. Rev. A* **35**, 3072 (1987).
- X. Xia and P. G. Wolynes, *Proc. Natl. Acad. Sci. U. S. A.* **97**, 2990 (2000).
- V. Lubchenko and P. G. Wolynes, *J. Chem. Phys.* **119**, 9088 (2003).
- W. Kob and H. C. Andersen, *Phys. Rev. E* **51**, 4626 (1995).
- W. Kob and H. C. Andersen, *Phys. Rev. E* **52**, 4134 (1995).
- W. Kob, T. Gleim, and K. Binder, *AIP Conf. Proc.* **489**, 68 (1999).
- S. M. Bhattacharyya, B. Bagchi, and P. G. Wolynes, *Proc. Natl. Acad. Sci. U. S. A.* **105**, 16077 (2008).
- M. K. Nandi and S. M. Bhattacharyya, *J. Phys.: Condens. Matter* **32**, 064001 (2019).
- S.-H. Chong, *Phys. Rev. E* **78**, 041501 (2008).
- E. Flenner and G. Szamel, *J. Chem. Phys.* **138**, 12A523 (2013).
- M. K. Nandi, A. Banerjee, S. Sengupta, S. Sastry, and S. M. Bhattacharyya, *J. Chem. Phys.* **143**, 174504 (2015).
- M. K. Nandi, A. Banerjee, C. Dasgupta, and S. M. Bhattacharyya, *Phys. Rev. Lett.* **119**, 265502 (2017).
- M. K. Nandi and S. M. Bhattacharyya, *arXiv:2011.02299* (2020).
- J. P. Garrahan and D. Chandler, *Phys. Rev. Lett.* **89**, 035704 (2002).
- Y. Jung, J. P. Garrahan, and D. Chandler, *J. Chem. Phys.* **123**, 084509 (2005).
- A. Ikeda and K. Miyazaki, *Phys. Rev. Lett.* **104**, 255704 (2010).
- B. Schmid and R. Schilling, *Phys. Rev. E* **81**, 041502 (2010).
- R. Mari and J. Kurchan, *J. Chem. Phys.* **135**, 124504 (2011).
- L. Berthier, G. Biroli, D. Coslovich, W. Kob, and C. Toninelli, *Phys. Rev. E* **86**, 031502 (2012).
- D. Coslovich, A. Ikeda, and K. Miyazaki, *Phys. Rev. E* **93**, 042602 (2016).
- A. Ikeda and K. Miyazaki, *J. Chem. Phys.* **135**, 054901 (2011).
- A. Ikeda and K. Miyazaki, *Phys. Rev. Lett.* **106**, 015701 (2011).
- M. K. Nandi and S. M. Bhattacharyya, *J. Chem. Phys.* **148**, 034504 (2018).
- S. Sengupta, S. Karmakar, C. Dasgupta, and S. Sastry, *J. Chem. Phys.* **138**, 12A548 (2013).
- P. Charbonneau, A. Ikeda, G. Parisi, and F. Zamponi, *Proc. Natl. Acad. Sci. U. S. A.* **109**, 13939 (2012).
- J. P. Hansen and I. R. McDonald, *Theory of Simple Liquids* (Elsevier, Amsterdam, 1986).
- D. Coslovich, M. Ozawa, and W. Kob, *Eur. Phys. J. E* **41**, 62 (2018).
- A. Banerjee, M. K. Nandi, S. Sastry, and S. Maitra Bhattacharyya, *J. Chem. Phys.* **147**, 024504 (2017).
- P. Chaudhuri, L. Berthier, P. I. Hurtado, and W. Kob, *Phys. Rev. E* **81**, 040502 (2010).
- S. Sastry, *Nature* **409**, 164 (2001).
- S. Sastry, *PhysChemComm* **3**, 79 (2000).
- U. K. Nandi, S. Sengupta, W. Kob, and S. M. Bhattacharyya, "Connecting real glasses to mean-field models: A thermodynamic study" (unpublished) (2020).
- C. A. Angell, *Science* **267**, 1924 (1995).
- R. Das, C. Dasgupta, and S. Karmakar, *Front. Phys.* **8**, 210 (2020).
- W. Kob and H. C. Andersen, *Phys. Rev. Lett.* **73**, 1376 (1994).
- A. Cavagna, I. Giardina, and G. Parisi, *J. Phys. A: Math. Gen.* **34**, 5317 (2001).
- T. R. Kirkpatrick and P. G. Wolynes, *Phys. Rev. B* **36**, 8552 (1987).
- T. R. Kirkpatrick and D. Thirumalai, *Phys. Rev. Lett.* **58**, 2091 (1987).
- C. Brangian, W. Kob, and K. Binder, *Europhys. Lett. (EPL)* **53**, 756 (2001).
- M. D. Ediger, *Annu. Rev. Phys. Chem.* **51**, 99 (2000).
- W. Kob, C. Donati, S. J. Plimpton, P. H. Poole, and S. C. Glotzer, *Phys. Rev. Lett.* **79**, 2827 (1997).
- C. Donati, J. F. Douglas, W. Kob, S. J. Plimpton, P. H. Poole, and S. C. Glotzer, *Phys. Rev. Lett.* **80**, 2338 (1998).
- B. Doliwa and A. Heuer, *Phys. Rev. Lett.* **80**, 4915 (1998).
- M. M. Hurlley and P. Harrowell, *J. Chem. Phys.* **105**, 10521 (1996).
- K. Kim and S. Saito, *J. Chem. Phys.* **138**, 12A506 (2013).
- T. Odagaki and Y. Hiwatari, *Phys. Rev. A* **43**, 1103 (1991).
- F. W. Starr, J. F. Douglas, and S. Sastry, *J. Chem. Phys.* **138**, 12A541 (2013).
- G. Buchalla, U. Dersch, W. Götze, and L. Sjögren, *J. Phys. C* **21**, 4239 (1988).
- T. Gleim, W. Kob, and K. Binder, *Phys. Rev. Lett.* **81**, 4404 (1998).
- M. Nauroth and W. Kob, *Phys. Rev. E* **55**, 657 (1997).
- R. Das, I. Tah, and S. Karmakar, *J. Chem. Phys.* **149**, 024501 (2018).
- L. Berthier, G. Biroli, J.-P. Bouchaud, W. Kob, K. Miyazaki, and D. R. Reichman, *J. Chem. Phys.* **126**, 184503 (2007).
- L. Berthier, G. Biroli, J.-P. Bouchaud, W. Kob, K. Miyazaki, and D. R. Reichman, *J. Chem. Phys.* **126**, 184504 (2007).
- C. Brangian, W. Kob, and K. Binder, *J. Phys. A: Math. Gen.* **35**, 191 (2002).
- E. Flenner and G. Szamel, *Phys. Rev. E* **72**, 011205 (2005).
- R. Böhmer, K. L. Ngai, C. A. Angell, and D. J. Plazek, *J. Chem. Phys.* **99**, 4201 (1993).
- X. Xia and P. G. Wolynes, *Phys. Rev. Lett.* **86**, 5526 (2001).
- K. Niss, C. Dalle-Ferrier, G. Tarjus, and C. Alba-Simionesco, *J. Phys.: Condens. Matter* **19**, 076102 (2007).
- J. C. Dyre, *J. Phys.: Condens. Matter* **19**, 205105 (2007).
- G. M. Hocky, D. Coslovich, A. Ikeda, and D. R. Reichman, *Phys. Rev. Lett.* **113**, 157801 (2014).